

Searches for new physics in final states with multiple top quarks with the ATLAS detector and upgrade of the ATLAS tracking detector

Dissertation
zur Erlangung des Doktorgrades

an der Fakultät für Mathematik, Informatik und Naturwissenschaften
Fachbereich Physik
der Universität Hamburg

vorgelegt von
Elizaveta Sitnikova

Hamburg
2025

Gutachter der Dissertation:

Prof. Dr. Kerstin Tackmann
Dr. Krisztian Peters

Zusammensetzung der Prüfungskommission:

Prof. Dr. Günter Sigl
Prof. Dr. Kerstin Tackmann
Dr. Krisztian Peters
Prof. Dr. Christian Schwanenberger
Dr. Sergio Díez Cornell

Vorsitzender der Prüfungskommission:

Prof. Dr. Günter Sigl

Datum der Disputation:

25.02.2025

Vorsitzender des Fach-Promotionsausschusses Physik:

Prof. Dr. Wolfgang J. Parak

Leiter des Fachbereichs Physik:

Prof. Dr. Markus Drescher

Dekan der Fakultät MIN:


Prof. Dr.-Ing. Norbert Ritter

Declaration on oath

I hereby declare and affirm that this doctoral dissertation is my own work and that I have not used any aids and sources other than those indicated.

If electronic resources based on generative artificial intelligence (gAI) were used in the course of writing this dissertation, I confirm that my own work was the main and value-adding contribution and that complete documentation of all resources used is available in accordance with good scientific practice. I am responsible for any erroneous or distorted content, incorrect references, violations of data protection and copyright law or plagiarism that may have been generated by the gAI.

Hamburg, den 06.01.2025



Elizaveta Sitnikova

Abstract

The Standard Model's known limitations drive the search for new physics, a major focus of modern experimental particle physics. This thesis presents two searches for Beyond the Standard Model physics in the four-top-quark final state at the ATLAS experiment. The first search focuses on final states with a single lepton. The mass of the resonance is explicitly reconstructed by using the products of its fully-hadronic decay. The presence of the signal is investigated both for a simplified vector top-philic boson model, and without model dependence by identifying localized deviations in data compared to the background. The data was found to be compatible with the background-only hypothesis, and exclusion limits were set. The second search investigates final states with at least two reconstructed leptons with the same-sign electric charge. This thesis presents the algorithm for reconstruction of the resonance in this final state and shows its potential application for obtaining model-independent results for final states with multiple leptons.

Before the next LHC phase, the current ATLAS tracking detector will be replaced by a new one, called the ITk. The outer part of the ITk is made using silicon strip sensors, and in the forward regions the tracking is performed in the endcaps. This thesis describes the work on production and quality control of ITk silicon strip endcap modules, the single sensitive units in the ITk strip endcaps. A tool for monitoring module production is presented, which allows to identify deviations in the production process in time and quickly mitigate them in order to ensure excellent quality of the produced modules. The most demanding module quality control step is thermal cycling, requiring a specific setup and dedicated software, both of which are described in this work.

Zusammenfassung

Die bekannten Einschränkungen des Standardmodells treiben die Suche nach neuer Physik voran und bilden einen zentralen Schwerpunkt der modernen experimentellen Teilchenphysik. Diese Dissertation präsentiert zwei Suchen nach Physik jenseits des Standardmodells am ATLAS Experiment, fokussiert auf Endzustände mit vier Top-Quarks. Die erste Analyse untersucht Endzustände mit einem einzelnen Lepton, wobei die Masse der Resonanz explizit rekonstruiert wird. Hierbei werden die Produkte des vollständig hadronischen Zerfalls verwendet. Das Vorhandensein eines Signals wird sowohl innerhalb eines vereinfachten top-philic Boson Models als auch modellunabhängig geprüft, indem lokale Abweichungen zwischen den Daten und dem Hintergrund identifiziert werden. Die Ergebnisse weisen eine Kompatibilität der Daten mit der Untergrundhypothese auf, und es wurden Ausschlussgrenzen festgelegt. Die zweite Untersuchung richtet sich auf Endzustände mit mindestens zwei rekonstruierten Leptonen gleicher elektrischer Ladung. In diesem Kontext wird ein Algorithmus zur Resonanzrekonstruktion vorgestellt, der eine vielversprechende Grundlage bietet, um modellunabhängige Ergebnisse für Endzustände mit mehreren Leptonen zu erzielen.

Für die nächste Phase des LHC wird der aktuelle ATLAS Spurendetektor durch den sogenannten ITk ersetzt. Der äußere Teil des ITk besteht aus Silizium-Streifensensoren, während in den Vorwärtsregionen die Spurrekonstruktion in den Endkappen erfolgt. Diese Dissertation beschreibt die Produktion und Qualitätssicherung der ITk-Silizium-Streifen-Endkappenmodule, den grundlegenden Einheiten in den Endkappen. Ein speziell entwickeltes Werkzeug zur Überwachung des Produktionsprozesses wird vorgestellt, das dazu dient, Abweichungen frühzeitig zu erkennen und zu beheben, um die hohe Qualität der Module sicherzustellen. Besonderes Augenmerk liegt auf die thermische Wechselbeanspruchung, dem anspruchsvollsten Schritt der Qualitätskontrolle. Dieses Verfahren erfordert eine eigens entwickelte Einrichtung und spezielle Software, die beide in dieser Arbeit detailliert beschrieben werden.

Contents

| | |
|---|-----------|
| Introduction | 1 |
| Author's contributions | 3 |
| 1 Theoretical overview | 5 |
| 1.1 The Standard Model | 5 |
| 1.2 Beyond the Standard Model theories | 13 |
| 1.3 Four top quark final state | 18 |
| 2 ATLAS and LHC | 21 |
| 2.1 LHC | 21 |
| 2.2 ATLAS | 23 |
| 3 ITk module assembly and testing | 29 |
| 3.1 Tracker upgrade for High-Luminosity LHC | 29 |
| 3.2 Overview of the strip module assembly and testing | 33 |
| 3.3 IV comparison studies | 36 |
| 3.4 Strip module electrical tests | 53 |
| 3.5 Thermal cycling | 59 |
| 4 Object reconstruction in the ATLAS experiment | 75 |
| 4.1 Common procedures | 75 |
| 4.2 Electrons | 76 |
| 4.3 Muons | 79 |
| 4.4 Jets | 81 |
| 4.5 Tau leptons | 86 |
| 4.6 Missing Transverse Momentum (MET) | 86 |
| 5 Search for heavy vector resonances in the four top quark final state | 89 |
| 5.1 Motivation | 89 |
| 5.2 Analysis strategy | 89 |
| 5.3 Data and Monte Carlo samples | 91 |
| 5.4 Object selection | 94 |
| 5.5 Event selection | 95 |
| 5.6 Analysis region definition | 96 |

| | | |
|----------|--|------------|
| 5.7 | Background estimation | 96 |
| 5.8 | Systematic uncertainties | 99 |
| 5.9 | Statistical analysis | 104 |
| 5.10 | Results | 109 |
| 5.11 | Preservation and reuse of the analysis framework | 116 |
| 6 | Method for model-independent search for heavy resonances in multi-lepton final states | 119 |
| 6.1 | Motivation | 119 |
| 6.2 | Analysis strategy | 120 |
| 6.3 | Data and Monte Carlo samples | 120 |
| 6.4 | Object selection | 122 |
| 6.5 | Event selection | 125 |
| 6.6 | Resonance mass reconstruction | 125 |
| 6.7 | Background estimation | 138 |
| 6.8 | Systematic uncertainties | 140 |
| 6.9 | Analysis region definition | 141 |
| 6.10 | Statistical analysis | 143 |
| | Conclusions | 153 |
| | Appendix | 155 |
| A | Variables for communication with the PLC | 155 |
| | Bibliography | 169 |
| | Acknowledgements | 181 |

Introduction

The Standard Model is the most successful theory in particle physics to date, providing an accurate description of nearly all experimentally observed phenomena in particle physics. Its final missing component, the Higgs boson, was discovered by the ATLAS and CMS experiments at the Large Hadron Collider (LHC) in 2012. This discovery was an important achievement, as it confirmed the mechanism responsible for giving mass to elementary particles. Despite its remarkable success, the Standard Model has major shortcomings. For example, it does not account for gravity, dark matter or dark energy. To address these limitations, multiple experimental searches are underway to explore physics beyond the Standard Model (BSM). These include analyses of cosmological data, studies of neutrinos from various sources, and investigations using data from particle colliders.

The LHC is the largest and the most energetic particle collider ever built. It currently accelerates and collides protons with the center-of-mass energy of 13.6 TeV. ATLAS is one of the experiments analyzing the collision data from the LHC. It utilizes a multipurpose detector, capable of measuring the kinematic characteristics of almost all long-living particles produced in a proton-proton collision. It is well suited for both precision measurement of the parameters of the Standard Model and for searches for new phenomena. The high collision energies and the large dataset recorded at the LHC facilitate opportunities for the new physics searches and enable exploration of previously inaccessible rare final states, such as those involving simultaneous production of multiple top quarks. A recent observation of four top quark production at the LHC by the ATLAS and CMS experiments and a measured excess in the rate of such events compared to Standard Model predictions motivates searches for BSM contributions to this final state. Such contributions are predicted by several BSM theories, postulating the existence of particles, which couple predominantly to top quarks.

Two searches for new physics in the multi-top-quark final states are presented in this thesis. The first search probes a theory that predicts a resonant production of a new particle in association with two top quarks, one of which decays to produce a lepton. This analysis, the first of its kind at the LHC, reconstructs the resonance directly, allowing for a model-independent result. Additionally, a model-dependent result is obtained for a simplified theory predicting a heavy vector boson, coupling exclusively to top quarks.

The second search focuses on the final states with several leptons, expanding and refining the first analysis. In addition to the previously mentioned theory, the two-Higgs doublet model is

also probed in this search. The search benefits from improved modeling and data reconstruction techniques and utilizes machine learning algorithms to separate signal and background events. An algorithm for explicit reconstruction of the resonance has been developed, which opens unique possibilities of obtaining a model-independent result in this search as well, which was never previously done for multi-lepton final states.

In the coming years, the LHC will be upgraded to provide a higher rate of proton-proton collisions, requiring upgrades to key components of the ATLAS detector. In particular, the tracking detector, that does not have enough radiation hardness or granularity to operate in these high luminosity conditions, will be replaced by an all-silicon Inner Tracker (ITk). This tracker, currently under construction, is a collaborative effort involving multiple institutions worldwide. The ITk consists of two parts, with the inner part made using silicon pixel sensors and the outer part made using silicon strip sensors. The individual sensitive units of the strip sub-detector are called modules, and their construction involves multiple steps and requires strict quality control at every step. The most complicated and demanding quality control procedure is thermal cycling, which is a stress test performed for every assembled module in dedicated testing setups. This thesis describes module assembly and quality control with focus on the thermal cycling procedure and presents a tool for monitoring the quality of the modules throughout the production steps.

The thesis is organized as follows. Chapter 2 provides an overview of the Large Hadron Collider and describes the subsystems of the ATLAS detector. Chapter 3 introduces the LHC upgrade and presents the Inner Tracker, including details on strip module assembly and quality control, the thermal cycling process and the module production monitoring tool. Chapter 4 describes the reconstruction of physics objects from the data gathered by the ATLAS detector. Chapter 1 presents the Standard Model and discusses its limitations, followed by an overview of BSM theories that motivate searches in multi-top-quark final states. Chapter 5 presents the search for a heavy vector boson in a single-lepton final state, detailing all steps of the analysis and the final results. Chapter 6 covers the ongoing search for BSM resonances in multi-lepton final states. Although this analysis is still in development, the chapter outlines the current plan and emphasizes the development of an algorithm for resonance mass reconstruction. The algorithm's sensitivity is evaluated using simulated events, and the expected results are presented. Finally, the Conclusions chapter summarizes the projects covered in the thesis and offers an outlook on their potential and future directions.

Author's contributions

Large experiments like ATLAS are only possible through collaborative efforts of thousands of people. The collaboration includes more than 3000 members, each contributing to various aspects of the experiment, including detector design, construction, operation, as well as data reconstruction and numerous physics analyses. The work presented in this thesis builds on the combined efforts of the entire collaboration. This section lists the author's direct contributions to these projects.

The author's primary contributions to the single-lepton resonance search include finalizing key aspects of the analysis, such as the classification of the $t\bar{t}$ +jets events and de-correlation of systematic uncertainty related to the choice of the Monte Carlo generator. The author also contributed to the inclusion of signals with various model parameters, performing signal bias uncertainty calculations for several individual signal samples and calculating the final exclusion limits. In addition, the author created an event display with one of the events collected by the ATLAS detector, implemented interaction between the analysis framework and the RECAST software, enabling future reuse of the framework and validated this workflow using an alternative signal model sample.

For the search for heavy resonances in the same-sign multi-lepton final states, the author developed an algorithm for reconstruction of the resonant particle mass, utilizing a previously existing algorithm for reconstruction of neutrino momenta. The mass reconstruction algorithm was validated and its expected performance was evaluated.

The author contributed to multiple steps of ITk strip endcap module production performed at DESY, including testing silicon sensors, assembled modules, and conducting module assembly. The author developed software for IV curve comparison and performed all related studies mentioned in this thesis. Furthermore, in collaboration with colleagues from DESY, the author integrated the PLC-based thermal cycling setup into the common software framework and automated the thermal cycling procedure. That involved implementation of all the classes in the `ColdJigLib2` software, that are specific to the PLC-based setups. The author optimized the parameters of the PLC program to ensure that the thermal cycling procedure fits the requirements and performed thermal cycling of several ITk strip endcap modules.

1. Theoretical overview

Particle physics aims to answer fundamental questions about the world that surrounds us, about its construction and interactions between its constituents. The Standard Model has been remarkably successful at this task, however it has significant limitations, as it fails to explain some of the observed phenomena.

This chapter gives an overview of the Standard Model, describes its shortcomings and details several theories Beyond the Standard Model, able to address some of the them. Finally, contributions to the four-top-quark final state from both Standard-Model and Beyond-the-Standard-Model processes are discussed.

1.1 The Standard Model

The Standard Model (SM) is the most complete theory to date describing nearly all observed phenomena in particle physics. The predictive ability of this theory was proven by many experimental observations, such as the discovery of Z [1] and W [2] bosons, gluon [3], and top [4, 5] and charm [6, 7] quarks. It was most recently shown in 2012 when the Higgs boson, the last missing piece of the Standard Model, was discovered [8, 9]. This section provides a brief overview of the most important aspects of the SM. More detailed descriptions can be found in [10–12].

1.1.1 Particles

All particles in the Standard Model can be classified by their spin, which is the intrinsic angular momentum of a particle. Particles with integer spin are called *bosons* and they follow Bose-Einstein statistics [13]. Particles with half-integer spin follow Fermi-Dirac statistics and are called *fermions* [14, 15]. While all known matter consists of fermions, bosons mediate interactions in the Standard Model. Three fundamental interactions are described by the Standard Model: electromagnetic, weak, and strong. The fourth interaction that can be observed is gravitation, which is not included in the SM, however its effects on particle physics are often several orders of magnitude weaker than those of the other tree forces, which makes it possible to neglect gravitation in most cases. The electromagnetic interaction is mediated by photons, and the weak interaction is mediated by an electrically neutral gauge Z -boson and the two charged gauge W^{\pm} -bosons. Above the so-called *electroweak unification energy*, these two interactions

are united into one electroweak interaction. This unification was proposed by S. Glashow [16], A. Salam [17], and S. Weinberg [18]. There are four electroweak charges that include the electric charge.

The electrically-neutral gluons mediate strong force interactions, and these mediators carry a so-called *color charge*. There are three color charges: red, green, and blue, each of which has a corresponding anticolor charge. Every gluon carries one color and one anticolor charge.

The fermions are represented by three generations of quarks and leptons. There are three *up-type* quarks: up, charm, and top, and three *down-type* quarks: down, strange, and bottom. The up-type quarks have an electric charge of $+2/3e$, where e is the fundamental electric charge, while the down-type quarks have a charge of $-1/3e$. Each quark carries a color charge and each antiquark carries an anticolor charge. The leptons can be divided into charged and neutral ones. The charged leptons include electron, muon, and tau lepton; the neutral leptons, called neutrinos, have three flavors, each corresponding to a charged lepton type. Fermions can be organized into three generations, with the masses of the fermions increasing in each subsequent generation. The schematic structure of these generations is shown in Figure 1.1. Each generation has one up-type and one down-type quark, one charged lepton, and one neutrino, as well as all of their antiparticles. Leptons only interact via the electromagnetic and weak interactions, while quarks can also interact via the strong interaction.

Due to the color confinement, quarks are always observed in bound states, called hadrons, which are color-neutral and have integer electric charges. Based on the number of quarks they are composed of, hadrons can be classified as *mesons* or *baryons*. Mesons consist of a quark-antiquark pair, and the color neutrality is ensured by the antiquark having the anticolor to the color carried by the quark. Baryons, on the other hand, are composed of three (anti-)quarks, each carrying a different (anti-)color, making them color neutral as well.

1.1.2 Symmetries and interactions

The Standard Model can be described in the mathematical framework of Quantum Field Theory (QFT) which combines the principles of classical relativistic field theory and quantum mechanics. The gauge symmetry group of the SM is

$$SU(3)_C \times SU(2)_L \times U(1)_Y, \quad (1.1)$$

which is the direct product of three fundamental gauge groups. $SU(3)_C$ is a special unitary group of degree 3, which describes the strong interaction. The subscript C denotes color. $SU(2)_L$ is a second-order special unitary group associated with weak interaction. The subscript L indicates that only the left-handed fermions carry this quantum number. $U(1)_Y$ is a unitary group of degree 1, which describes electromagnetic interaction, and the subscript Y refers to the weak hypercharge defined as $Y = 2(Q - T_3)$, where Q is the electric charge and T_3 is the z -component of the weak isospin.

To construct the Lagrangian of the Standard Model one needs to create a renormalizable Lagrangian from the fields in the system that respects the postulated symmetries. In the following sections the separate parts of the Lagrangian are explained in detail.

Electromagnetic interaction

Quantum electrodynamics (QED) describes the electromagnetic interaction in the Standard Model.

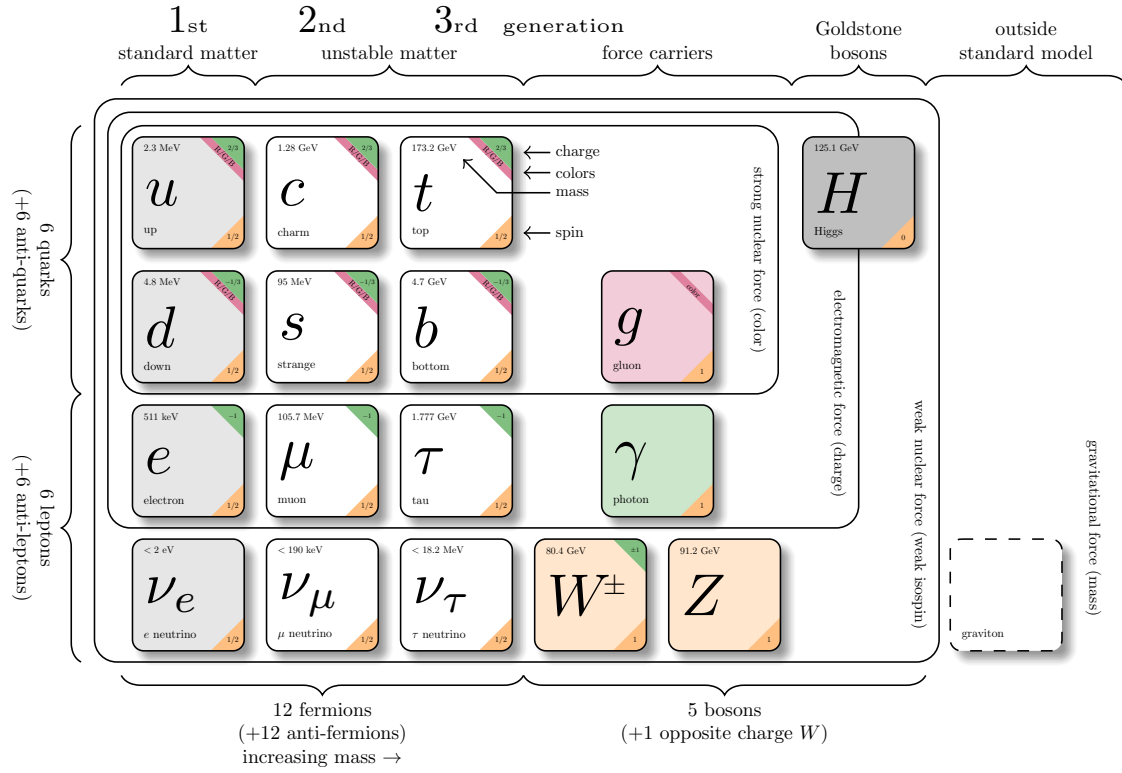


Figure 1.1: Schematic view of the Standard Model particles [19].

The Lagrangian of a free fermion field Ψ with mass m is given by

$$\mathcal{L}_0 = \bar{\Psi}(i\gamma^\mu\partial_\mu - m)\Psi, \quad (1.2)$$

where $\bar{\Psi} = \Psi^\dagger\gamma^0$ is the Dirac adjoint of Ψ , and γ^μ are the Dirac matrices. In this context and throughout the discussion, we apply the Einstein summation convention, assuming that summation occurs over the index μ or ν when in a product a same letter is used as an upper and a lower index (e.g. $\gamma^\mu\partial_\mu \equiv \sum_{\mu=0}^3 \gamma^\mu\partial_\mu$).

Although this Lagrangian is invariant under a global $U(1)$ transformation $\Psi(x) \mapsto e^{i\alpha}\Psi$, where α is constant, it is not invariant with respect to local $U(1)$ transformations $\Psi(x) \mapsto e^{iq\theta(x)}\Psi$, where q is the electric charge and θ is a local quantity. However, by introducing an additional field A_μ and replacing the partial derivative ∂_μ by the covariant derivative D_μ defined as

$$D_\mu \equiv \partial_\mu - iqA_\mu, \quad (1.3)$$

the Lagrangian can be made invariant under local $U(1)$ transformations as well. This additional field corresponds to the photon and transforms under local transformations as

$$A_\mu(x) \mapsto A_\mu(x) + \partial_\mu\theta(x). \quad (1.4)$$

The kinetic part of the photon Lagrangian is given by

$$\mathcal{L}_{kin} = -\frac{1}{4}F_{\mu\nu}F^{\mu\nu}, \quad (1.5)$$

where $F_{\mu\nu} = \partial_\mu A_\nu - \partial_\nu A_\mu$. If a mass term $-1/2 \times m_A^2 A^\mu A_\mu$ for the photon is added, the Lagrangian stops being invariant under the local $U(1)$ transformation, which means that the photon must be massless in QED.

The complete QED Lagrangian is therefore defined as follows:

$$\mathcal{L}_{\text{QED}} = -\frac{1}{4}F_{\mu\nu}F^{\mu\nu} + \bar{\Psi}(i\gamma^\mu D_\mu - m)\Psi. \quad (1.6)$$

Weak interaction and electroweak unification

The weak interaction in the SM is described together with the electromagnetic, following the electroweak unification proposed by Glashow, Weinberg, and Salam. The electroweak Lagrangian is invariant under $SU(2) \times U(1)$ transformations. Above the so-called unification energy equal to $\simeq 246$ GeV electromagnetic and weak forces unite into one electroweak force. Starting with the same Lagrangian for free fermions as in the beginning of the last section, while omitting the mass terms due to them violating the gauge symmetry, the Lagrangian for quarks and leptons can be written as

$$\mathcal{L} = \sum_f \bar{\Psi}_{L/R}^f(x) i\gamma^\mu \partial_\mu \Psi_{L/R}^f(x), \quad (1.7)$$

with

$$\Psi_{L/R}^f = \frac{1 \mp \gamma_5}{2} \Psi^f, \quad (1.8)$$

where index f denotes quarks and leptons, and the matrix $\gamma_5 \equiv i\gamma^0\gamma^1\gamma^2\gamma^3$. $\Psi_{L/R}$ denote left- and right-handed bispinor projections, which behave differently under the gauge group in the sense that left-handed components form doublets, while the right-handed ones are singlets. Therefore,

the mixed mass terms for fermions (e.g. $\bar{\Psi}_L \Psi_R$) are forbidden. The covariant derivative in this case is defined as

$$D_\mu \equiv \partial_\mu - ig \sum_{j=1}^3 \frac{\sigma^j}{2} W_\mu^j - ig' \frac{Y}{2} B_\mu, \quad (1.9)$$

where g and g' denote the gauge coupling constants for $SU(2)$ and $U(1)$ respectively, σ^j are the Pauli matrices, and Y is the weak hypercharge. The photon A_μ and the W^\pm and Z^0 bosons can be expressed in terms of the W_μ^j and B_μ boson fields:

$$W_\mu^\pm = \frac{1}{\sqrt{2}} (W_\mu^1 \mp i W_\mu^2), \quad (1.10)$$

$$Z_\mu^0 = \frac{1}{\sqrt{g^2 + g'^2}} (g W_\mu^3 - g' B_\mu), \quad (1.11)$$

$$A_\mu = \frac{1}{\sqrt{g^2 + g'^2}} (g' W_\mu^3 + g B_\mu). \quad (1.12)$$

The Weinberg angle θ_W is defined as

$$\cos \theta_W = \frac{g}{\sqrt{g^2 + g'^2}}, \quad \sin \theta_W = \frac{g'}{\sqrt{g^2 + g'^2}}. \quad (1.13)$$

Kinetic terms for W_μ^j and B_μ are

$$\mathcal{L}_{kin} = - \sum_{j=1}^3 \frac{1}{4} W_{\mu\nu}^j W_j^{\mu\nu} - \frac{1}{4} B_{\mu\nu} B^{\mu\nu}, \quad (1.14)$$

where $W_{\mu\nu}^j = \partial_\mu W_\nu^j - \partial_\nu W_\mu^j - \sum_{k=1}^3 \sum_{l=1}^3 g \epsilon^{jkl} W_\mu^k W_\nu^l$, $B_{\mu\nu} = \partial_\mu B_\nu - \partial_\nu B_\mu$, and ϵ^{jkl} is the totally antisymmetric Levi-Civita tensor.

Thus, the final electroweak Lagrangian without the mass terms reads

$$\mathcal{L}_{EW} = \sum_f \bar{\Psi}_{L/R}^f(x) i \gamma^\mu D_\mu \Psi_{L/R}^f(x) - \frac{1}{4} W_{\mu\nu}^j W_j^{\mu\nu} - \frac{1}{4} B_{\mu\nu} B^{\mu\nu}. \quad (1.15)$$

The mechanism of mass generation for gauge bosons and charged fermions is discussed below in the paragraph about the Higgs mechanism.

Strong interaction

The strong interaction in SM is described within the framework of quantum chromodynamics (QCD). An approach similar to the one used in the previous sections can be used to obtain the QCD Lagrangian. The six quark fields carry color charge and can be represented by

$$\Psi_q = \begin{pmatrix} \Psi_q^{\text{red}} \\ \Psi_q^{\text{green}} \\ \Psi_q^{\text{blue}} \end{pmatrix}, \quad (1.16)$$

where $q = u, d, c, s, t, b$ is the quark type. Considering these fields, the Lagrangian can be written as

$$\mathcal{L} = \sum_q \bar{\Psi}_q (i \gamma^\mu \partial_\mu - m_q) \Psi_q. \quad (1.17)$$

The covariant derivative for QCD is defined as

$$D_\mu \equiv \partial_\mu - ig_s \sum_a \frac{\lambda^a}{2} G_\mu^a, \quad (1.18)$$

where g_s is the strong coupling constant, λ^a are the Gell-Mann matrices, G_μ^a denotes the eight gluon fields, and index a denotes the gluon types. The commutation relation for the Gell-Mann matrices is

$$[\lambda_a, \lambda_b] = 2if^{abc}\lambda_c, \quad (1.19)$$

where f^{abc} are the structure constants, completely antisymmetric in the three indices. Defining $G_{\mu\nu}^a$ as

$$G_{\mu\nu}^a = \partial_\mu G_\nu^a - \partial_\nu G_\mu^a - g_s f^{abc} G_\mu^b G_\nu^c, \quad (1.20)$$

and adding the kinetic term for the gluons

$$\mathcal{L}_{kin} = -\frac{1}{4} \sum_a G_{\mu\nu}^a G^{\mu\nu a}, \quad (1.21)$$

the GCD Lagrangian can be written as

$$\mathcal{L}_{\text{QCD}} = \sum_q \bar{\Psi}_q (i\gamma^\mu D_\mu - m_q) \Psi_q - \frac{1}{4} \sum_a G_{\mu\nu}^a G^{\mu\nu a}. \quad (1.22)$$

Higgs mechanism

Due to the electroweak gauge symmetry bosons and fermions in the SM must be massless. This, however, contradicts the experiments in which masses of the particles, such as the gauge bosons, charged leptons and quarks, were measured with high precision. The solution to this problem involves introducing another field – *the Higgs field* – which gives mass to the particles via the *Higgs mechanism*. This solution was first proposed by Philipp Warren Anderson [20] and later developed independently by Robert Brout and François Englert [21]; Peter Higgs [22]; and Gerald Guralnik, Carl Richard Hagen and Tom Kibble [23].

Consider a Lagrangian

$$\mathcal{L} = (D_\mu \phi)^\dagger (D_\mu \phi) - V(\phi), \quad (1.23)$$

where ϕ is an $SU(2)$ doublet and the potential $V(\phi)$:

$$V(\phi) = -\mu^2 \phi^\dagger \phi + \lambda (\phi^\dagger \phi)^2. \quad (1.24)$$

Spontaneous symmetry breaking is possible when the minimum of that potential is obtained for non-zero values of ϕ . In the above-defined potential considering positive μ^2 , the minimum is at

$$\phi^\dagger \phi = \frac{\mu^2}{\lambda} \equiv v^2. \quad (1.25)$$

Without loss of generality the minimum is chosen as

$$\phi_0 = \frac{1}{\sqrt{2}} \begin{pmatrix} 0 \\ v \end{pmatrix}, \quad (1.26)$$

where v is called the vacuum expectation value (VEV) of ϕ .

Expanding the Lagrangian around ϕ_0 ,

$$\phi = \frac{1}{\sqrt{2}} \begin{pmatrix} 0 \\ v + h \end{pmatrix}, \quad (1.27)$$

the Lagrangian becomes

$$\mathcal{L} = (D_\mu \phi)^\dagger (D_\mu \phi) - \frac{1}{2}(2\mu^2)h^2 - \lambda u h^3 - \frac{1}{4}\lambda h^4 + \text{Const.} \quad (1.28)$$

This allows one to derive the mass of the Higgs boson from the quadratic term:

$$m_H = \sqrt{2\mu^2}. \quad (1.29)$$

With the electroweak covariant derivative defined as above in 1.9,

$$D_\mu \equiv \partial_\mu - ig \sum_{j=1}^3 \frac{\sigma^j}{2} W_\mu^j - ig' \frac{Y}{2} B_\mu \quad (1.30)$$

Mass terms for the gauge bosons can be derived by expanding the first term of the Lagrangian 1.28:

$$(D_\mu \phi)^\dagger (D_\mu \phi) = |(\partial_\mu - ig \frac{\sigma^j}{2} W_\mu^j - ig' \frac{Y}{2} B_\mu) \phi|^2. \quad (1.31)$$

$$\begin{aligned} \left| (-ig \frac{\sigma^j}{2} W_\mu^j - ig' \frac{Y}{2} B_\mu) \phi \right|^2 &= \frac{1}{8} \left| \begin{pmatrix} gW_\mu^3 + g'B_\mu & g(W_\mu^1 - iW_\mu^2) \\ g(W_\mu^1 + iW_\mu^2) & -(gW_\mu^3 - g'B_\mu) \end{pmatrix} \begin{pmatrix} 0 \\ v \end{pmatrix} \right|^2 \\ &= \frac{1}{8} \left| \begin{pmatrix} vg(W_\mu^1 - iW_\mu^2) \\ -v(gW_\mu^3 - g'B_\mu) \end{pmatrix} \right|^2 \\ &= \frac{1}{8} (v^2 g^2 (W_\mu^1 - iW_\mu^2)(W_\mu^1 + iW_\mu^2) + v^2 (gW_\mu^3 - g'B_\mu)^2) \\ &= \frac{1}{2} \left(\frac{vg}{2} \right)^2 W_\mu^+ W_\mu^- + \frac{1}{2} \left(\frac{\sqrt{g^2 + g'^2}}{2} \right)^2 Z_\mu^0. \end{aligned} \quad (1.32)$$

From this, masses of W and Z bosons are

$$m_W = \frac{vg}{2}, \quad m_Z = \frac{v\sqrt{g^2 + g'^2}}{2}, \quad (1.33)$$

while the photon remains massless as it does not get a mass term.

Fermions obtain their masses via Yukawa coupling with the Higgs field:

$$\mathcal{L}_{\text{Yukawa}} = \sum_f -g_Y^f (\bar{\Psi}_L^f \phi \Psi_R^f + \bar{\Psi}_R^f \bar{\phi} \Psi_L^f), \quad (1.34)$$

where g_Y^f represent the coupling constants, and masses of the fermions therefore are

$$m_f = \frac{vg_Y^f}{\sqrt{2}}. \quad (1.35)$$

1.1.3 Open questions

Despite its success in describing a large variety of processes, the Standard Model cannot be considered the theory of everything as it has its limitations:

- **Gravity** is not incorporated in the SM framework. The most successful theory that describes gravity is general relativity [24], and so far all attempts to quantize it and thus unite the two theories have not been successful.
- **Dark matter and dark energy.** According to many astrophysical observations, visible matter is not the only matter existing in our universe. For example, galaxies rotate at a higher speed than would be allowed if all their mass was contained in the visible matter [25, 26], therefore there needs to exist the invisible so-called *dark matter*. The name *dark matter* comes from the fact that this matter does not interact electromagnetically and therefore does not emit, reflect, or absorb light, making it impossible to see. Only $\sim 5\%$ of the universe consists of known matter, around 27% is dark matter and 68% is *dark energy*, an energy uniformly distributed through the spacetime, which is responsible for the accelerated expansion of the universe. Neither dark matter, nor dark energy are explained by the SM.
- **Neutrino masses and oscillations.** It has been experimentally observed that the three flavors of neutrinos can oscillate into each other, which is not explained by the Standard Model [27, 28]. Moreover, this oscillation is only possible if at least some neutrino flavors have non-zero masses, which also goes beyond the Standard Model predictions. The SM can be expanded to include massive neutrinos and their oscillations. In this case, the mass eigenstates are not the same as the flavor eigenstates, which makes the oscillation possible. The relation between the eigenstates is given by the Pontecorvo–Maki–Nakagawa–Sakata matrix (PMNS matrix) [29, 30]:

$$\begin{pmatrix} \nu_e \\ \nu_\mu \\ \nu_\tau \end{pmatrix} = \begin{pmatrix} U_{e1} & U_{e2} & U_{e3} \\ U_{\mu1} & U_{\mu2} & U_{\mu3} \\ U_{\tau1} & U_{\tau2} & U_{\tau3} \end{pmatrix} \begin{pmatrix} \nu_1 \\ \nu_2 \\ \nu_3 \end{pmatrix}, \quad (1.36)$$

where ν_e , ν_μ and ν_τ denote the flavor eigenstates and ν_1 , ν_2 and ν_3 – the mass eigenstates.

- **Hierarchy problem.** There is a big difference in scales between the mass of the Higgs boson ($\mathcal{O}(10^2)$ GeV) and the *Planck mass*, $m_P = \sqrt{\hbar c G^{-1}} = \mathcal{O}(10^{19})$ GeV, where \hbar is the reduced Planck constant, c is the speed of light and G is the gravitational constant. The Planck mass reflects the energy scale at which the quantum effects of gravity become significant.

As the Higgs boson’s mass is sensitive to quantum corrections from all scales present in nature, including the Planck scale, the mass that one would expect for the Higgs boson given the scale of these corrections is significantly higher than the experimentally observed mass. One possible explanation for this would be that there is a numerical cancellation, which reduces the mass to the observed value, however such a cancellation would require extreme fine-tuning of the parameters, which is considered unnatural. The mass of the Higgs boson is not a calculable parameter of the SM, and thus there is a need to search for a solution beyond the Standard Model.

- **Baryogenesis and matter-antimatter asymmetry.** In our universe, a dominance of matter over antimatter can be observed, and the Standard Model does not provide enough mechanisms that could lead to this. According to the SM, matter and antimatter in comparable amounts should have been created at the beginning of the universe, and

the amount of CP violation that exist in the SM is insufficient to explain the observed matter-antimatter asymmetry.

1.2 Beyond the Standard Model theories

To address the shortcomings of the Standard Model extensive searches for new physics are being conducted now in many experiments all over the world. In particular, many scientists hope that the LHC can provide an opportunity to find hints at this new physics due to the high statistics of gathered data and the high energies of the colliding protons.

Recent observation of four top quark production at the LHC by the ATLAS [31] and CMS [32] experiments motivates searches for Beyond Standard Model contributions to this final state. Many Beyond Standard Model (BSM) theories predict the existence of *top-philic* resonances, which couple more strongly to the top quark than to the light quarks, rendering other couplings negligible. In this section three such theories are presented and the production of the multi-top-quark final states is discussed.

1.2.1 A simplified model for a top-philic color-singlet Z'

This model, constructed with minimal assumptions about the properties of the Z' particle, is suitable for general searches for top-philic resonances [33]. The only postulated properties of the Z' are that it is a color-singlet, that it dominantly couples to the top quark pair and that it rarely interacts with the other SM particles. Such Z' boson could be a dark matter interaction mediator, and therefore this model allows one to probe the dark matter sector.

The interaction Lagrangian is

$$\mathcal{L} = \bar{t}\gamma_\mu (c_L P_L + c_R P_R) t Z'^\mu = c_t \bar{t}\gamma_\mu (\cos\theta P_L + \sin\theta P_R) t Z'^\mu, \quad (1.37)$$

where $P_{L/R} = (1 \mp \gamma_5)/2$ are the chirality projection operators, $c_t = \sqrt{c_L^2 + c_R^2}$ is the coupling strength of Z' to the top quarks, and the chirality angle θ is defined as $\tan\theta = c_R/c_L$.

The Lagrangian 1.37 yields the tree-level decay width

$$\Gamma(Z' \rightarrow t\bar{t}) = \frac{c_t^2 M_{Z'}}{8\pi} \sqrt{1 - \frac{4m_t^2}{M_{Z'}^2}} \left[1 + \frac{m_t^2}{M_{Z'}^2} (3\sin 2\theta - 1) \right] \approx \frac{c_t^2 M_{Z'}}{8\pi} \text{ for } m_t \ll M_{Z'}. \quad (1.38)$$

Therefore, when resonances with mass higher than the top quark mass are considered, the resonance is narrow for $c_t \sim 1$, as the relation $\Gamma/M_{Z'} \approx 1/8\pi$. Also worth noting is the fact that this model has only three parameters: the mass of the resonance $M_{Z'}$, the chirality angle θ and the coupling strength c_t .

On tree-level, the Z' resonance is always produced together with at least one more top quark. Sample Feynman diagrams of tree level production are shown in Figure 1.2. For $pp \rightarrow Z' + t\bar{t}$ production the channel $gg \rightarrow Z' + t\bar{t}$ gives the dominant contribution, accounting for up to 95% of the total production cross section. For the tqZ' and the tWZ' production, where q denotes a light quark, the dominant contribution comes from the initial states with b -quarks. The cross section of the tWZ' production is the smallest out of these three final states, the cross section of the tqZ' production is slightly larger, and the production cross section of $t\bar{t}Z'$ is around two times bigger as the ones for tWZ' and tqZ' . Therefore all three production modes give substantial contributions to the Z' production.

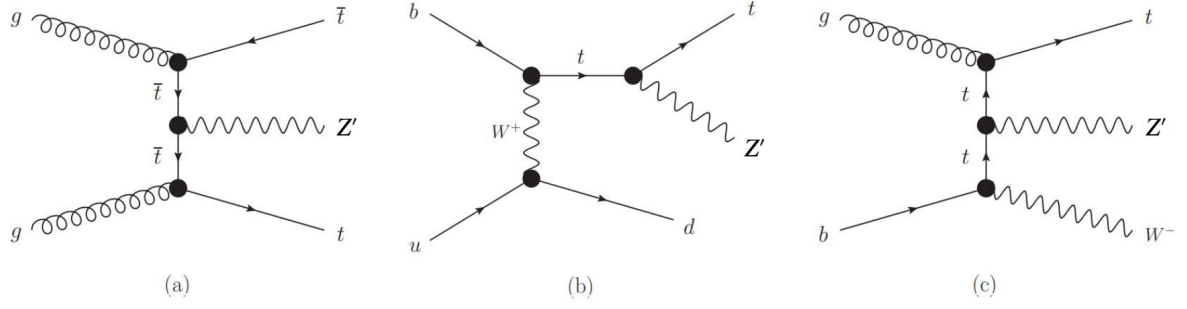


Figure 1.2: Sample diagrams for production of the Z' particle, showcasing different possible production modes. (a) s-channel production via strong interaction, (b) production along with a top quark and another quark via electroweak interaction, (c) production along with a top quark and a W boson via mixed strong and electroweak interactions [33].

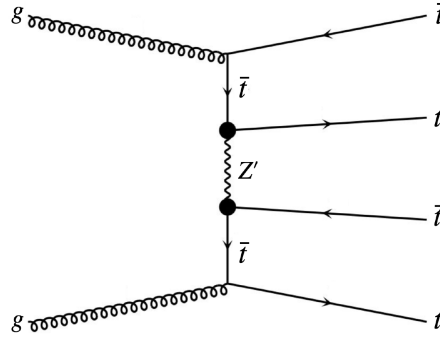


Figure 1.3: A Feynman diagram showing the t-channel production of the Z' particle.

The tWZ' and tqZ' production modes, the so-called *single top production modes*, strongly depend on the chirality parameter θ , because they are mediated by the $t - W - b$ interaction. For these processes, the value $\theta = 0$ corresponds to the pure left-handed interaction and leads to the largest cross-section for a given Z' mass, while $\theta = \pi/2$ corresponds to the pure right-handed interaction and leads to the smallest cross-section. For the $t\bar{t}Z'$ production mode there is no such dependence on the chirality angle, as the process does not include a $t - W - b$ coupling.

Additionally to production of the Z' resonance in the s-channel, as shown in Figure 1.2 (a), the t-channel production contributes to the four top quark final state. The Feynman diagram for this process is shown in Figure 1.3. This contribution is small, and for higher masses of Z' it increases the cross section by about 10%, while for lower masses this contribution is even smaller.

The search described in this thesis considers only tree-level Z' production to minimize model dependence.

1.2.2 Two-Higgs-doublet model

The two-Higgs-doublet model (or 2HDM) is an extension of the SM, in which the Higgs sector includes two doublets instead of just one [34]. This minimal extension of the Higgs sector may help explain baryogenesis and solve the hierarchy problem, mentioned in the previous section.

The most general scalar potential contains 14 parameters and can have CP-conserving, CP-violating, and charge-violating minima. In most studies, however, it is assumed that CP is

conserved and not spontaneously broken and that the quartic terms odd in either of the Higgs doublets are removed by discrete symmetries, but one usually considers all possible quadratic terms.

Thus, the most general potential for two doublets Φ_1 and Φ_2 is defined as follows:

$$V = m_{11}^2 \Phi_1^\dagger \Phi_1 + m_{22}^2 \Phi_2^\dagger \Phi_2 - m_{12}^2 (\Phi_1^\dagger \Phi_2 + \Phi_2^\dagger \Phi_1) + \frac{\lambda_1}{2} (\Phi_1^\dagger \Phi_1)^2 + \frac{\lambda_2}{2} (\Phi_2^\dagger \Phi_2)^2 + \lambda_3 \Phi_1^\dagger \Phi_1 \Phi_2^\dagger \Phi_2 + \lambda_4 \Phi_1^\dagger \Phi_2 \Phi_2^\dagger \Phi_1 + \frac{\lambda_5}{2} \left[(\Phi_1^\dagger \Phi_2)^2 + (\Phi_2^\dagger \Phi_1)^2 \right]. \quad (1.39)$$

Similarly to the SM Higgs potential before, the minimization of this potential gives

$$\langle \Phi_1 \rangle_0 = \begin{pmatrix} 0 \\ v_1/\sqrt{2} \end{pmatrix}, \quad \langle \Phi_2 \rangle_0 = \begin{pmatrix} 0 \\ v_2/\sqrt{2} \end{pmatrix}. \quad (1.40)$$

Thus, the scalars Φ_1 and Φ_2 can be expressed as

$$\Phi_a = \begin{pmatrix} \phi_a^+ \\ (v_a + \rho_a + i\eta_a)/\sqrt{2} \end{pmatrix}, \text{ where } a = 1, 2. \quad (1.41)$$

Three of the eight fields give mass to the three gauge bosons, Z^0 and W^\pm , which leaves five free physical scalar fields: two charged scalars, two neutral scalars, and one pseudoscalar.

Mass terms for the charged scalars are given by

$$\mathcal{L}_{\phi^\pm \text{ mass}} = \left[m_{12}^2 - (\lambda_4 + \lambda_5) v_1 v_2 \right] \begin{pmatrix} \phi_1^- & \phi_2^- \end{pmatrix} \begin{pmatrix} \frac{v_2}{v_1} & -1 \\ -1 & \frac{v_1}{v_2} \end{pmatrix} \begin{pmatrix} \phi_1^+ \\ \phi_2^+ \end{pmatrix}. \quad (1.42)$$

One of the eigenvalues of the matrix is 0 and it corresponds to the charged Goldstone boson G^\pm which is responsible for the mass of W^\pm . The second eigenvalue therefore gives the mass of the charged scalar particles:

$$m_+^2 = \left(\frac{m_{12}^2}{v_1 v_2} - \lambda_4 - \lambda_5 \right) (v_1^2 + v_2^2). \quad (1.43)$$

The mass term for the pseudoscalars is

$$\mathcal{L}_{\eta \text{ mass}} = \left[\frac{m_{12}^2}{v_1 v_2} - 2\lambda_5 \right] \begin{pmatrix} \eta_1 & \eta_2 \end{pmatrix} \begin{pmatrix} v_2^2 & -v_1 v_2 \\ -v_1 v_2 & v_1^2 \end{pmatrix} \begin{pmatrix} \eta_1 \\ \eta_2 \end{pmatrix}, \quad (1.44)$$

and in addition to the pseudoscalar Goldstone mode, this equation provides the mass of the physical pseudoscalar boson A :

$$m_A^2 = \left(\frac{m_{12}^2}{v_1 v_2} - 2\lambda_5 \right) (v_1^2 + v_2^2). \quad (1.45)$$

Finally, the mass term for the scalars is

$$\mathcal{L}_{\rho \text{ mass}} = - \begin{pmatrix} \rho_1 & \rho_2 \end{pmatrix} \begin{pmatrix} \frac{m_{12}^2 v_2}{v_1} + \lambda_1 v_1^2 & -m_{12}^2 + \lambda_{345} v_1 v_2 \\ -m_{12}^2 + \lambda_{345} v_1 v_2 & m_{12}^2 \frac{v_1}{v_2} + \lambda_2 v_2^2 \end{pmatrix} \begin{pmatrix} \rho_1 \\ \rho_2 \end{pmatrix}, \quad (1.46)$$

where $\lambda_{345} = \lambda_3 + \lambda_4 + \lambda_5$. The matrix can be diagonalized and α denotes the necessary rotation angle for that diagonalization. Another parameter of the model is β , defined as

$$\tan \beta \equiv \frac{v_2}{v_1}. \quad (1.47)$$

β is the rotation angle which diagonalizes the matrices of the charged scalars and pseudoscalars.

Given that there is no CP violation in the vacuum expectation values v_1 and v_2 , both can be assumed without loss of generality to be real and non-negative. Replacing in the definition 1.41 $v_1 = v \cos \beta$ and $v_2 = v \sin \beta$, one can derive the expressions for the neutral Higgs bosons:

- Goldstone boson:

$$G^0 = \eta_1 \cos \beta + \eta_2 \sin \beta; \quad (1.48)$$

- Physical pseudoscalar, orthogonal to G^0 :

$$A = \eta_1 \sin \beta - \eta_2 \cos \beta; \quad (1.49)$$

- Lighter (h) and heavier (H) physical scalars:

$$h = \rho_1 \sin \alpha - \rho_2 \cos \alpha, \quad (1.50)$$

$$H = -\rho_1 \cos \alpha - \rho_2 \sin \alpha. \quad (1.51)$$

In principle, under certain assumptions 2HDMs with flavor-changing neutral currents (FCNC) can be viable; however, in many applications, it is assumed that there are no tree-level FCNCs. Several types of the 2HDM theory are defined depending on the Higgs bosons, to which quarks and leptons couple, types I and II, and so-called *lepton-specific* and *flipped*. It is clear that when all fermions with the same quantum numbers are coupled to the same Higgs multiplet, such currents do not exist. In the quark sector of the 2HDM, there are only two possibilities to realize this condition:

- **Type I 2HDM** – all quarks couple to just one Higgs doublet (which is conventionally chosen to be Φ_2).
- **Type II 2HDM** – the quarks with electrical charge $Q = 2/3$ couple to one Higgs doublet (conventionally Φ_2), while the quarks with electrical charge $Q = -1/3$ couple to the other doublet Φ_1 .

In the above-defined models, leptons couple to the same Higgs doublet as the down-type quarks, however this is not required for the absence of FCNCs. Therefore, there are two options for the leptons: they can either couple to the same Higgs doublet as the down-type quarks or they can couple to the other one. In the second case, two more models arise, *lepton-specific* and *flipped*. All four cases are summarized in Table 1.1.

Type II 2HDM is the most studied out of these four models. For the 2HDM to be consistent with the existing data from direct searches for neutral bosons, performed by the ATLAS and CMS collaborations, as well as with the data from precision measurements of the parameters of the SM Higgs boson, the parameter space needs to be restricted to the so-called *alignment limit* $\cos(\beta - \alpha) \rightarrow 0$ [35]. Given this limit, the scalar boson h very closely resembles the SM Higgs boson.

For heavy neutral bosons H/A , the dominant decay mode would be into a pair of top and anti-top quarks. Due to destructive interference with the SM background $gg \rightarrow t\bar{t}$ in the final state with two top quarks, the searches in that final state depend on the exact parameters considered. The four top quark final state, on the other hand, does not suffer from this complication. The Feynman diagram of this final state production is shown in Figure 1.4.

Table 1.1: The 2HDM model types which lead to natural flavor conservation. The three right columns depict the Higgs doublet, to which the corresponding particles couple.

| Type | up-type quark | down-type quark | lepton |
|-----------------|---------------|-----------------|----------|
| Type I | Φ_2 | Φ_2 | Φ_2 |
| Type II | Φ_2 | Φ_1 | Φ_1 |
| Lepton-specific | Φ_2 | Φ_2 | Φ_1 |
| Flipped | Φ_2 | Φ_1 | Φ_2 |

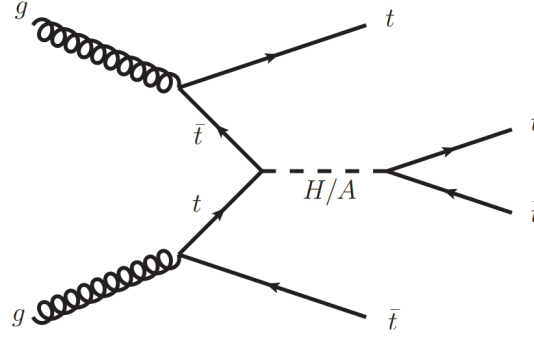


Figure 1.4: Feynman diagram showing the production of a scalar or pseudoscalar Higgs boson along with a pair of two top quarks, with the subsequent decay of the Higgs boson into a pair of top quarks.

1.2.3 Composite Higgs models

Composite Higgs models are extensions of the SM in which the Higgs boson is not considered to be a point-like elementary particle, but is a bound state of new interactions that has finite size [36]. The SM is extended by adding a composite sector with strongly-coupled dynamics characterized by an exact global symmetry that is spontaneously broken. The symmetry group needs to be large enough to allow for at least four Goldstone bosons to arise from its breaking. These bosons are defined as the Higgs doublet. In the modern composite Higgs models, an important feature is the so-called *partial compositeness*, where the SM particles are linear combinations of elementary and composite states:

$$|SM\rangle = \cos\theta|\text{Elementary}\rangle + \sin\theta|\text{Composite}\rangle. \quad (1.52)$$

Thus, in addition to the SM particles, additional heavy resonances are expected:

$$|\text{Heavy}\rangle = -\sin\theta|\text{Elementary}\rangle + \cos\theta|\text{Composite}\rangle. \quad (1.53)$$

Fermions are not coupled to the Higgs boson itself but to its parts with proto-Yukawa couplings depending on the mixing between the fundamental states and composite fields. Moreover, a composite Higgs boson acquires its mass by a different mechanism than a fundamental Higgs boson in the SM, which could explain the small size of the experimentally measured Higgs boson mass without fine-tuning.

It is possible to probe composite Higgs models at LHC, in particular, in four-top-quark final states. The SM production of this final state has low cross section, and in composite Higgs models one can expect couplings between composite bosons and the top quark, which would

Table 1.2: Distribution of final state composition by lepton count.

| Number of leptons | Fraction of final states, % |
|-------------------|-----------------------------|
| 0 | 20.15 |
| 1 | 39.70 |
| 2 | 29.33 |
| 3 | 9.63 |
| 4 | 1.19 |

add a BSM contribution to the final state. This can be modelled by extending the SM as $SU(3)_C \times SU(2)_L \times U(1)_Y \times U(1)_X$, where $U(1)_X$ is linked to a symmetry breaking resulting in creation of a massive particle Z' . The width of this particle is calculated as

$$\Gamma = \frac{g_{t_R}^2}{24\pi} \left(m_{Z'} - 2 \frac{m_t^2}{m_{Z'}} \right) \sqrt{1 - 4 \frac{m_t^2}{m_{Z'}^2}}, \quad (1.54)$$

where g_{t_R} is its coupling to the right-handed top quark.

1.3 Four top quark final state

This thesis presents two searches for Beyond Standard Model physics in the four-top-quark final state. Such searches are well motivated by the theories presented above, and in this section, production of such final states is discussed in more detail. Moving away from a purely theoretical discussion and looking at the final state from an experimental point of view, it is important to note that it is impossible to observe four top quarks, as their short lifetime ($\mathcal{O}(10^{-25})$ s [37]) means that they decay almost immediately after being produced. Therefore, in addition to the four top quark final state, a different composition of particles can be referred to as *the final state*. Namely, the set of all particles, resulting from the decays of the four top quarks.

The top quark has one main decay mode $t/\bar{t} \rightarrow bW^\pm$, which accounts for more than 99% of all decays. The W boson in turn also promptly decays [37]:

$$W^+ \rightarrow l^+ \nu \text{ in } \sim 33\% \text{ of all cases, } W^+ \rightarrow q\bar{q} \text{ in } \sim 67\% \text{ of all cases.}$$

Therefore, each top quark results in a b -quark and either a quark-antiquark pair or a lepton and a neutrino. In the first case, the top quark will be referred to as *hadronically decaying*, and in the latter as *leptonically decaying*.

Table 1.2 shows the final state composition by lepton count. While final states with fewer leptons are more frequent, they are also more complicated to analyze because of increased background compared to the final states with higher numbers of leptons.

Sample Standard Model diagrams for a four-top-quark final state production is shown in Figure 1.5.

At $\sqrt{s} = 13$ TeV, the production cross section of this final state has been calculated to be $\sigma_{t\bar{t}t\bar{t}} = 13.4_{-1.8}^{+1.0}$ fb at next-to-leading order in QCD including electroweak corrections [39]. The results of the recently observed production of the four-top-quark final state show an excess in the number of produced events, but are in agreement with the SM prediction. This excess, however, motivates searches for BSM contributions to the production of this final state. While in the SM there is a possibility for resonant four-top-quark production, as shown in Figure 1.5

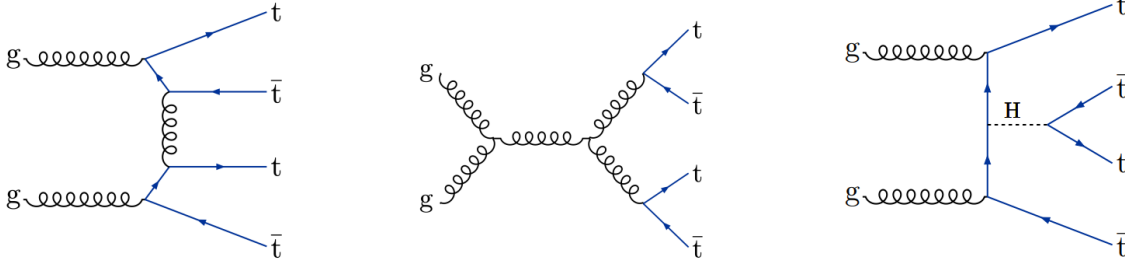


Figure 1.5: Sample Feynman diagrams of four top quark production at leading order in the SM [38].

on the right, it has a very small cross section due to the Higgs boson being strongly off-shell. Many BSM theories predict such production with resonances heavier than the Higgs boson.

Generally speaking, there are two main strategies that can be used for searches for new physics: model-independent and model-dependent. The first possibility to probe BSM in this final state arises from explicitly reconstructing the resonance and thus obtaining a model-independent result. The second possibility is obtaining model-dependent results by fitting the measured data using simulated samples which were generated using a particular model. Both approaches are touched on in Chapters 5, where a single lepton final state is considered, and in Chapter 6, where multilepton final states are studied.

The strategies have both advantages and disadvantages: model-dependent searches are significantly more sensitive to each individual BSM model, while model-independent analyses can probe various models at the same time. Perhaps, since it is currently unclear where the new physics lies, model-independent searches with their broad but coarse results can first roughly point to the regions of interest, where afterwards other searches, each tailored to an individual BSM model, can focus in more detail.

2. ATLAS and LHC

The data for testing the theoretical predictions is obtained experimentally using many different setups targeted at various areas of particle physics. On the Large Hadron Collider (LHC), protons of high energies are collided and the data about the products of these collisions is collected using detectors, such as the ATLAS detector. This data is then used to both measure the parameters of the SM precisely and to probe new physics theories. This chapter describes the purpose and operation of the LHC and its four major experiments with a particular focus on the ATLAS experiment.

2.1 LHC

The Large Hadron Collider (LHC) in Geneva, Switzerland is the most powerful particle accelerator ever built [40], occupying the tunnels, previously used by The Large Electron-Positron Collider [41]. Along its circumference of 27 km, it collides high energy protons in four interaction points, where the four major LHC experiments are located, ATLAS [42], CMS [43], ALICE [44] and LHCb [45]. While ATLAS and CMS (Compact Muon Solenoid) experiments are multipurpose, able to detect a wide range of physics processes, ALICE and LHCb are targeted at more specific studies. ALICE (A Large Ion Collider Experiment) is designed, as is evident from the name, for studying heavy-ion physics. LHCb (Large Hadron Collider beauty) aims to investigate the differences between matter and antimatter by studying the properties of the B-mesons.

The protons for collisions are obtained from hydrogen ion gas, in which ions are stripped from electrons using a strong electric field. Before the protons reach the four interaction points, they undergo a series of accelerations. A sketch of the acceleration chain is shown in Figure 2.1. First, the particles are accelerated to energies of 50 MeV by a linear accelerator, LINAC2, and then injected into the Proton Synchrotron Booster, a circular accelerator with the circumference of 157 m, and accelerated to the energy of 1.4 GeV. After this they are accelerated up to 25 GeV inside of the Proton Synchrotron and then in the Super Proton Synchrotron they are accelerated up to the energy of 450 GeV. At this point, the protons are injected into the LHC ring and it takes less than half an hour for the particles to reach the energy of 6.8 TeV (6.5 TeV during the years 2015–2018) and be ready for the collisions.

The data taking periods are called *runs*. During the shutdown periods between runs, essential maintenance work is carried out on the accelerators and detectors. This downtime also provides an opportunity for the installation of detector upgrades and necessary equipment enhancements.

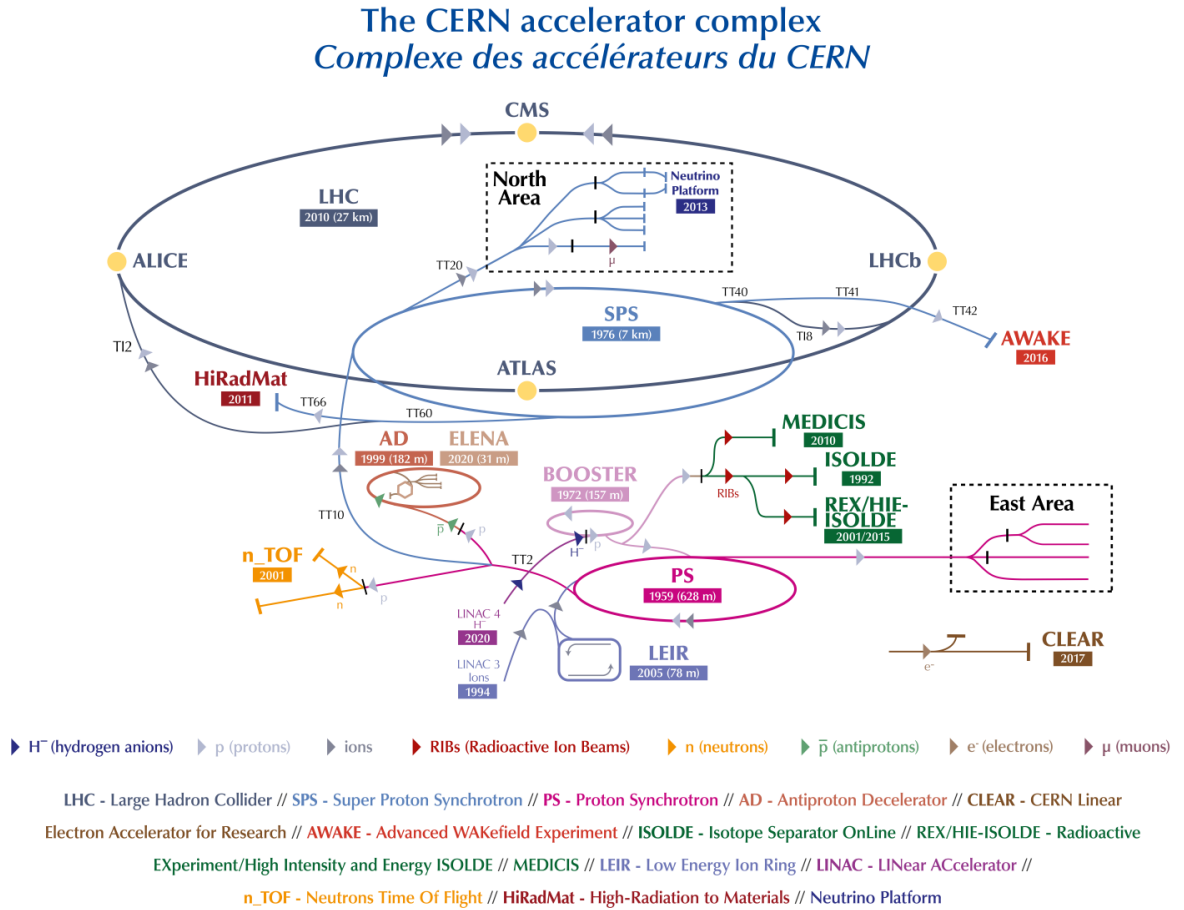


Figure 2.1: Structure of the CERN accelerator complex [46].

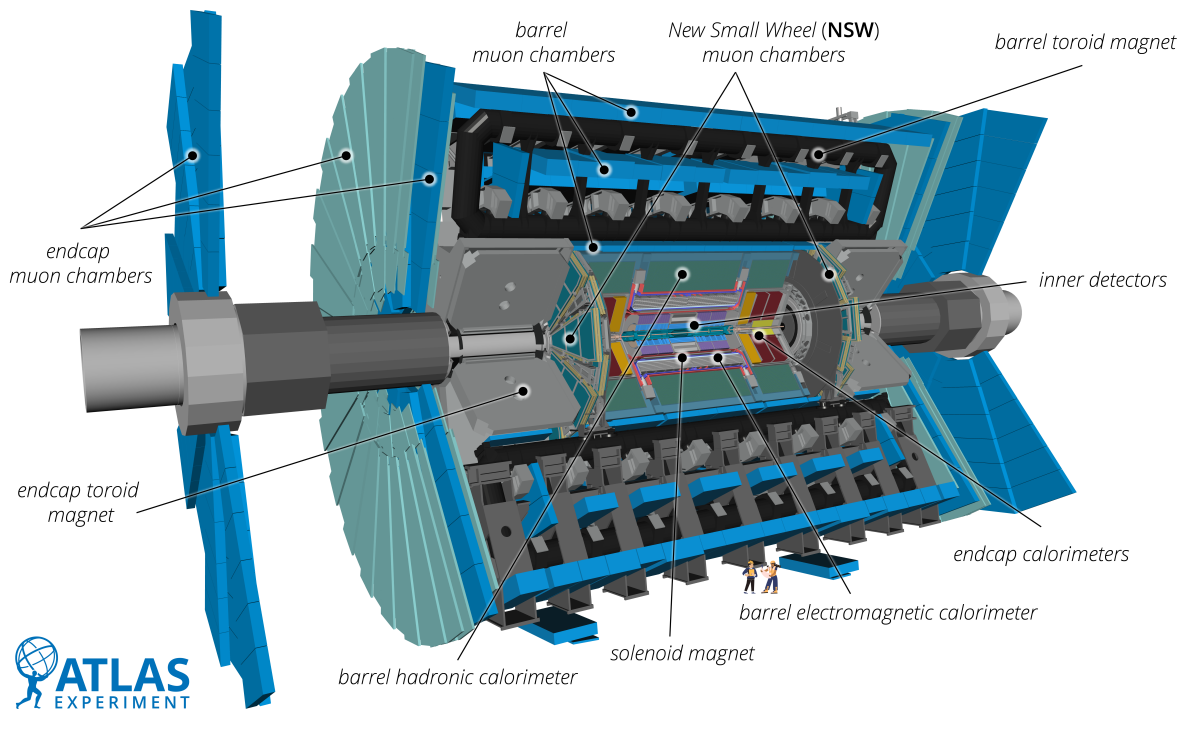


Figure 2.2: Schematic view of the ATLAS detector [48].

2.2 ATLAS

The ATLAS experiment is one of the two general purpose experiments at the LHC [47]. The detector is aimed at registering a wide variety of particles in a nearly 4π solid angle, making it a great tool for precision studies of the Standard Model, as well as for searching for new physics. Figure 2.2 shows a schematic view of the ATLAS detector. The main subsystems include the Inner Detector, which provides information about trajectories of the charged particles, the electromagnetic and hadronic calorimeters, which are used for measuring the energy of the particles, the magnets for creating a magnetic field around the interaction point, the muon spectrometer for muon detection, and the forward detectors for measuring the luminosity and beam characteristics. Luminosity is a parameter characterizing the number of collisions that happen in a detector. A simplified expression for luminosity is

$$L = \frac{fN^2}{4\pi\sigma^2}, \quad (2.1)$$

where it is assumed that the two colliding bunches of particles contain the same number of particles N , f is the crossing frequency of the bunches, and each bunch has a transverse size of σ .

To extract the data measured by the detector subsystems, the ATLAS experiment is equipped with a Trigger and Data Acquisition system.

2.2.1 Coordinate system

A right-handed coordinate system is utilized in ATLAS, with the x -axis pointing to the center of the LHC ring, the z -axis along the beam counter-clockwise if seen from above, and the y -axis is pointing upwards. Along with the Cartesian coordinate system, a cylindrical one, with R

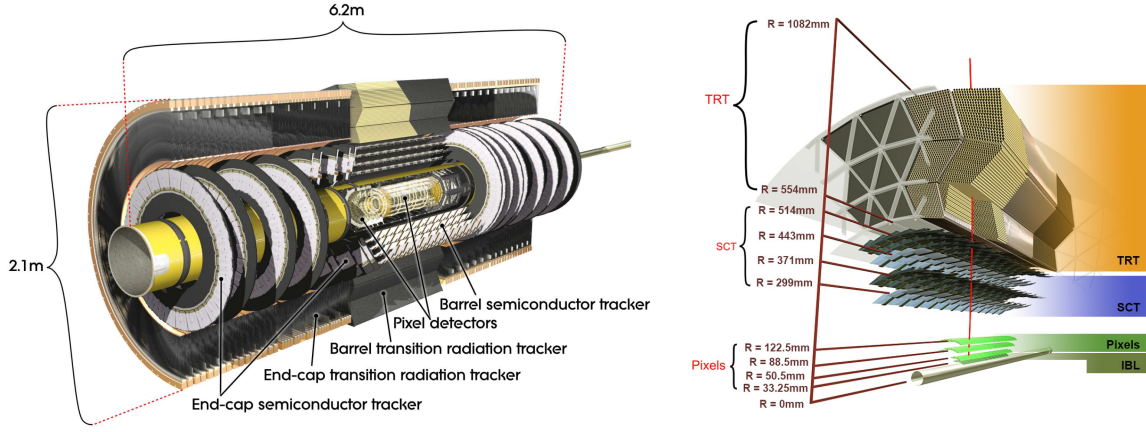


Figure 2.3: Schematic view of the ATLAS Inner Detector [47, 50].

being the distance from the beam in the transverse plane, ϕ – azimuthal angle around the beam axis and θ – polar angle to the beam axis. Other important parameters include pseudorapidity $\eta = -\ln \tan \theta/2$, distance $\Delta R = \sqrt{\Delta \eta^2 + \Delta \phi^2}$ and transverse momentum p_T , which is defined as the projection of particle momentum on the plane, perpendicular to the beam.

2.2.2 Inner detector

The Inner Detector (ID) is pictured in Figure 2.3. It is immersed in a magnetic field of 2 T and consists of three independent parts: silicon pixel detector, silicon microstrip SemiConductor Tracker (SCT) and a Transition Radiation Tracker (TRT). Together they provide track, vertex and momentum reconstruction for particles with transverse momenta above a given threshold (nominally set to 0.5 GeV, but it can go as low as 0.1 GeV), as well as electron identification for electrons with transverse momenta between 0.5 and 150 GeV. The pixel detector and the SCT cover the region $|\eta| < 2.5$, while the TRT allows tracking for $|\eta| < 2$. Each sub-detector has a barrel region, where the module layers for the SCT and the pixel detector or straw tubes for TRT are placed parallel to the beam pipe, and two endcap regions, where the layers and the tubes are perpendicular to the direction of the beam.

The track density is the highest close to the collision point, therefore a high detector granularity is required close to the beam pipe. Moreover, radiation hardness is another crucial quality for the detector so close to the beam. Over the years of operation, the trackers accumulated a substantial amount of radiation damage, which worsened their performance and precision, and for that reason during the long LHC shutdown in 2013–2014 a new layer of pixel modules, a so-called *Insertable B-Layer* or IBL, was inserted between the beam pipe and the innermost pixel barrel layer [49]. It improves low- p_T tracking and provides useful information for jet flavor-tagging, described in more detail in Chapter 4.

On average, a particle, passing through the detector, crosses three layers of pixel modules and six layers of microstrip modules and leaves 36 “hits” in the TRT. The pixel detector and the SCT provide information both about the transverse ($R - \phi$) and the longitudinal (z) position of the particle track. The spatial precision of the pixel detector is $10 \mu\text{m}$ in $R - \phi$ and $115 \mu\text{m}$ in z , the precision of the SCT is $17 \mu\text{m}$ in $R - \phi$ and $580 \mu\text{m}$ in z . The pixel detector and the SCT have approximately 80.4 and 6.3 million readout channels respectively. The TRT with 351,000 readout channels is segmented only in the transverse plane, and it has a spatial precision of $130 \mu\text{m}$ per straw.

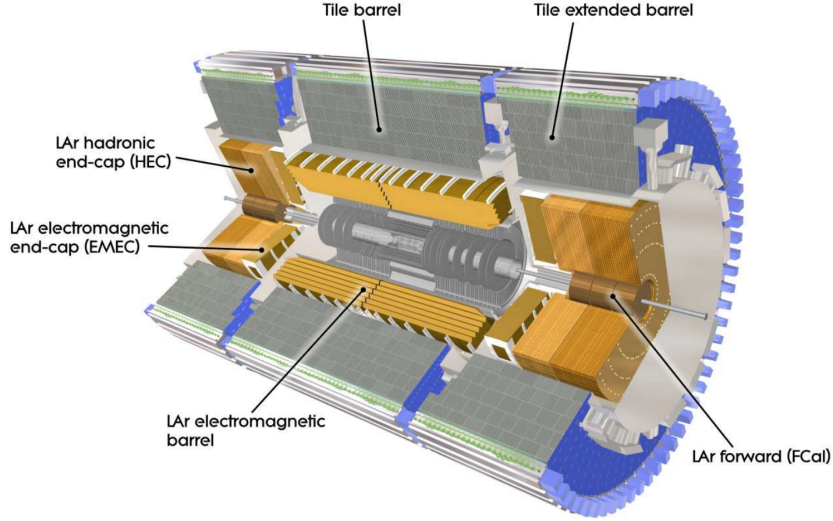


Figure 2.4: Schematic view of ATLAS calorimeters [47].

2.2.3 Calorimeters

The schematic view of ATLAS calorimeters is shown in Figure 2.4. They operate in the range $|\eta| < 4.9$, utilizing various technologies, and have a higher granularity in $|\eta|$ range, compared to the Inner Detector. This allows for precision measurement of electrons and photons in the $|\eta|$ region of the Inner Detector, complementing its data, as well as for reconstruction of jets and missing transverse energy outside of that region.

The inner-most part is the Electromagnetic Calorimeter (EM), divided into a barrel part, covering the range $|\eta| < 1.475$ and two endcaps with ranges $1.375 < |\eta| < 3.2$. It has an accordion geometry and consists of lead and liquid argon. Such geometry provides ϕ symmetry. The calorimeter is more than 22 *radiation lengths* thick, which ensures good containment for the electromagnetic showers. Radiation length is defined as the mean distance in the material, after passing which an electron's energy is reduced by $1/e$.

In the pseudorapidity region $0 < |\eta| < 1.8$ the EM calorimeters are complemented by presampler, a single argon layer that allows to account for energy lost in front of the EM calorimeters.

Directly outside of the EM calorimeter is the hadronic Tile Calorimeter. It is a sampling calorimeter made from steel and scintillating tiles and it covers the ranges $|\eta| < 1.0$ with a barrel and $0.8 < |\eta| < 1.7$ with two extended barrels.

Along the beam pipe right behind the EM endcaps are the Hadronic Endcap Calorimeters (HEC). They extend to the range $1.5 < |\eta| < 3.2$, therefore overlapping with the Tile Calorimeter at the lower end and with the forward calorimeter at the upper. HEC consists of two independent copper wheels with gaps for the active material – liquid argon.

Inside of HEC wheels and closest to the beam pipe are the forward calorimeters (FCal), covering the pseudorapidity range $3.1 < |\eta| < 4.9$. Each calorimeter consists of three modules: a copper one, optimized for precise electromagnetic measurements, and two tungsten ones for measuring the energy of hadronic interactions. As in the previous calorimeters, the sensitive medium in the FCal is liquid argon in the gaps between metal parts.

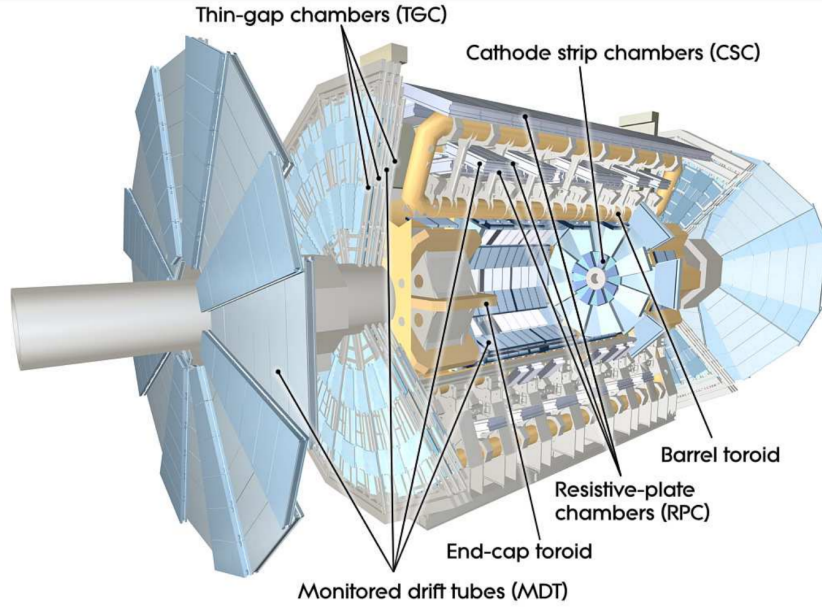


Figure 2.5: Schematic view of the ATLAS Muon System [47].

2.2.4 Muon spectrometer and magnet system

The Muon Spectrometer (MS) and the magnets creating the magnetic field are shown in Figure 2.5. The MS is targeted at detecting muons, deflected by the magnetic field. In the range $|\eta| < 1.4$ the magnetic field is provided by the toroid magnets, in the range $1.6 < |\eta| < 2.7$ by two smaller endcap magnets, the range $1.4 < |\eta| < 1.6$ is the transition range, where both magnet types contribute to the magnetic field. Each toroid magnet consists of 8 coils, assembled radially and symmetrically around the beam pipe.

The Muon Spectrometer has a barrel part with three layers of measuring chambers, parallel to the beam pipe, and two endcap parts, where the measuring chambers are installed in three planes, perpendicular to the beam. The track coordinates in most of the pseudorapidity range are measured by Monitored Drift Tubes (MDT's), and at the large pseudorapidities by Cathode Strip Chambers (CSC's), which are multiwire proportional chambers with cathodes segmented into strips. They have higher granularity than MDT's and therefore are more suitable for higher rate. Before LHC Run 3 the innermost planes of the endcaps have been replaced by New Small Wheels [51], utilizing two chamber technologies: small-strip Thin Gas Chambers and micro-mesh gaseous structure (Micromegas). This update provides robust, fast, high-resolution performance required by conditions of High Luminosity LHC and LHC Run 3. [52]

Additionally, the muon system includes a trigger system that covers the range $|\eta| < 2.4$. It consists of Resistive Plate Chambers in the barrel region and Thin Gas Chambers in the endcap regions. The goal of this system is to provide bunch crossing information and well-defined p_T -thresholds, as well as to measure the muon coordinate in the direction, perpendicular to the direction of the precision-tracking chambers.

2.2.5 Forward detectors

LUCID (LUMinosity measurement using Cerenkov Integrating Detector) is the main online relative-luminosity monitor for ATLAS. It measures inelastic $p - p$ scattering in the forward region and is located 17 m from the interaction point on both sides of the ATLAS detector. Further, at ± 140 m from the interaction point, are the Zero-Degree Calorimeters, which help

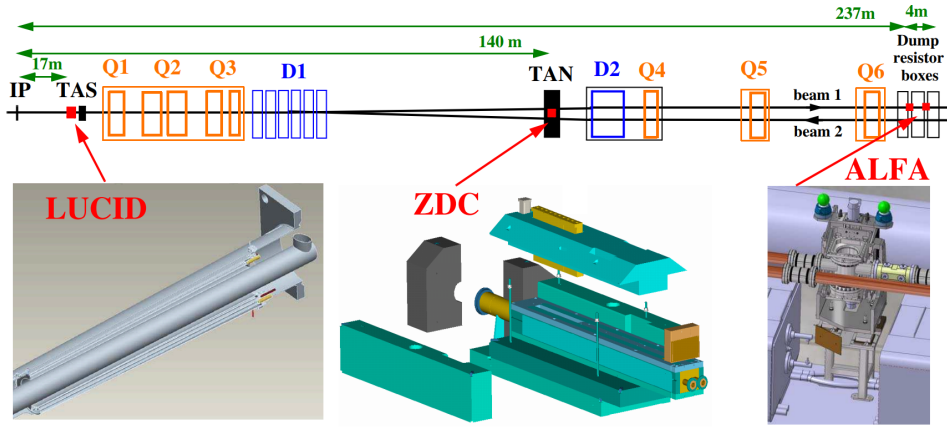


Figure 2.6: Schematic view of the ATLAS forward detectors. IP – particle interaction point in the middle of ATLAS detector [47].

to determine centrality of the heavy ion collisions. Finally, at the distance of 240 m from the interaction point on each side are ALFA (Absolute Luminosity For ATLAS) detectors, which measure elastic $p - p$ scattering at small angles.

2.2.6 Trigger and data acquisition

The Trigger and Data Acquisition (TDAQ) systems, as well as the timing and trigger control logic, and the Detector Control System (DCS), are organized into sub-systems, often associated with specific sub-detectors [53]. The trigger system has two levels, with the second level improving the decisions made at the first level and, when necessary, applying additional selection criteria to identify events of interest.

The L1 (Level 1) trigger is hardware-based. It uses only a subset of detectors, namely the trigger chambers of the spectrometer, as well as reduced granularity information from all calorimeters. It looks for the presence of objects with high transverse momentum and for large missing transverse momentum. In addition to selecting events, the L1 trigger also highlights Regions-of-Interest (RoI), the areas of the detector, where interesting features were observed. Events that pass the L1 trigger are passed to the next trigger level. The L1 trigger reduces the event rate from 40 MHz to around 100 kHz.

The second level is the High Level Trigger (HLT). It is software-based and runs on CPU farms. It performs online reconstruction with respect to the RoI, obtained from the L1 trigger, and reduces the event rate to approximately 1 kHz.

In the beginning of Run 3, the electronics used for the triggers were updated [54]. New FPGA-based feature extractors were introduced, and the online readout capability of the hadronic calorimeter was improved, making the granularity of the calorimeter information finer. This has achieved better selection of electrons and photons. Moreover, additional systems, such as the New Small Wheel, were introduced into the ATLAS detector, improving the work of the L1 trigger as well.

Furthermore, the HLT software framework was reorganized using multithreading, which supports efficient memory use. Due to a significant increase of the track reconstruction speed, for some trigger signatures, the HLT can now be run for the full detector volume, providing an improvement for online energy calibration. In addition, machine learning techniques allow for a further increase in processing speed without a significant loss of sensitivity.

3. ITk module assembly and testing

The Inner Detector, described in the previous chapter, is reaching the end of its operating life. After the end of the current run it will be replaced by a new fully-silicon Inner Tracker or ITk. The construction of the ITk is a complex process that requires the joint effort of various institutions worldwide. One of the silicon strip *endcaps* is assembled at DESY. This chapter describes the ITk in detail with focus on the strip endcap building efforts at DESY Hamburg. In addition, module quality control procedures are described, in particular the module thermal cycling.

3.1 Tracker upgrade for High-Luminosity LHC

The current ATLAS Inner Detector was designed to work in conditions with instantaneous luminosity up to $10^{34} \text{ cm}^{-2}\text{s}^{-1}$ [55]. During the High Luminosity LHC phase, the instantaneous luminosity will increase by almost one order of magnitude, up to $7.5 \times 10^{34} \text{ cm}^{-2}\text{s}^{-1}$ [56]. In order to cope with this increase, multiple parts of the ATLAS detector will need replacement. The Inner Detector will be completely replaced by the Inner Tracker (ITk), which is a fully-silicon detector with higher granularity, higher radiation hardness and faster readout, better suited for work in high luminosity conditions. The ITk has two subsystems: the pixel subsystem, located closest to the beam pipe [57], and the strip subsystem, situated outside of the pixel subsystem [58]. Figure 3.1 shows the schematic view of the ITk, and Figure 3.2 depicts individual layers of the detector.

The number of readout channels is increased tenfold, and a novel powering scheme is employed in order to provide a more efficient power budget per channel. The design minimizes the *material budget* (the total amount of material in the detector) to limit the production of secondary particles in the bulk of the detector outside of the active volume. Figure 3.3 shows the material distribution in units of *radiation length* (the mean distance that an electron will travel through the material until its energy is reduced by $1/e$) for various detector subsystems. Below, a description of both ITk subsystems with more focus on the strip part is provided.

3.1.1 ITk pixel

The pixel detector consists of a five-layered barrel, located in the central region of the detector, and two endcaps, located in the forward regions of the detector. It covers the pseudorapidity

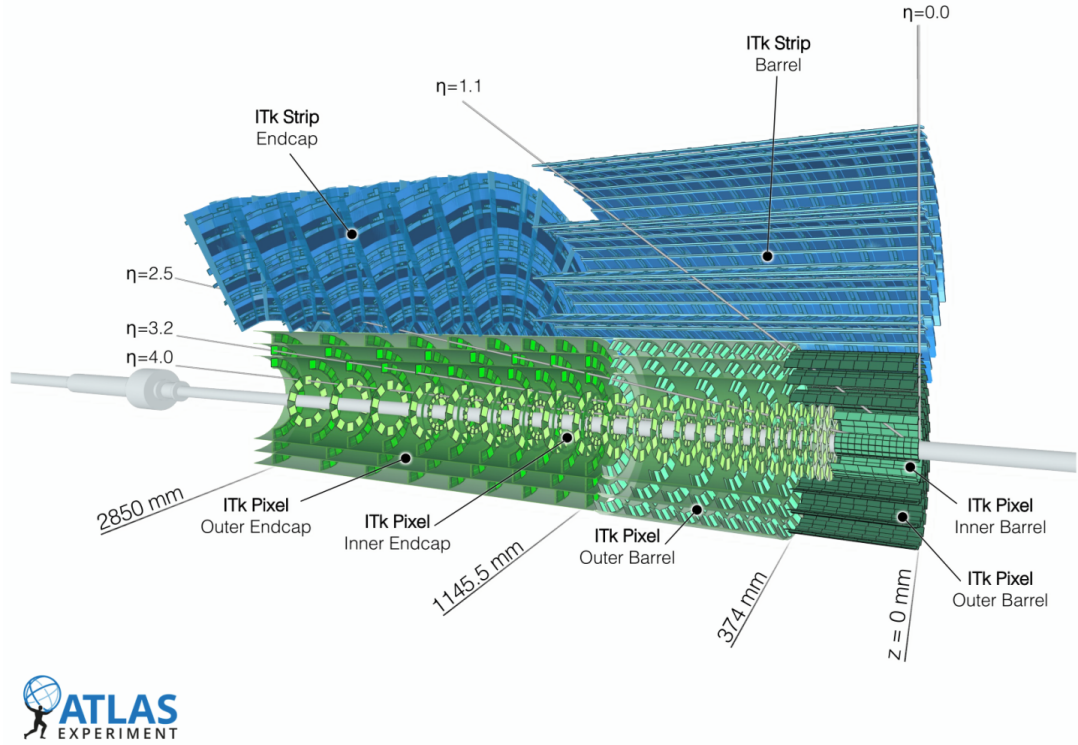


Figure 3.1: Visualization of a quadrant of the ITk [59]. Only the sensitive units of each system are shown without support structures and cabling. The pixel subsystem is shown in green, and the strip subsystem is shown in blue. The beam collision point is marked with $\eta = 0.0$, $z = 0$ mm lines.

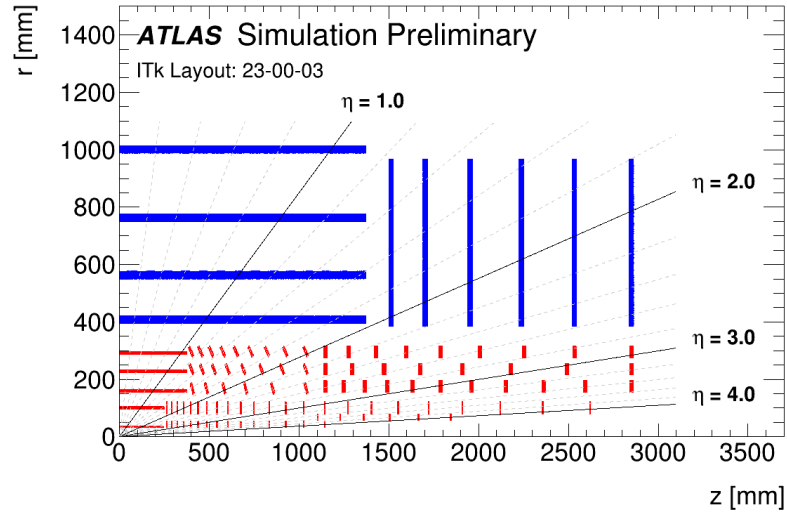


Figure 3.2: Cross-sectional view of a quadrant of the ITk. The horizontal axis is directed along the beam with the interaction point being at $z = 0$, the vertical axis shows the radial distance from the interaction point. The pixel layers are shown in red and the strip layers are shown in blue [60].

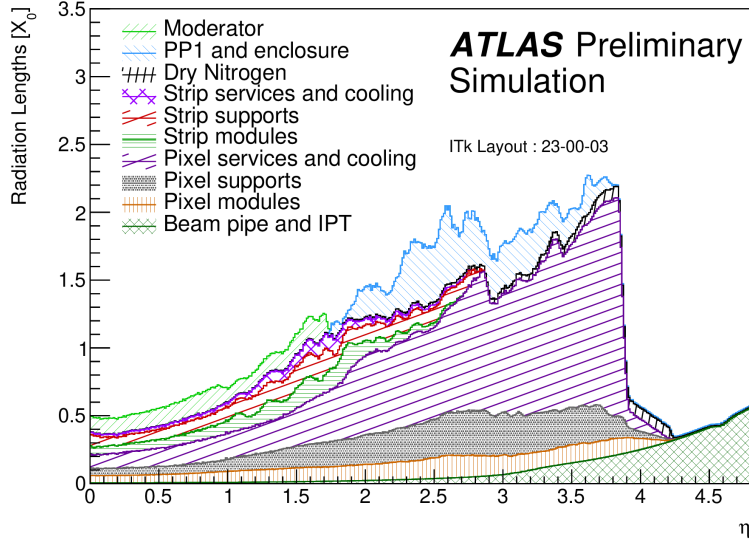


Figure 3.3: Material distribution within the ITk volume in units of radiation length for various ITk components [60].

range $|\eta| < 4$. In each layer of the barrel, the central sensors are placed parallel to the beam pipe, while the outermost sensors are placed at an angle with respect to the beam axis. In the endcaps, the sensors are perpendicular to the beam axis. 3D pixel sensors are used in the barrel and endcap layers that are closest to the beam and that will be most affected by radiation. The outermost layers are made using planar pixel sensors [61]. The design of the detector allows for replacement of the two innermost barrel layers and the innermost endcap layers. These parts are the most susceptible to radiation damage and therefore will need to be replaced after some runtime.

3.1.2 ITk strip

The strip detector consists of a four-layered barrel and two six-layered endcaps and covers the pseudorapidity range $|\eta| < 2.7$.

Strip barrel

The single sensing units of the ITk strip tracker are called *modules*. The two innermost barrel layers are made using modules with shorter strip length than the modules used for the two outermost layers. This is done in order to achieve higher granularity of the detector closer to the beam axis. The modules are placed parallel to the beam pipe on both sides of local support structures called *staves*. Staves are low-mass carbon-fiber structures [62]. They are mechanically stable, precisely made, exhibit good thermal and electrical performance, and have titanium lines for CO₂ cooling. The modules on the two sides of the stave are rotated by 26 mrad in opposite directions with respect to the stave axis, so that the stave is able to provide 3D information about the passing particles [58]. A single strip module is able to detect the coordinate of the passing particle on an axis, orthogonal to the strip direction. When the modules are placed at an angle to each other, these axes do not coincide, and therefore the approximate point where the particle crosses the stave can be measured. Each stave holds 28 modules, and the total number of staves in the barrel is 392. Figure 3.4 shows a photograph of an assembled short strip stave.

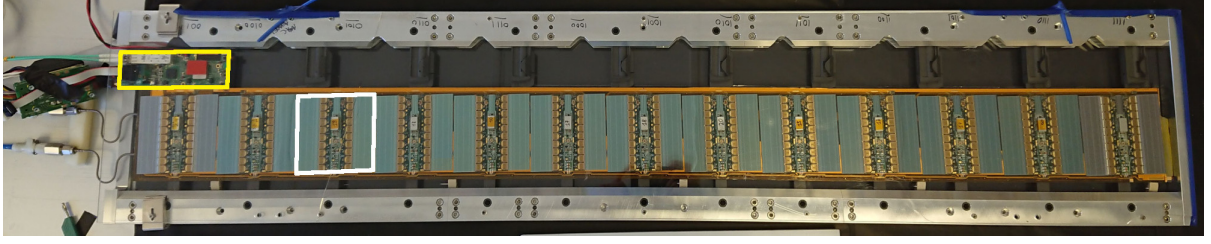


Figure 3.4: Picture of an assembled stave [63]. A module is shown by the white rectangle, and the yellow rectangle surrounds the electronics used for reading out the data from the whole stave.

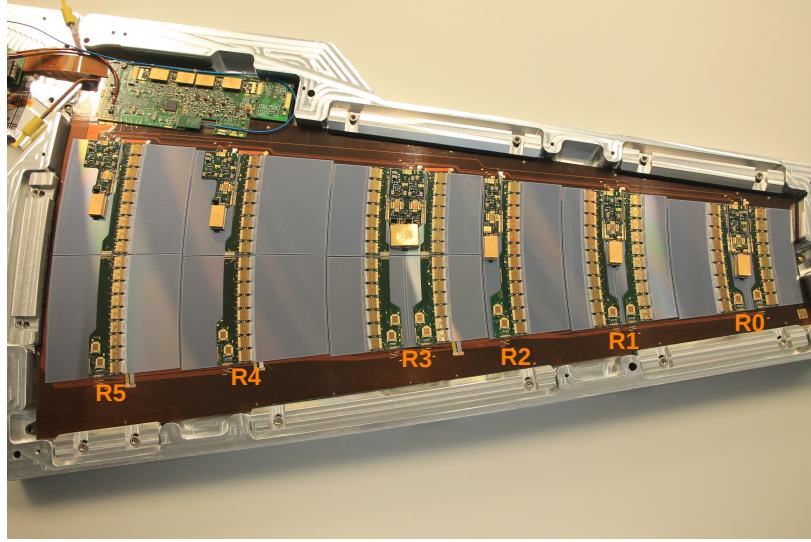


Figure 3.5: Picture of an assembled petal with module type labels [62].

Strip endcaps

Each silicon strip endcap consists of six disk-shaped layers, each of which is made of 32 petals. Six modules of different types are mounted on both sides of the so-called *petal cores*. Petal cores are similar to staves in construction, but are different in shape. Modules are placed on both sides of the petal cores, rotated by 20 mrad with respect to the petal axis to enable stereo measurements [58]. Figure 3.5 shows a photo of an assembled petal, on which the six module types are labeled.

Strip endcap modules

The strip endcap modules have arc segment shape and are labeled R0 to R5 from the innermost to the outermost with respect to the beam axis, as labeled in Figure 3.5. The three innermost modules R0, R1 and R2 are made using one silicon sensor per module, while each of the outermost modules R3, R4 and R5 is made using two sensors. Each module consists of a silicon strip sensor, readout electronics and a powerboard that controls the module's operation. Figure 3.6 shows an exploded view of a strip module with all its parts labeled and a photograph of an endcap R4 module.

Silicon strip sensors, manufactured by Hamamatsu Photonics on 6-inch wafers, are the medium for particle detection. The n^+ -in- p semiconductor type was chosen because it offers better signal speed and radiation hardness than the p -in- n type and can provide good signals even when the

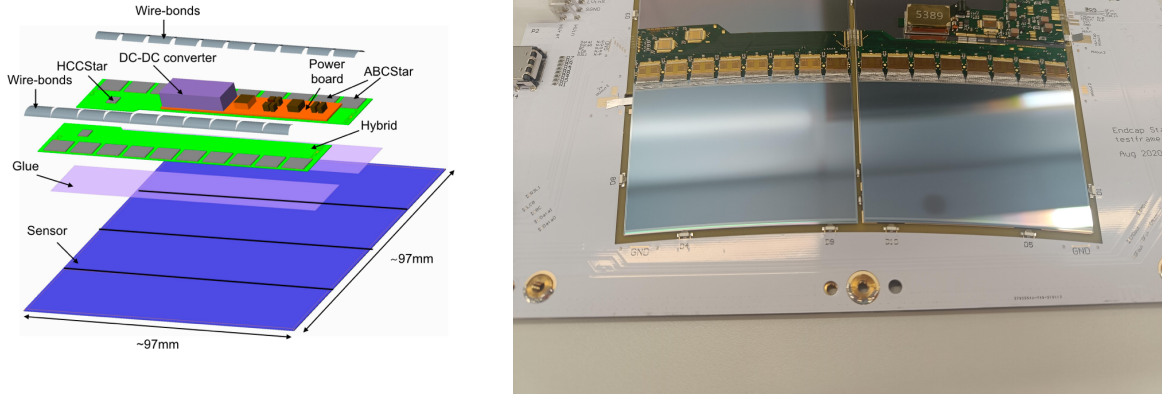


Figure 3.6: Schematic view of ITk strip module parts (left) [58], and a photo of an ITk strip endcap R4 module assembled at DESY. The module is placed on a test frame, used for testing it electrically.

sensors are partially depleted [64]. There are six different types of sensors for the endcap with strips placed radially in order to give a measurement of the $R - \phi$ coordinate. The strip lengths are chosen to balance the strip occupancy. Sensors for the R0, R1 and R3 modules have four rows of strips, while sensors for the R2, R4 and R5 modules have two rows.

The front-end readout chips are called ABCStar (ATLAS Binary Chip) [63], and they are glued on top of hybrid flex-PCBs (Printed Circuit Board). Each chip reads out the data from 256 individual strips, and the data from the ABCStar chips is then gathered by the HCCStar (Hybrid Controller Chip) chips that are also located on the hybrids. The gathered data is repackaged and sent out of the module. Powering and monitoring of the module are controlled by the AMACStar (Autonomous Monitor and Control Chip) chip on the powerboard. The hybrid and the powerboard are glued on top of the silicon sensor, and the electrical connection between the components is achieved through wire bonds, thin wires ultrasonically welded to the components. The module construction process has multiple manufacturing and testing steps and requires regular strict quality control [63].

3.2 Overview of the strip module assembly and testing

Dedicated tooling have been designed for each module type, taking into account the various shapes of the modules [63]. The tools are made of stainless steel and aluminum, which is hard anodized to prevent scratching. Vacuum is used to hold the components in place, and locating pins are used to precisely position the components. Glue layer thickness is controlled by setting the distance between the components during gluing using spacing pads on the tooling. A set of tooling for one module type includes jigs for holding the components with vacuum, a tray for readout chips where they are placed before being glued to the hybrid flex, weights that are used to press down on the components while they are being glued, and several pickup tools: one for the powerboard and one for each hybrid type that is used for both separate chips and the assembled hybrid. As an example, the tooling for the R2 module type is shown in Figure 3.7.

Electrical connections to both sensor planes are required for biasing a sensor, and once the modules are mounted onto support structures, the back plane is no longer accessible. For this reason, a flat aluminum tab, called an HV-tab, is attached to the back of the sensor using

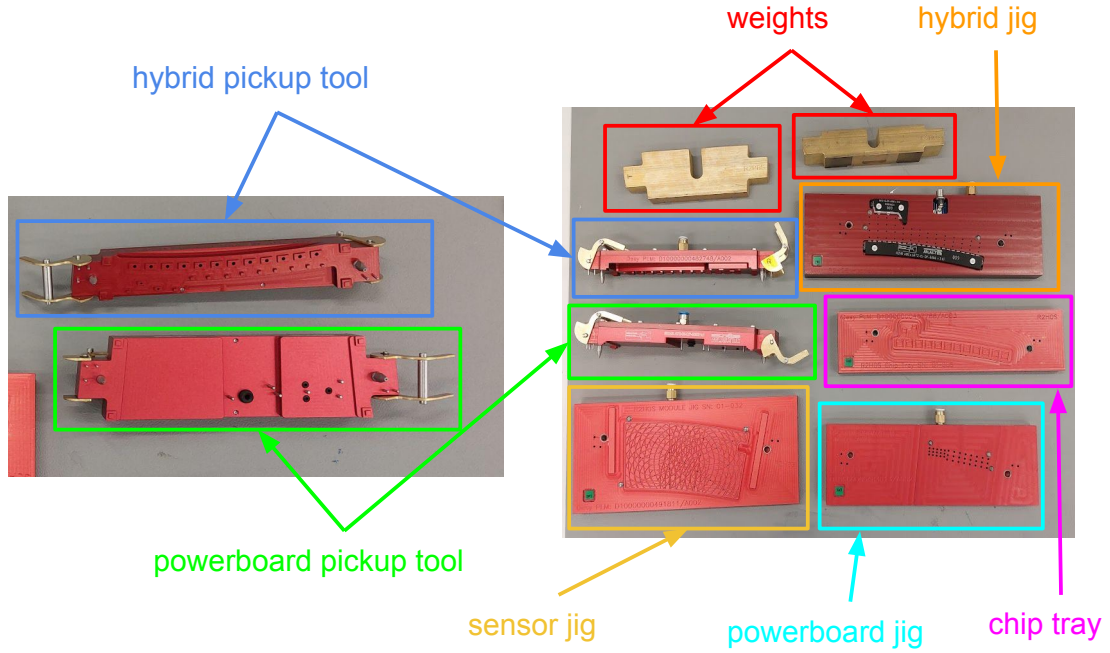


Figure 3.7: Tooling for assembling R2 modules.

automated tab bonding, a procedure of ultrasonically welding the tab directly to the sensor's back plane. Figure 3.8 shows the process of attaching an HV-tab to the back of a sensor.

The next step of module building is gluing of the electronics on top of the silicon sensor using Loctite Eccobond F112 glue [65], that can be applied either using a stencil or by a glue dispensing robot. At DESY, the latter approach is used. The glue is loaded into a pressure-actuated syringe, and the pressure is adjusted over time to account for the change of the glue viscosity as it cures. The glue dispensing patterns are tailored to each module and component type in order to achieve uniform coverage, especially under the pads for wire bond placement. The complete curing takes up to 12 hours. Figure 3.9 shows the glue dispensing robot.

25- μm -thick aluminum wires are then used to connect the components electrically. Advances in bonding techniques allow for angled wire bond placement, eliminating the need for intermediate

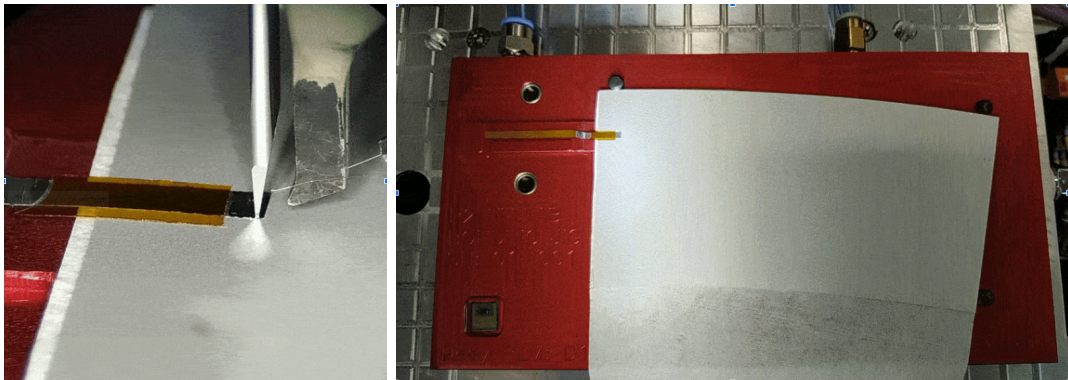


Figure 3.8: Left: the process of attaching an HV-tab. Right: the attached tab on the back plane of an R2 sensor. The sensor is placed on a sensor jig with the back side facing up.

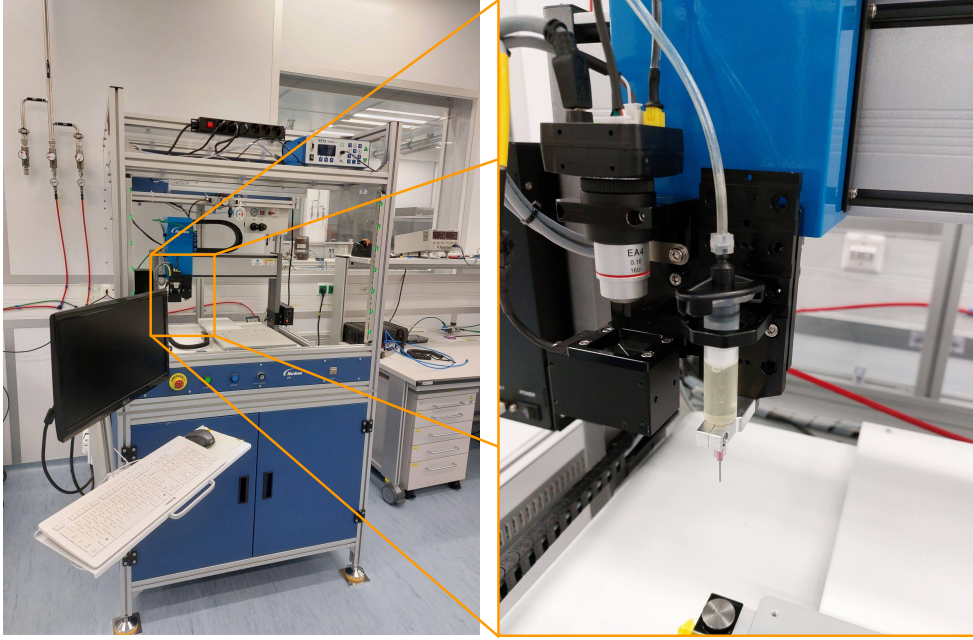


Figure 3.9: The glue dispensing robot (left) and a close-up view showing the position of a syringe filled with glue (right).

bond connections, necessary for straight bonds. The front-end wire bonds, or the wire bonds that connect the sensor strips to readout chips, are placed in four rows, each row over the previous one, as shown in Figure 3.10. This precise technique has now been proven reliable [63].

Quality control tests are performed throughout module assembly to ensure good quality of the assembled components.

To assess whether the module geometry fits the requirements, module metrology is performed using a 3D microscope (Smartscope Flash CNC 300 [66]). The horizontal placement of the electronics is evaluated, along with the thickness of the glue and the so-called *module bow*. The powerboard and the hybrids must not be shifted from their nominal position by more than 0.1 mm in the direction orthogonal to the strips and by more than 0.3 mm in the direction along the strips. This measurement is important to ensure that the modules do not clash with neighboring modules and other structures of the detector and to ensure that the performance of the silicon sensor does not degrade. The thickness of the glue is important for reliable placement of the wire bonds and for providing good electrical and thermal performance. The nominal glue thickness is $120 \pm 40 \mu\text{m}$. For the module bow test, the sensor is not held with vacuum to the holding jig, but is instead allowed to bend under the influence of the glued components. A maximum deviation from flatness of $150 \mu\text{m}$ in the case when the center of the sensor is below its edges when placed on the back surface and $50 \mu\text{m}$ for bowing in the opposite way is allowed by the specifications.

For the *split* modules (the modules that are built using two sensors), each half is assembled separately and is called a *half-module*. After assembly, modules and half-modules are placed onto *test frames*, which allow their electrical testing to ensure good performance.

Electrical tests are performed multiple times throughout the module assembly process. These tests will be covered in more detail in the following sections, and here only a brief overview is presented.

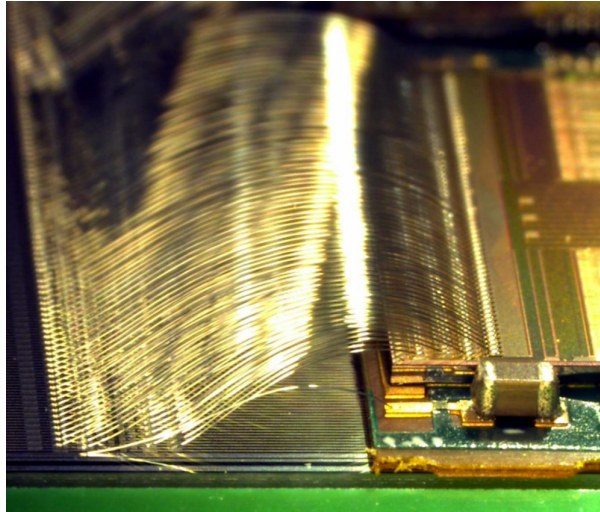


Figure 3.10: Front-end wire bonds, that connect the front-end chips to the sensor strips, placed in four rows [63].

An IV curve, a dependence of the sensor leakage current on the bias voltage, serves as a good indicator of the performance of the silicon strip sensor. This test is performed at every step of module assembly: for bare sensors with no electronics components attached, for sensors with an HV-tab attached, for complete modules, and after all other major handling steps that could affect the quality of the sensor, such as shipment. This test is described in Section 3.3.

Tests aimed at evaluating performance of the readout electronics are conducted for hybrids and powerboards that are not yet part of the module, and then for assembled modules. These tests are described in Section 3.4.

A quality control step that unites all these tests is the module thermal cycling, described in Section 3.5.2. It is a stress-test, performed for every fully-assembled module, and it involves multiple IV curve measurements, as well as electrical tests, while the temperature of the module is changed several times between the room temperature and the temperature of the ITk operation.

3.3 IV comparison studies

An important step in sensor and module quality control is the *IV curve* measurement [58, 63]. As such measurements are performed multiple times during the module assembly, comparison of these curves for the same component at different times during module construction allows monitoring of the quality of the sensor. In this section, the test itself is described, as well as the developed criteria for IV curve comparison and the software created for that purpose [67]. The developed software was first used to determine whether the number of required tests could be reduced. Next, it was modified to allow for a more thorough production monitoring and for identifying deviations in module assembly and handling procedures at different institutions and for different module types.

3.3.1 IV test description

An IV curve is the dependence of the leakage current of the sensor on the applied bias voltage and it is a good characteristic of a semiconductor's quality. An example of a nominal IV curve is shown in Figure 3.11 on the left.

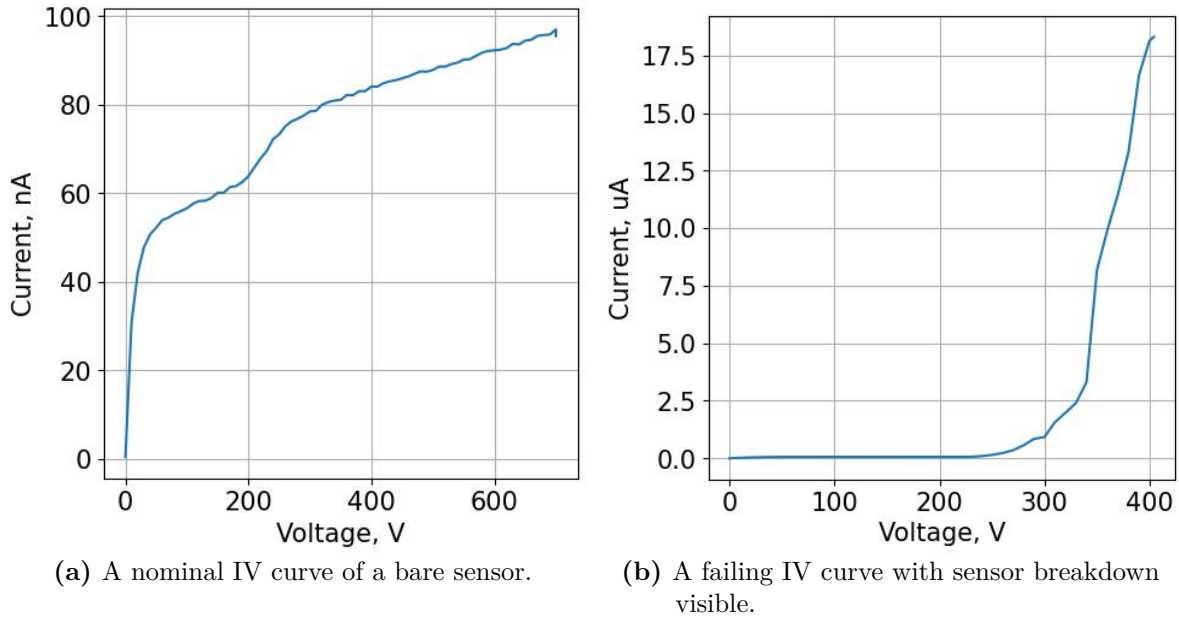
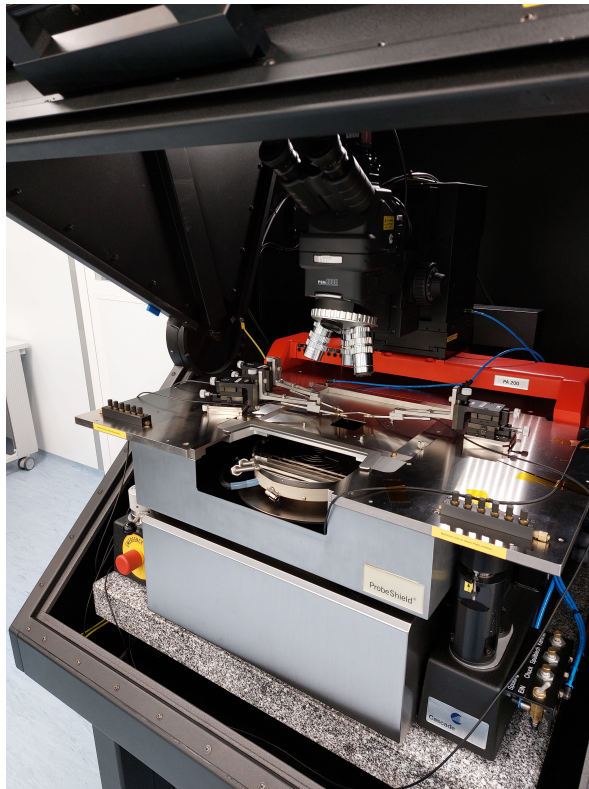


Figure 3.11: Examples of nominal and failing IV curves.

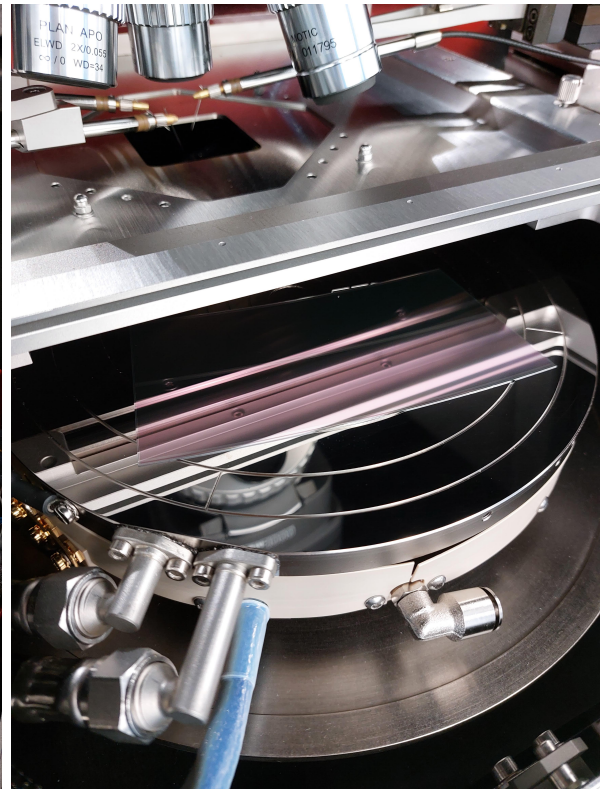
A *breakdown* is an important concept for sensor characterization. Due to defects, surface charges or high humidity a semiconductive sensor can become conductive, which leads to a sudden big increase in the leakage current with small increases in voltage, as shown on the right in Figure 3.11. Normally, this happens in small, point- or line-like areas on the sensor surface. When the breakdown happens due to reasons such as high humidity or presence of surface charges, the sensor can be recovered and used, however when it is caused, for example, by mechanical damage, the sensor is typically not recoverable.

In order to monitor the characteristics of the sensors, multiple IV curves are measured during the production of each module: after reception of a sensor at each sensor site, after attaching the HV-tab and after the module is finished, as well as after each shipment and whenever it is necessary to check the performance of a module. At DESY, the IV curve of a bare sensor (a sensor with no other components attached to it) is measured using a probe station. The sensor is held onto a *chuck* (metal plate) with vacuum, and the opening in the *bias ring* (an implant used to establish and maintain the electric field necessary for the operation of the sensor [63]) of the sensor is touched with a thin grounded needle. The high voltage is applied to the chuck, and module's surroundings are flushed with dry air to ensure low humidity during the measurement. Figure 3.12 shows the probe station itself, as well as a microscope picture depicting the needle touching the opening in the bias ring. The temperature and humidity during measurement are monitored, but not controlled. The dry air flow quickly reduces the relative humidity to almost 0%, so it is roughly constant in all tests, and the temperature during the test is determined by the room temperature, which is constant typically within 0.5°C .

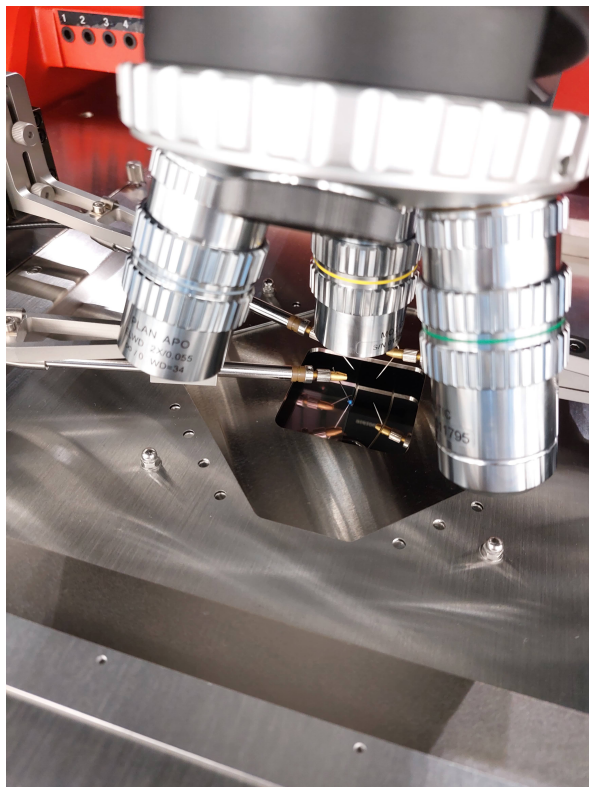
After the HV-tab is attached, the next IV curve is measured using a different setup, shown in Figure 3.13. The module is wire-bonded to a test frame, which is connected to high voltage using dedicated power cables attached to connectors on the test frame. Although the HV-tab is already in place, it is not used for biasing the sensor during this test. Instead, wire bonds are in place for that purpose. This allows to assess the effect that HV-tab attachment had on the sensor and does not take into account the quality of the tab itself. As before, a constant flow of dry air is provided in order to ensure low humidity, and the environment parameters are also



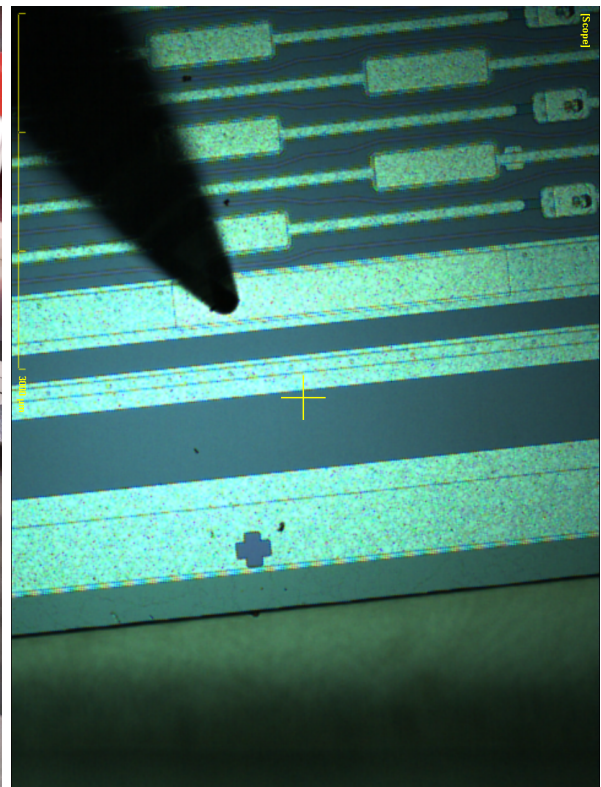
(a) Probe station.



(b) Sensor on the probe station's chuck.



(c) Probe station needles, with one of them touching the opening in the bias ring of the sensor.



(d) A microscope image of the needle touching the opening in the sensor's bias ring.

Figure 3.12: Setup for measuring IV curves for bare sensors.

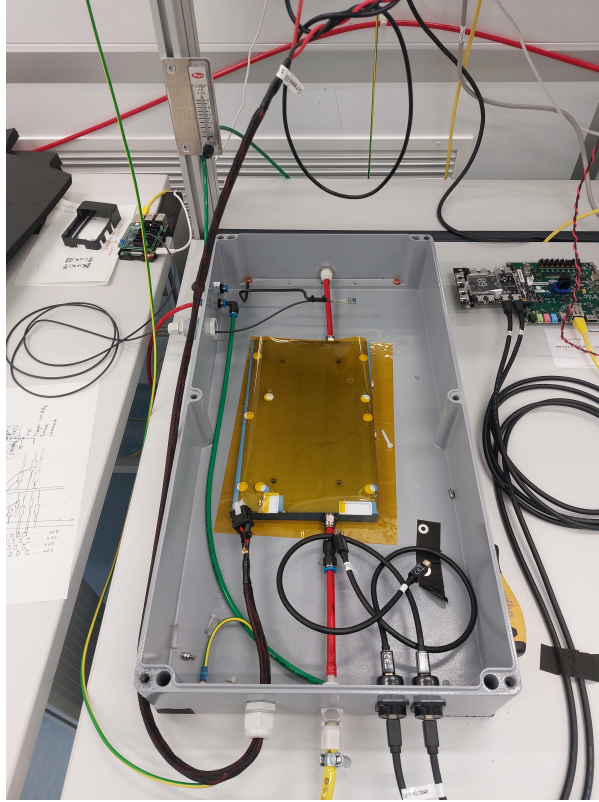


Figure 3.13: Setup for single module testing: a light-tight box with an electrically insulated jig for module placement. Dry air is supplied to the setup, humidity and temperature inside of the box are measured by environment sensors.

monitored. The leakage current at this stage is normally higher than before this attachment, however it is still at an acceptable level.

The measurement procedure changes once again once the full module is built. Whereas before the leakage current was measured by the power supply, and a $1\text{ M}\Omega$ resistor was connected externally in series with the module to prevent possible sudden changes in current or voltage from damaging the sensor, the powerboard of an assembled module is capable of both of these functions. This measurement is also performed on a test frame. Apart from the power cables, two mini-Display Port cables for reading out the data from the powerboard and hybrids are connected as well. The leakage current is measured by the AMACStar chip instead of by the power supply, as before, and biasing the sensor is achieved in a way, close to real detector operation, through the HV-tab and controlled by the AMACStar.

Since IV curves are measured repeatedly throughout module production, these results can be used for assessing the quality of the module construction process and identifying factors that result in worsening of sensor quality.

All the data about the ITk strip components, as well as the results of the performed tests are stored in a dedicated database, the *ITk production database*, designed specifically for this purpose [68]. A tool for production monitoring, which interfaces with this database and allows to compare the IV curves at various module production stages, was designed.

3.3.2 Comparison procedure

For IV curve comparison, criteria need to be designed that would allow to mark the cases where the IV curve has changed. The most important characteristic of an IV curve is the sensor's breakdown voltage that needs to be above the maximum ITk strip operation voltage of 500 V. Another important value is the leakage current at 500 V, which cannot be too large as it would hinder charge collection. Finally, the shapes of the curves have to be similar enough in order to prove that the sensor's properties have not changed significantly.

The goal of the study is to compare the sets of IV curves for the same sensor before and after the HV-tab attachment, shipping of sensors between ATLAS sites, and long storage. The first two categories are designed to monitor the sensor quality and to study if the attachment of the HV-tab and the shipment of the sensor affect it. When sensors are used for module assembly more than three months after the last IV test, they are required to be tested again. The last comparison category is aimed at determining the necessity of this requirement.

The study is focused on identifying the stages of module production, which do not change the quality of the sensors, with the purpose of reducing the required amount of testing. This reduction is important as every test adds a risk of damaging the sensor during its handling. Additionally, conducting fewer tests for each sensor would save significant time during production, as measuring of an IV curve for one sensor can take up to one hour. The possible changes that were considered include removing the requirement to test the sensors at certain stages, performing the tests after shipping only when issues during shipping were observed, and testing only a few sensors from each shipment instead of all of them.

As the leakage current depends on the sensor temperature, before comparing the two curves, it is necessary to normalize the currents to the same temperature. However, the temperature data provided in the database are not always reliable, and it is possible that the actual temperature was different from the one reported in the database due to measurement errors and errors in entering the numbers when uploading the test results. For this purpose, a temperature correction procedure is applied to account for possible inaccuracies in temperature measurement.

Temperature correction

The leakage current at an arbitrary target temperature can be derived from the current at the source temperature as

$$I_{\text{target}} = I_{\text{source}} \times \left(\frac{T_{\text{target}}}{T_{\text{source}}} \right)^2 \times e^{-\frac{E}{2k_B} \left(\frac{1}{T_{\text{target}}} - \frac{1}{T_{\text{source}}} \right)}, \quad (3.1)$$

where $E = 1.2$ eV is the silicon band gap energy, and $k_B = 8.6 \times 10^{-5}$ eV/K is the Boltzmann constant [64].

The scaling coefficient $C(T_{\text{source}}, T_{\text{target}})$ for current conversion is defined as

$$C(T_{\text{source}}, T_{\text{target}}) = \left(\frac{T_{\text{target}}}{T_{\text{source}}} \right)^2 \times e^{-\frac{E}{2k_B} \left(\frac{1}{T_{\text{target}}} - \frac{1}{T_{\text{source}}} \right)}. \quad (3.2)$$

If the temperature at the time of measurement can deviate from the value stored in the database by $\Delta T = 5^\circ\text{C}$, the scaling coefficient has a maximum allowed range $[C(T_{\text{source}} + \Delta T, T_{\text{target}}); C(T_{\text{source}} - \Delta T, T_{\text{target}})]$ for this ΔT , as $C(T_{\text{source}}, T_{\text{target}})$ decreases monotonically with increase of T_{source} for a fixed T_{target} .

For this correction, it is assumed that the IV curves have the same shape. If this is not the case, the correction will be wrong, but it will not interfere with the goal of the comparison, which is to identify the discrepant test pairs.

The measured currents of the two IV curves are $I_{\text{source}}^{(1)}$ and $I_{\text{source}}^{(2)}$. To correct for temperature effects, the scaling coefficients are adjusted to minimize the difference between the scaled currents defined as

$$D(I_{\text{target}}^{(1)}, I_{\text{target}}^{(2)}) \equiv \sum_i (I_{\text{target } i}^{(1)} - I_{\text{target } i}^{(2)})^2, \quad (3.3)$$

where the index i denotes a point of an IV curve, corresponding to a certain bias voltage. As the currents can be unstable at low voltages and after the breakdown occurs, the current values, corresponding to voltages between 30 V and the smallest breakdown voltage of the two measurements, are used.

For obtaining the optimal scaling coefficients, one needs to minimize the difference between the two target currents by varying the coefficients C_1 and C_2 :

$$D(I_{\text{target}}^{(1)}, I_{\text{target}}^{(2)}) = D(C_1 \times I_{\text{source}}^{(1)}, C_2 \times I_{\text{source}}^{(2)}). \quad (3.4)$$

Instead of varying two coefficients, one can vary one combined coefficient, defined as

$$C_{12} = \frac{C_1}{C_2}, \quad (3.5)$$

in the following difference:

$$D(C_{12} \times I_{\text{source}}^{(1)}, I_{\text{source}}^{(2)}). \quad (3.6)$$

Thus, $I_{\text{source}}^{(1)}$ is effectively scaled to the temperature of the measurement of $I_{\text{source}}^{(2)}$.

Given the maximum potential deviation of the temperature measurements ΔT , the allowed ranges for the coefficients C_1 and C_2 are

$$C_1 \in [C(T_{\text{source}}^{(1)} + \Delta T, T_{\text{target}}), C(T_{\text{source}}^{(1)} - \Delta T, T_{\text{target}})], \quad (3.7)$$

$$C_2 \in [(C(T_{\text{source}}^{(2)} + \Delta T, T_{\text{target}}), C(T_{\text{source}}^{(2)} - \Delta T, T_{\text{target}})] . \quad (3.8)$$

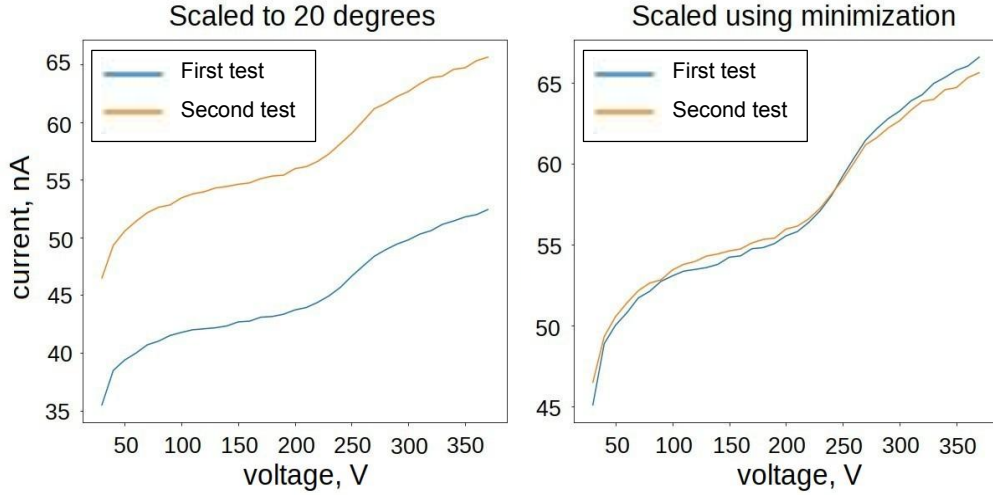
As the function 3.2 monotonically decreases for T_{source} for each fixed T_{target} , the allowed range for the combined coefficient C_{12} is

$$C_{12} \in \left[\frac{C(T_{\text{source}}^{(1)} + \Delta T, T_{\text{target}})}{C(T_{\text{source}}^{(2)} - \Delta T, T_{\text{target}})}, \frac{C(T_{\text{source}}^{(1)} - \Delta T, T_{\text{target}})}{C(T_{\text{source}}^{(2)} + \Delta T, T_{\text{target}})} \right]. \quad (3.9)$$

For each pair of compared tests, the currents of the first test are multiplied by C_{12} , and afterwards the curves are compared. That way the inaccuracies of the T values in the database are accounted for. In Figure 3.14 an example of temperature correction is shown. It is clear that curve shapes are similar, and after temperature correction the curves almost completely overlap.

When both currents are scaled to 20°C using the temperature stated in the database, a combined coefficient can be obtained in the same way as in Equation 3.9 by dividing the coefficient for the first current by the coefficient for the second current.

Figure 3.15 shows distributions of the combined coefficient for scaling to +20°C using the temperature during the test stated in the database and the combined coefficient obtained with



(a) IV curves scaled from the temperature reported in the database to 20°C with the scaling coefficient determined purely by the temperature values.

(b) IV curves scaled using the combined scaling coefficient determined using the minimization procedure.

Figure 3.14: Example of two IV curves and the different current scaling approaches

minimization. Both distributions have peaks around 1, corresponding to cases when the reported temperature was correct and close to 20°C , but the shapes are different.

Due to the database being at early stages of its development at the time of this study, the uploading process was not the same for all test data. In some results, the currents were automatically corrected from the test temperature to $+20^{\circ}\text{C}$ with no indication of it and the test temperature stated in the database being different from $+20^{\circ}\text{C}$, while in others the measured currents were reported. This ambiguity affects the IV curve comparison and it can be addressed by the temperature correction, introduced here, to some extent. After this was noticed, the uploading procedures were unified, and the currents in the database now correspond to the ones measured during test without any temperature correction applied during data upload.

3.3.3 Comparison criteria

As stated above, the important characteristics of an IV curve comparison are the breakdown voltage, the leakage current at 500 V and the curve shape, so a comparison of these parameters will provide information about the changes in the sensor's quality. Apart from the absolute value of the breakdown voltage, its change from the earlier test to the later one holds information about the changes in the quality of the sensor, so this change enters the comparison as well.

Two IV curves are considered similar if

1. Breakdown voltages in both tests are > 500 V. This criterion is referred to as the *Vbd value* criterion.
2. The breakdown voltage of the second (later in time) test is not smaller than breakdown voltage of the first test. If it is smaller, then the difference should not exceed 100 V. This criterion is later referred to as the *Vbd diff* criterion.
3. The leakage current at 500 V of the second (later in time) test is smaller than of the first test. If it is bigger, then the difference should not exceed 50% of the current in the first test. This criterion is later referred to as the *I500 diff* criterion.

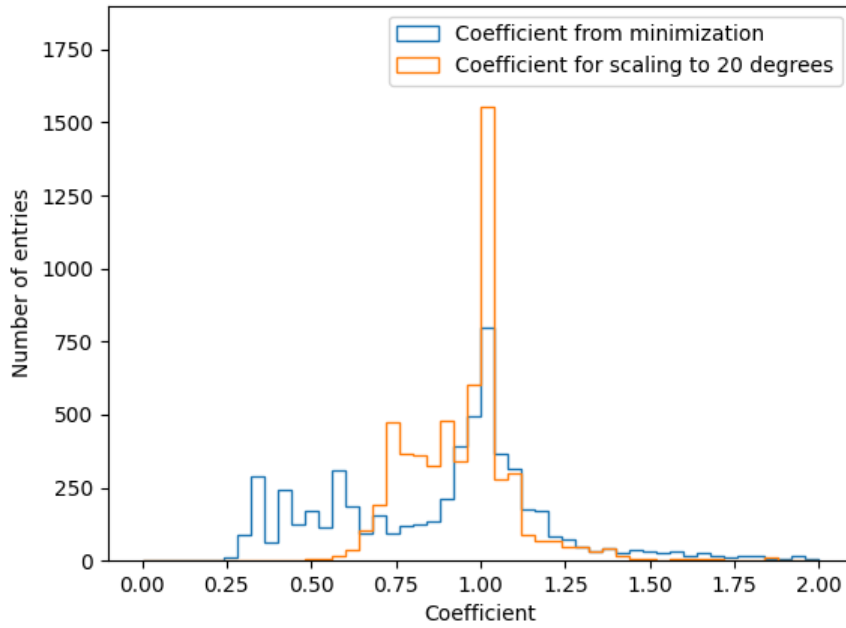


Figure 3.15: Distribution of coefficients for scaling from the reported test temperature to $+20^{\circ}\text{C}$ and coefficients obtained with minimization.

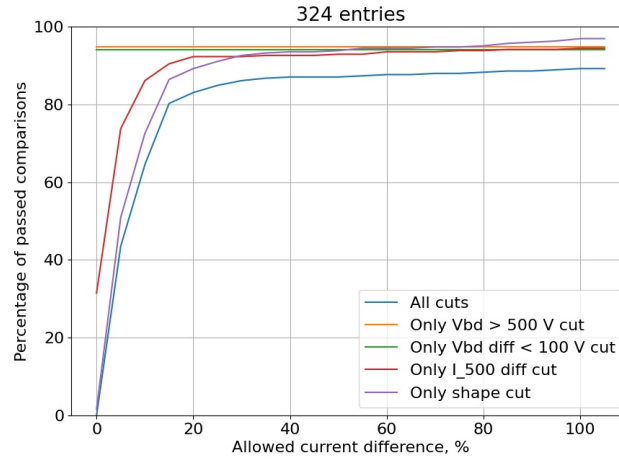
4. The curve shapes are similar enough (this criterion is later referred to as the *Shape* criterion):
 - All voltage values, for which the leakage current is measured in both curves, are used.
 - For those common voltage points the values of the current are compared.
 - If less than half of compared currents differ no more than 50%, the curves are considered to have the same shape.

Comparison of IV curves before and after a given handling procedure allows us to draw conclusions about the impact of this specific procedure on an individual sensor. A procedure (shipment, HV-tab attachment or storage) is considered *flagged* if at least one of the comparison criteria is not met and *non-flagged* otherwise.

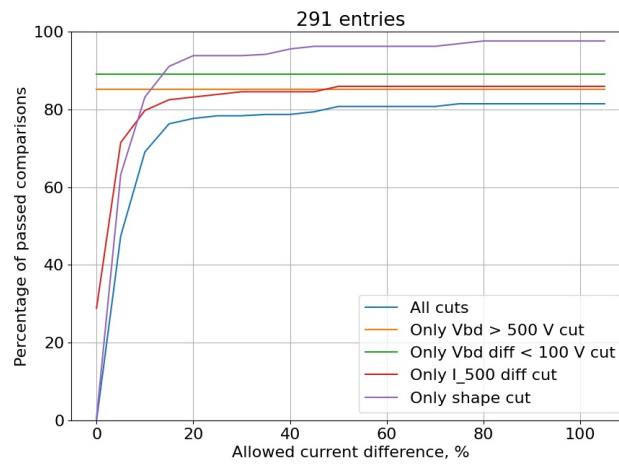
In order to establish the proper allowed changes for the different parameters used in the comparison, the full range of changes was studied, both simultaneously and independently. The allowed leakage current difference affects criteria *I500 diff* and *Shape*. Figure 3.16 shows the dependence of the fraction of non-flagged procedures on the allowed current difference for each criterion separately, as well as for all of them applied together. Based on these plots, an allowed difference of 50% was selected.

The allowed breakdown voltage decrease affects criterion *Vbd diff*. The dependence of the fraction of non-flagged procedures on allowed breakdown voltage decrease is shown in Figure 3.17. Based on these plots, the allowed decrease of the breakdown voltage is set to 100 V.

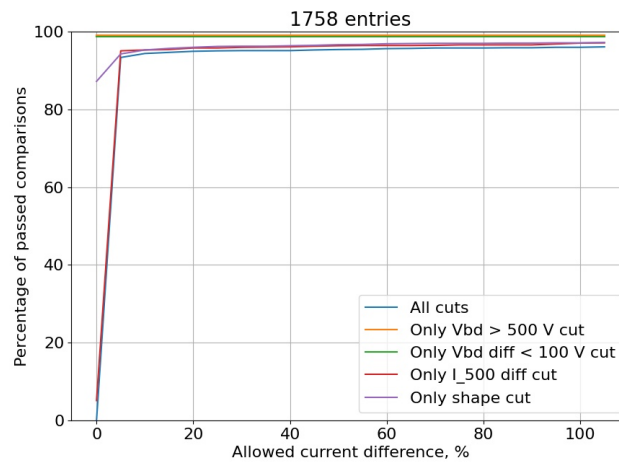
The criteria in this list are sorted from most important to least important. If a more important criterion is not satisfied in a comparison, this would be noted as the cause for flagging the test pair. For example, if for a pair of tests the breakdown voltage is 400 V and the shapes are



(a) HV-tab attachment

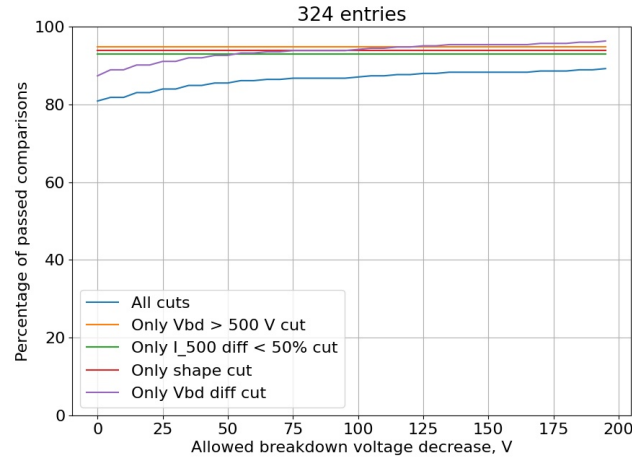


(b) Shipping

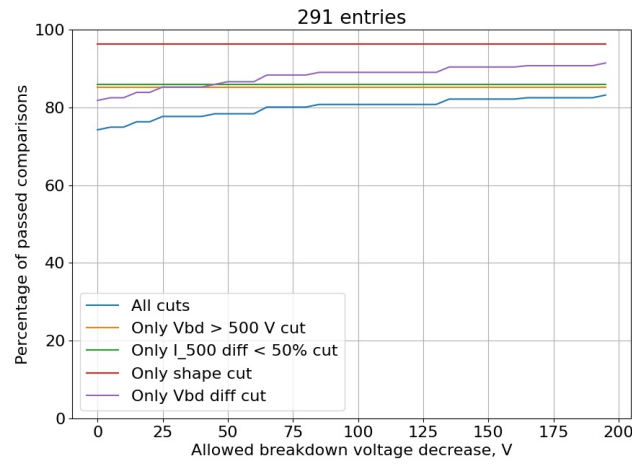


(c) Storage

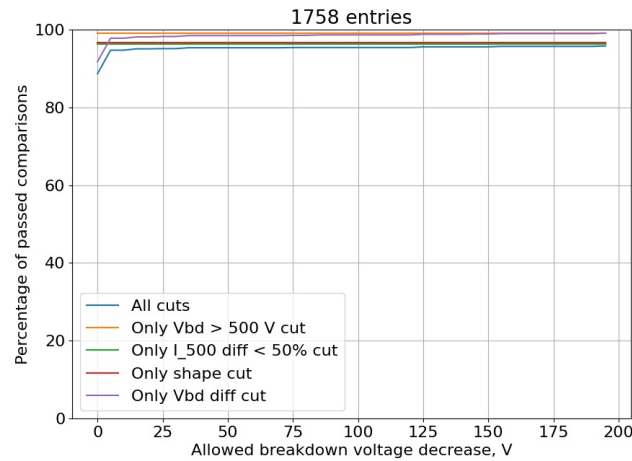
Figure 3.16: Dependence of the ratio of non-flagged procedures on the allowed current difference for the (a) – HV-tab attachment, (b) – shipping, (c) – storage. Orange, green, red and purple lines show the fractions of passed comparisons if only one of the criteria is used. Blue line shows the fraction if all criteria are used together.



(a) HV-tab attachment



(b) Shipping



(c) Storage

Figure 3.17: Dependence of the ratio of non-flagged procedures on the allowed breakdown voltage difference for the (a) – HV-tab attachment, (b) – shipping, (c) – storage. Orange, green, red and purple lines show the fractions of passed comparisons if only one of the criteria is used. Blue line shows the fraction if all criteria are used together.

different, the cause of flagging would be criterion *Vbd value*, as it is more important than the *Shape* criterion.

3.3.4 Results of the study

The results for all three categories are presented in Table 3.1.

Table 3.1: Results of IV comparison for all three studied categories, broken down by individual comparison criteria.

| Criterion | HV-tab attachment | Shipping | Storage |
|-------------------------|-------------------|---------------|-------------|
| Total number of entries | 1216 | 1790 | 941 |
| Vbd value | 84 (6.91%) | 110 (6.15%) | 12 (1.28%) |
| Vbd diff | 54 (4.44%) | 50 (2.79%) | 10 (1.06%) |
| I500 diff | 149 (12.25%) | 75 (4.19%) | 56 (5.95%) |
| Shape | 19 (1.56%) | 456 (25.47%) | 33 (3.51%) |
| Non-flagged | 910 (74.84%) | 1099 (61.40%) | 830 (88.2%) |

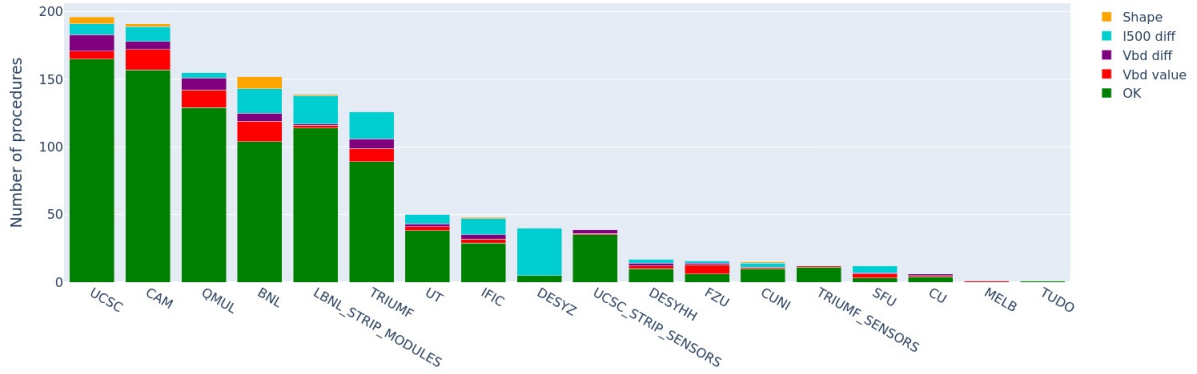
For all categories, a possible correlation with the institution, where the sensor was tested, was studied, as shown in Figure 3.18.

For comparison of tests before and after shipping, correlations with issues and humidity level during shipping were considered, as shown in Figure 3.19 and 3.20. Due to low statistics in many institutions and very few issues during shipping, no such correlations can be determined. The comparison of IV curves before and after shipping is particularly sensitive to differences in the format of the uploaded data as the tests that are compared were uploaded at different sites, in particular some tests were uploaded with leakage current normalized per sensor area, and others without that normalization. For this reason, many shipments in that comparison were flagged by the Shape criterion. Each such case was investigated individually to ensure that no other underlying issue is present. As the vast majority of IV curves stay the same after the long storage, the requirement to retest the sensors if they are used more than three months after the last IV test was removed.

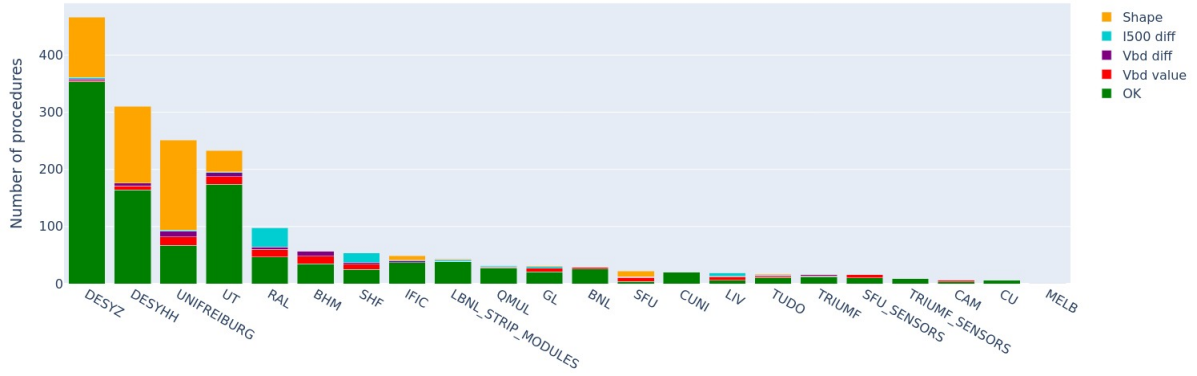
For shipping, a possibility to test only a part of the sensors in the shipment was considered. Figure 3.21 shows the fraction of flagged procedures for shipments containing different numbers of sensors. The relatively constant and high ratio of flagged sensors does not allow sample testing, which means that every sensor in a shipment needs to be tested.

3.3.5 Further development for production monitoring purposes

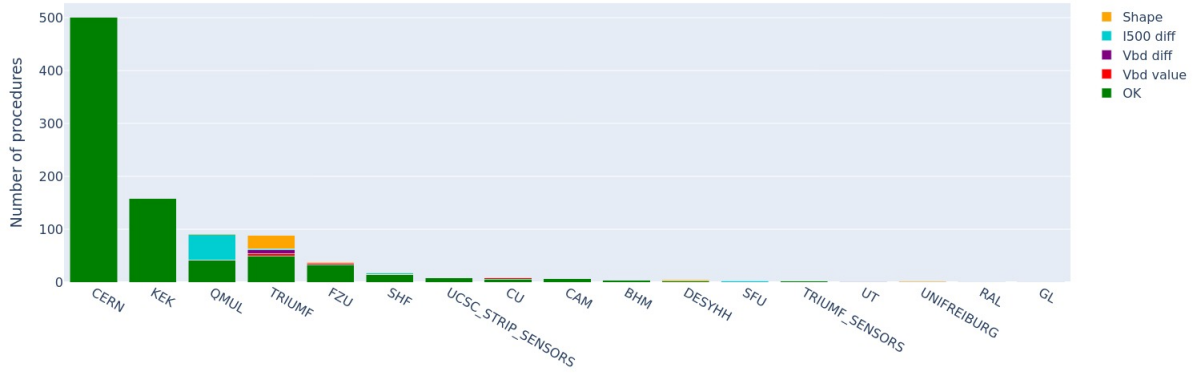
For monitoring production, the goal of the comparison shifts from identifying the stages of module production that do not affect the quality of the sensors to identifying sensor types or institutions that suffer from a particularly high test failure rate. During the previous comparison the aim was to modify the handling procedure in order to reduce testing time, while maintaining high quality of the sensors. Now that the procedure is established it becomes more important identify and react to problematic setups, test conditions or procedures at specific sites in order to maintain a high sensor quality throughout the collaboration. This change of goal means that the selection of the tests needs to be adjusted from the previously described. Comparing the IV curves before and after HV-tab attachment is not changed, while the other categories have to be modified. The focus is shifted from shipping (i.e. physical movement of the sensors) to distribution (i.e. changing the status of the sensor in the database that does not always require shipping). This includes the sites that do both sensor testing and module assembly,



(a) HV



(b) shipping



(c) storage

Figure 3.18: Numbers of flagged procedures for various institutions doing the test before HV-tab attachment (a), after shipping (b) and after long storage (c).

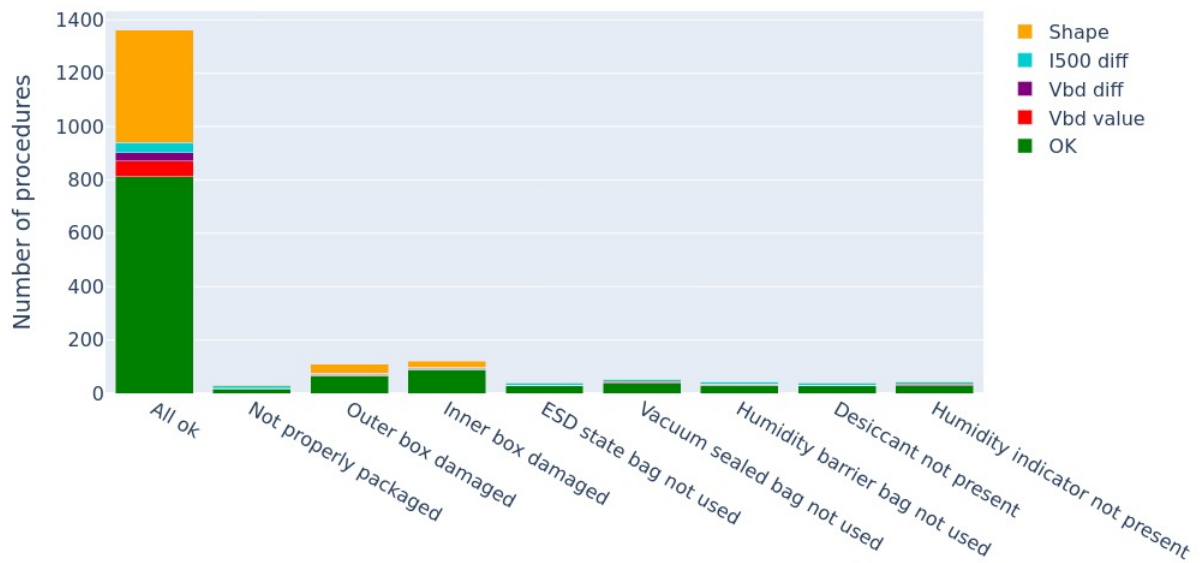


Figure 3.19: Numbers of flagged shipments for issues which occurred during shipping for comparison of IV curves before and after shipping between ATLAS sites. "All ok" means that no issues were observed for the shipping.

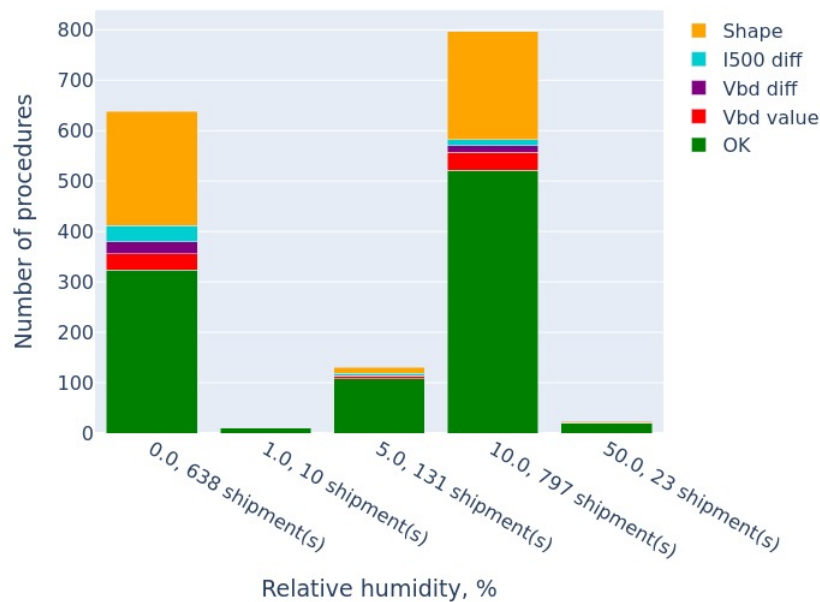


Figure 3.20: Numbers of flagged shipments for relative humidity level during shipping for comparison of IV curves before and after shipping between ATLAS sites.

The sensors that are selected for the comparison, are supposed to pass the first IV by design of the selection – only the sensors that have successfully passed the test, are moved up to the selected stage in the database. Thus, in the criteria only passing or failing of the second IV test is mentioned. Moreover, the updated selection is focused more on the sensor itself than on the specific handling procedure, and therefore the sensors are labeled as flagged or non-flagged in this comparison and not the procedures.

The criterion for the shape difference is the same: for no more than half of the applied voltage values, the measured leakage currents are different by more than 50%.

The sensors are labeled as follows:

1. *Pass (similar IV)*: the second IV curve passes the test, the breakdown voltage decreases by no more than 100 V, the leakage current at 500 V increases by no more than 50%, and the curve shapes are similar.
2. *Pass (Vbd diff)*: the second IV curve passes the test, the leakage current at 500 V increases by no more than 50%, but the breakdown voltage decreases by more than 100 V.
3. *Pass (I500 diff)*: the second IV curve passes the test, the breakdown voltage decreases by no more than 100 V, but the leakage current at 500 V increases by more than 50%.
4. *Pass (Vbd+I500 diff)*: the second IV curve passes the test, but the breakdown voltage decreases by more than 100 V and the leakage current at 500 V increases by more than 50%.
5. *Pass (shape diff)*: the second IV curve passes the test, the leakage current at 500 V increases by no more than 50%, the breakdown decreases by no more than 100 V, but the curve shapes are different.
6. *Fail*: the second IV curve fails the test, i.e. the breakdown voltage is lower than 500 V or the leakage current at 500 V is higher than $0.1 \mu\text{A}/\text{cm}^2$.

Comparison criteria for monitoring sensor recovery

The goal of this study is not monitoring the differences in the IV curves, but monitoring the recovery of sensors. In addition to the IV curve data, the information about the recovery measures carried out is provided in the database. The sensors that are selected for this study, did not pass the first IV test. Each sensor is then labeled as

- *Recovered*, if the second IV curve passes the test, and there is data in the database about the measures, carried out to recover the sensor.
- *Not recovered*, if the second IV curve fails the test, and there is data in the database about the measures, carried out to recover the sensor.
- *Not attempted*, if there is a failed IV curve test, and no further information is uploaded,
- *No recovery data*, if there is a passed IV test after the failed one, but no information about recovery measures is uploaded.

Effects of HV-tab attachment

For this comparison, the last IV curve measured before the HV-tab attachment is compared to a measurement after its attachment. Two comparisons are done for each sensor: comparison with the first IV curve after the HV-tab attachment and with the last IV curve after HV-tab attachment measured in the same institution as the first one. The first comparison allows to

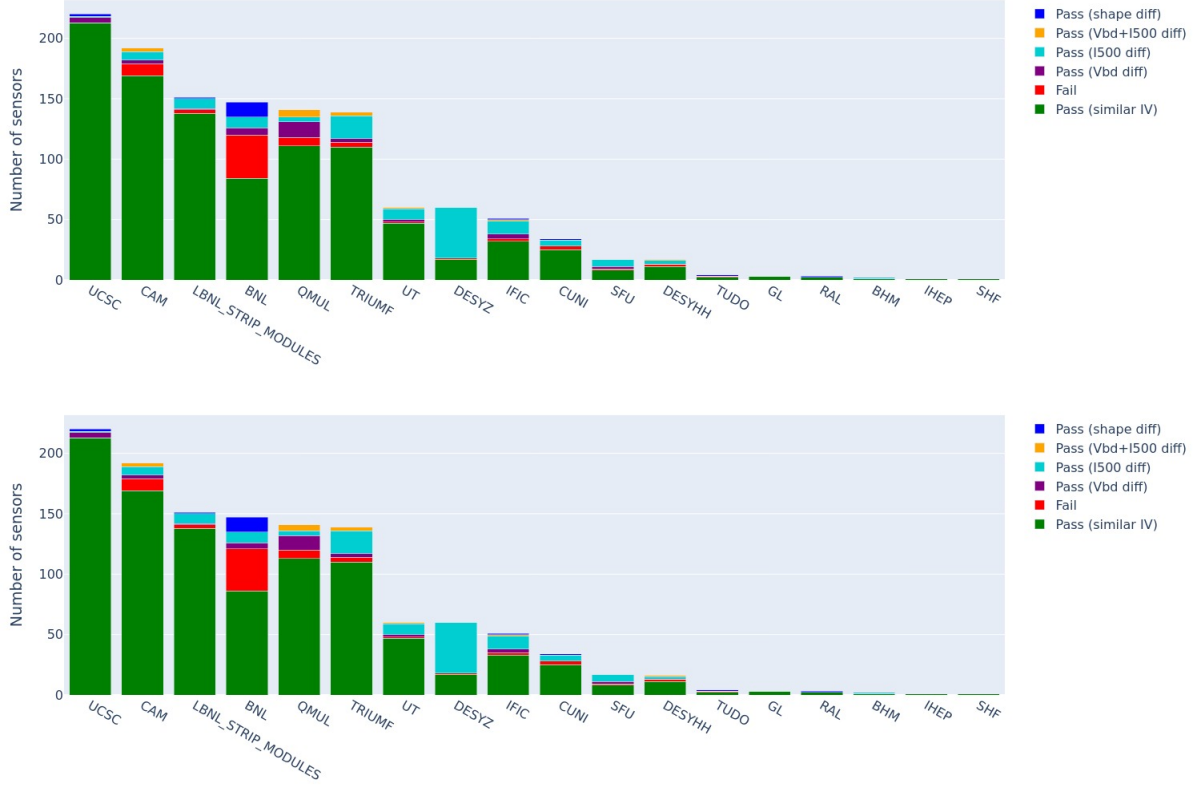


Figure 3.22: Results of the comparison of the IV curves of the last test before HV-tab attachment and the first test after HV-tab attachment at the top, and the last test after the HV-tab attachment at the bottom, for different institutions.

monitor the effects that the procedure had on the sensor. The second comparison allows to assess the quality of the future module and takes into account the possible recovery that took place.

Figure 3.22 shows the results of the study for different HV-attachment institutions for comparison with the first and the last IV curve measured after the HV-tab is attached. Figure 3.23 shows the same information, given for different sensor types.

Effects of sensor distribution

For this comparison, the last IV curve measured during sensor quality control tests at sensor testing site is compared to an IV measured at the module assembly site. As with the previous category, the second IV curve can be the first or the last in time at that module stage, which allows to see potential recovery and the effects of distribution.

Figure 3.24 shows the results of the study for different module assembly institutions for comparison with the first and the last IV curve measured after the sensor distribution. Figure 3.25 shows the same information, given for different sensor types.

Sensor recovery monitoring

For this comparison, the sensors that have a failed IV test at the module assembly site are chosen.

The possible methods used for recovery include:

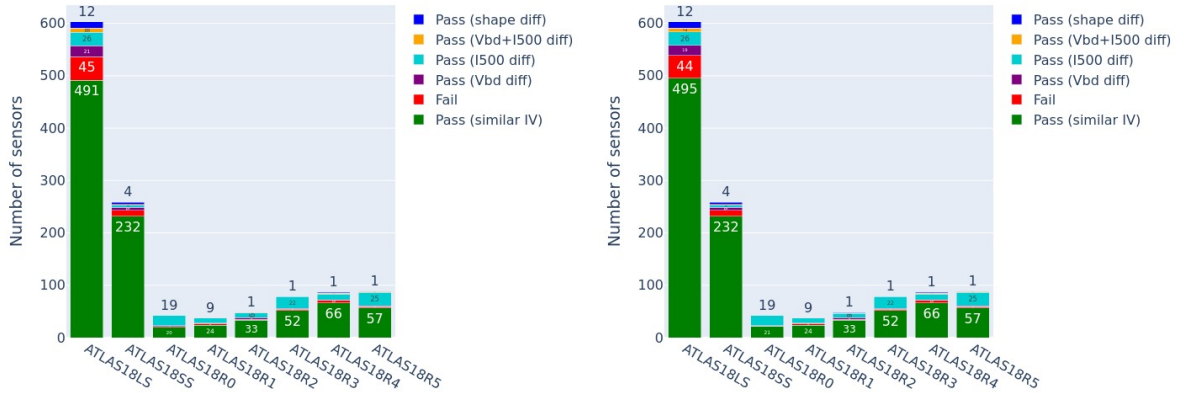


Figure 3.23: Results of the comparison of the IV curves of the last test before HV-tab attachment and the first test after HV-tab attachment on the left, and the last test after HV-tab attachment on the right, for different sensor types.

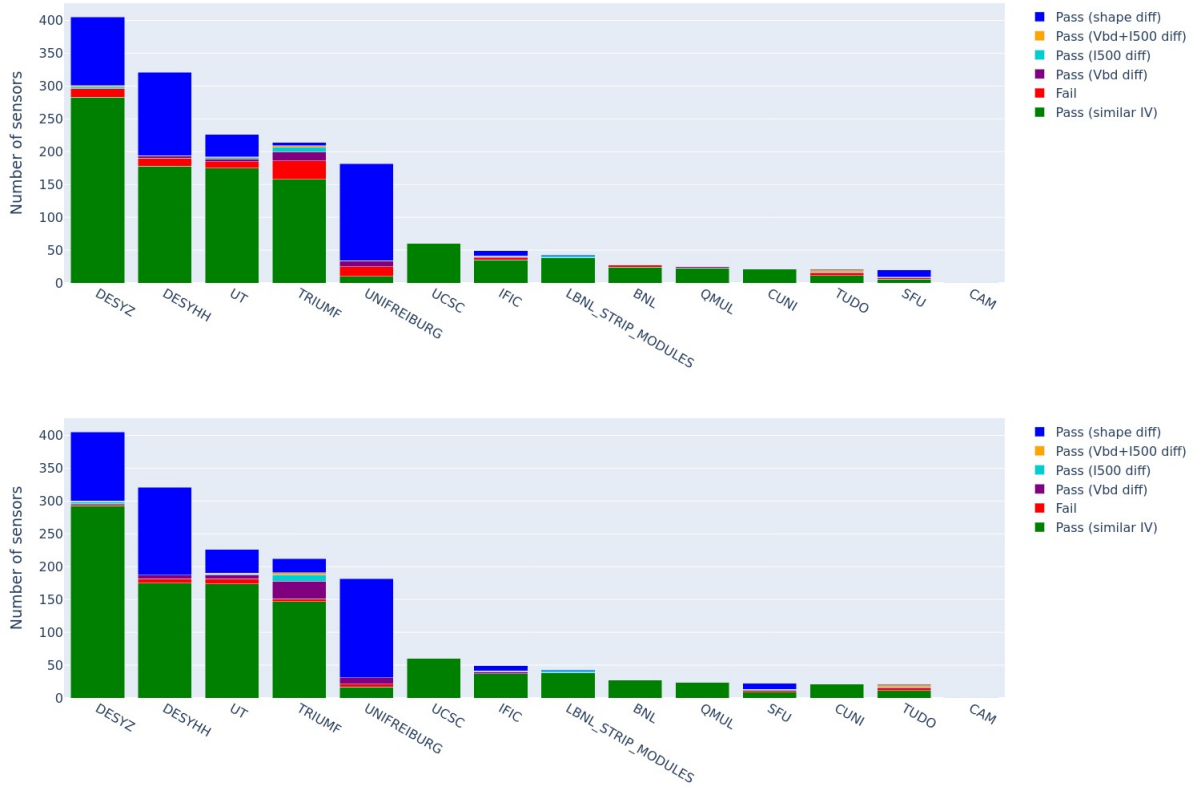


Figure 3.24: Results of the comparison of the IV curves of the last test before distribution and the first test after it at the top, and the last test after the distribution at the bottom, for different institutions.

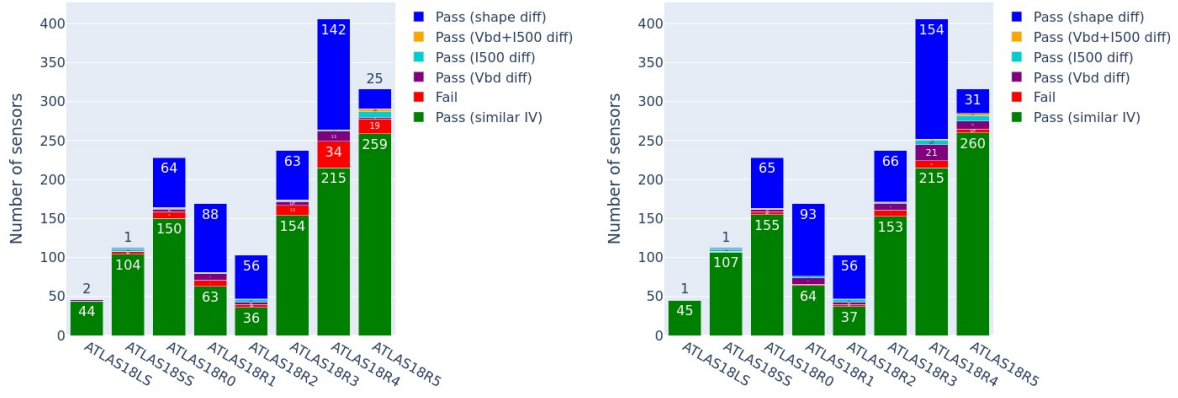


Figure 3.25: Results of the comparison of the IV curves of the last test before distribution and the first test after it on the left, and the last test after distribution on the right, for different sensor types.

- Annealing – heating the sensor up to 160°C for up to 15 hours;
- UV irradiation;
- Storage in a dry environment for an extended period of time;
- Long term HV – keeping the sensor at 450 V for 40 hours;
- Repeating the IV curve measurement;
- Plasma cleaning;
- De-ionization.

Annealing is performed in order to treat defects in the bulk of the semiconductor [64], while all other methods are aimed at releasing charges trapped in the oxide layer of the sensor and are an established standard in the microelectronics industry.

Figure 3.26 on the left shows the recovery success rate for various recovery methods that were used. Due to insufficient statistics, no conclusions can be drawn on the comparison between the methods, however it is shown that most of the sensors are recovered. On the right, recovery information is shown for different sensor types.

Figure 3.27 shows the information about sensor recovery for different sensor testing institutions. Currently there is not enough data about the recovery measures in the database, however from this plot it can be seen that many sensors can be recovered. As more recovery data is obtained, conclusions could be drawn from these about the recovery measures that should be used and the institutes with anomalous sensor recovery rate could be identified.

3.4 Strip module electrical tests

After the modules are assembled, a thorough electrical test program is performed as part of the module quality control in order to assess the parameters of the module, such as input and output noise and the gain of the amplifiers on the readout electronics. The parameters are introduced in more detail below in the description of the tests.

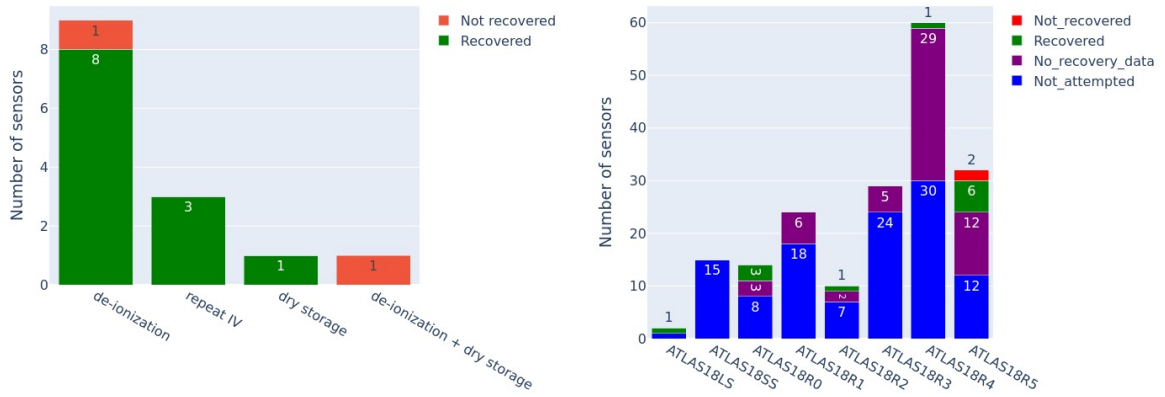


Figure 3.26: Results of the sensor recovery monitoring for various recovery techniques (left) and sensor types (right).

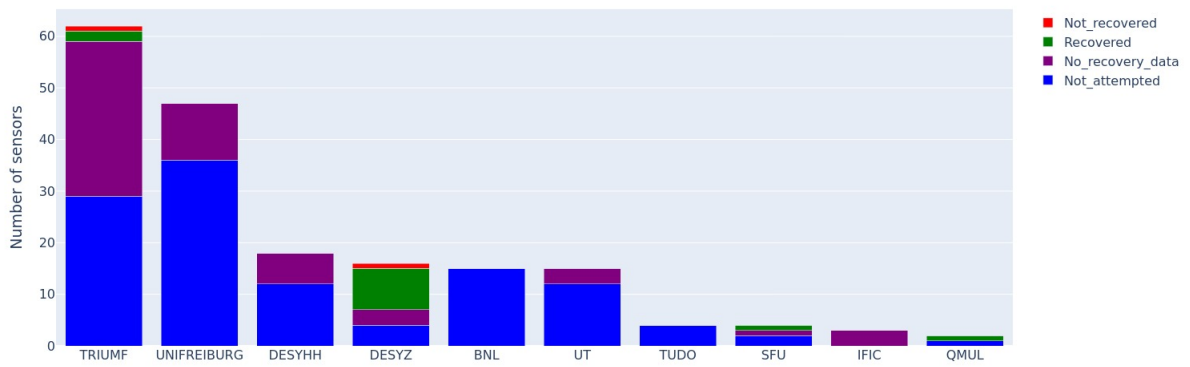


Figure 3.27: Sensor recovery information for sensor testing institutions.

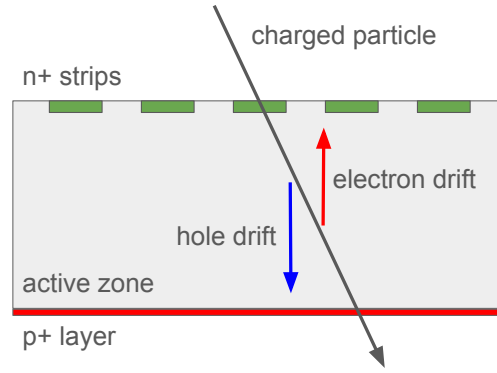


Figure 3.28: Schematic cross section of a fully depleted silicon strip sensor. A depleted active zone without free charge carriers is maintained by applying bias voltage, and the charges created by a passing charged particle drift to the electrodes in the electric field. Image adapted from [69].

3.4.1 Charge collection and binary readout

Biasing a semiconductor sensor creates a *depletion zone* in its bulk, with electric field, but without free charge carriers. Passage of a charged particle through the depletion zone creates free charge carriers, electron and hole pairs, through ionization. Electron-hole pairs begin to drift under the influence of the electric field in the depletion zones to the sensor surfaces, each carrier type to the corresponding electrode, as shown in Figure 3.28.

Induced currents on the electrodes are created as a result of this drift, and the current pulses can be amplified and measured by the readout electronics. The ITk strip detector is designed with binary readout architecture, which means that the current pulses with amplitudes exceeding a predefined threshold are considered *signal*, and the pulses below that threshold are not considered signal. Due to electronic noise, the detection of current pulses with amplitudes close to the threshold can be ambiguous. Figure 3.29 (a) shows the signal pulses of different amplitude in the absence of noise. For this case, pulses with amplitudes bigger than that of the middle pulse would be identified as signal and the pulses with amplitudes lower than the amplitude of the middle pulse would be identified as no signal. Figure 3.29 (c) depicts the non-ideal case with presence of noise, which is represented by the gray-shaded area for the middle charge pulse. In the presence of noise, the pulse detection becomes ambiguous, and not all pulses with amplitudes close to the threshold would be correctly identified. For a *threshold scan*, a charge is repeatedly injected at the input of the amplifier of a readout channel. Pulse detection efficiency is measured for a wide range of threshold values, and the dependence of this efficiency on the threshold value is called an *S-curve*. Without any noise, the distribution would be a step function, as shown in Figure 3.29 (b), however when noise is present, the distribution becomes an *S-curve*, as is shown in Figure 3.29 (d).

3.4.2 Description of the electrical tests

The module quality control tests are listed below [63, 70], and some of these tests are also performed for hybrids before module assembly. *Full test* in the following descriptions will refer to a combination of all of these tests. The tests with current pulse injection are performed by injecting a charge into the input of the amplifier of each readout channel using dedicated calibration capacitors included in the front-end circuitry.

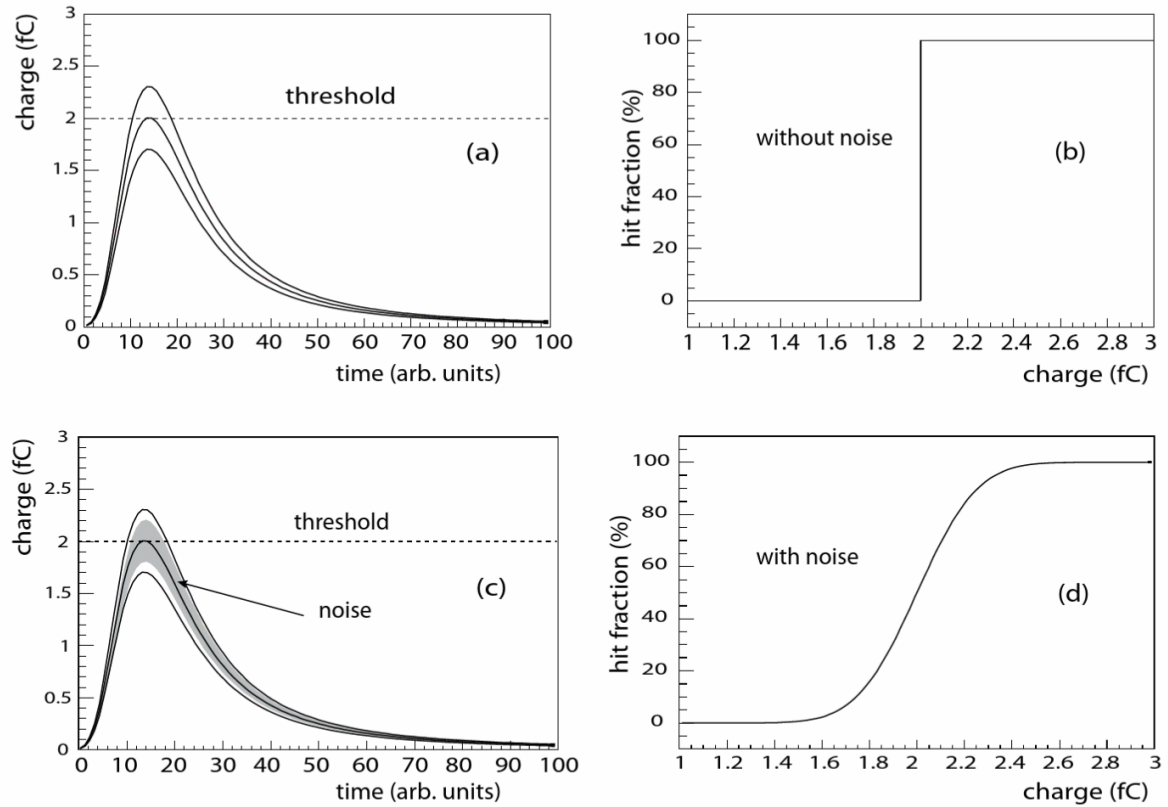


Figure 3.29: The principle of binary readout. (a): current pulses of different amplitudes without noise. (b): dependence of hit fraction on the threshold charge for the case without noise. (c): current pulses of different amplitudes in the non-ideal case, the noise for the middle pulse is represented by the gray-shaded area. (d): dependence of hit fraction on the threshold charge for the case with noise. [64]

Chip communication test

Chip communication test is used to ensure that the wire bonds, connecting the chips to the hybrids and the hybrids to the test frames, are present. During these tests, the IDs of the HCCStar and the ABCStar chips are extracted, verifying also that the chips are functional and the communication with them is possible.

Strobe delay

Strobe delay test is performed in order to ensure that the injected calibration pulse is synchronized with the discriminators, always firing at clock frequency. Since there is a delay between issuing the command to inject the pulse and the actual injection, the time of sending this command needs to be adjusted in order for the pulses to be injected at the right times. The time varies between the chips due to small differences between them. It is also sensitive to environment conditions.

Three-point gain

In a threshold scan, the threshold value that provides an efficiency of 50% is called $Vt50$, the efficiency of 50% is chosen for this definition arbitrarily. The first derivative of the S-curve has a maximum at $Vt50$, and the standard deviation of that distribution corresponds to the output noise of the amplifier. For the three-point gain test, a threshold scan is performed for three different injected charges – 0.5 fC, 1.0 fC and 1.5 fC, and the dependence of $Vt50$ on the injected charge can be approximated using a linear function. The slope of this line is the signal amplification, called gain. The input noise at the amplifier circuitry can be calculated by dividing the output noise by the gain of the amplifier. Example plots from a three-point gain measurement are shown in Figure 3.30.

Trim range

The readout threshold values for module operation are set globally for each readout chip and not for individual channels. The threshold value for the chip is chosen to be as low as possible, while also providing an acceptable noise occupancy. The S-curves for different channels are naturally slightly shifted with respect to each other due to slight differences between the channels. A scan is performed in order to find a threshold to which a majority of channels can be trimmed, and a charge is injected into the front ends, artificially shifting some of the S-curves. After this procedure, the $Vt50$ values are distributed uniformly across the channels of the chip.

Response curve

For the response curve test, a threshold scan is performed for ten different injected charges up to 6 fC, expanding their range compared to the three-point gain test, and therefore exploring the non-linearity in the relationship between the injected charges and the thresholds. This test is done after the channels have been trimmed.

Noise occupancy

For the noise occupancy test, a threshold scan is performed with no injected charge, and the noise level for each threshold value is determined. The testing conditions are close to those during detector operation. This test gives an idea of the effect of the electronic noise on a threshold scan and its influence on the noise figure.

Based on this result and on the efficiency curve provided by measurements, for example from a test beam campaign, an *operational window* can be constructed as a range of thresholds which provide sufficient signal detection efficiency while at the same time having sufficiently low noise levels.

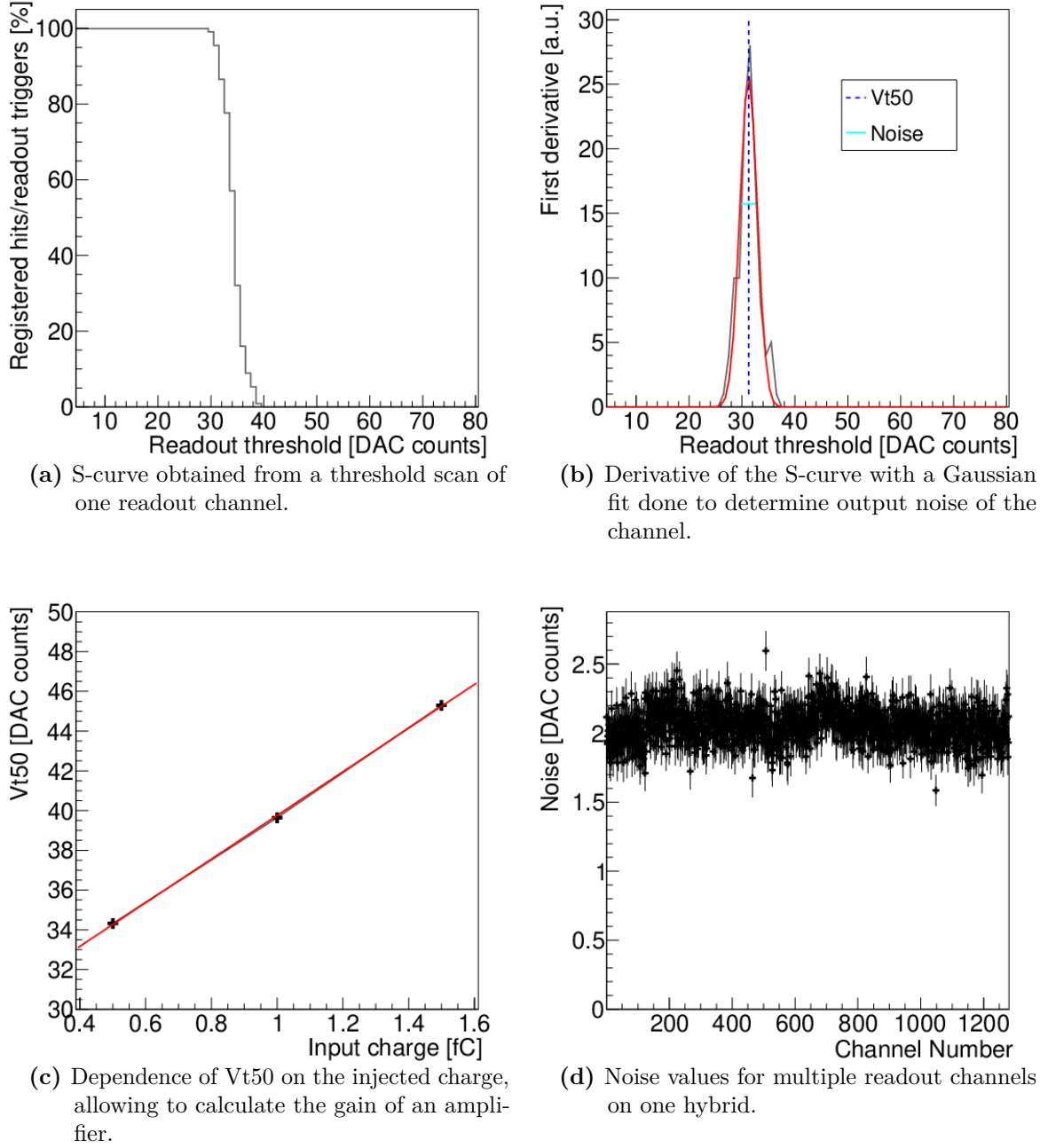


Figure 3.30: Example plots of a three-point gain measurement. Image adapted from [63].

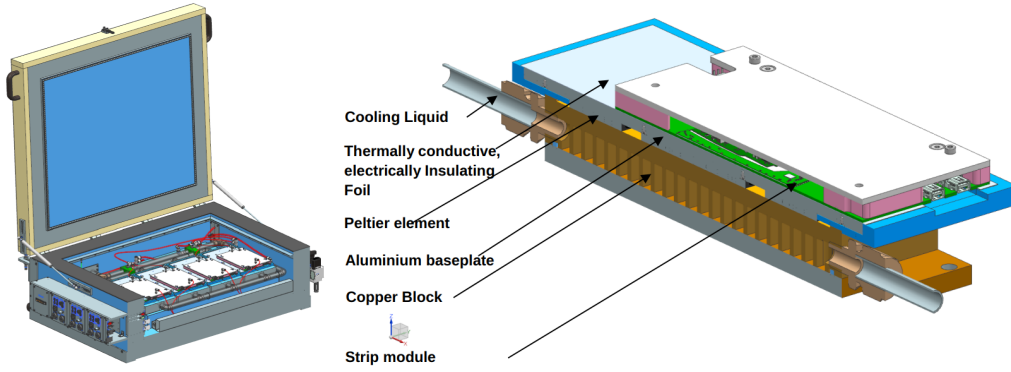


Figure 3.31: Left: 3D model of an endcap coldbox. Right: Cross section of a chuck.

Open channel search

Open channel search is designed to check the quality of the front-end wire bonds. The bias voltage during the test is 10 V, and the noise of the channels is measured as described above. The electronics channels that are disconnected from the strips have a significantly lower level of noise than the ones that are connected, as they have a lower coupling capacitance than the ones attached to a strip channel, which can be used to identify the lower-quality wire bonds.

3.5 Thermal cycling

One of the most important and demanding module quality control steps is the thermal cycling. It involves placing the assembled modules into a special setup, called a *module coldbox*, and subjecting it to 10 cycles of temperature changes between -35°C and $+20^{\circ}\text{C}$ with electrical testing at both temperature extremes. The aim of the procedure is to test the robustness of every produced module and to ensure that it is suitable for becoming a part of the final detector. Endcap coldboxes were designed and assembled centrally at DESY, and then distributed to every endcap module assembly site [71]. The DESY Hamburg setup is controlled by a Programmable Logic Controller (PLC) SIMATIC S7-1200 [72]. While other approaches exist, they are not covered in this thesis [70]. This section describes in detail the thermal cycling procedure, the construction of the setup with all the hardware components, the structure of the software and the modifications that had to be implemented in order to integrate the PLC-controlled setup into the common software framework. At the end, results of successful automatic thermal cycling are presented.

3.5.1 Coldbox hardware

An endcap coldbox is a light-tight and thermally insulated chamber that can hold up to four modules at once. The locations for modules are called *chucks*. Figure 3.31 shows a 3D model of the endcap coldbox and a cross section of a chuck. The temperature is maintained using a chiller and Peltier elements. The Julabo DYNEO DD-1000F [73] chiller is used mainly to cool the Peltier elements and prevent overheating of the system. Figure 3.32 shows the three main parts of the setup: the coldbox itself, the chiller, and the cabinet that holds the electronics, including the PLC. The PC for operating the setup is located on the same support frame as the other components, behind the electronics cabinet. Close to the PC, a Diligent Nexys Video board [74] is placed with the firmware for reading out the module data. The interface with the modules is done using a custom FMC-DP (*FPGA Mezzanine Card-Display Port* [75]) board, to which the mini-Display-Port cables, going to the modules, are connected.



Figure 3.32: The main components of the thermal cycling setup.

The setup also includes data readout cables and power supply cables for four modules, as well as a dry air supply in order to maintain a low humidity level during testing. There are lines to supply dry air to the chiller in order to reduce the water content in the coolant, to the coldbox chamber, and to each module enclosure separately. Figure 3.33 shows the dry air supply to the chamber and to the modules. Modules are placed on test frames and secured by ESD-safe foam and Plexiglas covers, which can hold in- and outgoing pipes with dry air supply. Temperature and humidity monitoring sensors are installed at the points where the output dry air flows for pairs of chucks are united. Peltier elements are placed under each chuck, and a thermally conductive and electrically insulating mat is placed on top, which prevents the formation of charges on the test frame or on the module itself, while facilitating an even heat transfer. To prevent overheating, current is supplied to the Peltier elements through thermal fuses that are placed close to the coolant pipes that enter each chuck. At temperatures higher than $+66^{\circ}\text{C}$, the fuses melt and the Peltier elements can no longer produce heat. During testing, each module is attached to the chuck using plastic screws and one metal screw for grounding. Figure 3.33 also shows the placement of the modules in the box. Additional thermally insulating foam is placed around the modules to improve the thermal performance of the setup.

Figure 3.34 shows the interior of the electronics cabinet with the PLC, high voltage (HV) and low voltage (LV) supplies for the modules, a power supply for the Peltier elements, relays that change the polarity of the voltage of the Peltier elements (and therefore the heat transfer direction) and the ones that switch them on and off, and an interlock control module.

Two different chiller coolants were tested: silicone oil [76] and a mixture of 40% water and 60% ethylene glycol. While silicone oil provides better thermal performance, potential leaks can heavily contaminate the clean room environment. Ethylene glycol leaks are less harmful, and the thermal performance that it provides is sufficient for thermal cycling of two modules at once; however, it still needs to be clearly assessed for use with four modules as this is the design capacity of the coldbox. In this chapter, the parameters tuned for use with water-glycol coolant are described. An important difference in operation of the setup with these different coolants arises from the fact that silicone oil, unlike the water and ethylene glycol mixture, is hygroscopic. When in contact with humid environment it can absorb water, which then leads to

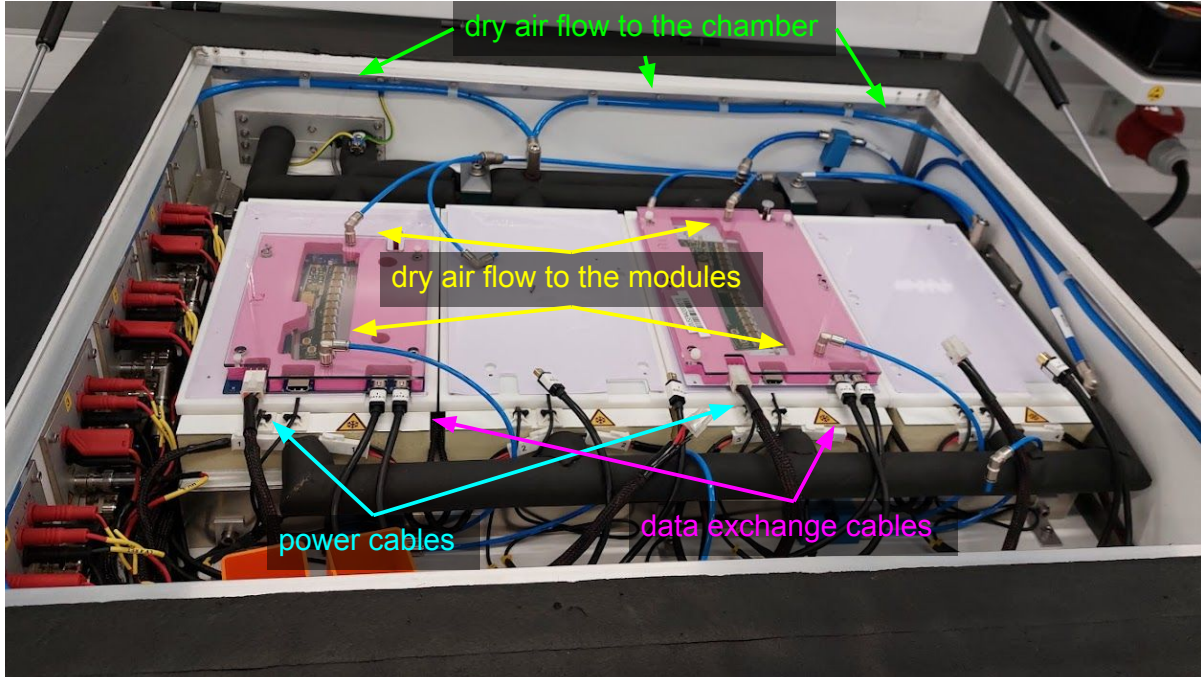


Figure 3.33: Module placement inside of the coldbox and the flow of dry air.

formation of ice when the chiller is cooled down below 0°C and to clogging of the pipes and their damage. To mitigate this, dry air is supplied to the chiller when silicone oil is used to reduce the water content in the coolant. With a water-glycol mixture coolant, no dry air flow needs to be supplied.

In order to speed up the thermal cycling process, the chiller is cooled down only once during the initial cooldown and then kept cold. The inside of the box can be disconnected from the cooling loop during warmups. This is achieved by using a bypass that, when switched on, cuts off the flow of the coolant to the coldbox and sends the liquid back to the chiller instead, so it circulates in a smaller loop. The bypass is shown on the right in Figure 3.35. The interlock is depicted on the left. When the lid is open, the high voltage is turned off for operator's safety. The interlock is described in more detail in Section 3.5.3 in the paragraph about safety features.

3.5.2 The thermal cycling procedure

Figure 3.36 shows the schematic timeline of the thermal cycling and the tests performed at each step.

All steps can be divided into *temperature change* and *module testing* steps. While the module testing steps are the same for all types of setups, the temperature change steps are specific to each type. Below, the procedure for the PLC-controlled setup with the water-glycol coolant is discussed.

For setting the chuck temperature to the target value, the currents in the Peltier elements are determined using PID (Proportional-Integral-Derivative) controllers, a control loop mechanism employing feedback. It uses the following formula to calculate its output:

$$u(t) = K_P e(t) + K_I \int_0^t e(\tau) d\tau + K_D \frac{de(t)}{dt}, \quad (3.10)$$

where K_P , K_I and K_D are the coefficients for the proportional, integral and derivative terms, $e(t)$ is the error value, equal to the difference between the measured and the target value, and t

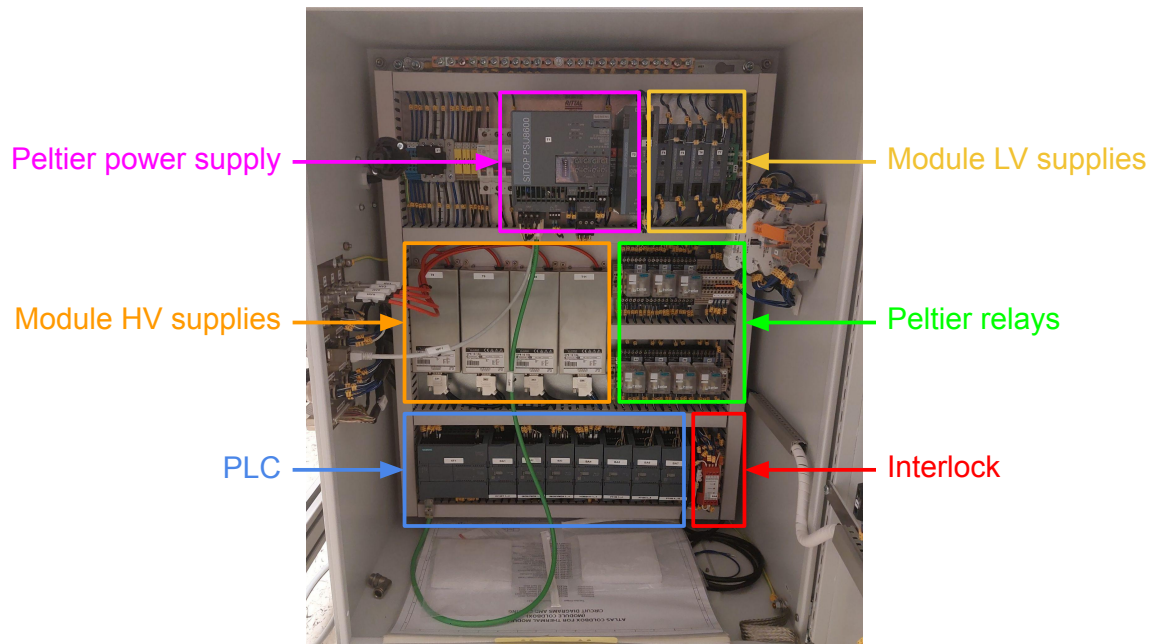


Figure 3.34: The electronics of the thermal cycling setup, including the PLC, the power supplies for the modules and the Peltier elements, the interlock control module and the relays for switching the state of the Peltier elements and the polarity of their voltage.



Figure 3.35: Left: coldbox safety interlock. Right: chiller flow bypass.

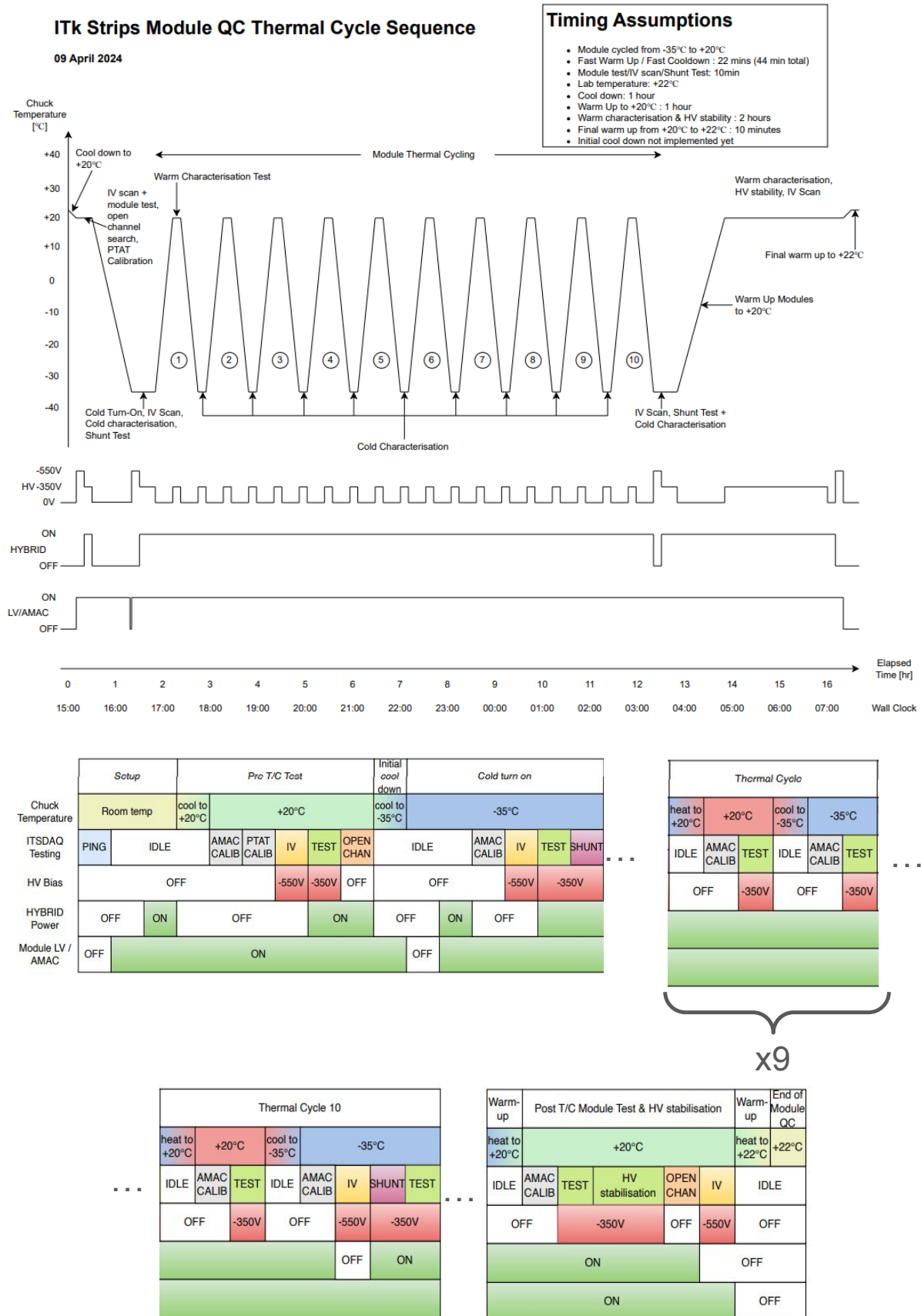


Figure 3.36: Top: schematic timeline of the thermal cycling procedure. Bottom: overview of the performed tests and the states of the module's components [77].

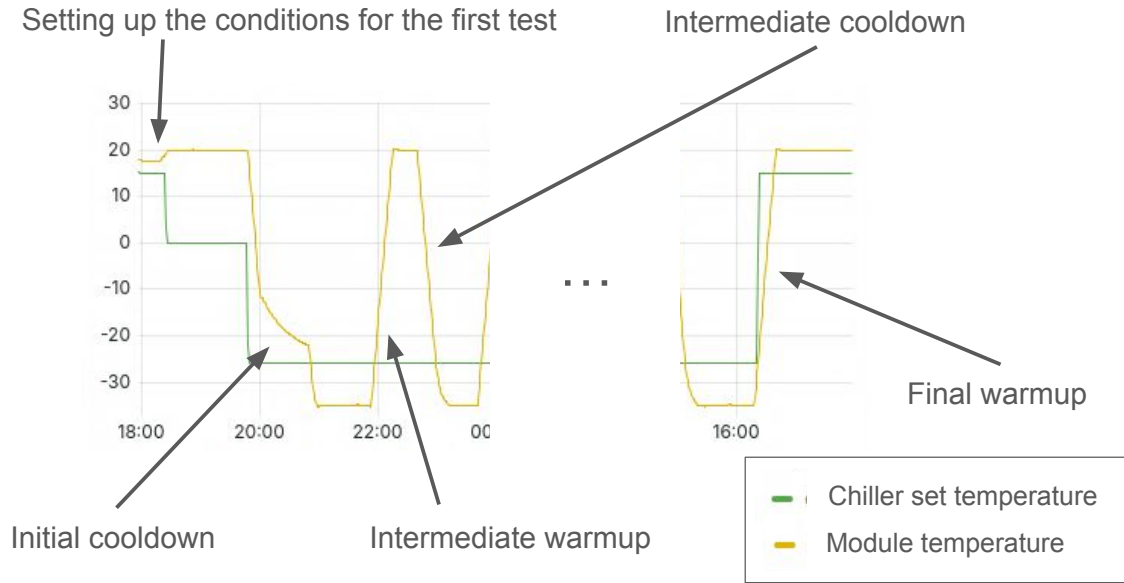


Figure 3.37: Temperature change steps. Only the beginning and the end of the thermal cycling procedure is shown. The yellow line shows the temperature of the module and the green line shows the temperature that the chiller is set to.

is the time [78]. Therefore, the output value of a PID controller takes into account the difference between the measured and the target value using the proportional term, the information about the effect of the previous output on the behavior of the controlled value using the integral term, and an estimate of the future changes using the derivative term. In the case of setting currents of the Peltier elements, K_D is set to 0, so the controller effectively becomes a PI controller. The values of the other coefficients are $K_P = 1.0$, $K_I = 20.0$. The PID controller takes the measured and the target chuck temperatures as input and uses them to calculate the value of $e(t)$. The output $u(t)$ ranges between 0 and 100% and is multiplied by the limit on the Peltier element current set to 6 A to obtain the value that should be set.

In order to prevent damage to modules due to rapid temperature changes, the temperature change rate is limited to a maximum of $2.5^\circ\text{C}/\text{min}$. This is controlled by the PLC by ramping the target temperature provided to the PID controllers at that rate, so the temperature change is gradual and slow.

The change between warming up and cooling down the chucks is achieved by changing the polarity of the voltage supplied to the Peltier elements. Thus, there are two modes of their operation – *cooldown mode* and *warmup mode*. To ensure that the temperature changes gradually, change between these two modes is only performed when the current in the Peltier elements is at 0.

Figure 3.37 shows the temperature change steps, which are performed as follows:

- **Setting up the conditions for the first test.** During this step, the modules are brought to $+20^\circ\text{C}$ for the initial test. The chiller temperature is set to 0°C in order for it to start cooling, so less time is spent on that during the initial cooldown. The temperature of the chucks is controlled with the Peltier elements for the duration of the test.

- **Initial cooldown** is performed once the initial testing is finished. During this step, the modules are cooled down to -35°C . The Peltier elements are on during the entire step. The chiller temperature is set to -26°C , and until it cools to -19°C , the current of the Peltier elements is limited, so that the temperature of the chucks is not more than 2°C below the chiller temperature. This is done in order to limit the waste heat produced by the Peltier elements and let the chiller cool down, while also bringing modules to lower temperatures than that of the chiller. When the chiller reaches -19°C , the restriction is lifted, and the Peltier elements are used to linearly bring the temperature down to -35° at the allowed rate.
- **Intermediate warmup** is done at the beginning of each of the 10 cycles. The bypass is turned on, so that the chiller is not thermally connected to the inside of the box, and the Peltier elements are used to bring the module to $+20^{\circ}\text{C}$.
- **Intermediate cooldown** is done after the test at $+20^{\circ}\text{C}$ in each of the 10 cycles. The Peltier elements start decreasing the module temperature by decreasing their current. When the current reaches 0, the mode of the Peltier elements changes from warmup to cooldown, and the bypass is switched off. At this moment, the chiller slightly warms up as it suddenly is connected to a warmer system. Then, the temperature of the chucks is brought to -35°C .
- **Final warmup** is performed once the last test at -35°C is finished. The bypass stays off, and the chiller target temperature is set to 15°C . The Peltier elements are used to gradually bring the temperature of the modules to $+20^{\circ}\text{C}$.

There are several test steps that can be performed. Some test types were introduced in Sections 3.4 and 3.3, and two additional tests are defined for the thermal cycling procedure: an HV stability test, aimed at checking the stability of leakage current of a biased module over several hours, and a Shunted Full Test, a modification of the Full Test, mentioned in Section 3.4. During a shunted test, the power consumption of the module is artificially increased to stress test the module and model the worst case scenario within the operational range of the module.

During thermal cycling, the tests are performed in different combinations, as shown in Figure 3.36:

- **IV curve measurement + Full Test** are performed at $+20^{\circ}\text{C}$ before the thermal cycling.
- **IV curve measurement + Full Test + Shunted Full Test** are performed the first and the last time that the module is at -35°C .
- **Full Test** is performed twice every cycle, at $+20^{\circ}\text{C}$ and at -35°C .
- **IV curve measurement + Full Test + HV stabilization** is performed at $+20^{\circ}\text{C}$ after the final warmup.

3.5.3 PLC software

The logic of the thermal cycling and the interaction between the hardware components is governed by the PLC. During the thermal cycling, the only ongoing communication with the PLC is about the start and end of the module testing, as the testing itself is done externally. As a target temperature is reached, the PLC confirms that the test can be started, and as soon as it receives the signal that the test is finished, the cycling is continued. The PLC program is written using a combination of a graphical Function Block Diagram (FBD) and a text-based Structured Control Language (SCL) programming languages in Siemens TIA Portal software [79]. In this section, the features and purposes of the main parts of the program are explained.

Chiller control

The chiller is not directly connected to the PLC, so an additional software driver, based on the `serial` library for Python [80], is used. This driver is integrated into the `ColdJigLib2` software [81], introduced later in Section 3.5.5. The PLC program outputs the target chiller temperature and the target flow of the coolant, and receives the information about the measured temperatures of the cooling liquid inside the chiller and inside of the box, and its flow from the external driver.

Peltier elements control

Each set of Peltier elements, corresponding to one chuck, is controlled separately with PID controllers, introduced above. Each of the two operating modes, cooldown and warmup, are operated with its own PID controller. As the change between the modes is achieved with switching polarity of applied voltage, increase in current leads to decrease in chuck temperature for the cooldown mode and to increase in chuck temperature for the warmup mode. This can only be taken into account with the introduction of two controllers, each expecting the corresponding behavior.

At any point during the thermal cycling, the Peltier elements for separate chucks can be enabled or disabled. This way, thermal cycling of fewer than four modules is possible without putting unnecessary stress on the system.

Power supply control

The low voltage power supplies for powering the modules constantly provide 11 V. There is a switch controlled by the PLC that turns all four of the power supplies on or off.

The high voltage power supplies require an additional software wrapper to better fit the requirements for module testing. Firstly, the voltage ramping speed needs to be an adjustable parameter to ensure that voltage change is not too fast and does not endanger the module. Every PLC program cycle, the function adjusts the voltage by $v_{\text{ramp}} \times (t_{\text{now}} - t_{\text{previous}})$ if necessary, where v_{ramp} is the voltage ramp rate, and t_{now} and t_{previous} are the timestamps of this and the previous program cycle. Secondly, the compliance limit for the current cannot be set by hardware below 1 mA, but for the module testing purposes it needs to be set to lower values. This functionality is implemented in the PLC program as well. When compliance limit set by the user is reached, the power supply outputs a corresponding signal, and the voltage is not ramped up further, however it can be ramped down as it can only decrease the current.

Environment sensors

The data from all environment sensors is read out by the PLC. There are four humidity sensors in total: one at the input of dry air into the chamber, one on the wall of the chamber to monitor the ambient humidity and two sensors for monitoring the humidity of the air exiting the modules – one for chucks 1 and 2 and another one for chucks 3 and 4. The two latter humidity sensors are also accompanied by temperature sensors. A combination of temperature and humidity of the air close to the modules allows to derive the dew point. Dew point is the temperature, at which, given the current level of humidity, condensation will appear. Monitoring the dew point is crucial for ensuring the safety of the modules as condensation can damage them. Additionally, each chuck is equipped with two temperature sensors: one at the top side of the Peltier elements to measure the temperature of the module, and one at the bottom side to better control the functioning of the Peltier elements.

Thermal cycling steps

The steps of the thermal cycling, as they are described in Section 3.5.2, are executed in a separate program block, where the requirements are checked to proceed to the next step. The elapsed number of cycles is also controlled in this block, so that when all testing is finished, the procedure is terminated and the setup is switched off.

Safety features

In order to prevent damage to modules and to the coldbox, and to ensure operator safety, safety features are included in the program in addition to the thermal fuses described above:

- Neither high voltage for biasing the modules, nor the Peltier elements, are allowed to turn on unless the humidity values are below 20% and the values of the dew points are at least 5°C below the current temperatures of the chucks. This is aimed at preventing water condensation on the surface of the module, which can lead to its damage.
- To prevent system overheating, the power for the Peltier elements is turned off if any of the temperatures measured by temperature sensors is higher than 25°C or if the temperature difference between the sides of the Peltier elements is above 50°C. This is the first measure that takes effect in case of overheating danger, and if it fails, the thermal fuse mentioned in Section 3.5.1 ensures that the setup stays safe. This feature is in place in order to prevent damage to the setup caused by overheating due to malfunction of some of the system's components.
- An interlock is placed onto the box, so that when the lid is (or can be) opened, the high voltage is switched off for the safety of the operator. When the high voltage is on, the lid is locked, and if it is manually unlocked, the high voltage is immediately switched off. The interlock is shown on the left in Figure 3.35 and the control module for it is located in the electronics cabinet, shown in Figure 3.34.

3.5.4 Software. InfluxDB and Grafana

Influx database [82] is used for several purposes in the workflow, as shown in Figure 3.38:

- Passing signals about start and end of tests between the thermal cycling software `ColdJigLib2` and the module testing software ITSDAQ [83]. This communication is shown by green arrows in the figure.
- (only in the PLC-controlled setups) Establishing communication between ITSDAQ and the power supplies for powering and biasing the modules. This communication is shown by red arrows in the figure.
- Storing data about the system for logging and monitoring purposes.

The information from the Influx database is displayed using a Grafana dashboard [84], which provides an easy and convenient way to monitor the status during thermal cycling, as well as for accessing the data about the previous tests.

3.5.5 Software. ColdJigLib2

A software library called `ColdJigLib2` has been created for thermal cycling [81]. It is modular and flexible, and can work with a variety of setups. Moreover, a web GUI is provided for ease and convenience of thermal cycling [85]. The parts, specific to each setup, are integrated in separate classes, while the general structure and logic is universal. The interaction between

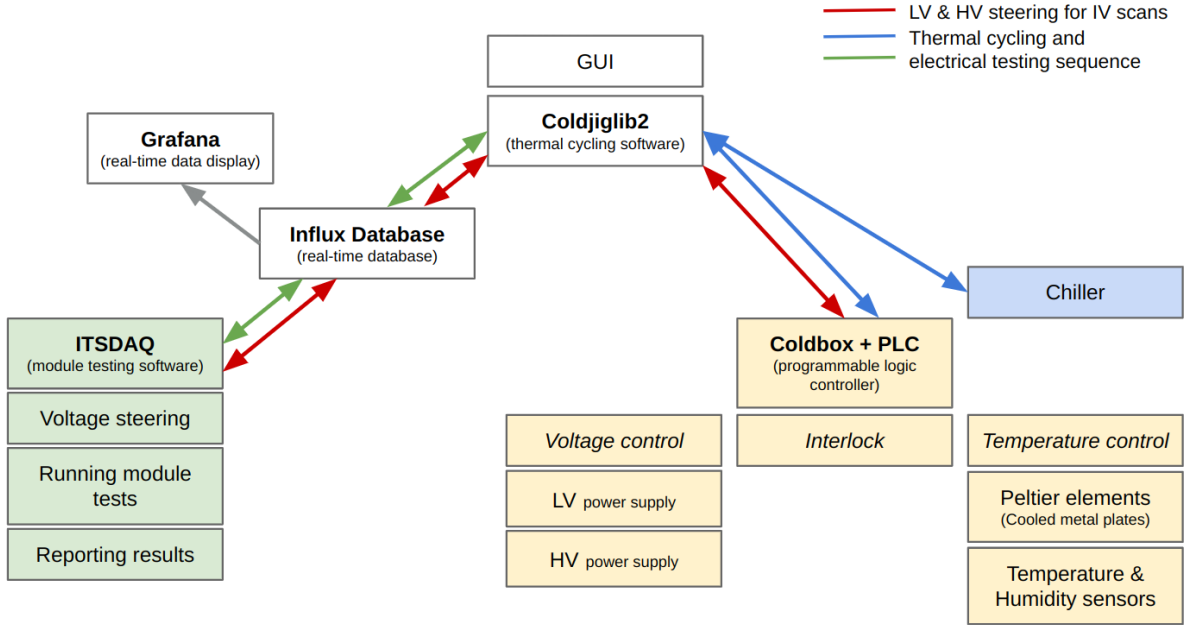


Figure 3.38: Components required for the thermal cycling, including software and hardware parts (image made by Lukas Bayer).

different parts of the framework is achieved through passing the parameters in a global dictionary called `data_dict`. The values from that dictionary are written into an Influx database. After the program is started, all the defined hardware components are initialized, and then a so-called *core loop* is launched, which monitors the state of all the components, triggers software interlocks if the system state requires it, sets the parameters of the hardware components based on the values in the `data_dict`, and uploads the contents of the `data_dict` to the database. Once the user starts the thermal cycling, another thread is created in addition to the core loop thread, where the steps of the thermal cycling are performed.

For the setups, where the logic is controlled by a PLC, the classes in `ColdJigLib2` serve more as interfaces with the PLC and not as logic blocks. The MODBUS protocol [86] is used for communication with the PLC, and the exchanged data is divided into two categories: input variables, which are changed from the outside and which the PLC can only monitor, and output variables, which are set by the PLC and monitored from the outside. The variables are listed in Appendix A.

The classes that need to be implemented separately for each setup type can be split into two categories: the ones that implement the necessary control elements for the thermal cycling itself and the actions that need to be taken in case of emergencies, and the ones that implement interaction with the hardware components. Both categories are described in detail below. Since there are other setups that use the same chiller, the chiller communication part is shared between multiple sites and is not limited to the sites with the PLC setups.

Hardware implementation

The structure of the framework implies that handles for all hardware components (Peltier elements, power supplies, environment sensors, etc.) are implemented as individual classes, and the interaction between them is controlled by higher-level program parts. However, since for the PLC setups the interaction is already implemented in the PLC software, only two hardware

components are defined: the `HHChiller` and the `HHColdbox`. The `PLCConnector` class takes care of communication with the PLC, while the `HHColdbox` class has a more high-level implementation, it interprets the PLC variables and interacts with the `data_dict`. Similarly, the `HHChiller` class serves as a high-level interface enabling the communication with a lower-level driver for the chiller used in multiple setup types. There is one additional class called `ITSDAQConnector`, which serves as an interface for interaction of module testing software ITSDAQ and the power supplies accessible only through the PLC.

Thermal cycling control

The class `endCapHH_TC` implements the thermal cycling steps, which include setting up the parameters before the start of thermal cycling, finishing the procedure either after successful cycles, aborting the thermal cycling when necessary, as well sending signals for cooling the coldbox down or warming it up. As the logic is implemented in the PLC, all these steps have a rather simple structure, usually involving setting one or several PLC variables. In addition, the `endCapHH_TC` class sends commands to the module testing software ITSDAQ through the Influx database. Most of such functions are universal, and no special implementation for the PLC-controlled setups is required. After the modules reach -35°C for the first time, a *cold turn-on* is performed, which involves switching the low voltage powering the modules off and then back on to check that the modules can still be initialized at cold temperatures. When the power supplies are separate units, they are connected to ITSDAQ individually and can therefore be controlled independently. In this case a signal to turn the voltage off is sent from `ColdJigLib2` to ITSDAQ for each power supply. However, in the PLC-controlled setups, these power supplies share one power switch that is controlled by the PLC, and it is more convenient to exclude ITSDAQ from this process and just switch the low voltage off and on directly from `ColdJigLib2`. This is the only module testing step that is done differently in the PLC-controlled setups compared to the other setups.

3.5.6 Software. ITSDAQ

ITSDAQ is the software, which is used for all electrical tests of individual sensors and electronic components, as well as for testing of complete modules, staves and petals [83]. It can be launched with a GUI for manually running individual tests, and it can also be run in a terminal, where it operates in an infinite loop and waits for signals from other software components through an Influx database. The latter is used for thermal cycling, and two instances of ITSDAQ are running at the same time, one for reading out data from the AMACStar and the other one for running the tests. For interaction with the PLC-controlled setups, dedicated implementation of the power supplies is done in ITSDAQ. To control the power supplies, ITSDAQ sends commands through an Influx database, and the exchange of data requested in these commands between the PLC and the database is performed by the `ITSDAQConnector` class of `ColdJigLib2`.

3.5.7 Thermal cycling results

Automatic thermal cycling has been performed at DESY multiple times, Figures 3.39, 3.40, and 3.41 show the monitoring plots for cycling two modules at once. The temperature change is well controlled and is constant at the allowed rate of $2.5^{\circ}\text{C}/\text{min} = 0.042^{\circ}\text{C}/\text{s}$. The whole process for ten cycles takes slightly more than 24 hours. This is longer than the time estimate in Figure 3.36 for two main reasons. Firstly, the cooling power of the chiller is too low, and at the end of each cooldown the temperature change is no longer linear, as seen at the top panel in Figure 3.39. For this reason, the initial cooldown takes longer as well. Secondly, all communication with the individual components going through the PLC is a bottleneck for

module testing, and the testing takes a longer time than when ITSDAQ communicates directly and separately to each power supply. The second reason contributes to difficulties during cooldowns as well – the longer the module is tested at $+20^{\circ}\text{C}$, the warmer the lower sides of the Peltier elements become and therefore the harder it is for the chiller to cool it down.

Several ways of estimating the dew point from relative humidity and temperature exist, and the PLC software calculation is slightly different from the one adopted in `ColdJigLib2`. The lower panel in Figure 3.41 shows the dew points calculated using both approaches. While the results are close, for consistency, the numbers calculated by the PLC are only used in the PLC-internal safety features, while the numbers calculated by `ColdJigLib2` are used within `ColdJigLib2`.

With this setup, DESY has successfully qualified for module production, meaning that all requirements for this QC procedure were satisfied, and it was shown that it works reliably. Automation of the thermal cycling is an important step towards entering module production and a crucial milestone for the DESY ATLAS group.

Multiple modules have been successfully tested in the setup. As an example, Figure 3.42 shows the values of noise in all channels of one hybrid of a preproduction R4 module obtained using a response curve test performed multiple times during the thermal cycling. The noise level is within the allowed range for all channels, and it is clearly visible that at colder temperatures the noise value is reduced, as expected due to reduction of thermal movement of the charge carriers. The module shows good reliability, as the noise level stays the same throughout the thermal cycling procedure.

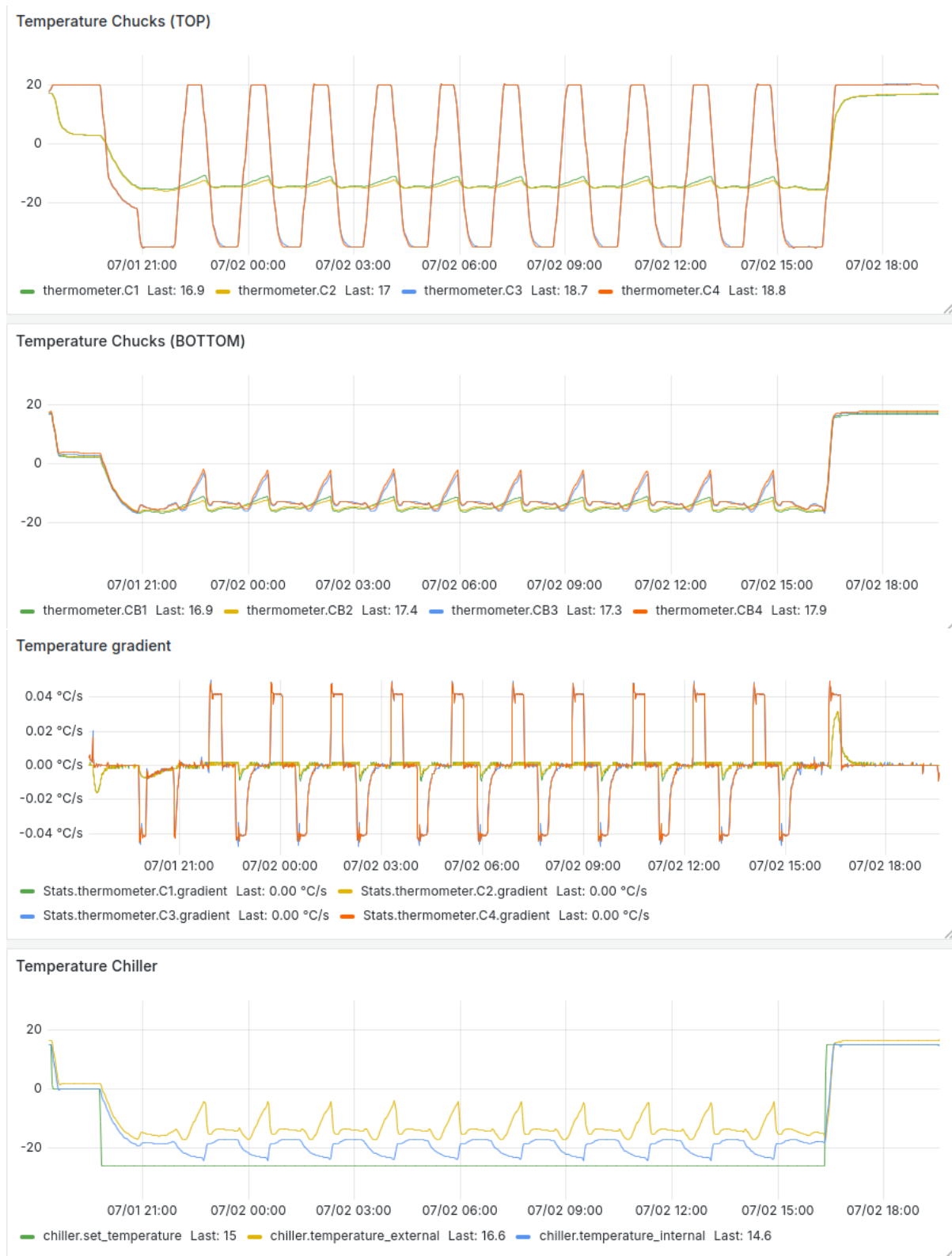


Figure 3.39: Grafana display with plots from successful thermal cycling of two modules on chucks 3 and 4. The plots of the temperature of the Peltier elements, of the gradient of the modules' temperature, and of the temperature of the coolant are shown. The temperature gradient of $2.5^{\circ}\text{C}/\text{min}$ corresponds to $0.042^{\circ}\text{C}/\text{s}$.



Figure 3.40: Grafana display with plots from successful thermal cycling of two modules on chucks 3 and 4. The plots of the temperature of dry air at the output from the modules, the flow of dry air, relative humidity, and the dew point are shown.



Figure 3.41: Grafana display with plots from successful thermal cycling of two modules on chucks 3 and 4. The plots of the module bias voltage, the current powering the modules, and the current in the Peltier elements are shown.

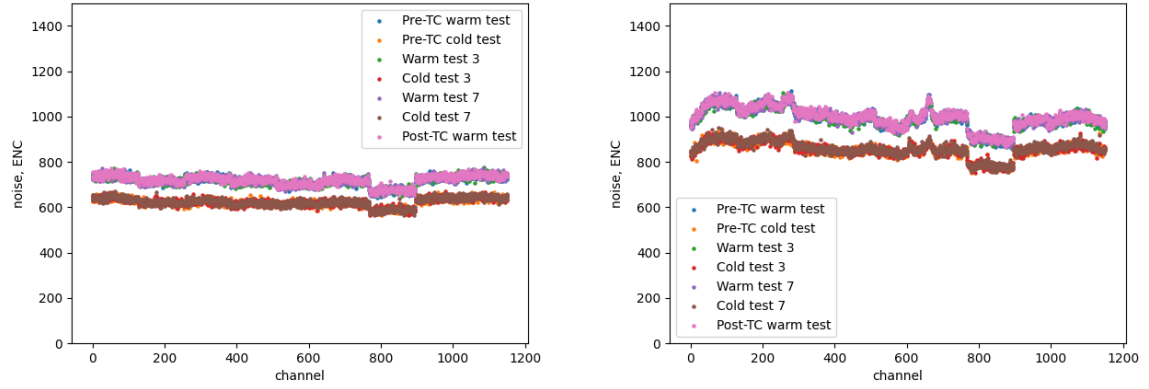


Figure 3.42: Noise measurements for one of the hybrids of a preproduction R4 module. Each point corresponds to one channel. The left plot shows the channels corresponding to strips not covered by the hybrid, and the right plot shows the channels corresponding to the strips that the hybrid is glued on top of. The noise is given in units of equivalent noise charge (ENC).

4. Object reconstruction in the ATLAS experiment

After the particles born in the proton-proton collision pass through the detector, leaving traces, all the measured data is processed and the basic physics objects are reconstructed, which are used in physics analyses. This chapter describes the reconstruction of physics objects in the ATLAS detector.

4.1 Common procedures

Basic objects, such as tracks, vertices and energy clusters, are used in reconstruction of different more complex physics objects.

4.1.1 Tracking

Tracks are reconstructed using the data gathered by the Inner Detector. At first, tracking is performed *inside-out*, with reconstruction starting from hits in the silicon part of the Inner Detector, and then being extended to the TRT. Clusters of hits are assembled in the SCT and pixel detectors. Three-dimensional measurements called *space-points* are created using these clusters. Whereas in the pixel detector each cluster can be turned into a space-point, in the strip system, clusters from both stereo views are required to form one space-point. Track seeds are formed from sets of three space-points, defined by hits in the pixel and SCT detectors. A Kalman filter [87] is used to build track candidates from the seeds by incorporating additional hits in pixel and SCT systems. The track candidates are assigned a score reflecting the track quality, and ambiguities in reconstruction are solved based on these scores. Afterwards, the tracks are extended to the TRT region [88].

Outside-in tracking starting from hits in the TRT is performed in order to reconstruct the tracks that were missed by the inside-out tracking, for example those that are shadowed by other tracks in the silicon detectors or those coming from secondary decay vertices or photon conversion. Therefore, a pattern recognition algorithm starting with hits in the TRT detector and then following the hits back into the silicon detector is used to perform this outside-in track reconstruction [89].

Before LHC Run 3, the tracking software was optimized to work with data collected under high pileup conditions [90].

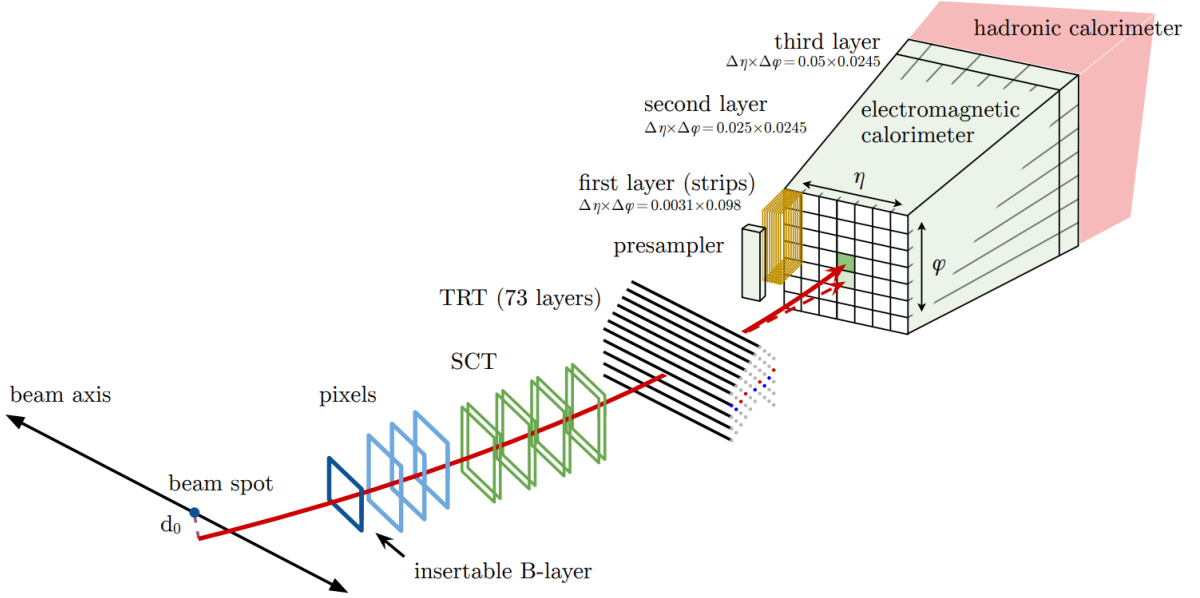


Figure 4.1: Schematic passage of an electron through the ATLAS detector. The solid red line shows the trajectory of the electron, and the dashed line shows the trajectory of a photon produced by the interaction of the electron with detector material [92].

4.1.2 Vertexing

A vertex is a point where particles interact or decay. The proton-proton interaction vertices, also called the primary vertices, are reconstructed using tracks via an iterative vertex finding algorithm [91]. The z coordinates of the reconstructed tracks at the beamline are used to create vertex seeds, and afterwards an iterative χ^2 fit is performed to reconstruct the vertices and associate tracks with them. Each vertex is required to contain at least two tracks, and tracks displaced by more than 7σ from the vertex are used to create a new vertex seed. This process is repeated until no new vertices can be identified.

4.1.3 Topo-cluster reconstruction

The topo-clusters are reconstructed using the energy deposits left by the particles in the calorimeters. This process begins by identifying the *proto-clusters* using a set of thresholds. Cells that are identified as proto-clusters are required to have significance above a certain threshold, so that the signal in this cell is most likely to be caused by a real particle and not by a noise spike. After the identification of proto-clusters, neighboring cells that pass a lowered threshold are added to the corresponding proto-clusters. If a cell is shared by several proto-clusters, the clusters are merged. Next, a crown of nearest-neighbor cells is added to each cluster independent of their energy. If a proto-cluster has several local maxima, it is split into several parts, each corresponding to a separate maximum.

4.2 Electrons

Electrons are reconstructed using the topo-clusters constructed from the energy deposits in the electromagnetic calorimeter and tracks left in the tracking part of the detector [92, 93]. Figure 4.1 shows an illustration of passage of an electron through the detector.

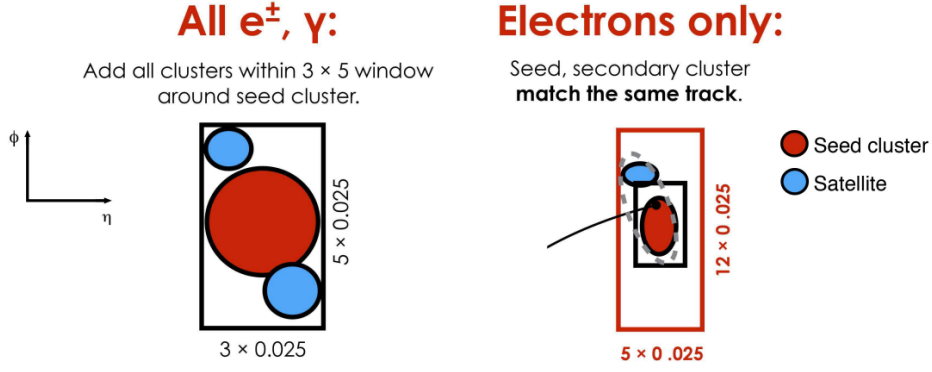


Figure 4.2: Schematic diagram of the supercluster reconstruction procedure. The seed clusters are shown in red, and the satellite clusters in blue [93].

4.2.1 Track reconstruction

Track seeds are reconstructed as described in Section 4.1.1. They are extended to contain at least seven hits in silicon layers, taking into account possible energy loss due to bremsstrahlung, and loosely matched to EM energy clusters.

After this, a procedure based on a Gaussian-sum filter [94], a generalization of the Kalman filter, is applied in order to better account for energy loss of charged particles in the detector material. This procedure also takes into account detector noise.

4.2.2 Track-cluster matching

During track reconstruction, tracks are loosely matched to a topo-cluster, however at this step the criteria are tightened. In the case where several tracks are matched to one cluster, the tracks are ranked and the highest-ranking track is chosen as an electron-candidate. In this process, tracks with hits in the pixel detector are preferred over tracks with hits only in the strip detector, and tracks with smaller ΔR with respect to the energy cluster in the second layer of the calorimeter are favored.

The object is considered to be an electron-candidate if there are at least four hits in the silicon layers and it is not associated with a photon conversion vertex.

4.2.3 Supercluster reconstruction

Several topo-clusters can originate from one electron either because the electron radiated a particle or because of cluster splitting. For this reason, in such cases the topo-clusters are merged into superclusters. The procedure is shown schematically in Figure 4.2.

Around each topo-cluster (which would be referred to as a supercluster seed) other satellite clusters are located and added to the supercluster if they satisfy the requirements. Electron supercluster seeds need to have minimal transverse energy of 1 GeV and have to be matched to tracks with at least four hits in the silicon detectors. The satellite clusters that are in the $\Delta\eta \times \Delta\phi = 0.075 \times 0.125$ window around the supercluster seed are usually formed by secondary EM showers and originate from the same electron. The clusters that are in the $\Delta\eta \times \Delta\phi = 0.125 \times 0.300$ window around the supercluster seed and that are matched to the same track as the supercluster seed are likely left by a bremsstrahlung photon radiated by the

electron. Both types of satellite clusters along with the supercluster seed are united into one supercluster.

The calorimeter cells contributing their energy to one supercluster are taken only from the presampler layer and the first three EM calorimeter layers, in the transition region $1.4 < |\eta| < 1.6$ the energy from the scintillators between the calorimeter cryostats is also added. In order to limit the effects of pileup noise, the clusters are limited in width in the η direction. Since the magnetic field configuration causes the showers to spread mostly in the ϕ direction, this restriction does not prevent superclusters from capturing all the electron energy.

4.2.4 Energy calibration

Electron energy calibration consists of several steps. First, a multivariate regression algorithm trained on simulated samples of shower development in the calorimeter is applied to data in order for it to better match the simulation. Additionally, all physical irregularities of the calorimeter itself, as well as differences of energy deposition in different layers are taken into account. After this a general scale factor for energy is obtained by analyzing the well-known $Z \rightarrow e^+e^-$ decays and adjusting the measured data so that it matches with that energy distribution. As a final check, another well-known decay is used, $J/\Psi \rightarrow e^+e^-$. At this step, the energy distribution in the experimental data is compared to the reference distribution.

4.2.5 Electron identification

In order to improve the quality of the reconstructed electrons, a likelihood discriminant constructed from quantities measured in the Inner Detector is applied. An electron track needs to satisfy requirements on the number of hits in the two innermost layers of the tracker as well as on the number of hits in the SCT. The parameters used in the likelihood discriminant include information about the so-called hadronic leakage (the fraction of the energy left in the hadronic calorimeter compared to the EM calorimeter cluster), the energy deposits in different layers of the EM calorimeter, shower width, numbers of hits in various parts of the silicon tracker, the impact parameter of the track with respect to the beam line, relative momentum loss, particle identification information from the TRT, geometric parameters of the track-cluster matching, and the ratio of the cluster energy to the track momentum. The discriminant is trained using the well-known $Z \rightarrow e^+e^-$ and $J/\Psi \rightarrow e^+e^-$ decays [92].

Loose, Medium and Tight working points of electron identification are defined depending on the pre-defined efficiency of the discriminant, determined using simulated events. The efficiency for the Tight working point is 80%, for the Medium working point it is 88% and for the Loose working point the efficiency is 93%. While the tighter working points identify electrons less efficiently, they also provide a lower rate of misidentification.

4.2.6 Electron isolation

In order to balance the high efficiency electron identification working points, a set of electron isolation criteria is applied. This helps reject fake or non-prompt electrons and select only those that have low amount of nearby activity. Two types of isolation are defined: calorimeter isolation and track isolation. For each isolation type an isolation variable is defined. In the calorimeter isolation a cone of a certain radius is constructed with the energy cluster in its center. The amount of “extra” energy inside of this cone, consisting of the total energy deposit within the cone, from which the energy deposit of the electron and the pileup are subtracted, is the calorimeter isolation variable. For the track isolation a cone is constructed around the track, and the isolation variable is formed from the sum of the transverse momenta of all tracks

in this cone, excluding the original track. Whereas the granularity of the calorimeter does not allow constructing cones of small radius, the cones for the track isolation can be narrow, and moreover, their width can be dependent on the transverse momentum of the track.

Depending on the isolation variables, several isolation working points are defined. They allow to select the levels of isolation efficiency suitable for different analysis purposes.

4.2.7 Electron charge identification and misidentification

The particle charge is measured using the track curvature in the detector's magnetic field. Charge misidentification can occur in cases where the wrong track was matched to the calorimeter energy cluster, as well as in cases with wrong measurement of the track curvature. The most significant process for the charge misidentification is the emission of a bremsstrahlung photon with the subsequent electron-positron pair production. Since the probability of such process increases with the amount of material that the particle traverses, charge misidentification occurs more frequently in the parts of the detector with higher amount of inactive material, in the pseudorapidity range $1.5 < |\eta| < 2.2$. In such cases, three tracks in close proximity can be observed in the detector, which makes it likely that the wrong one will be matched to the energy cluster. Moreover, hits from several tracks can be used for track reconstruction, and thus the curvature measurement could be wrong. Additionally, reconstruction errors can occur in the cases where the track shape is distorted because of a big energy loss and in the cases, where the tracks have low curvature which is hard to measure. A BDT algorithm, constructed from variables characterizing the track quality, the lateral EM shower development, and other tracking and calorimeter quantities, is used to identify the electrons with misidentified charge.

4.3 Muons

The muons are reconstructed using primarily the information gathered by the ID and the MS [95]. Energy deposits in the calorimeter are also used, especially in cases with significant energy losses.

4.3.1 Tracking

The tracking in the Inner Detector is the same as described in the previous section for electrons.

Stand-alone track reconstruction in the Muon System is also possible. First, the straight line track segments are reconstructed using hits in the individual MS stations using a Hough transform [96]. Then, the segments are roughly united into tracks under the assumption that the track has a parabolic shape. Next, the information from the trigger detectors is added in order to increase the precision of the track. After this, a global χ^2 fit is performed in order to refine the track shape.

In the next step, the hits that do not fit well with the track are discarded. Additionally, the hits that were not considered previously and fit the track are then added to it. Ambiguities in cases when two tracks share many hits are resolved by discarding the track with lower quality, except for cases when both tracks share hits in the first two layers and do not share hits in the third layer to ensure high tracking efficiency for detecting boosted low mass dimuon systems. Finally, the tracks are fitted again taking into account the energy loss in the calorimeter and extrapolated to the beam line, where the transverse momentum is calculated at the point of origin.

4.3.2 Reconstruction

There are several strategies of muon reconstruction using the full detector information:

- **Combined (CB).** The track reconstructed in the MS is matched to an ID track, and a global fit using all the hits is performed to obtain a combined track. A subset of these muons is called silicon-associated forward (SiF) muons. These are the muons in the range $|\eta| > 2.5$, for which the MS track is matched to short track segments, reconstructed in the silicon part of the Inner Detector.
- **Inside-out combined (IO).** This is a complementary strategy to the previous one. Unlike the CB muons, the IO muons start with a track, reconstructed in the Inner Detector. After this, a search for at least three loosely-aligned hits in the MS followed by a global fit of all hits is performed.
- **Muon spectrometer extrapolated (ME)** approach starts with a reconstructed MS track that cannot be matched to an ID track. In this case the MS track is simply extrapolated to the beamline.
- **Segment-tagged (ST)** muons are formed when an ID track could be reconstructed, however no full MS track can be matched to it. At least one track segment in the muon system is required to match to the ID track.
- **Calorimeter-tagged (CT)** muons are formed when an ID track could be matched to an energy deposit in the calorimeter that is compatible with a minimally-ionizing particle. No participation of the muon system is required in this case.

4.3.3 Identification

As with electrons, several working points are defined for muon identification. In addition to the Loose, Medium and Tight, similar to the ones mentioned before, so-called *High- p_T* and *Low- p_T* working points are defined in order to suit a wide variety of physical analyses.

For all working points, a muon is required to have at least one hit in the pixel detector, at least 5 hits in the SCT detector, and no more than two hits are allowed to be missing in the silicon tracker.

The Medium working point, which is the default working point in ATLAS, includes only CB and IO muons. It is suitable for a wide range of physics analyses, and it is designed to have the efficiency and purity suitable for the majority of the analyses, while keeping the systematic uncertainties in the prompt-muon efficiency and background rejection small.

For the Loose working point all muon types are used. It is optimized for the reconstruction of Higgs boson decays in the four-muon final state. This working point has a high efficiency, but lower purity of muon identification.

The Tight working point accepts only CB and IO muons. It has the lowest efficiency of the three working points and the highest purity, which benefits analyses limited by background coming from non-prompt muons.

The High- p_T working point ensures an optimal momentum measurement for muons with transverse momenta over 100 GeV. It is optimized for searches for new W' and Z' bosons. Only CB and IO muons that pass the Medium working point selection are chosen for this working point.

The Low- p_T working point is optimized for muons with low transverse momentum, which are less likely to be reconstructed as full tracks in the MS. Only CB and IO muons are used for this working point.

The efficiency of these working points depends on the transverse momentum of the muon, and in non-extreme p_T ranges the Loose working point has 97-99% efficiency, the Medium working point has 97% efficiency, and the Tight working point has 90-93% efficiency. The High- p_T working point has around 80% efficiency for muons with transverse momenta of 100 GeV. The Low- p_T working point accepts additional 16-18% of prompt muons with low transverse momenta compared to the Medium working point.

4.3.4 Vertex association

In order to reject muons not originating from the initial proton-proton collision, requirements are imposed on the impact parameter of the muon track. The distance between the muon track and the beam line is called the transverse impact parameter d_0 . This parameter does not depend on the primary vertex, and the so-called d_0 significance, defined as $d_0/\sigma(d_0)$ is required to be less than 3. The longitudinal impact parameter z_0 is defined as the longitudinal coordinate of the point of closest approach of the muon track to the reconstructed primary vertex. Tracks that are compatible with the primary interaction vertex are defined as the tracks with $|z_0|\sin\theta < 0.5$, where θ is the angle between the muon track and the beam axis.

4.3.5 Muon isolation

The isolation requirements for muons can be split into three groups: track-based which use only ID tracks, calorimeter-based which use only energy deposits in the calorimeter, and particle-flow-based which combine both sources of data. For the track-based isolation, an $\eta - \phi$ cone of a given size is defined around the muon track. The isolation variable in this case is defined as the sum of transverse momenta of all tracks in this cone, excluding the muon track itself. For the calorimeter-based isolation, a cone is defined around the position of the muon, extrapolated to the calorimeter. The isolation variables are the sum of all transverse energy deposits in this cone, excluding the energy deposit of the muon itself and corrected for pileup. Combining both isolation methods provides better result than using just one of them as both methods provide complementary information. When both track-based and calorimeter-based criteria are included, an independent set of requirements can be imposed, but in order to mitigate the overlapping information provided by the isolation requirements, an additional particle-flow isolation method is introduced. It combines track- and calorimeter-based isolation, while decreasing the correlation between them. Depending on the parameters of the isolation methods, several working points are defined, each of which includes track-based isolation requirements: Loose and Tight particle-flow working points; Loose and Tight working points which independently combine track- and calorimeter-based isolation; as well as Loose and Tight working points which include only track-based requirements. In addition, two working points are defined using a BDT classifier trained to reject non-prompt tracks with high efficiency.

4.4 Jets

Quarks and gluons cannot exist solitarily due to color confinement, leading to the phenomenon of hadronization and the production of particle showers. In the detector, the signals from this shower are collected, and then assumptions about the properties of the initiating quark or gluon can be made.

Jet reconstruction is performed in several steps. First, the *particle-flow* objects are reconstructed [97], then they are clustered using the anti- k_t algorithm [98] and their energy is calibrated [99].

4.4.1 Particle-flow algorithm

The reconstruction starts with a track selection requirement to minimize the number of badly measured tracks. They are required to have at least 9 hits in the silicon detector and no missing pixel hits. Moreover, they are required to have $p_T < 40$ GeV as the majority of tracks in a jet satisfy that requirement, and for tracks with higher p_T it is hard to separate the particle from the surrounding activity. If a track is matched to an electron or a muon, it is discarded.

Next, the selected tracks are matched to topo-clusters, reconstructed in the hadronic calorimeter in the same way as described in Section 4.1.3. First, the algorithm attempts to match each track to just one topo-cluster. For each track, the distance metric is used to select the best-matching topo-cluster:

$$\Delta R' = \sqrt{\left(\frac{\Delta\phi}{\sigma_\phi}\right)^2 + \left(\frac{\Delta\eta}{\sigma_\eta}\right)^2}, \quad (4.1)$$

where $\Delta\eta$ and $\Delta\phi$ are the distances between the track and the cluster's barycenter, and σ_η and σ_ϕ represent the angular topo-cluster widths.

The *layer of highest energy density (LHED)* is defined as the calorimeter layer that has the largest increase rate of energy density as a function of the number of radiation lengths from the front of the calorimeter.

In some cases the particle does not deposit all its energy in only one topo-cluster, and assignment of more than one cluster to a track is required. In order to determine the number of required topo-clusters, the significance of the difference between the expected energy and that of the matched topo-cluster is used:

$$S(E^{\text{clus}}) = \frac{E^{\text{clus}} - \langle E_{\text{dep}} \rangle}{\sigma(E_{\text{dep}})}, \quad (4.2)$$

where $\langle E_{\text{dep}} \rangle$ is the average energy deposit in the calorimeter that is calculated for each track momentum using single-particle data samples without pileup.

If $S(E^{\text{clus}})$ is smaller than -1 , all topo-clusters in the cone of radius $\Delta R = 0.2$ of the track position extrapolated to the calorimeter are matched to the track.

After each track is matched to one or more topo-clusters, the energy subtraction takes place in order to avoid double-counting of energy deposits. Rings of increasing diameter are constructed around the LHED, and if the sum of the energy deposits in the cells within the ring is smaller than the remaining energy required to reach the $\langle E_{\text{dep}} \rangle$, the cells are removed. Otherwise, the energy deposits in the cells are scaled down in order to subtract the necessary amount of energy left to reach $\langle E_{\text{dep}} \rangle$. The rings are constructed in all calorimeter layers and are ranked in descending order of energy density within them. The subtraction starts with the highest-ranking ring.

After the energy subtraction, if the total energy in the clusters that are left is consistent with the hypothesis that it was left by a shower energy fluctuation, the cells are removed. If not, it is likely that more than one particle deposited its energy in one topo-cluster, and the cells are retained.

Finally, the set of the selected tracks and the topo-clusters that were retained should accurately represent the reconstructed event without double-counting of the energy deposits.

4.4.2 Jet reconstruction

Jets are reconstructed from particle-flow objects using the anti- k_t algorithm [98]. It is designed in a way that the shape of the jet is affected mostly by hard particles and has a circular cross section in most cases. The distance between two objects is defined as

$$d_{ij} = \min(p_{Ti}^{2p}, p_{Tj}^{2p}) \frac{\Delta_{ij}^2}{R^2} = \min(p_{Ti}^{2p}, p_{Tj}^{2p}) \frac{(y_i - y_j)^2 + (\phi_i - \phi_j)^2}{R^2}, \quad (4.3)$$

and the distance between an object and the beam line as

$$d_{iB} = p_{Ti}^{2p} \quad (4.4)$$

where p_T , y and ϕ denote transverse momentum, rapidity and azimuthal angle respectively. R and p are parameters of the algorithm, affecting the jet radius and the sensitivity of the jet border to soft radiation. Anti- k_t algorithm uses $p = -1$.

For each event, the distances defined above are calculated. At each step of the algorithm, the smallest distance is selected. If this distance is between an object and the beam line, the object is considered a finished jet and removed from consideration. Otherwise, the two objects are merged, and the distances are calculated again. The process is repeated until there are no more objects left.

The negative parameter p ensures that the soft particles are much more likely to be merged with hard particles before they start merging with each other. This ensures that the hard particles gather all soft radiation around themselves in a cone of radius R . In the cases when two hard particles are close to each other, the jets are no longer conical. If the distance between the hard particles is smaller than $2R$, but bigger than R , two jets are formed, and the border between them reflects the difference in p_T between the hard particles. If the hard particles are closer to each other than R , the resulting single jet is formed by the union of the cones around both particles.

The most common radius for jet reconstruction in ATLAS is 0.4. The tracks that are matched to the primary interaction vertex and the remaining after energy subtraction clusters serve as input to the algorithm. Such tracks are required to satisfy the condition $|z_0 \sin \theta| < 2$ mm, where z_0 is the longitudinal coordinate of the point of closest approach of the track to the primary interaction vertex. Before the jet reconstruction process begins, the η and ϕ parameters of the topo-clusters are recalculated with respect to the position of the primary vertex instead of the detector origin.

4.4.3 Jet energy calibration

After the jets are reconstructed, their energy needs to be corrected to take into account the pileup and the energy that was not captured by the detector [99]. Figure 4.3 schematically shows the steps of the jet energy calibration process.

Pileup correction occurs in two steps, for which simulated data is used: p_T -density-based pileup correction and a residual pileup correction. During the first step, the pileup contribution is estimated using the median p_T density, ρ , of jets in the $\eta - \phi$ plane, and the jet area A . The correction factor ρA is then subtracted from the jet transverse momentum. For the calculation of ρ , the jets reconstructed using the k_T algorithm are used [100]. Since the first correction step is based on the central calorimeter region, there are still large discrepancies in the higher-occupancy forward region of the calorimeter, and therefore a residual correction is required. For the simulated Monte Carlo (MC) events, the difference between the transverse momenta of the

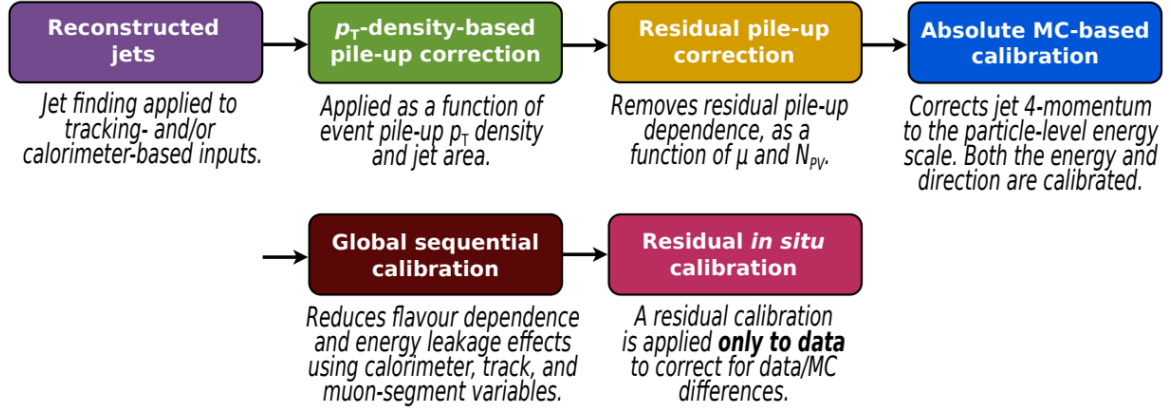


Figure 4.3: Jet energy calibration steps [99].

reconstructed jet and of the truth jet is derived, and that dependence is used to provide the residual correction. The jet transverse momentum corrected for pileup is therefore

$$p_T^{\text{corr}} = p_T^{\text{reco}} - \rho A - \alpha(N_{PV} - 1) - \beta\mu, \quad (4.5)$$

where p_T^{corr} is the transverse momentum after the corrections, p_T^{reco} is the initially reconstructed transverse momentum, N_{PV} is the number of reconstructed primary vertices, μ is the mean number of interactions per bunch crossing, and α and β are the separately derived coefficients for the residual correction.

The next step accounts for possible irregularities in the calorimeter response, energy loss in passive materials, contributions from outside of the jet cone and biases in η reconstruction. As previously, this correction is done using simulated samples. The average jet energy response \mathcal{R} is defined as the mean of the Gaussian fit to the core of the $E^{\text{reco}}/E^{\text{true}}$. This parameter is then used to calibrate the jet energy. The bias in η reconstruction is most pronounced when a jet encompasses two calorimeter regions of different geometry or technology: EM and hadronic, barrel and endcap, endcap and forward calorimeter. A second correction depending on the value of η is derived and used to diminish the bias.

The last simulation-based correction aims to account for the differences between the jets themselves. The jet parameters depend on the flavor and energy distribution of the constituent particles, as well as on the initiating particle. The global sequential calibration accounts for these differences with several multiplicative corrections. For this calibration, six observables are defined, and for each of them a correction factor is calculated.

Finally, a residual in situ calibration is performed in order to account for differences between experimental and simulated data. Jet response is compared between data and simulation, where the jet p_T is balanced against the p_T of a well-calibrated object. The ratio between jet responses in data and simulation is used as a scale factor for this final correction. There are three steps in this process, each using a different reference object for this calibration. First, the p_T balance in dijet systems is used to calibrate the forward jets to match the central ones. Then the jets are balanced against the calibrated Z bosons or photons in $Z + \text{jet}$ and $\gamma + \text{jet}$ systems. Next, several low- p_T jets are used to calibrate one high- p_T jet.

4.4.4 Flavor tagging

Identification of jets originating from b - and c -quarks and their separation from the other, *light*, jets is called flavor tagging and it is crucial to many analysis areas. Since the searches presented

in this thesis do not use c -tagged jets, this section will focus on the procedure of identification of b -jets. b -hadrons born in the primary interaction will decay shortly after, however due to a relatively long lifetime their decay point will be displaced from the primary vertex. Different flavor tagging algorithms have been created for LHC Runs 2 [101] and 3 [102, 103], with the Run 3 ones utilizing more advanced machine learning algorithms and thus being able to reach higher precision levels. The updated algorithms can be also applied to data collected during LHC Run 2 in order to obtain results using combined datasets from these two runs.

Flavor tagging in Run 2

Flavor-tagging algorithms use tracks, which are matched to jets and are well measured. There are two levels of flavor tagging. On the low level, the characteristic features of the jet are reconstructed, and on the high level multivariate classifiers are utilized to assign the jet flavor.

Several different algorithms belong to the low-level category:

- **Impact-parameter-based algorithms – IP2D and IP3D.** IP2D uses the signed transverse impact parameter of the tracks, and IP3D additionally uses the longitudinal impact parameter of the tracks. The jet's flavor tag is determined by the sum of logarithms of per-track probability ratios of each flavor hypothesis.
- **Track-based recurrent neural net tagger – RNNIP.** Whereas the two previous algorithms considered the tracks independently, the RNNIP allows to take into account the correlations between the tracks as it utilizes a recurrent neural network. The network provides three scores – one for each possible jet flavor, and the b -tagging discriminant is constructed as

$$D_{\text{RNNIP}} = \ln \left(\frac{p_b}{f_c p_c + (1 - f_c) p_{\text{light}}} \right), \quad (4.6)$$

where p_b , p_c and p_{light} are the three flavor scores, and f_c denotes the fraction of c -jets.

- **Secondary-vertex-tagging algorithm – SV1.** This algorithm attempts to construct a secondary vertex using the tracks that are assigned to the jet. The number of tracks in this secondary vertex, among other variables, is used as input to high-level algorithms.
- **Topological multi-vertex finding algorithm – JetFitter.** A modified Kalman filter [87] is used in order to reconstruct the full decay chain of b - and c -hadrons. Compared to the SV1 algorithm, *JetFitter* [104] can reconstruct a secondary vertex even in cases when only one track can be assigned to it. The multiplicity at the reconstructed displaced vertex is used as input to high-level taggers.

The high-level algorithms are constructed using multi-layer feed-forward neural networks, and the DL1r algorithm exploits the output of all low-level algorithms mentioned before, as well as the jet p_T and $|\eta|$, in order to construct tree flavor scores. Similar to RNNIP algorithm, the final b -tagging score of DL1r is defined as

$$D_{\text{DL1r}} = \ln \left(\frac{p_b}{f_c p_c + (1 - f_c) p_{\text{light}}} \right). \quad (4.7)$$

Four working points are defined based on the average b -tagging efficiency: 70%, 77%, 80%, and 85%.

Flavor tagging in Run 3

Two algorithms have been created for Run 3 – *DL1d* [103] and *GN2* [102].

DL1d follows the approach established for Run 2, replacing the Recurrent Neural Network tagger (RNNIP) with the Deep Sets based tagger (DIPS).

The main ATLAS flavor tagging algorithm for Run 3 is GN2, which establishes a new approach. The major improvement in flavor tagging performance originates from the use of transformer networks operating directly on tracking information instead of the two-tiered approach described above. This algorithm uses the information about the jet and associated tracks to predict the flavor of the jet. In addition to identifying b - and c -jets, GN2 is also capable of identifying jets originating from hadronic τ lepton decays. The working points of the GN2 algorithms are defined with the average b -tagging efficiency of 65%, 70%, 77%, 85% and 90%.

4.5 Tau leptons

τ -leptons have a short lifetime of 290×10^{-15} s [37], and therefore the τ -leptons born in the proton-proton collision decay within the beam pipe before they reach the detector. The decay modes include leptonic, with production of electrons or muons along with the corresponding antineutrino and a τ -neutrino, and hadronic, usually resulting in production of one or three charged hadrons, a τ -neutrino and possibly some neutral hadrons. In the case of leptonic decays, the produced leptons are indistinguishable from the prompt leptons, produced in the initial collision, so the only decay modes, in which taus can be reconstructed, are the hadronic ones.

The signature that defines a tau lepton is a narrow jet in the calorimeter, associated with one or three tracks in the tracking detector [105, 106]. The jet is reconstructed using the anti- k_t algorithm with the radius 0.4, and is required to have $p_T > 5$ GeV and $|\eta| < 2.5$. A dedicated algorithm is used to reconstruct the tau decay vertex. Afterwards, a recurrent-neural-network-based algorithm is used to distinguish the jets that originate from τ -leptons from other jets mimicking the signature.

4.6 Missing Transverse Momentum (MET)

Due to the conservation of the transverse momentum, the sum of all transverse momenta in an event should be zero. However, some particles, such as neutrinos, escape detection and carry a fraction of transverse momentum away. The negative sum of transverse momenta of all detected particles in an event is called missing transverse momentum (MET). Not only the creation of Standard Model neutrinos, but also the presence of new physics and SM particles that were out of detector acceptance result in non-zero MET. Reconstruction of MET is challenging as it involves all detector subsystems.

The contributions to the MET can be divided into hard, coming from fully reconstructed and calibrated particles, and soft, which are associated with reconstructed tracks, but with no hard particles [107].

Since the reconstruction procedures of different objects are independent from each other, it is likely that the same calorimeter signal is used in reconstruction of several objects. Therefore, for reconstructing the MET, measures need to be taken to avoid double-counting of the same energy deposit. The reconstructed objects are ranked in the following order: electrons, photons, hadronically decaying τ -leptons, jets. The lower-ranking objects are fully rejected or corrections are made to the energy deposit if their calorimeter signal overlaps with that of a higher-ranking

object. Muons usually have little or no overlap with the other objects, which is why they are excluded from the list.

The full expression for the missing transverse momentum is given by

$$\mathbf{E}_T^{\text{miss}} = - \underbrace{\sum_{\text{selected electrons}} \mathbf{p}_T^e - \sum_{\text{accepted photons}} \mathbf{p}_T^\gamma - \sum_{\text{accepted } \tau\text{-leptons}} \mathbf{p}_T^\tau - \sum_{\text{selected muons}} \mathbf{p}_T^\mu - \sum_{\text{accepted jets}} \mathbf{p}_T^{\text{jet}}}_{\text{hard term}} - \underbrace{\sum_{\text{unused tracks}} \mathbf{p}_T^{\text{track}}}_{\text{soft term}}, \quad (4.8)$$

where unused tracks refer to the tracks that are associated with a primary vertex, but not with any hard object.

All \mathbf{p}_T and $\mathbf{E}_T^{\text{miss}}$ vectors are two-dimensional and are located in the transverse plane of the coordinate system that is perpendicular to the beam axis. In addition to the $\mathbf{E}_T^{\text{miss}}$ itself, that has two coordinates, $E_{T,x}^{\text{miss}}$ and $E_{T,y}^{\text{miss}}$, the defined set of observables includes its absolute value $E_T^{\text{miss}} = |\mathbf{E}_T^{\text{miss}}| = \sqrt{(E_{T,x}^{\text{miss}})^2 + (E_{T,y}^{\text{miss}})^2}$ and its azimuthal angle $\phi^{\text{miss}} = \tan^{-1}(E_{T,y}^{\text{miss}}/E_{T,x}^{\text{miss}})$.

In order to provide the most fitting missing transverse momentum calculations for various physics analyses, several working points are defined with different jet selections [108]:

- For the **Loose** working point all jets with $p_T > 20$ GeV are selected, and the jets with $|\eta| < 2.4$ and $p_T < 60$ GeV have to pass a set of additional jet requirements.
- The **Tight** working point was developed to reduce the dependence on pileup. Forward jets with $|\eta| < 2.4$ and $20 < p_T < 30$ GeV are not selected. While the pileup dependence is reduced, the resolution of MET also gets worse.
- The **fJVT** working point utilizes the so-called Jet Vertex Tagger (JVT) algorithm, which suppresses forward pileup jet contamination. This working point helps to suppress the tails in the E_T^{miss} distribution. The jets that are selected need to have $p_T > 20$ GeV, and the jets that have $|\eta| > 2.5$, $20 < p_T < 50$ GeV and fail the requirements of the JVT algorithm, are rejected. The same additional requirements as for the Loose working point are applied to jets with $|\eta| < 2.4$ and $p_T < 60$ GeV.

5. Search for heavy vector resonances in the four top quark final state

In this chapter, the search for heavy vector resonances in the four top quark final state is described. This is the first analysis of its kind at LHC, providing model-independent results in a search for BSM physics in multi-top-quark final states.

5.1 Motivation

Recent observation of four top quark production at the LHC by the ATLAS [31] and CMS [32] experiments motivates searches for Beyond the Standard Model (BSM) contributions to this final state, as in both experiments an excess of produced events compared to the prediction of the SM was observed. Many BSM theories predict existence of *top-philic* resonances, which couple more strongly to the top quark than to the other quarks, rendering other couplings negligible. High collision energy, sufficient for simultaneous production of multiple top quarks, opens the possibility to study the four-top-quark final state at the LHC and to search for BSM contributions to its production.

Explicit reconstruction of the BSM resonance provides opportunities for model independent searches in final states with resonant production of two top quarks. This is explored in a search for a color singlet Z' particle with masses between 1 and 3 TeV utilizing the data gathered by the ATLAS experiment during LHC Run 2 [109]. Because of the high mass of the resonant particle, the two top quarks coming from its decay are expected to be boosted, which was utilized in the search by assuming that their decay products can be contained in jets of large radius. Figure 5.1 shows tree-level diagrams for the production of a top-philic resonance Z' . While the main motivation for the search is resonant production, the t-channel contribution, shown in Figure 5.2, cannot be disregarded as its production cross section is comparable to the s-channel one.

5.2 Analysis strategy

Tree-level production of top-philic resonances is only possible alongside one or more top quarks, motivating searches in multi-top final states [33]. The main signal contribution comes from the final states with four top quarks, where the resonance is produced in the s-channel, however

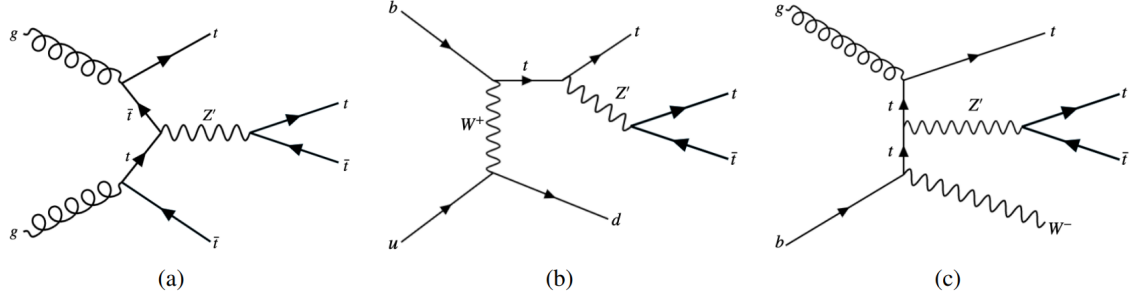


Figure 5.1: Sample Feynman diagrams of the tree-level s-channel production of Z' with association with (a) $t\bar{t}$, (b) tj , where j denotes any light quark, (c) tW . [109]

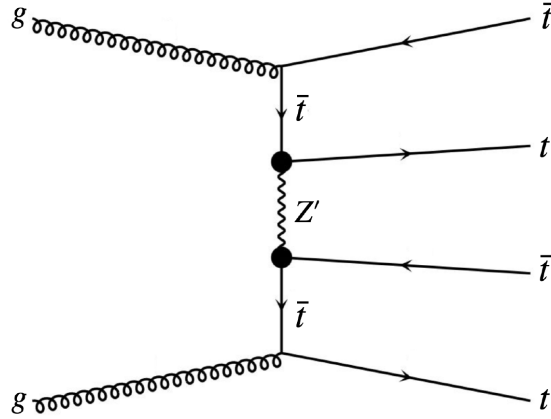


Figure 5.2: Feynman diagram of tree-level t-channel Z' production in association with $t\bar{t}$.

contributions from three-top-quark final states and the t-channel resonance production are also considered. This resonance reconstruction benefits from having no missing transverse momentum in the event, which can be achieved only by considering fully-hadronic final states, where all four top quarks decay hadronically. However, such final states suffer from high background from multi-jet processes and provide no clear signature that can be selected by triggers, so a single-lepton final state is considered instead, which has lower background rates and enables use of single lepton triggers for the event selection.

The assumption that both resonant top quarks (the top quarks originating from the decay of the BSM particle) decay hadronically is made in this analysis, though no dedicated selection can be applied to enforce this. Therefore, final states with leptonically-decaying resonant top quarks receive no special treatment, and their presence reduces the accuracy of the result. Because of the high mass of the resonance, the two resonant top quarks are highly boosted, and therefore their decay products can be contained in Reclustered jets (RC jets), which are described in more detail in Section 5.4. The main observable of the search is the ditop mass, the invariant mass of these two RC jets, which for signal events is also the mass of the resonant particle Z' .

The analysis regions are defined using the number of b -tagged jets (b -jets) and the number of jets that are not part of an RC jet (additional jets). A description of the analysis regions can be found in Section 5.6. Due to sizable background modeling uncertainties and known mismodeling of the most significant background process, $t\bar{t}$ +jets, a data-driven approach to background estimation is taken, described in Section 5.7. The shape of the background distribution is estimated using data in a *source region* and then the background is propagated to the signal regions using scale factors obtained from simulated events. This procedure is validated using dedicated validation regions.

The model-independent result is obtained using the BUMPHUNTER tool [110] by identifying the most significant localized deviation of data from the background in the distribution of the ditop mass. Additionally, a model-dependent result is obtained with a profile likelihood fit using the signal samples modeled with the simplified Z' model, described previously in Chapter 1.

5.3 Data and Monte Carlo samples

Simulated Monte Carlo samples created using known SM parameters and the parameters of the BSM model are used to develop and verify the analysis strategy and to estimate the contribution of background processes. The strategy is then applied to the experimental data. This section describes the samples that were used in the analysis.

5.3.1 Data samples

The data collected by the ATLAS detector between 2015 and 2018 is used. The center of mass energy is 13 TeV, and the full dataset corresponds to an integrated luminosity of $139.0 \pm 2.4 \text{ fb}^{-1}$ [111]. Only events taken when all detector subsystems were fully operational are selected.

5.3.2 Simulated signal samples

The signal samples for the simplified Z' model described in Chapter 1 are generated using MADGRAPH5_AMC@NLO 2.8.1 generator [112] at leading order (LO) in the strong coupling with the NNPDF3.1LO set of parton distribution functions (PDF) [113]. The events are interfaced with PYTHIA 8.244 [114] using the A14 tune [115] and the NNPDF2.3LO PDF set [113].

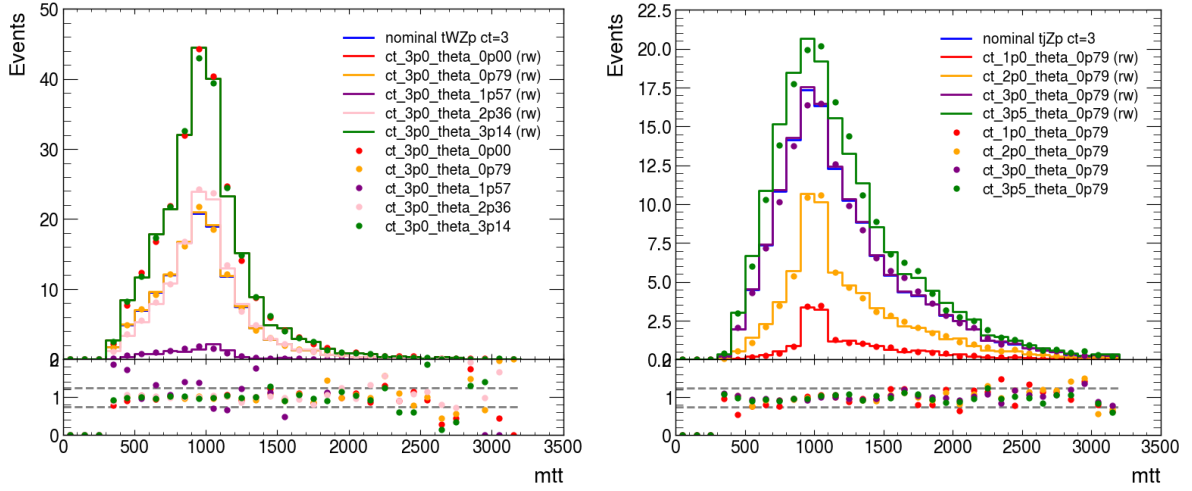


Figure 5.3: Examples of ditop mass distributions made using reweighted samples and the samples generated with the required parameters. The left plot shows reweighting applied for varying the chirality angle for the tWZ' events with the mass of the Z' boson of 1 TeV, and the right plot shows the reweighting applied in order to vary the coupling strength for the tjZ' events with the mass of the Z' boson of 1 TeV. For each plot, the nominal sample (solid blue line) was reweighted to different c_t or θ hypotheses (solid lines of other colors). The distributions for the generated signals are shown as dots.

The samples for resonance masses of 1.0, 1.25, 1.5, 2.0, 2.5, 3.0 GeV are produced. Both s- and t-channel production of the four-top-quark final state is taken into account, as well as the interference between them. Furthermore, tWZ' and tjZ' samples are produced assuming on-shell decay of the Z' boson.

The samples are generated using the chirality angle $\theta = \pi/4$ and the coupling of Z' to top quarks $c_t = 3$. Samples with other values of those parameters, $\theta = 0$ and $\theta = \pi/2$, as well as $c_t = 1$, $c_t = 4$, and $c_t = 4.5$ are obtained using MADGRAPH matrix element reweighting [116]. Figure 5.3 shows several examples of the ditop mass distribution compared between reweighted samples, plotted with solid lines, and the ones generated directly with the required parameters, represented with dots. The left plot shows the reweighting applied to the tWZ' sample to vary the chirality angle, and the right plot shows the reweighting applied to the tjZ' sample to vary the coupling strength.

Although the distributions show overall good agreement, due to a small number of events with exceptionally large weights, the distributions in the signal regions have significant fluctuations, especially for the mass point of 3 TeV. As the samples were generated with the $c_t = 3$, the fluctuations are most pronounced when reweighting to $c_t = 1$ is done and are not relevant for the other values of the coupling strength. In order to address the issue, 0.1% of events with the largest weights were removed. This allows to decrease fluctuations significantly, while keeping the majority of the events.

The removal of some events needs to be accounted for in the normalization of the remaining events, which is implemented by introducing a correction factor, such that the target cross section is not affected by the event removal.

5.3.3 Simulated background samples

The main background process after event preselection, explained in more detail below, is the SM production of $t\bar{t}$ +jets. Other background categories include production of $t\bar{t}$ pair in association with a vector or a Higgs boson, production of single top quarks and of vector bosons in association with jets, diboson production and the SM production of four-top-quark events.

Simulated event samples are processed through the full ATLAS detector simulation [117] using GEANT4 [118], except for the SM four-top-quark samples and the samples for studying systematic variations of the $t\bar{t}$ simulation, which are processed using fast simulation with parametrized calorimeter showers [119].

Additional samples were generated for pileup modeling using PYTHIA 8.186 using the A3 tune [120] and the MSTW2008LO PDF set [121].

All simulated samples undergo the same reconstruction and analysis procedures as the real data. For all samples that were not generated using SHERPA [122], the EVTGEN 1.2.0 [123] program was used to describe the decays of b - and c -hadrons. The specifics of generation of each background process are described below.

The modeling of $t\bar{t}$ events is done using the POWHEGBOX 2 [124–127] generator at next-to-leading order (NLO) with the NNPDF3.0NLO PDF set [113]. The h_{damp} parameter that controls the transverse momentum of the first additional emission is set to $1.5m_t$, where m_t is the mass of the top quark [128]. Alternative $t\bar{t}$ samples were generated with MADGRAPH5__AMC@NLO and interfaced with PYTHIA 8 in order to evaluate the generator-related uncertainties.

Samples of s- and t-channel production of a single top quark in association with another quark, as well as samples of single top quark production in association with a W boson, were generated using the POWHEGBOX 2 generator at NLO in QCD. The five-flavor scheme with the NNPDF3.0LO PDF set was used for the generation of s-channel samples, and the four-flavor scheme with the NNPDF3.0NLONF4 PDF set [113] was used for the generation of the t-channel production. The overlaps with the $t\bar{t}$ samples were removed using the *diagram removal* scheme [129]. To evaluate the uncertainties, related to the showering algorithms, alternative single top and $t\bar{t}$ samples were generated using the POWHEGBOX 2 generator, but HERWIG 7.04 [130, 131] for parton showering and hadronization with the H7UE tune [131] and the MMHT2014LO PDF set [132].

The $t\bar{t}+H$ events are modeled using the POWHEGBOX 2 generator at NLO with the NNPDF3.0NLO PDF set. The $t\bar{t}+V$ samples are produced using the MADGRAPH5__AMC@NLO generator at NLO with the NNPDF3.0NLO PDF. SM four top quark production is modeled using the MADGRAPH5__AMC@NLO generator at NLO with the NNPDF3.1NLO PDF set. The tZ samples are modeled using the MADGRAPH5__AMC@NLO generator at LO using the NNPDF3.0 PDF set.

All events in the background samples mentioned above are interfaced with PYTHIA 8.230 for the parton showering and hadronization using the A14 set of parameters and the NNPDF2.3LO PDF set.

The V +jets samples are produced with the SHERPA 2.2.1 generator with up to two partons at NLO in QCD and up to four partons at LO. The diboson processes are modeled with the SHERPA 2.2.1 generator as well. In both cases, the NNPDF3.0NNLO PDF set is used with a dedicated set of tuned parton shower parameters provided by the SHERPA authors.

Table 5.1 summarizes the generators used for all produced MC samples.

Table 5.1: The generators and the parameters used to model the signal and background processes.

| Sample | Generator and hadronization | PDF set | Order |
|-----------------------|----------------------------------|----------|-------|
| Signal $t\bar{t}Z'$ | MADGRAPH5_AMC@NLO + PYTHIA 8.244 | NNPDF3.1 | LO |
| $t\bar{t}$ | POWHEGBOX 2 + PYTHIA 8.230 | NNPDF3.0 | NLO |
| Single top | POWHEGBOX 2 + PYTHIA 8.230 | NNPDF3.0 | NLO |
| $t\bar{t} + H$ | POWHEGBOX 2 + PYTHIA 8.230 | NNPDF3.0 | NLO |
| $t\bar{t} + V$ | MADGRAPH5_AMC@NLO + PYTHIA 8.230 | NNPDF3.0 | NLO |
| SM $t\bar{t}t\bar{t}$ | MADGRAPH5_AMC@NLO + PYTHIA 8.230 | NNPDF3.1 | NLO |
| tZ | MADGRAPH5_AMC@NLO | NNPDF3.0 | LO |
| V +jets | SHERPA 2.2.1 | NNPDF3.0 | NNLO |
| Diboson | SHERPA 2.2.1 | NNPDF3.0 | NNLO |

5.4 Object selection

Reconstruction of the objects used in this analysis was described in Chapter 4. In this section only the specific requirements to the objects are mentioned.

5.4.1 Charged leptons

Electrons are required to pass the tight identification criteria and have $p_T > 28$ GeV and $|\eta_{\text{cluster}}| < 2.47$, where p_T is the transverse momentum and η_{cluster} is the pseudorapidity of the energy cluster. The electrons within the transition region between the barrel and the endcap regions of the EM calorimeters are excluded ($1.37 < |\eta| < 1.52$). The electrons must pass the Tight isolation requirements.

The muons that pass the medium selection criteria and have $p_T > 28$ GeV and $|\eta| < 2.5$ are selected. They must also pass the *TightTrackOnly* isolation requirements: only muons with transverse momentum larger than 1 GeV are selected and the scalar sum of transverse momenta of all tracks, associated with the primary vertex, in a variable-size cone around the muon track must not exceed 6% of the transverse momentum of the muon itself.

Additional criteria are placed on matching of the leptons to a primary vertex:

$$|z_0 \sin \theta| < 0.5 \text{ mm}, \quad (5.1)$$

$$\left| \frac{d_0}{\sigma(d_0)} \right| < 5(3) \text{ for electrons (muons)}, \quad (5.2)$$

where θ is the polar angle of the lepton track, z_0 is the longitudinal impact parameter and d_0 is the transverse impact parameter.

5.4.2 Jets

The selected jets are required to have $p_T > 25$ GeV and $|\eta| < 2.5$. Additional requirements are placed on the jets with $p_T < 60$ GeV and $|\eta| < 2.4$ to ensure that they originate from the hard-scatter interaction. Radius $R = 0.4$ is used in the anti- k_t algorithm for jet reconstruction.

The 77% working point of the DL1r algorithm for b -jet identification is used.

5.4.3 Overlap removal

An overlap removal procedure needs to be applied to avoid double-counting of detector information. The distance metric used for this procedure is $\Delta R = \sqrt{\Delta\phi^2 + \Delta y^2}$, where ϕ is the azimuthal angle and y is the rapidity. First, lower- p_T electrons that share tracks with higher- p_T electrons are removed. Next, Calorimeter-tagged muons are removed if they share tracks with electrons. After this, electrons that share tracks with muons are removed. Then, the jets with $\Delta R < 0.2$ to electrons are removed, and afterwards the remaining electrons that have $\Delta R < 0.4$ with a jet are removed. Finally, overlapping jets and muons are addressed: jets with fewer than three tracks and $\Delta R < 0.2$ with a muon are rejected, and then muons with $\Delta R < \min(0.4, 0.04 + 10 \text{ GeV}/p_T(\mu))$ to jets are removed. In cases when multiple jets satisfy overlap removal criteria with electrons, only the closest in ΔR is removed.

5.4.4 Missing transverse momentum

Missing transverse momentum is defined as the negative sum of all the selected objects in the event. Its reconstruction is described in detail in Chapter 4, and the Tight working point is used.

5.4.5 Reclustered jets

For reconstruction of the reclustered jets, the remaining after the overlap removal procedure small-radius jets with $p_T > 25 \text{ GeV}$ and $|\eta| < 2.5$ are taken [133]. Anti- k_t algorithm with $R = 1.0$ takes these jets as input and constructs the reclustered jets (RC jets). Constituent jets with p_T below 5% of the p_T of the RC jet are removed to reduce the contribution from pileup [134].

The RC jets with $p_T > 300 \text{ GeV}$, $|\eta| < 2$ and $m > 100 \text{ GeV}$ are selected for reconstructing the top quarks. These requirements aim to select the jets that contain all decay products of hadronic top decays, as they are usually contained within jets of radius $R = 2m_t/p_T$ and have higher mass than the ones containing the products of leptonic top decays. Additionally, the RC jets are required to have at least two constituent jets.

5.5 Event selection

The selected events are required to have at least one reconstructed vertex with at least two associated tracks with $p_T > 0.4 \text{ GeV}$. In the events that have multiple reconstructed primary vertices, the vertex with the highest sum of squared transverse momenta of the assigned tracks is selected. Only the events fulfilling the quality criteria, ensuring that all detector subsystems were operational and that the beam conditions were stable, are selected.

In order to select events with the final state that is in focus of this analysis, trigger selection is applied. The utilized triggers select events with at least one lepton in the final state. Lowest unscaled single electron and muon triggers were used for each data taking period with different lepton transverse momentum thresholds for each such period: p_T threshold for muons was 20 GeV for the 2015 run, and 26 GeV for the 2016-2018 runs [135], for the electrons it was 24 GeV during the 2015 run, and 26 GeV during the 2016-2018 runs [136].

After the trigger selection, kinematic requirements are applied in order to further focus on the target final state and increase the sensitivity to the signal. The selected events are required to have exactly one lepton, at least two RC jets, at least two b -tagged jets, and at least two small-radius jets which are not part of the two leading- p_T RC jets. Figure 5.4 shows the final state with all small-radius jets labeled. Only two leading- p_T RC jets are used for the analysis

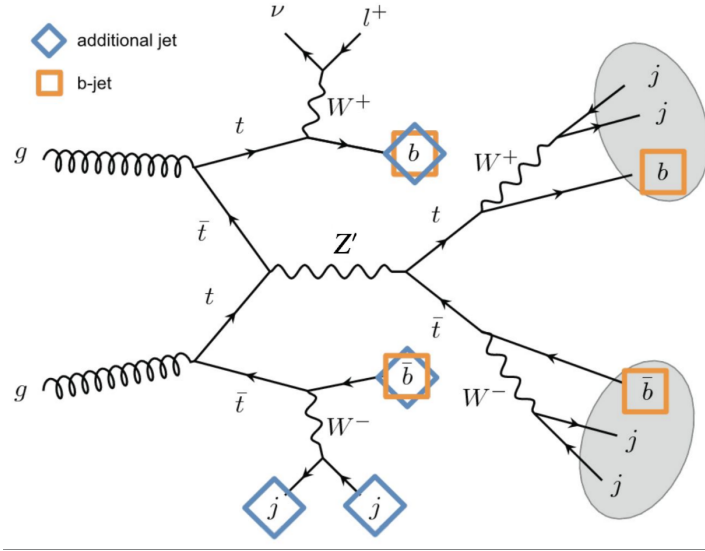


Figure 5.4: The Feynman diagram of the single lepton final state with highlighted b - and additional jets.

even if more were reconstructed. The number of events with more than two reconstructed RC jets is two orders of magnitude smaller than the number of events with exactly two RC jets, so this selection does not have a significant effect. The b -jets are counted regardless of whether they are a part of an RC jet or not.

5.6 Analysis region definition

Further background rejection is achieved after the preselection by classifying the events into several regions: the *source* region, where the shape of the background for the data-driven background estimation will be taken from, the *validation* regions for validating the background estimation strategy, and the *signal* regions, the regions most enriched in signal events used to obtain the result of the search. Figure 5.5 shows distributions of the number of b -jets and the number of additional jets for the signal and background samples. These jet multiplicities clearly have separation power and thus the analysis regions are defined based on them. Three values of each jet multiplicity are considered: 2, 3 and ≥ 4 . The regions are presented in Figure 5.6, where “a” stands for additional jets and “b” – for b -jets. The source region is colored in blue, the validation regions in green, and the signal regions in red. The region with the highest signal to background ratio is the $(\geq 4a, \geq 4b)$, however it has low event count.

Figure 5.7 shows the visualization of one of the data events from the most signal-like $(\geq 4a, \geq 4b)$ region made using the ATLAS VP1 visualization software [137]. The event display shows the track of the reconstructed muon (red track), nine particle jets (the yellow cones), four b -tagged jets (the blue cones) and two large radius jets (green cones). The length of the jet cones depends on the jet’s energy, however the scaling for the large radius jets is 1.4 times smaller than for the regular jets to make them fit into the picture. Some jets have low energy and therefore the cones are too small to be seen in the picture.

5.7 Background estimation

Poor modeling of the top-quark kinematics in $t\bar{t}$ events leads to discrepancies in transverse momenta of leptons and jets between data and simulation, noticed by previous searches [138, 139].

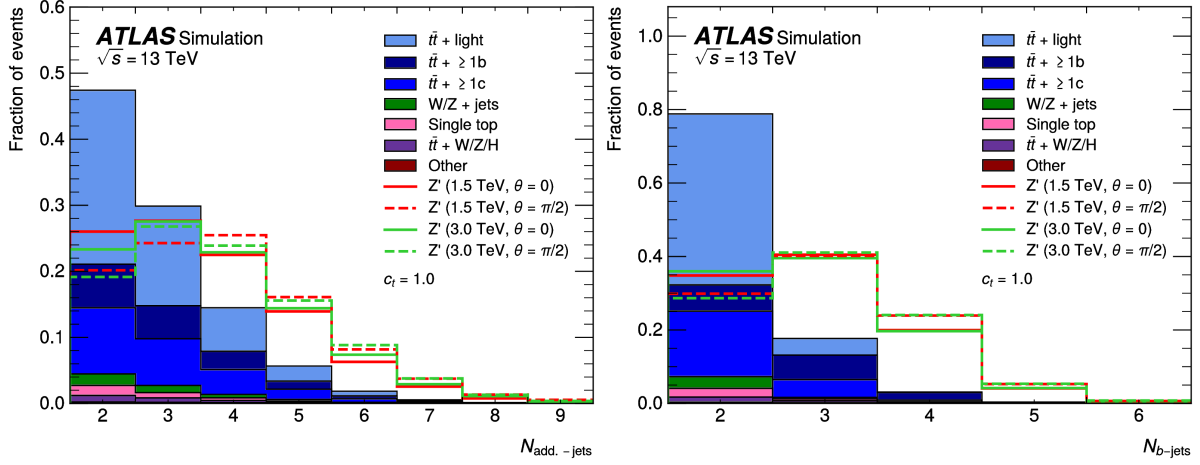


Figure 5.5: Distributions of the number of additional jets on the left and the number of b -jets on the right for signal samples with different masses of the Z' particle and for the most significant background samples [109].

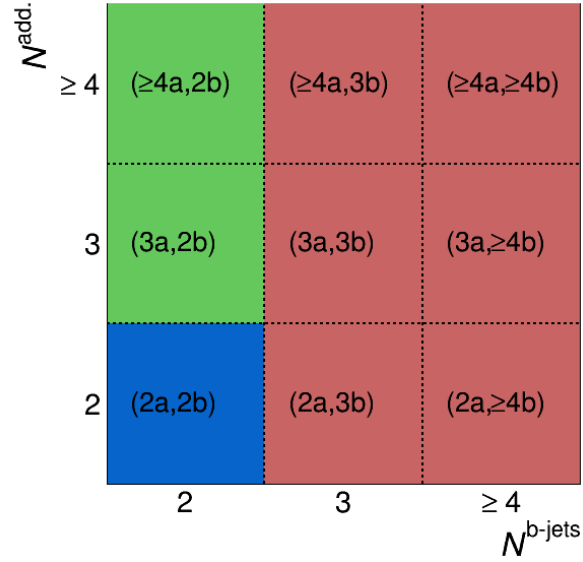


Figure 5.6: Analysis regions defined using the number of additional jets (“a”) and the number of b -jets (“b”) in an event. Blue – source region, green – validation regions, red – signal regions [109].

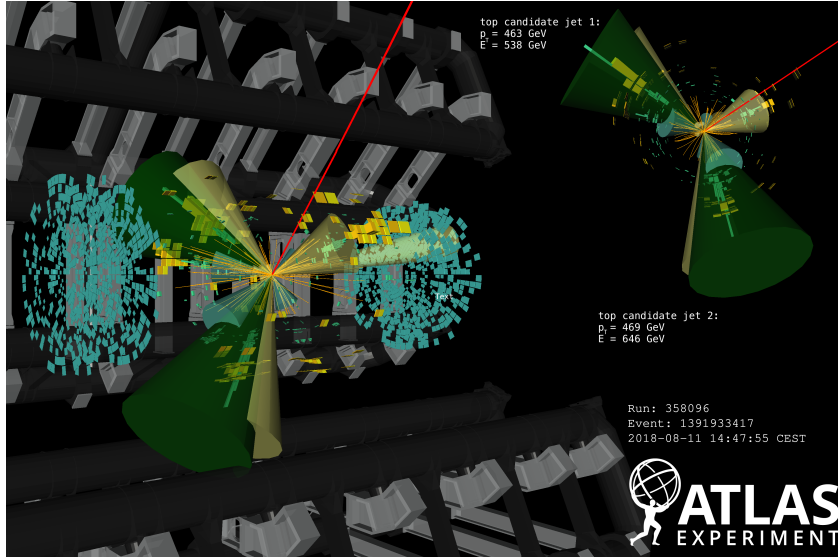


Figure 5.7: Visualization of one of the real data events in the $(\geq 4a, \geq 4b)$ region. Red line is the muon track, b -tagged jets are shown in blue, RC jets in green and small-radius non- b -tagged jets in yellow [109].

Due to mismodeling of heavy flavor radiations produced in association with a $t\bar{t}$ pair, the b -jet multiplicity distribution also shows discrepancies between data and simulation, as noticed previously in [138, 140]. As the $t\bar{t}$ events are the main background for the analysis, these modeling discrepancies are addressed with a data-driven background estimation strategy.

The background estimation process has two key parts. First, the shape of the background in the source region is extracted from data. Then it is extrapolated to the signal regions using scaling functions, obtained using simulated events.

While the background composition in different regions is different, as demonstrated in Figure 5.8, the shape of the ditop mass distribution is very similar. Figure 5.9 shows the background distributions in all analysis regions plotted using simulated data, compared to the scaled distribution from the source region.

The source region has negligible signal contamination, and therefore the ditop mass distribution in that region can serve as an accurate estimate for background distribution. The effect of systematic uncertainties on the shape of the background distribution are taken into account separately for each uncertainty.

5.7.1 Functional fit

A dijet function is used to fit the shape of the background distribution in the source region:

$$f(x) = (1 - x)^{p_1} \times x^{p_2 + p_3 \log(x)}, \quad (5.3)$$

where $x = m_{t\bar{t}}/\sqrt{s}$ is the ditop mass divided by the center-of-mass energy. Such functions are commonly used in high-mass resonance searches [141, 142]. The fit to source region data is shown in Figure 5.10.

5.7.2 Background extrapolation

The extrapolation factors are derived from the ditop mass distribution in all regions obtained from simulated events. To reduce fluctuation effects due to limited statistics, a fit with the

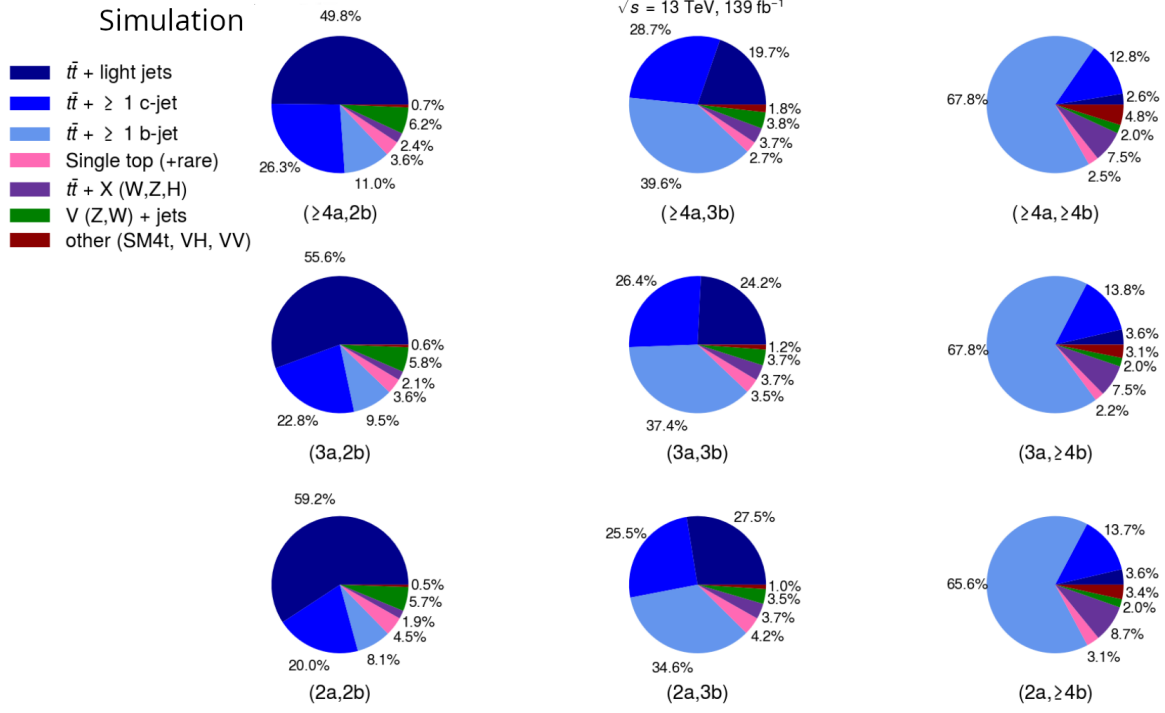


Figure 5.8: Background composition in the analysis regions.

dijet function is performed for all distributions first. The extrapolation factors are the result of division of the dijet fit in the target region by the dijet fit in the source region. For a given region, the background prediction is given by

$$B^{\text{reg}}(m_{t\bar{t},i}) = f(m_{t\bar{t},i}) \times C^{\text{source} \rightarrow \text{reg}}(m_{t\bar{t},i}), \quad (5.4)$$

where “reg” is the target region, $f(m_{t\bar{t},i})$ is the dijet fit function in the source region, obtained from data, and $C^{\text{source} \rightarrow \text{reg}}(m_{t\bar{t},i})$ is the extrapolation function from the source region to the target region obtained from simulated samples by taking the ratio between the dijet functions to the simulated events in the two regions.

5.7.3 Uncertainty propagation

For each systematic uncertainty, the extrapolation function is derived separately, and the background prediction in the target region for this systematic variation is given by

$$B_{\text{syst}}^{\text{reg}}(m_{t\bar{t},i}) = f(m_{t\bar{t},i}) \times C_{\text{syst}}^{\text{source} \rightarrow \text{reg}}(m_{t\bar{t},i}), \quad (5.5)$$

where $C_{\text{syst}}^{\text{source} \rightarrow \text{reg}}(m_{t\bar{t},i})$ is that extrapolation function. Therefore the variation of the background prediction due to this uncertainty variation can be obtained from

$$\frac{\Delta B^{\text{reg}}(m_{t\bar{t},i})}{B^{\text{reg}}(m_{t\bar{t},i})} = 1 - \frac{C_{\text{syst}}^{\text{source} \rightarrow \text{reg}}(m_{t\bar{t},i})}{C^{\text{source} \rightarrow \text{reg}}(m_{t\bar{t},i})}. \quad (5.6)$$

5.8 Systematic uncertainties

The analysis is affected by a number of uncertainties, including the luminosity uncertainty, the uncertainties on object reconstruction, and the theoretical uncertainties. Each uncertainty

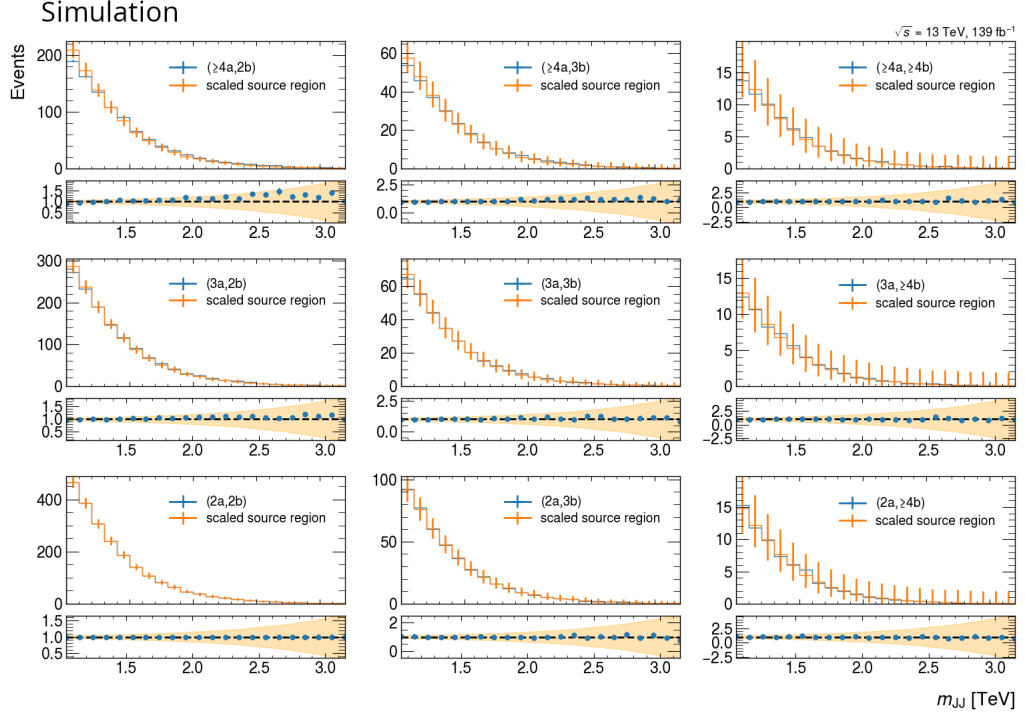


Figure 5.9: Comparison of the shapes of the ditop mass (m_{JJ}) distribution for the simulated background events in the analysis region with the shape of that distribution in the (2a, 2b) source region. For each region, the distribution from the source region is scaled to match the integral of the background distribution in that region. The lower panel shows the ratio with the orange area showing the Poisson uncertainty of the denominator (2a, 2b) scaled.

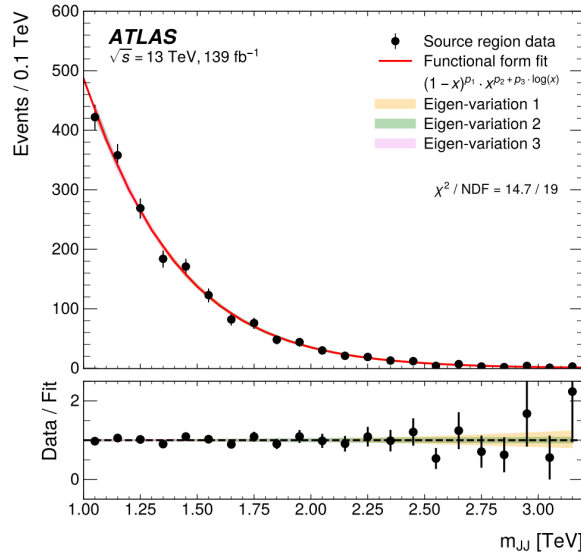


Figure 5.10: The distribution of the ditop mass (m_{JJ}) for the data in the source region and the fitted to it dijet function. The bands show the uncertainties of the fit due to variations of the three parameters of the function. [109]

can affect both the shape and the normalization of the background and signal distributions. As mentioned previously, each uncertainty is propagated individually through the background estimation procedure in order to address the possible variations of the distribution in the source and target regions.

5.8.1 Experimental uncertainties

The experimental uncertainties are related to effects in the detector, as well as to the reconstruction and calibration of physics objects.

- **Luminosity.** Since the background extrapolation is taken from data and scaled by a ratio of MC histograms, the background estimate is not affected by luminosity uncertainties. The signal prediction is taken directly from the simulated data, and therefore is affected by the luminosity uncertainty, which is 1.7% for the Run 2 dataset [111].
- **Jets.** Due to the complex nature of the jet reconstruction procedure, three sources of uncertainty need to be taken into account. These uncertainties are related to the jet vertex tagging (JVT) [143], jet energy scale (JES) [144] and fractional jet energy resolution (JER) [145]. The JVT systematic uncertainty is obtained by varying the JVT cut used during jet reconstruction. It accounts for the remaining pileup contamination after pileup suppression has been applied. The JES uncertainty is implemented as a set of 29 nuisance parameters, including the ones related to η intercalibration, pileup subtraction and punch-through effect treatment. Finally, the JER uncertainties are represented as a set of 9 nuisance parameters and they take into account differences in energy resolution between data and simulation and the uncertainties of the JER measurement.
- **Flavor-tagging.** The systematic uncertainties are represented by a set of eigenvector variations. 19 nuisance parameters in total are used to represent these uncertainties, and they include parameters that account for efficiency of tagging b -jets, as well as for mistagging c - and light-flavor-jets [146–148]. Estimation of these uncertainties involves eigenvector decomposition in order to provide a set of statistically independent parameters.
- **Leptons.** The lepton-related uncertainties arise from differences in reconstruction, identification, isolation and trigger performances between data and simulation [93, 149]. As a result, the electrons are affected by 7 nuisance parameters, related to their energy scale, energy resolution, trigger efficiency, reconstruction, identification, and isolation. The muons have 13 nuisance parameters in total, including the Inner Detector track smearing, muon spectrometer track smearing, charge-dependent and charge-independent scale momentum, trigger efficiency, track-to-vertex association, identification, and isolation.
- **Pileup.** The uncertainty arises from the reweighting of the number of additional proton-proton interaction vertices in simulation, that is applied in order for this number to match the one observed in data.

5.8.2 Dijet fit uncertainties

Three uncertainties are associated with each dijet fit, corresponding to parameters p_1 , p_2 and p_3 of the dijet function from Equation 5.3. Due to high correlation of the parameters, eigenvector decomposition is performed to obtain three independent linear combinations. For background uncertainty estimation, the systematically varied distributions are obtained from the dijet function by variations of the three parameters. After the fit in the source region, the varied distributions are propagated to the signal regions to obtain the final uncertainty values. For obtaining the uncertainties for the dijet fits to the simulated data, a different approach

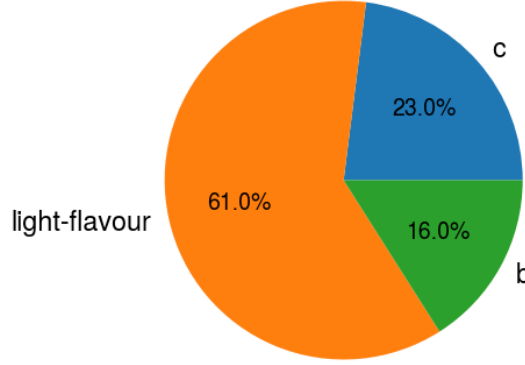


Figure 5.11: $t\bar{t}$ +jets background composition.

is used, involving 1000 toy distributions, Gaussian sampled from the MC histogram. The fit is applied to each distribution and the central values of the fit are recorded. Using this set of pseudoexperiments, the covariance matrix is calculated, its eigenvector decomposition is performed, and these variations are then applied on top of the nominal fit to obtain the final systematic variations.

In total, there are three nuisance parameters related to the dijet fit of data in the source region, three nuisance parameters for the fit of simulated events in the source region, and three nuisance parameters for each of the dijet fits to simulated events in the signal regions, which makes the total number of nuisance parameters 24.

5.8.3 Theoretical uncertainties

The systematic variations of the background prediction due to uncertainties on the cross sections of the background processes are obtained as described in Section 5.7.3. Each variation is applied to the background distribution, and the dijet fit is repeated in order to obtain the variation of the background prediction in the signal regions.

The uncertainty on the $t\bar{t}$ +jets background flavor composition is estimated in the same way, with the background events classified as either $t\bar{t}$ + b -jets, $t\bar{t}$ + c -jets or $t\bar{t}$ +light-flavor-jets and the contribution from each group scaled by the appropriate uncertainty. The generated events are classified according to the flavor of particle jets by matching the generator-level hadrons to reconstructed jets. The idea of such a classification is to identify the flavor of the additional jet that does not originate from the $t\bar{t}$ pair. As both top quarks decay to a b -quark which results in the formation of a b -jet, and a W -boson, which can produce a c -quark in its decay, b - and c -jets are expected to be present in the event of any category.

The events are labelled as $t\bar{t}$ + b -jets if it has at least one b -tagged jet which is not matched to a top quark decay. Then, the events with at least one c -tagged jet that is not matched to a top quark decay are labelled as $t\bar{t}$ + c -jets, and the rest are assigned the label of $t\bar{t}$ +light-flavor-jets. The composition of the $t\bar{t}$ +jets background is shown in Figure 5.11.

An uncertainty of 50% is assigned to the normalization of the $t\bar{t}$ + b -jets and $t\bar{t}$ + c -jets categories, and an uncertainty of 10% is assigned to the $t\bar{t}$ +light-flavor jets category [150, 151]. A summary of all cross section uncertainties is shown in Table 5.2. The conservative uncertainty for the single top quark events is motivated by uncertainties of modeling of large numbers of associated jets. The uncertainties for the $t\bar{t} + W$, $t\bar{t} + Z$ and $t\bar{t} + H$ are motivated by Ref. [152–154], the

Table 5.2: Cross section uncertainties for background processes.

| Background process | Cross section uncertainty |
|-------------------------------|---------------------------|
| Single top | 30% |
| VV, VH | 50% |
| $t\bar{t} + W$ | 60% |
| $t\bar{t} + Z$ | 15% |
| $t\bar{t} + H$ | 20% |
| V+jets | 59% |
| SM $t\bar{t}t\bar{t}$ | 20% |
| $t\bar{t}+b$ -jets | 50% |
| $t\bar{t}+c$ -jets | 50% |
| $t\bar{t}$ +light-flavor jets | 10% |

evaluation of the V +jets uncertainty value follows Ref. [155], and the 20% uncertainty for the SM four top events is motivated by Ref. [156]. A conservative uncertainty of 50% is applied to the other background processes.

The higher order QCD corrections are estimated by varying the renormalization and the factorization scales by a factor 2 and 0.5 and taking the envelope of the resulting distributions.

The uncertainties on the amount of initial and final state radiation are accounted for by varying the modeling parameters in PYTHIA 8.

The uncertainties related to the generator choice for the $t\bar{t}$ +jets and single top background processes are estimated using alternative simulated samples. The samples generated with MADGRAPH5_AMC@NLO are compared to the nominal samples generated using POWHEGBOX 2. The corresponding systematic variations for the $t\bar{t}$ +jets background are further decorrelated into four components, each affecting either the shape or the normalization of the ditop mass distribution in $3b$ or $\geq 4b$ signal regions. Similarly, the uncertainties in parton shower modeling are estimated using alternative showering predictions of HERWIG 7.04 and comparing them to the nominal predictions made by PYTHIA 8.

The PDF-related uncertainties are estimated by computing the standard deviation of the eigenvariations of the NNPDF3.1 set and applying it as a single symmetric nuisance parameter [157].

Every uncertainty corresponds to a nuisance parameter of the fit. Pruning of the nuisance parameters that have shape or normalization variation under 0.5% with respect to the nominal prediction is applied. It was verified that the result is not affected by this choice of pruning threshold.

5.8.4 Signal bias uncertainty

Extracting the background shape with a functional fit, that does not capture all aspects of the shape of the distribution, introduces a bias, resulting in appearance of a spurious signal contribution. In order to account for this bias, a *signal bias* uncertainty is introduced in the model-dependent interpretation of the results.

As the introduced bias has different effects when fitting different signal variants, the signal bias uncertainty must be calculated separately for each of them. An example for one configuration of the parameters, $c_t = 1$ and $\theta = 0$, is shown in this section, and the uncertainty is calculated in the same way for the rest of them. First, 500 pseudo-data sets are sampled from the background

distribution and each of them is passed as input to the profile likelihood for the “signal + background” hypothesis (the details of the procedure are described below in Section 5.9.1). The distribution of the obtained signal strengths is then fitted with a Gaussian distribution, as shown in Figure 5.12, and the mean of the distribution is taken as the mean signal bias. The mean biases are then plotted for all signal masses, and the three highest values are used to construct a second-order polynomial function that provides a conservative estimate of this uncertainty over the whole mass range. Figure 5.13 shows that plot with the constructed envelope on the left. On the right, the plot shows the values of the Gaussian fit mean divided by the fit’s standard deviation. According to Ref. [158], for an acceptable signal bias uncertainty, this value should be less than 20–50%.

In the model-dependent interpretation, this uncertainty enters as an additional signal contribution on top of the background prediction. Therefore, the total number of fitted signal events is

$$N_{\text{signal}}(m_{Z'}) = N_{\text{real signal}} + S_{\text{modeling}}^0(m_{Z'}) \times \theta_{\text{signal bias}}, \quad (5.7)$$

where $N_{\text{real signal}}$ denotes the number of observed signal events, $S_{\text{modeling}}^0(m_{Z'})$ is the signal bias uncertainty, and $\theta_{\text{signal bias}}$ is the value of the corresponding nuisance parameter obtained from the fit.

The addition of the signal bias uncertainty decreases the sensitivity of the search, however it is crucial as it covers potential modeling biases and decreases the possibility of a false discovery.

5.9 Statistical analysis

Both model-independent and model-dependent interpretations of the analysis test the hypothesis of signal presence. For this purpose, a so-called *null* hypothesis H_0 is defined, which assumes the presence of only Standard Model physics, considered background in the search.

Data is compared to H_0 and a single number called *test statistic* is used to quantify the difference between the data and the null hypothesis. Several different approaches can be chosen for the definition of this statistic, one of which is provided in BUMPHUNTER, used for the model-independent interpretation in this analysis. Other definitions are provided, for example, for the profile likelihood fit, discussed below, or in the χ^2 and the Kolmogorov-Smirnov tests.

For a given test statistic, the p-value is defined as the probability that, given the H_0 hypothesis, the test statistic will be greater or equal than the t_o obtained from comparing data to H_0 :

$$\text{p-value} \equiv P(t \geq t_o | H_0). \quad (5.8)$$

Given that the probability density function $\rho(t|H_0)$ is known, the p-value can then be calculated as

$$\text{p-value} = \int_{t_o}^{\infty} \rho(t|H_0) dt. \quad (5.9)$$

The probability density function can be derived analytically or calculated numerically from pseudo-experiments. In the latter case the p-value can be estimated as a binomial success probability:

$$p = \binom{N}{S} \text{p-value}^S (1 - \text{p-value})^{N-S} \quad (5.10)$$

where N is the number of pseudo-experiments, and S is the number of experiments that had $t \geq t_o$.

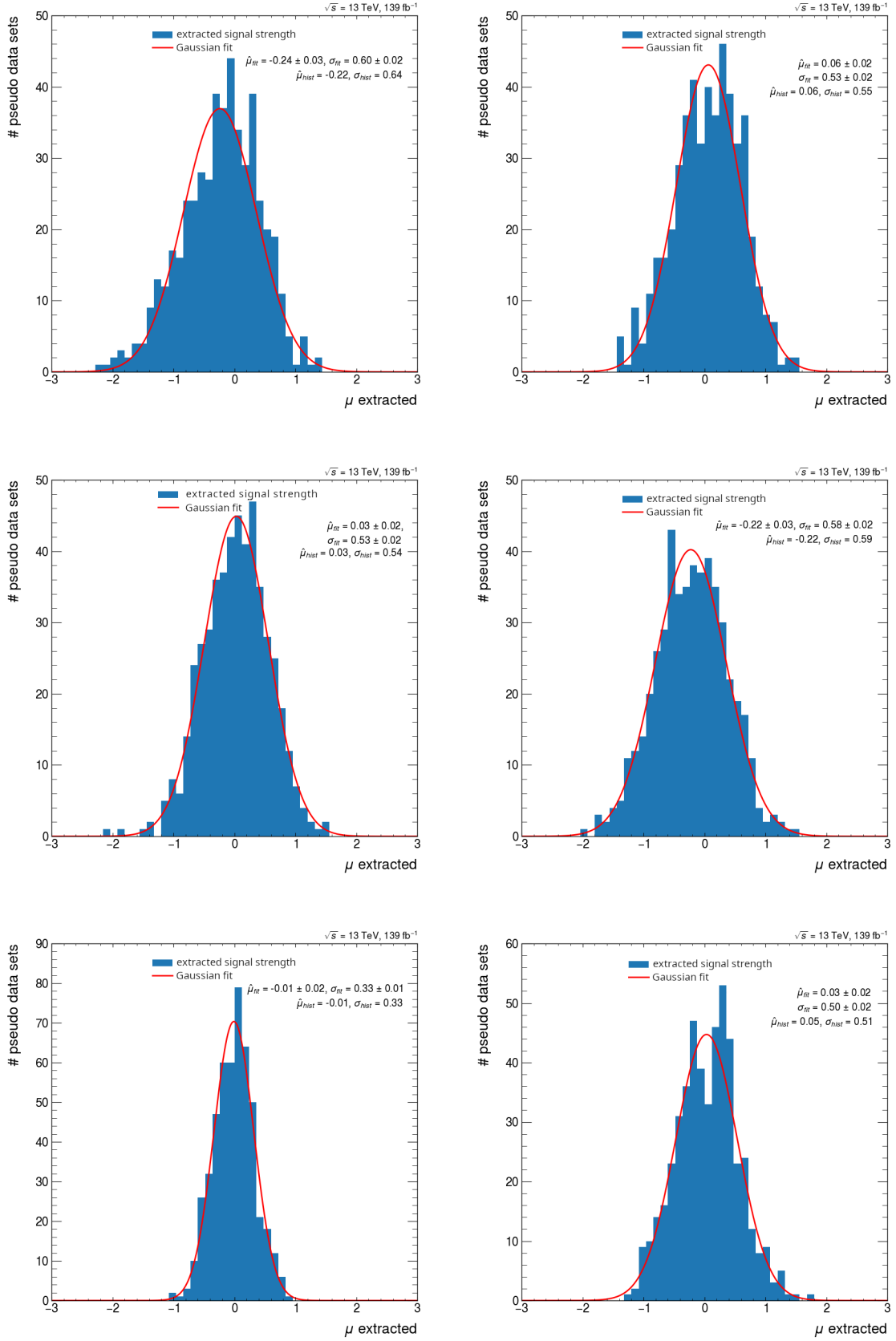


Figure 5.12: The distribution of the fitted signal strengths for the 500 pseudo-data sets sampled from the background distribution. All signal masses between 1 and 3 teV are presented, the signal model parameters are $c_t = 1$, $\theta = 0$.

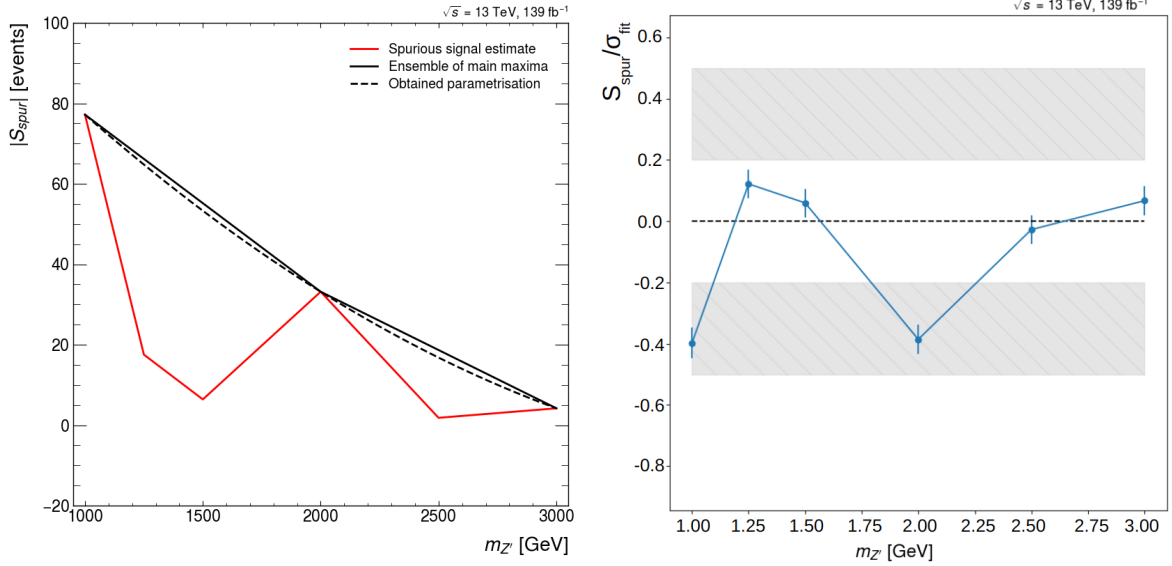


Figure 5.13: Left: the mean signal bias values and the constructed polynomial envelope. Right: the mean of the Gaussian fit to the signal bias distribution divided by the standard deviation of that fit. All values are for the signals in the whole mass range, $c_t = 1$ and $\theta = 0$.

It can be shown that the p-value corresponds to the probability of the so-called *Type-I error*, or the probability of falsely excluding the null hypothesis given the observed data. By requiring that the p-value is less or equal to some cutoff value α , the null hypothesis can be rejected at α confidence level.

5.9.1 Profile likelihood fit

The statistical analysis is based on a profile likelihood fit performed for the binned distribution of the ditop mass [159].

The expected number of events in each bin is given by

$$n_i^{\text{exp}} = \mu s_i(\theta) + b_i(\theta), \quad (5.11)$$

where μ is the signal strength, and s_i and b_i denote the number of signal and background events in the bin. Signal strength 0 corresponds to the background-only hypothesis, and signal strength equal to 1 corresponds to the nominal signal hypothesis. Both numbers of expected signal and background events depend on the nuisance parameters θ .

The likelihood function is defined as the product of Poisson probabilities for all bins:

$$L(\mu, \theta) = \prod_{i=1}^N \frac{(\mu s_i(\theta) + b_i(\theta))^{n_i}}{n_i!} e^{-(\mu s_i(\theta) + b_i(\theta))}. \quad (5.12)$$

The profile likelihood ratio is defined as

$$\lambda(\mu) = \frac{L(\mu, \hat{\theta})}{L(\hat{\mu}, \hat{\theta})}, \quad (5.13)$$

where $\hat{\boldsymbol{\theta}}$ denotes the nuisance parameter values that maximize the likelihood function for a given signal strength μ , and $\hat{\mu}$ and $\hat{\boldsymbol{\theta}}$ correspond to the parameters that maximize the likelihood function unconditionally. Due to presence of nuisance parameters, the profile likelihood as a function of μ broadens and thus some information about the signal strength is lost due to systematic uncertainties.

It follows from the definition of the profile likelihood ratio that $0 \leq \lambda(\mu) \leq 1$, with 1 implying the best agreement between the data and the given signal strength value. The test statistic can be defined as

$$t_\mu = -2 \ln \lambda(\mu), \quad (5.14)$$

with higher values of t_μ corresponding to increasing incompatibility between data and the signal hypothesis. The p-value for such test statistic is given by

$$p_\mu = \int_{t_\mu, \text{ obs}}^{\infty} f(t_\mu|\mu) dt_\mu, \quad (5.15)$$

where $t_\mu, \text{ obs}$ is the observed value of the test statistic, and $f(t_\mu|\mu)$ is the probability density function for the test statistics given the signal strength μ .

In studies with the aim of discovering positive signals, the test statistic for probing the background-only hypothesis is defined as

$$q_0 = \begin{cases} -2 \ln \lambda(0) & \text{if } \hat{\mu} \geq 0, \\ 0 & \text{otherwise.} \end{cases} \quad (5.16)$$

Here, $\lambda(0)$ is the profile likelihood ratio for the background-only hypothesis. This statistic considers data to be inconsistent with the background-only hypothesis only in cases of excess of events. The p-value for this statistic is calculated as

$$p_0 = \int_{q_0, \text{ obs}}^{\infty} f(q_0|0) dq_0, \quad (5.17)$$

where $f(q_0|0)$ is the probability density function of q_0 under background-only hypothesis.

5.9.2 Model-independent search

The model-independent interpretation is performed using the BUMP HUNTER tool [110], which looks for most significant localized deviations between data and background distributions. Before the tool itself is described, it is necessary to introduce some definitions.

When multiple statistical tests are considered, the *look-elsewhere effect* needs to be taken into account. For example, when looking for any discrepancies between the data and background distributions, a random fluctuation in one bin should not be considered a significant reason to exclude the background-only hypothesis. In order to address this issue, a parameter called *the trials factor* is defined, which reflects the effective number of uncorrelated tests. The probability of observing one small p-value in this case increases with the increase of the trials factor:

$$P(\text{at least one test p-value} \leq \alpha) \equiv 1 - (1 - \alpha)^N, \quad (5.18)$$

where α is the p-value threshold and N denotes the trials factor.

A following test statistic can be defined:

$$t = -\log(\min_i(\text{p-value}_i)), \quad (5.19)$$

where p-value_i is the p-value of the trial i . This new test is called a *hypertest* as it combines results of multiple tests.

BUMPHUNTER can be used to analyze histograms and compare data and background distributions. It uses windows of varying widths in order to find the most significant deviation. All allowed widths and positions of the window are considered, and every time the test statistic is calculated as

$$t = \begin{cases} 0 & \text{if } d_W \leq b_W, \\ f(d_W - b_W) & \text{otherwise,} \end{cases} \quad (5.20)$$

where d_W and b_W represent the number of data and background events in the window, and f can be any positive monotonically increasing function.

The corresponding p-value is therefore

$$\text{p-value} = \begin{cases} 1 & \text{if } d_W \leq b_W, \\ \mathcal{P}(d_W, b_W) & \text{otherwise,} \end{cases} \quad (5.21)$$

where $\mathcal{P}(d_W, b_W)$ is the probability function. It is defined as

$$\mathcal{P}(d, b) = \begin{cases} \Gamma(d, b) & \text{if } d \leq b, \\ 1 - \Gamma(d + 1, b) & \text{otherwise,} \end{cases} \quad (5.22)$$

where the gamma function is

$$\Gamma(d, b) = \sum_{n=d}^{\infty} \frac{b^n}{n!} e^{-b}. \quad (5.23)$$

After all possible window positions and widths are considered, the test statistic is calculated as defined in 5.19. The test statistic distribution obtained from pseudo-experiments is used to determine the p-value of the whole hypertest.

In the analysis presented here, the background distribution that is used for model-independent interpretation is obtained from the profile likelihood fit assuming background-only hypothesis.

5.9.3 Model-dependent interpretation

Profile likelihood fit is used for the model-dependent interpretation. To evaluate compatibility between the data and the background-only hypothesis, the test statistic q_0 from Eq. 5.16 is used, and the p-value p_0 is calculated. A small p-value would mean significant deviations between data and the background-only prediction, and a potential discovery.

In the absence of deviations, a common way of presenting the results is setting an upper limit on the signal strength. This effectively means specifying the maximum signal strength that could be unnoticed by the analysis and thus excluding all signal hypothesis with signal strengths greater than this limit. The limit setting is performed using the CL_s approach [160].

The approach utilizes the probability density functions $f(Q) = -2 \ln Q$, where $Q = L(s+b)/L(b)$ is the ratio of likelihood functions of the hypothesis of a signal presence and the hypothesis of only background. The p-values of both hypotheses are calculated:

$$\text{p-value}_{s+b} = \mathcal{P}(Q \geq Q_{\text{obs}} | s+b) = \int_{Q_{\text{obs}}}^{\infty} f(Q | s+b) dQ, \quad (5.24)$$

$$\text{p-value}_b = \mathcal{P}(Q \leq Q_{\text{obs}} | b) = \int_{Q_{\text{obs}}}^{\infty} f(Q | b) dQ. \quad (5.25)$$

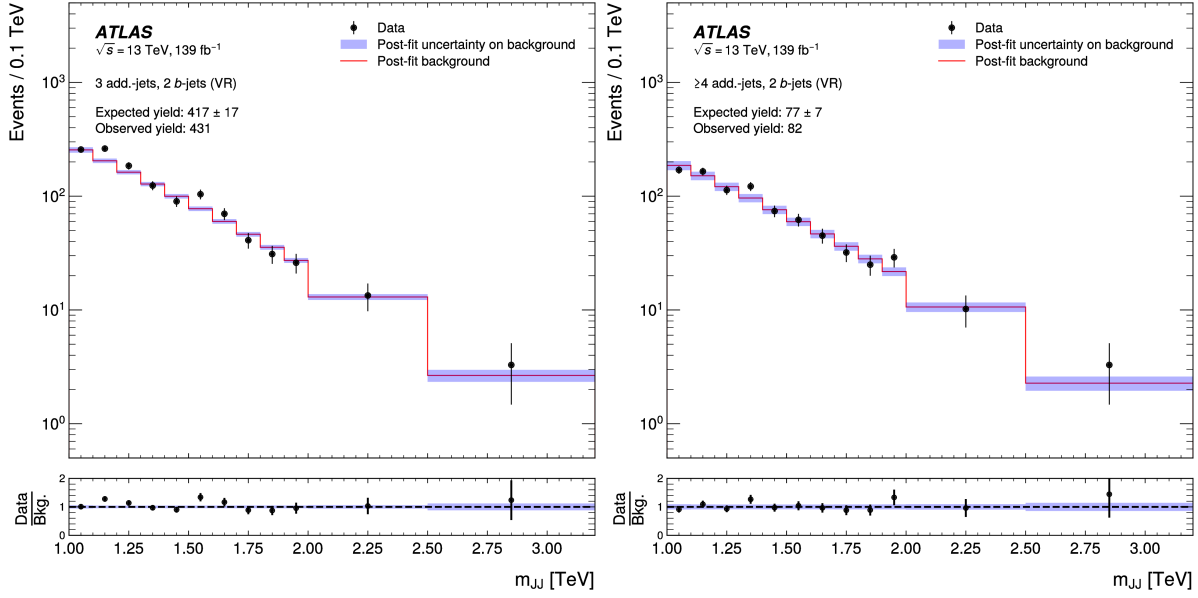


Figure 5.14: Comparison of the ditop mass (m_{JJ}) distribution obtained from data and the background prediction in the validation regions. The plot on the left corresponds to the (2a, 3b) region, and the plot on the right corresponds to the (≥ 4 a, 2b) region. The data distribution agrees with the background prediction, and signal contamination for a Z' signal with mass 1.5 TeV $c_t = 1$ and $\theta = \pi/2$ is negligible in both validation regions [109].

The $p\text{-value}_{s+b}$ reflects the probability to obtain a result with equal or lesser compatibility to the observed, given that there is actual signal present in the data. The $p\text{-value}_b$ reflects the probability of obtaining a result with equal or lesser compatibility with the background-only hypothesis, given only background presence in the data.

The CL_s quantity is calculated as

$$CL_s = \frac{p\text{-value}_{s+b}}{1 - p\text{-value}_b}, \quad (5.26)$$

and the upper limit on signal strength on a confidence level α can be set by requiring $CL_s \leq \alpha$.

5.10 Results

Model-independent and model-dependent interpretations of the search are presented in this section.

5.10.1 Model-independent results

The background prediction is obtained by propagating the results of a background-only profile likelihood fit in the source region to the signal regions. Before considering the signal regions, the background propagation procedure is validated in the two validation regions. The background prediction histograms for the validation regions is shown in Figure 5.14. The distribution of the ditop mass, given that a signal with an arbitrarily large cross section is present, is shown with the green dashed line. The background prediction is consistent with data, and it is visible that the signal contamination is negligible.

After the background prediction validation, BUMPHUNTER is used to search for deviations from the background prediction in the signal regions. Figure 5.15 shows the ditop mass distributions in the signal regions and the windows of most significant deviation found by BUMPHUNTER. For reference, the expected distribution with presence of a 1.5 TeV signal with $c_t = 1$ and $\theta = \pi/2$ is presented in all panels. The signal cross section is scaled to an arbitrary large number of 51 fb^{-1} for visualization purposes.

The most significant deviation is observed in the (2a, $\geq 4b$) region at 1.2 TeV. The p-value of that window is 0.15 and it corresponds to 1.04σ significance of the result.

5.10.2 Model-dependent results

For the model-dependent interpretation, binned profile likelihood fit with a signal presence hypothesis is used. The bins of the ditop mass distribution have width of 100 GeV, except for the two wider bins towards the higher-mass end of the distribution, which have widths of 500 and 700 GeV, to account for the expected low event yields. As no deviation between the data and background is observed, the result is presented as a limit computation. An unconditional profile likelihood fit for all signal regions simultaneously is performed for each considered signal variant.

Sample fit

As an example, a fit for the 1.5 TeV signal with $c_t = 1$, $\theta = 0$ and cross section $\sigma = 143 \text{ fb}$ will be discussed in this section. The same procedures are performed for the other signal hypotheses.

All uncertainties, described previously, enter the fit, and the data distribution is compared to the sum of signal and background distributions. The resulting signal strength value is 0.00 ± 0.12 , and the observed significance of the fit is 0.08σ , with the expected significance being 7.96σ , which indicates that no significant discrepancies between the data and the background are observed. Figure 5.16 shows the ditop mass distribution in the signal regions before the profile likelihood fit, and Figure 5.17 shows the same distributions after the fit. In both figures the signal distribution is shown as both stacked and overlaid in each panel. As the background distribution describes the observed data well, no signal contribution is visible on the post-fit plots. All best-fit values of the nuisance parameters are within 1σ of the expected values, and their pulls and constraints are similar for the background-only fit and the fit that considers the presence of a signal.

The goodness of fit is evaluated to ensure that the fit describes the background adequately, and the p-value of the fit is 0.47, which corresponds well to the background-only hypothesis.

Limit computation

The limits are computed using the CL_s approach, described in Section 5.9.3. Figure 5.18 shows the expected signal strength limits for all considered signals, and Figure 5.19 shows the observed limits. The parameter combinations with the observed limits on signal strength below 1 are excluded by the search at 95% CL_s . Therefore, signals with mass 1.0 TeV and coupling strength 4 and 4.5 can be excluded for both values of the chirality parameter. Additionally, the 1.25 TeV signal can be excluded for the values $c_t = 4.5$ and $\theta = 0$. Figure 5.20 shows the expected and observed cross section limits for signals with $\theta = \pi/2$ on the left and $\theta = 0$ on the right. On each plot the limits for the parameter $c_t = 1$ and $c_t = 4$ are shown, as well as theoretical predictions for the considered signals.

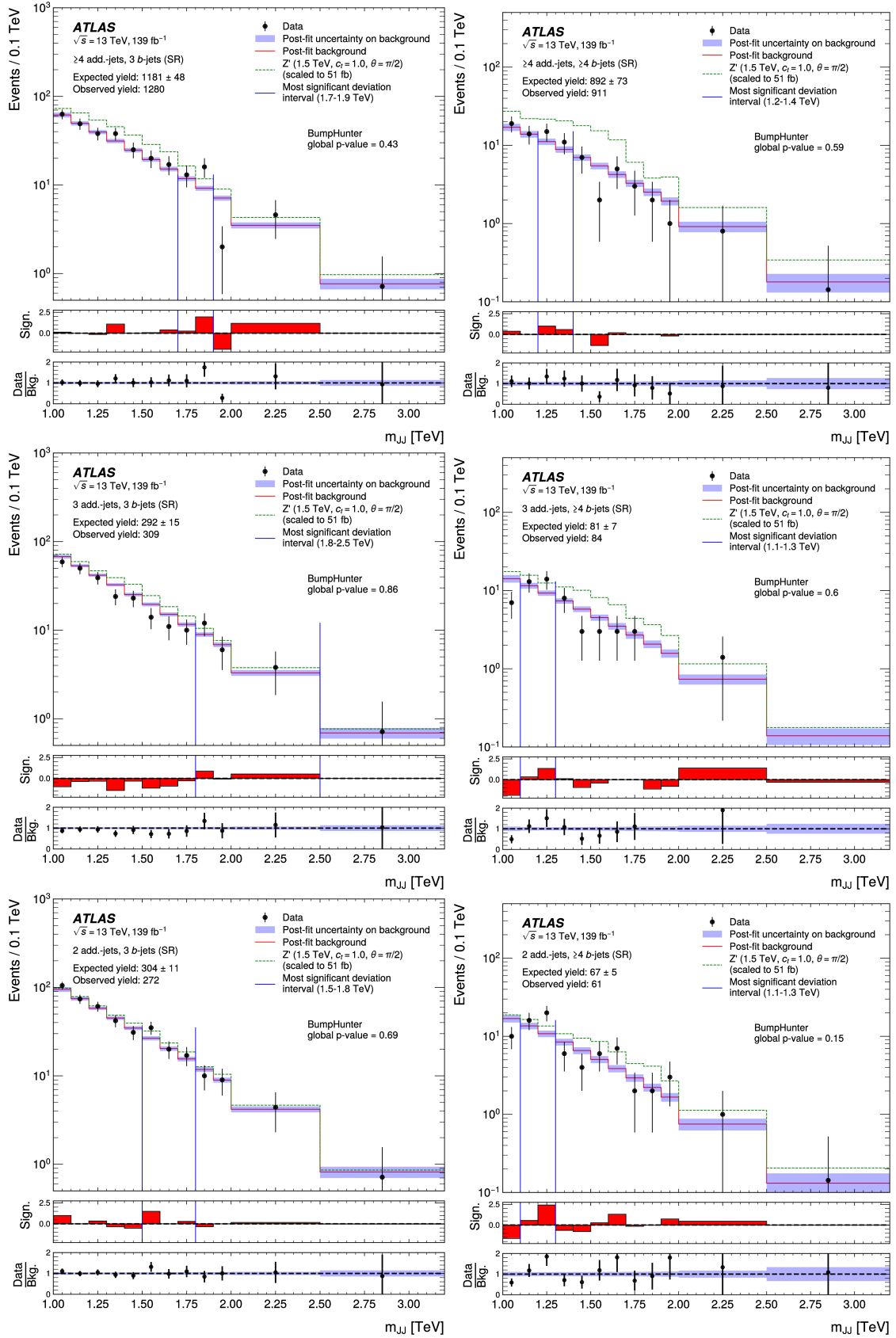


Figure 5.15: Results of the model-independent search in the signal regions with the windows with the most significant deviation highlighted by the two vertical lines. For reference, the expected distribution given a presence of a signal with mass 1.5 TeV $c_t = 1$ and $\theta = \pi/2$ and with an arbitrarily large cross section is shown on each plot [109].

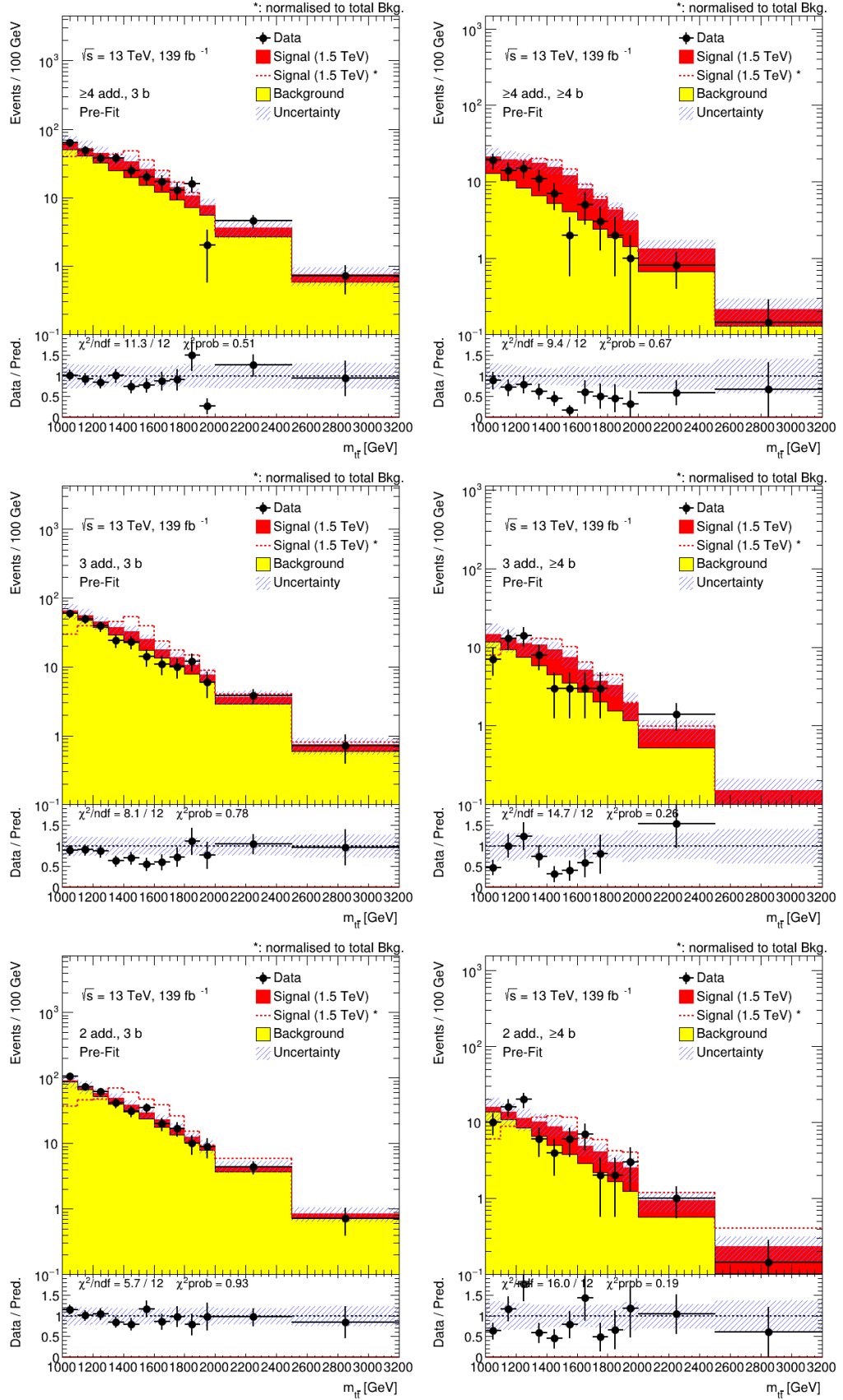


Figure 5.16: The ditop mass distributions in the signal regions before the profile likelihood fit. The colored red histogram shows the signal stacked on top of the background, and the dotted line shows the signal distribution normalized to the total number of background events overlaid with the background histogram.

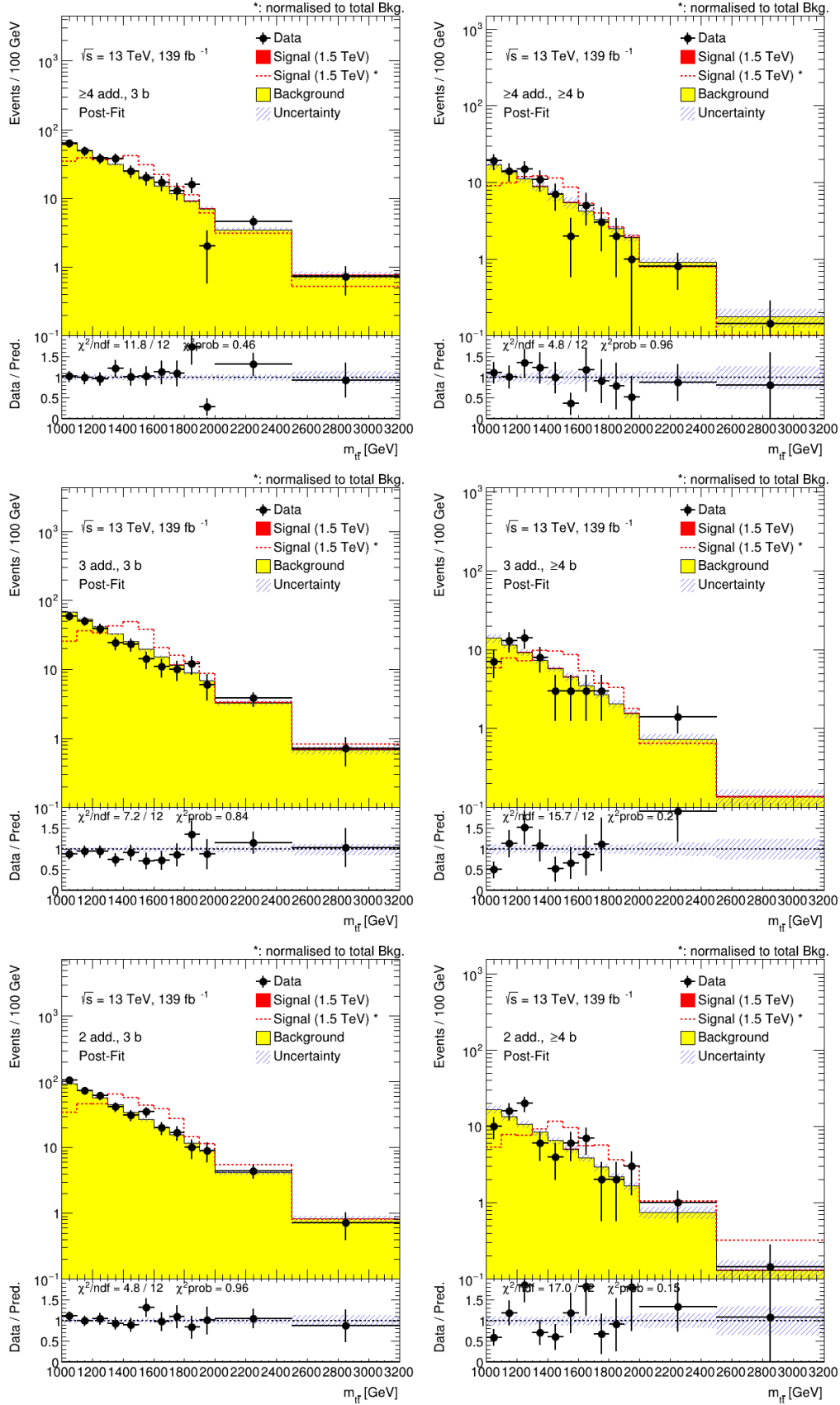


Figure 5.17: The ditop mass distributions in the signal regions after the profile likelihood fit. The colored red histogram shows the signal stacked on top of the background, and the dotted line shows the signal distribution normalized to the total number of background events overlaid with the background histogram.

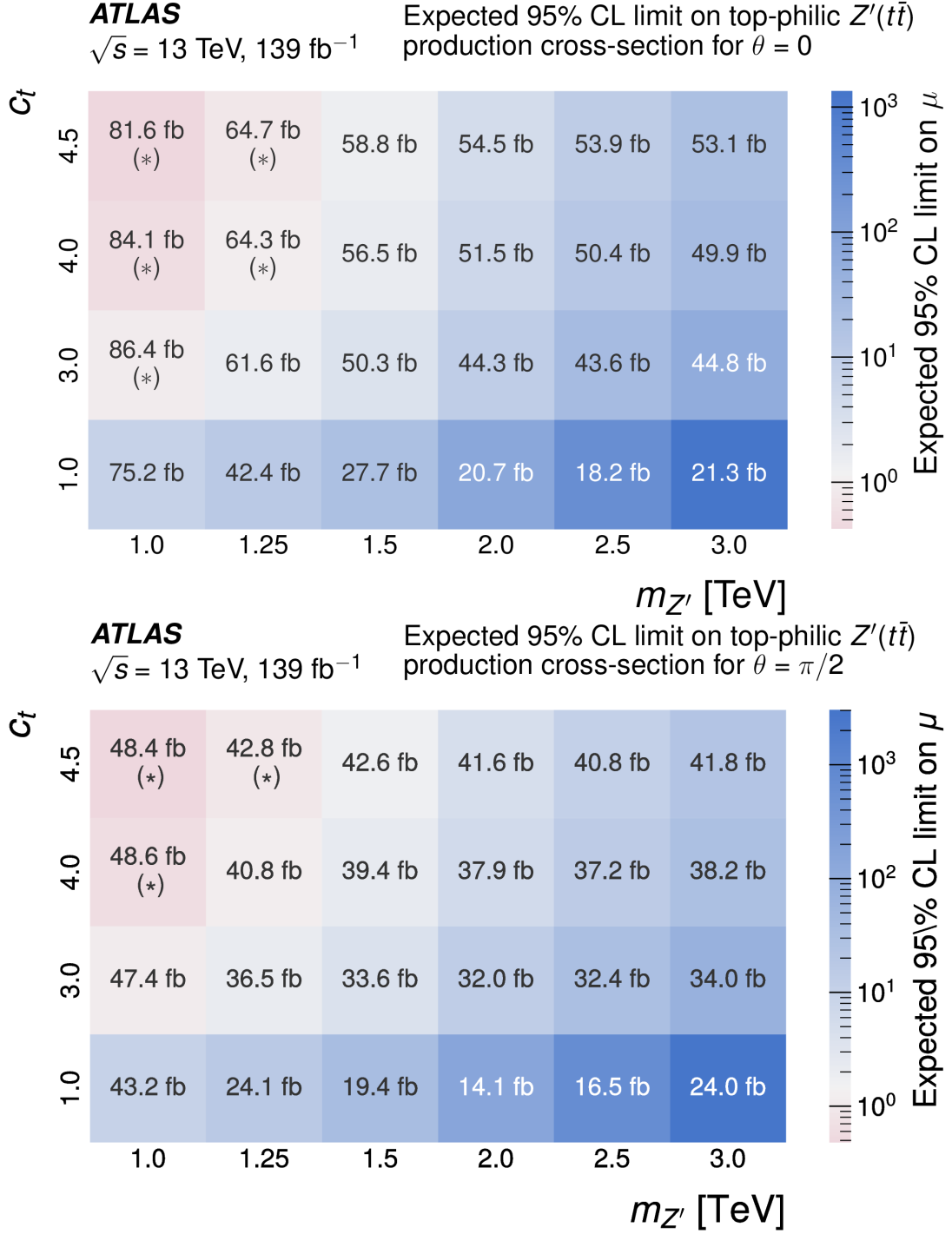


Figure 5.18: The expected signal strength limits for all considered parameters of the signal. The top table shows the limits for $\theta = 0$, while the bottom table shows the limits for $\theta = \pi/2$. All considered masses and coupling strengths are presented in each table [109].

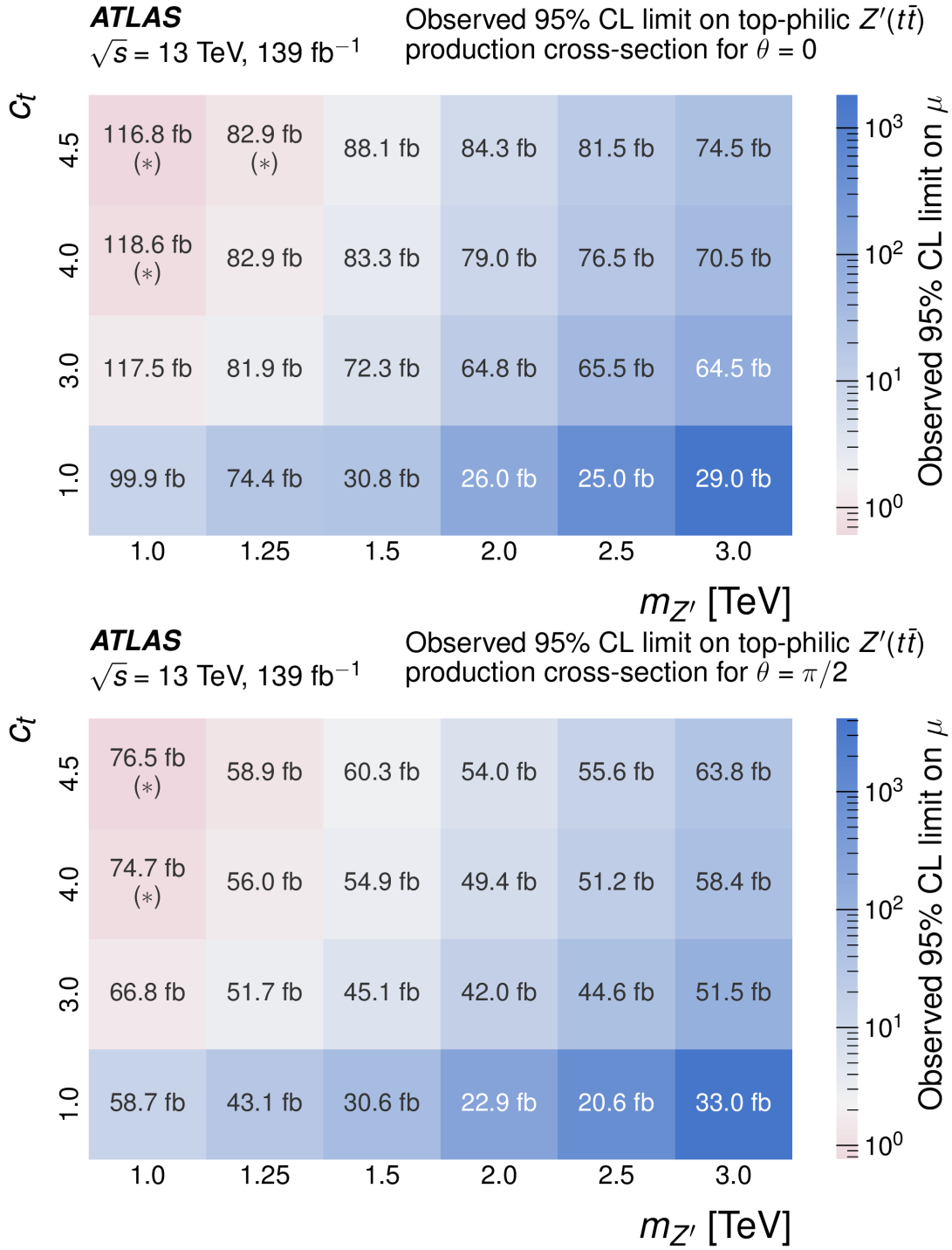


Figure 5.19: The observed signal strength limits for all considered parameters of the signal. The top table shows the limits for $\theta = 0$, while the bottom table shows the limits for $\theta = \pi/2$. All considered masses and coupling strengths are presented in each table [109].

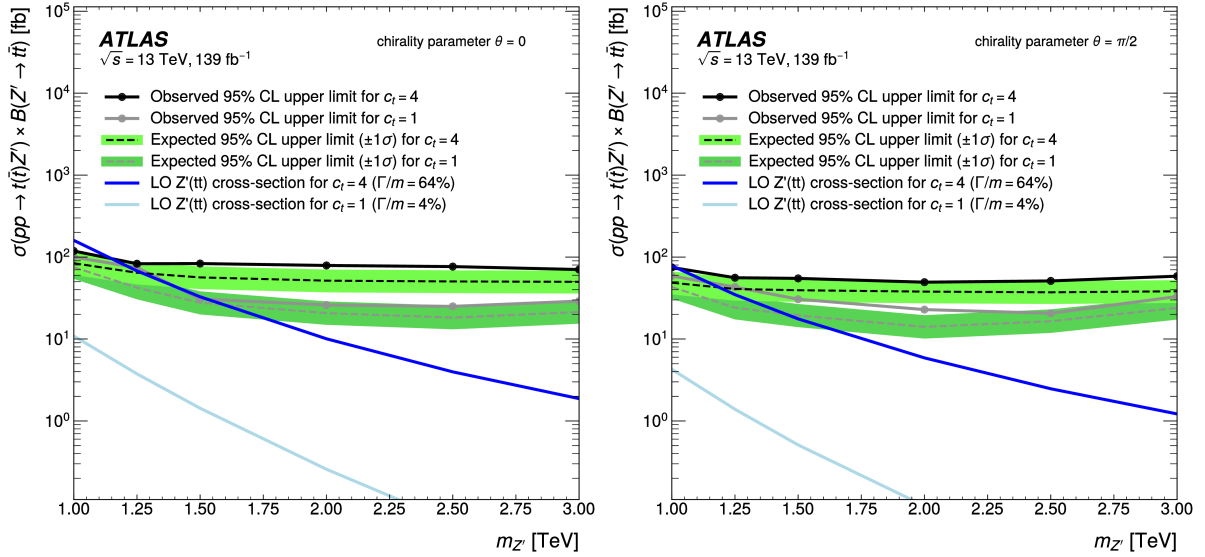


Figure 5.20: The expected and observed cross section limits as function of the signal mass for chirality angle $\theta = 0$ on the left and $\theta = \pi/2$ on the right. Both plots show the limits for $c_t = 1$ and $c_t = 4$, as well as the theoretical predictions for these parameters of the signal model [109].

Uncertainty evaluation

Table 5.3 lists the relative contributions of the uncertainties for two example signal models with parameters $m_{Z'} = 1.5$ TeV, $c_t = 1$, $\theta = 0$, and $m_{Z'} = 3$ TeV, $c_t = 1$, $\theta = \pi/2$.

In order to evaluate the impact of a group of uncertainties, these uncertainties are fixed to their post-fit values and the fit is repeated. The impact is then calculated as the quadrature subtraction $\sqrt{(\Delta\mu)^2 - (\Delta\mu')^2}$, where $\Delta\mu$ is the total uncertainty with all nuisance parameters free, and $\Delta\mu'$ is the total uncertainty with the nuisance parameters of this group fixed. The percentage is calculated relative to the total uncertainty of the full fit. Due to correlations between the uncertainties, the total systematic uncertainty is different from the sum in quadrature of the individual components.

The results of the analysis are dominated by systematic uncertainties. As expected, the largest contribution arises from the modeling of the $t\bar{t}$ +jets background. The jet-related uncertainties, the uncertainties of the fit and the ones related to the signal bias also have significant contributions.

5.11 Preservation and reuse of the analysis framework

In order to preserve the analysis framework and allow for easy evaluation of other signal models with it, an interaction with the RECAST software [161] was implemented. It involves creating Docker containers [162] for all the framework elements and preparation of scripts to run the analysis steps. In order to run the analysis for a specific signal model, the user needs to propagate the events simulated using this model through the ATLAS detector simulation, and provide the samples along with a configuration file.

All aspects of the preserved workflow are done the same way as in the analysis described above, except for the calculation of the signal bias uncertainty. As it needs to be done separately for

Table 5.3: The contribution from different systematic uncertainties relative to the total uncertainty for two signal scenarios.

| Uncertainty category | Relative contribution to the total uncertainty, % | |
|--------------------------------------|---|-------------------------------------|
| | 1.5 TeV, $c_t = 1$, $\theta = 0$ | 3 TeV, $c_t = 1$, $\theta = \pi/2$ |
| $t\bar{t}$ +jets modeling | 78 | 87 |
| Jet energy scale and resolution | 40 | 46 |
| Functional fit and extrapolation | 41 | 23 |
| Signal bias | 35 | 7.3 |
| Statistical uncertainty on signal MC | 26 | 19 |
| Single-top-quark modeling | 11 | 8.9 |
| Flavor tagging | 9.4 | 9.8 |
| Minor backgrounds modeling | 6.9 | 5.3 |
| Other uncertainties | 1.5 | 2.1 |
| Luminosity | 0.2 | 2.0 |
| Total systematic uncertainty | 95 | 96 |
| Statistical uncertainty | 32 | 29 |

Table 5.4: Obtained limits for $t\bar{t}Z'$ and $t\bar{t}H/A$ signals with mass of 1 TeV.

| | $t\bar{t}H/A$ | $t\bar{t}Z'$ |
|--------------------------|--------------------|------------------|
| Model parameters | mass 1 TeV | |
| | alignment limit | $c_t = 1.0$ |
| | $\tan\beta \sim 1$ | $\theta = \pi/4$ |
| Prediction cross section | 3.601 fb | 41.0 fb |
| Expected limit | 25.96 fb | 44 fb |
| Observed limit | 28.72 fb | 57.2 fb |

each signal model, this uncertainty is omitted in the RECAST workflow. In the end, the result of the final fit is returned.

The workflow was executed for the $t\bar{t}Z'$ signal of mass 1 TeV with only s-channel production of the four-top-quark final state and the model parameters $c_t = 1.0$, $\theta = \pi/4$ and for the $t\bar{t}H/A$ signal of the same mass, where H/A stands for the scalar Higgs bosons, predicted by the 2HDM theory described in Chapter 1 with the assumption that the alignment limit is satisfied and $\tan\beta \sim 1$.

The signal shape comparison for these two signals in the ($\geq 4a$, $\geq 4b$) region is depicted in Figure 5.21, and the fit results are presented in Table 5.4. The limits for both signals were found to be close, which is consistent with the similarity in signal shapes. The predicted cross section for the $t\bar{t}H/A$ signal is ten times smaller than the one predicted for the $t\bar{t}Z'$ signal, and therefore the sensitivity of this search is not enough to probe the 2HDM model in the single lepton final state. However, the resulting limits are smaller for the $t\bar{t}H/A$ signal than for the $t\bar{t}Z'$ one, which can be explained by the narrower width of the scalar signal distribution in Figure 5.21.

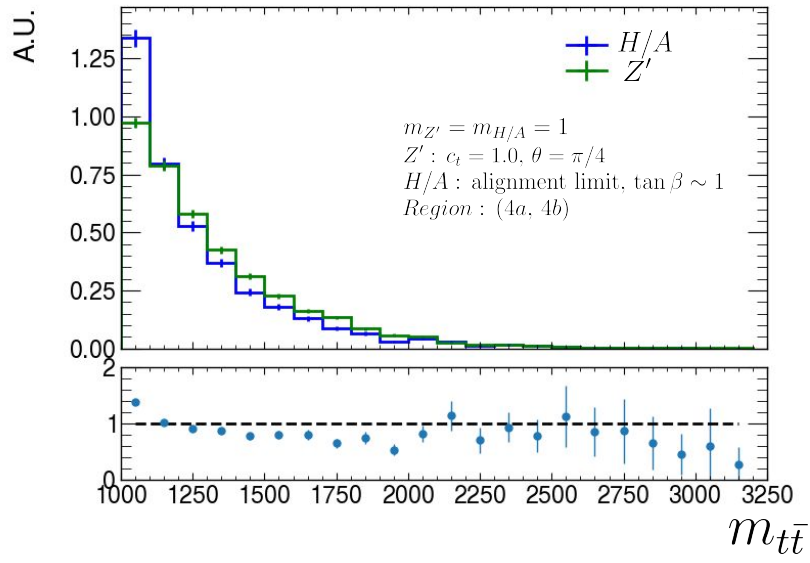


Figure 5.21: $t\bar{t}Z'$ (vector) and $t\bar{t}H/A$ (scalar) signal invariant mass distribution comparison in the ($\geq 4a, \geq 4b$) region. The histograms are normalized to the same area.

6. Method for model-independent search for heavy resonances in multi-lepton final states

An improved search for Beyond the Standard Model physics using combined Run 2 and Run 3 data aims to enhance the sensitivity achieved before. It is a continuation of the previous Run 2 $t\bar{t}H/A$ [163] search and the first probe of the $t\bar{t}Z'$ production in the multi-lepton final state. In addition to using more experimental data, it includes other possible signal variants, utilizes modern analysis techniques, and benefits from better Monte Carlo modeling of signal processes. Unlike the $t\bar{t}Z'$ search, described in the previous chapter, this analysis studies the *same-sign multi-lepton* (SSML) final state. In this final state, exactly two leptons with the same sign of electric charge or at least three leptons are required in an event. While this final state has fewer background events than the single lepton final state, used in the $t\bar{t}Z'$ analysis, it is harder to obtain a model-independent result due to complications of reconstructing the resonance. Such reconstruction is beneficial for not only model-independent results, but it can also potentially provide improvements for the model-dependent results by improving the separation between signal and background events.

This chapter briefly describes analysis motivation and strategy and mainly focuses on the development of an algorithm for resonance mass reconstruction in the SSML final state. Discussion of the feasibility of this method, as well as estimations of possible results and improvements are also presented.

6.1 Motivation

The large Yukawa coupling of the top quark to the Higgs boson serves as a strong motivation for searching for top-quark-based resonances in many BSM theories, predicting the existence of other Higgs bosons of an extended Higgs sector, for example the two-Higgs-doublet model (2HDM) [34] that was introduced in Chapter 1. This was explored in an ATLAS Run 2 search for new heavy-scalar or pseudo-scalar Higgs bosons (H/A) in the four-top-quark final state. The masses considered in this search were between 400 and 1000 GeV, and the resonance was not reconstructed [163].

After the completion of this analysis and the one described in the previous chapter, a new and improved search for BSM physics in the four top final state commenced. The analysis

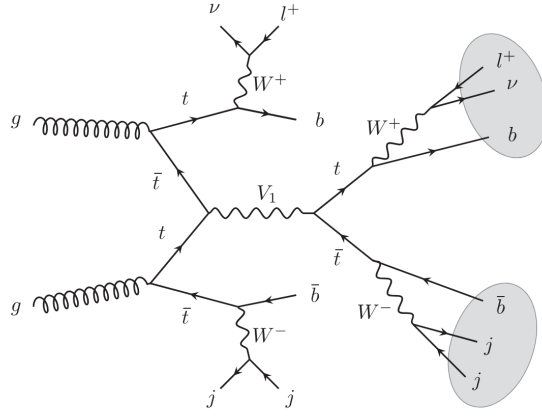


Figure 6.1: A Feynman diagram of the SSML four top final state with exactly two leptons with the same sign electric charge [164].

focuses on SSML final state, and the purpose of the analysis is to refine and enhance the results obtained from the initial analyses, using the combined data sets of full Run 2 and partial Run 3 and expanding the range of BSM particle masses and signal model interpretations that are considered.

A sample Feynman diagram of the studied process resulting in a SSML final state is shown in Figure 6.1.

6.2 Analysis strategy

The strategy for this analysis is similar to the one described in Chapter 5. First, the events that have at least two leptons with the same sign of electric charge are selected. Afterwards, two interpretations can be carried out. For obtaining a model-dependent result the events are divided into analysis regions, and a profile likelihood fit is performed in order to search for a BSM contribution. Reconstructed mass of the resonance can be used in order to obtain a model-independent result using the distribution of this mass in a signal-enriched region.

6.3 Data and Monte Carlo samples

This section describes the samples used in the analysis at the time of writing this thesis, however it may not be the final choice. Most of the samples for Run 2 are the same as used in the $t\bar{t}Z'$ search described in Chapter 5.

6.3.1 Data samples

The data used in the analysis consists of the full Run 2 dataset collected between 2015 and 2018 with the center of mass energy 13 TeV, and partial Run 3 dataset collected in the years 2022–2023 with the center of mass energy 13.6 TeV. The integrated luminosity of Run 2 is 140.0 fb^{-1} [111], and for Run 3 it is 51.8 fb^{-1} [165]. The uncertainty of the combined luminosity is 2%. Only data collected while all detector systems were fully operational is used.

6.3.2 Simulated signal samples

This analysis considers several signal models described in Chapter 1, Type II 2HDM and the generic top-philic Z' signal model that was also used in the search in Chapter 5.

Type II 2HDM model

Samples are generated at leading order using MADGRAPH5_AMC@NLO [112]. The samples are generated using Type II 2HDM with $\tan\beta = 1$ and no mixing between the H/A bosons. Samples with masses of the heavy Higgs bosons of 400, 500, 600, 800, 1000, 1100, 1200, 1300, 1500, 2000, 2500, and 3000 GeV are generated. The samples used for the studies described in this chapter include only s-channel four-top-quark final state production, but t-channel production and the production of final states with three top quarks will also be included in the search once the samples are generated. The t-channel contribution increases with the increase of the Higgs boson mass. The calculation of matrix elements is performed at leading order using five-flavor-number scheme using MADSPIN [166] using NNPDF3.0_lo_as_0118 PDF set [113]. The samples are interfaced with PYTHIA 8.3 [167] with the A14 tune [115] for showering and hadronization.

Interference effects with the SM $t\bar{t}t\bar{t}$ background is expected for these signal samples, therefore, a 2HDM interpretation will be performed for signals with masses up to 1 TeV, and a generic narrow resonance search will be performed for higher mass points.

Generic top-philic Z' model

The samples used for this signal model are generated the same way as described in Section 5.3, but reprocessed in a new ATLAS software release.

6.3.3 Simulated background samples

Background sample generation for Runs 2 and 3 is performed in the same way unless stated otherwise.

The Standard Model $t\bar{t}t\bar{t}$ samples were generated using MADGRAPH5_AMC@NLO 3.5.3 generator at next-to-leading order using the NNPDF3.0NLO PDF set [113]. The top quark decays are performed at leading order using MADSPIN to preserve all spin correlations. The events are interfaced with PYTHIA 8.230 [114] for Run 2 samples and with PYTHIA 8.310 for Run 3 samples using the NNPDF2.3LO PDF set [113] and the A14 parameter tune. The decays of b - and c -hadrons are simulated using the EVTGEN 1.6.0 [123]. To evaluate the impact of the parton shower and hadronization model choice, the generated samples were interfaced with HERWIG 7.04 with H7UE set of tuned parameters [130] and the MMHT2014LO PDF set [132]. In addition, alternative samples were generated with the SHERPA 2.2.11 [168] with the NNPDF3.0NNLO PDF set [113] to evaluate the uncertainty of the generator choice. For all these samples, the ATLAS detector response is simulated using the fast simulation with parametrized calorimeter showers [119].

Production of nominal $t\bar{t}W$ samples in QCD is performed using SHERPA 2.2.10 for Run 2 and SHERPA 2.2.14 for Run 3 with the NNPDF3.0NNLO PDF set with up to one extra parton at NLO and up to two additional partons in LO. Samples with only electroweak corrections from NLO3 diagrams are modeled at LO using the same setup as for the QCD-only production. The production of $t\bar{t}W$ events with one extra parton are modeled in QCD using MADGRAPH5_AMC@NLO 3.3.1 with the NNPDF3.0LO PDF set. Showering and hadronization is done with PYTHIA 8.308 using the A14 tune and the NNPDF2.4LO PDF set [113].

Production of $t\bar{t}Z$ samples is done with MADGRAPH5_AMC@NLO 2.8.1 for Run 2 and MADGRAPH5_AMC@NLO 3.4.2 for Run 3 at NLO with NNPDF3.0NLO PDF set. The events are interfaced with PYTHIA 8.244 for Run 2 and PYTHIA 8.309 for Run 3 using the A14 tune

and the NNPDF2.3LO PDF set. An alternative sample is generated with SHERPA 2.2.11 at NLO with the NNPDF3.0NNLO PDF set in order to account for generator uncertainty.

For $t\bar{t}H$ production, a nominal sample is generated using POWHEGBOX 2 generator [124–126] at NLO using the NNPDF2.0NLO PDF set and interfaced with PYTHIA 8.230 for Run 2 and PYTHIA 8.308 for Run 3 using the A14 tune and the NNPDF2.3LO PDF set. An alternative sample is created using the same generator, but interfaced with HERWIG 7.2.3 with the NNPDF2.0NLO PDF set for showering and hadronization to evaluate the impact of the showering and hadronization model.

$t\bar{t}$ events are modeled using POWHEGBOX 2 generator at NLO with the NNPDF3.0NLO PDF set and the h_{damp} parameter set to $1.5m_t$. The events are interfaced with PYTHIA 8.230 using the A14 tune and the NNPDF2.3LO PDF set.

Single-top tW associated production is modeled using the POWHEGBOX 2 generator at NLO in QCD using the five-flavor scheme with the NNPDF3.0NLO PDF set. The diagram removal scheme was used to remove overlaps with the $t\bar{t}$ production samples. The s-channel single top $t(q)b$ production is modeled using the same setup, whereas for the t-channel production the four-flavor scheme is used instead of the five-flavor one. All events are interfaced with PYTHIA 8.230 for Run 2 and PYTHIA 8.308 for Run 3 using the A14 tune and the NNPDF2.3LO PDF set.

The tWZ events are generated at NLO using MADGRAPH5_AMC@NLO 2.3.3 for Run 2 and MADGRAPH5_AMC@NLO 3.5.1 for Run 3 with the NNPDF3.0NLO PDF set, and interfaced with PYTHIA 8.212 for Run 2 and PYTHIA 8.309 for Run 3 using the A14 tune and the NNPDF2.3LO PDF set.

The three top samples are generated using the MADGRAPH5_AMC@NLO at LO in QCD using the NNPDF3.0NLO PDF set and interfaced with PYTHIA 8 using the A14 tune in the five-flavor scheme.

tZ production is modeled using the MadGraph5_aMC@NLO generator at leading order and the NNPDF3.0NLO four-flavor scheme PDF set. Production of $t\bar{t}WW$, $t\bar{t}WZ$, $t\bar{t}HH$, $t\bar{t}WH$, and $t\bar{t}ZZ$ is modeled using MADGRAPH5_AMC@NLO generator at LO with the NNPDF3.0NLO PDF set. All these samples are interfaced with PYTHIA 8 for showering and hadronization using the A14 tune.

The V +jets samples are modeled using SHERPA 2.2.11 with the NNPDF3.0NNLO PDF set.

The VV +jets samples are modeled using SHERPA 2.2.14 and the NNPDF3.0NNLO PDF set. The triboson samples are simulated with SHERPA 2.2.2 for Run 2 and with SHERPA 2.2.14 for Run 3.

The WH and ZH processes are generated using the POWHEGBOX 2 generator with the NNPDF3.0AZNLO PDF set [113], and interfaced with PYTHIA 8.230 with the A14 tune and NNPDF2.3LO PDF set.

Table 6.1 summarizes the generators used for all produced MC samples.

6.4 Object selection

Reconstruction of the objects is described in Chapter 4, while this section details the specific selection criteria applied in the analysis.

Table 6.1: Summary of the simulated background samples used in the analysis.

| Process | Order | PDF Set | Generator and Showering/ Hadronization |
|--------------------|-----------|---------------|---|
| $t\bar{t}t\bar{t}$ | NLO | NNPDF3.0NLO | MADGRAPH5_AMC@NLO 3.5.3 + PYTHIA 8.230 (Run 2), PYTHIA 8.310 (Run 3) |
| $t\bar{t}t\bar{t}$ | NLO | NNPDF3.0NLO | MADGRAPH5_AMC@NLO 3.5.3 + HERWIG 7.04 (H7UE tune) |
| $t\bar{t}t\bar{t}$ | LO | NNPDF3.0NNLO | SHERPA 2.2.11 |
| $t\bar{t}W$ | NLO (QCD) | NNPDF3.0NNLO | SHERPA 2.2.10 (Run 2), 2.2.14 (Run 3) + PYTHIA 8.308 (A14 tune) |
| $t\bar{t}W$ | LO (QCD) | NNPDF3.0LO | MADGRAPH5_AMC@NLO 3.3.1 + PYTHIA 8.308 (A14 tune) |
| $t\bar{t}Z$ | NLO | NNPDF3.0NLO | MADGRAPH5_AMC@NLO 2.8.1 (Run 2), 3.4.2 (Run 3) + PYTHIA 8.244 (Run 2), PYTHIA 8.309 (Run 3) |
| $t\bar{t}H$ | NLO | NNPDF3.0NLO | POWHEGBOX 2 + PYTHIA 8.230 (Run 2), PYTHIA 8.308 (Run 3) |
| $t\bar{t}H$ | NLO | NNPDF3.0NLO | POWHEGBOX 2 + HERWIG 7.2.3 |
| $t\bar{t}$ | NLO | NNPDF3.0NLO | POWHEGBOX 2 + PYTHIA 8.230 |
| Single-top tW | NLO (QCD) | NNPDF3.0NLO | POWHEGBOX 2 + PYTHIA 8.230 (Run 2), PYTHIA 8.308 (Run 3) |
| tWZ | NLO | NNPDF3.0NLO | MADGRAPH5_AMC@NLO 2.3.3 (Run 2), 3.5.1 (Run 3) + PYTHIA 8.212 (Run 2), PYTHIA 8.309 (Run 3) |
| Three-top | LO | NNPDF3.0NLO | MADGRAPH5_AMC@NLO + PYTHIA 8 |
| $tZ, t\bar{t}VV$ | LO | NNPDF3.0NLO | MADGRAPH5_AMC@NLO + PYTHIA 8 |
| V +jets | LO | NNPDF3.0NNLO | SHERPA 2.2.11 |
| VV +jets | LO | NNPDF3.0NNLO | SHERPA 2.2.14 |
| Triboson | LO | NNPDF3.0NNLO | SHERPA 2.2.2 (Run 2), SHERPA 2.2.14 (Run 3) |
| WH, ZH | NLO | NNPDF3.0AZNLO | POWHEGBOX 2 + PYTHIA 8.230 |

Table 6.3: Overlap removal criteria

| Reject | Against | Criteria |
|----------|----------|--|
| Electron | Electron | shared track, $p_{T,1} < p_{T,2}$ |
| Muon | Electron | is Calo-Muon and shared ID track |
| Electron | Muon | shared ID track |
| Jet | Electron | $\Delta R < 0.2$ |
| Electron | Jet | $\Delta R < 0.4$ |
| Jet | Muon | fewer than 3 tracks in the jet and (ghost-associated or $\Delta R < 0.2$) |
| Muon | Jet | $\Delta R < \min(0.4, 0.04 + 10 \text{ GeV}/p_T(\mu))$ |

6.4.1 Charged leptons

Electrons are required to pass the tight identification and isolation requirements and have transverse momentum $p_T > 15 \text{ GeV}$ and pseudorapidity $|\eta| < 2.47$. The electrons within the transition region between the barrel and the endcap regions of the EM calorimeters are excluded ($1.37 < |\eta| < 1.52$). Additional requirements are set on dilepton channels with at least one electron. A Boosted-Decision-Tree-based classifier that uses the properties of the calorimeter energy cluster and of the track is applied to filter out the events with wrong electron charge assignment. This selection for Run 2 is performed using **ElectronChargeIDSelector** tool [169] (ECIDS) and it removes around 90% of electrons with a wrong charge assignment, while keeping 98% of electrons with correctly measured charge. For Run 3, this tool is unavailable, and other options are under investigation.

The muons, that satisfy the medium identification and tight isolation criteria, and have transverse momentum $p_T > 15 \text{ GeV}$ and pseudorapidity $|\eta| < 2.5$, are selected. For both electrons and muons, conditions for longitudinal (z_0) and transverse (d_0) impact parameters are also applied: $|z_0 \sin \theta| < 0.5 \text{ mm}$ and $|d_0|/\sigma(d_0) < 3$, where θ is the polar angle of the lepton track.

6.4.2 Jets

Jets are reconstructed using the anti- k_t algorithm with $R = 0.4$. The jets are required to have transverse momentum $p_T > 25 \text{ GeV}$ and pseudorapidity $|\eta| < 2.5$. Additional requirements are applied to jets with $p_T < 60 \text{ GeV}$ and $|\eta| < 2.4$ to reduce the effects of pileup. Jet flavor tagging is performed using the **GN2v01** algorithm with the 85% working point.

6.4.3 Missing transverse momentum

Missing transverse momentum is defined as the negative sum of transverse momenta of reconstructed objects in the event. Its reconstruction is defined in Chapter 4, and in this analysis the Tight working point is used.

6.4.4 Overlap removal

Overlap removal procedure is applied to ensure that the same calorimeter cluster or track is not used for reconstruction of multiple objects in the event. The overlap removal criteria are listed in Table 6.3. The distance metric used for the procedure is defined as $\Delta R = \sqrt{\Delta\phi^2 + \Delta y^2}$, where ϕ is the azimuthal angle and y is the rapidity.

6.5 Event selection

In order to ensure data quality and reduce background contribution in the analyzed events, event selection criteria are applied. As mentioned before, only the data gathered while all detector systems were fully operational is used. In addition, the events are required to have at least one reconstructed primary vertex with at least two tracks with $p_T > 500$ GeV associated with it. Events must pass at least one of the single lepton or dielectron triggers and have exactly two leptons with the same sign of electric charge or at least three leptons. The events are classified as either two (SS2L), three (3L) or four (4L) lepton events based on the number of leptons satisfying the lepton selection requirements introduced in the previous section. For the SS2L events the invariant mass of the two leptons with opposite sign of electric charge and same flavor must not coincide with the mass of the Z boson ($m_{ll} \notin [81, 101]$ GeV), and for the 3L and 4L events all pairs of opposite-charged same-flavor leptons must satisfy this requirement.

6.6 Resonance mass reconstruction

In order to obtain a model-independent interpretation of the results, a strategy similar to the one described in Chapter 5 can be used: a search for a localized excess in the invariant mass distribution can be performed in a signal-enriched region. However, as multiple neutrinos are present in the final state, some of them originating from the decay of the resonant particle, more advanced algorithms than previously described in Chapter 5 need to be developed to reconstruct the mass of the resonance. This section outlines the design and implementation of such an algorithm, tailored to address these challenges.

6.6.1 Assumptions and strategy

Before describing the reconstruction algorithm developed, it is necessary to discuss and motivate the assumptions that were made and to list the characteristics of the underlying processes that were taken into account.

Though contributions from the t -channel production of the BSM particle in final states with four top quarks and from production of final states with three top quarks are taken into account in the analysis, this method aims to detect the resonant s -channel production, as it is the dominant production mode involving resonant production and therefore allowing to observe a peak in the reconstructed mass distribution. A sample Feynman diagram with an SSML final state is shown in Figure 6.1. The top quark decays primarily to a W boson and a b quark. The W boson decays further to either a lepton-neutrino pair or to a pair of quarks. In a multi-lepton final state, two or more W bosons decay leptonically and since in the SSML final state the two leptons are required to have the same sign charge, one of the leptons must come from the resonant top quark decay (the top quarks originating from the BSM particle), while the other must originate from the decay of one of the spectator top quarks (the top quarks not originating from the BSM particle). This means that there is at least one neutrino among the decay products of the two resonant top quarks, which is not detected. In order to reconstruct the invariant mass, it is necessary to not only reconstruct the neutrino momenta, but also to identify the two resonant top quarks. Neutrino presence in an event can only be measured as MET. The longitudinal momentum in hadron-hadron collisions is not conserved due to the internal structure of the hadrons, which means that only individual partons interact with each other, which normally do not carry the whole hadron's momentum. Because of this, the longitudinal component of the missing energy is unknown. This makes it impossible to unambiguously reconstruct the neutrino momenta, however one can still limit the possible momenta using kinematic restrictions from the decays of the top quark and the W boson, as described in Section 6.6.2.

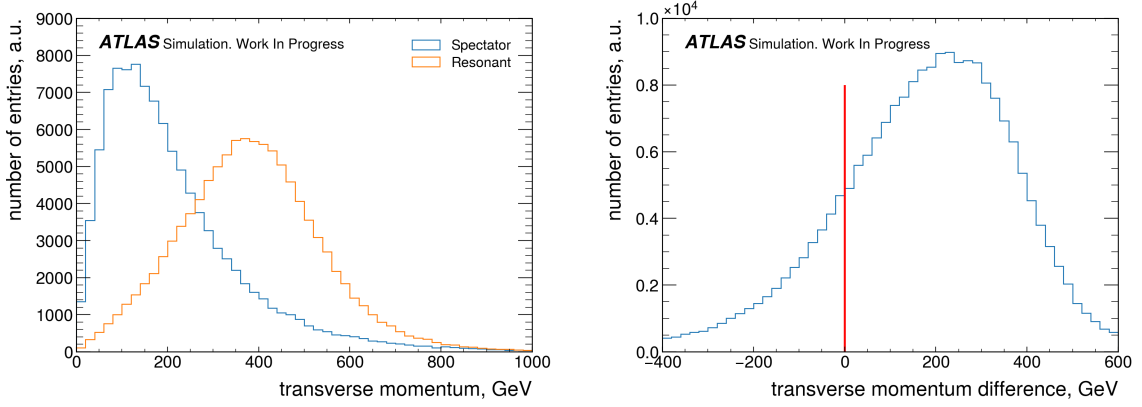


Figure 6.2: Comparison of transverse momenta of resonant and spectator top quarks. Left: the absolute values of the transverse momenta. Right: the difference between the momenta of the resonant and spectator top quarks in every event. For entries to the right of the red line the transverse momenta of the resonant top quarks are bigger than the transverse momenta of the spectator top quarks.

Certain assumptions about the objects in every event need to be made in order to make the resonance reconstruction possible:

1. All reconstructed objects in an event originate from decays of four top quarks. This is not true even for signal events as there might be pileup contamination. For background events the final state rarely contains four top quarks, however the same logic is applied with the expectation that the resulting mass distribution will differ from the signal resonant peak and therefore it will be possible to distinguish between signal and background.
2. The decays are approximated to be strictly on-shell, meaning that the masses of top quark and W boson are known and are always the same.
3. The resonant top quarks have higher transverse momentum than the spectator top quarks. While this is true in general, as shown in Figure 6.2 on the left, in some events this is not the case, as shown on the right. However, this assumption is still made in order to select the resonant top quarks during the reconstruction. The plots are obtained using a simulated signal sample.

Given all these assumptions, the mass reconstruction strategy is described in the following. For each event, all initially available objects (leptons, b -jets and regular, or non- b -tagged, jets) and reconstructed neutrinos are put into four groups, with each group containing the decay products of one top quark. These groups will be referred to as *top candidates*. Then the two top candidates, corresponding to resonant top quarks, are chosen. A combination of four top candidates with all objects being sorted is called a *final state candidate*. The available algorithm for reconstructing neutrino momenta cannot reconstruct momenta of more than two neutrinos, as extending it to more neutrinos introduces significant computational complexity and ambiguity. In order to obtain some value of reconstructed mass for events with more than two leptons, and therefore more than two produced neutrinos, the algorithm is still applied as if all MET is coming from two neutrinos.

The reconstruction is performed in multiple steps:

1. If the event contains more than four b -tagged jets, the ones with the lowest transverse momentum are not considered b -tagged, but regular jets instead. After this step, there are no more than four b -jets in every event.
2. All b -jets are assigned to separate top candidates. In the events with fewer than four b -jets some of the top candidates are not assigned a b -jet. Since these are the first objects to be assigned, the order in which this assignment is done is not significant.
3. For each event, all possible combinations of assigning leptons to top candidates are considered. For each combination, the following steps are performed:
 - If in a given combination there are fewer than two top candidates with both a b -jet and a lepton, the combination is discarded as the two neutrinos cannot be reconstructed.
 - If there are two or more top candidates with b -jets and leptons, all pairs of such top candidates are considered and double neutrino reconstruction (see Section 6.6.2) is applied for each pair. If neutrino reconstruction fails, this combination is discarded.
4. The reconstructed neutrinos are added to the top candidates. The top candidates with reconstructed neutrinos in them are labeled as *leptonic* top candidates and the top candidates without reconstructed neutrinos are labeled as *hadronic* top candidates.
5. After this, all possible assignments of regular jets to the hadronic top candidates are considered ensuring that all possible configurations are taken into account. Each such assignment completes a final state candidate.
6. For each final state candidate, a *loss function* is calculated.
7. The final state candidate with the smallest value of loss function is chosen.
8. Transverse momenta of all four top candidates are calculated. The top candidate with the highest transverse momentum is chosen among leptonic top candidates, the same is done for the hadronic top candidates. These two top candidates are considered to be coming from the decay of the BSM resonance, and the invariant mass of the objects assigned to these two top candidates is considered to be the mass of the resonance.

Note that all possible combinations of assigning leptons to top candidates are considered, and for each such combination with successfully reconstructed neutrinos, all possible combinations of assigning regular jets to the remaining top candidates are also considered.

The loss function is defined as follows:

$$L = \sum_{\text{top candidates}} \left(\text{mean}_{\text{objects}} \Delta R + 10^{-2} \times \left(|M_{\text{all}} - m_t|[\text{GeV}] + |M_{\text{all except } b} - m_W|[\text{GeV}] \right) \right), \quad (6.1)$$

where $\Delta R = \sqrt{\Delta\eta^2 + \Delta\phi^2}$ is the distance between two objects, and a mean of all such distances between objects assigned to a top candidate is taken, M_{all} is the invariant mass of all objects assigned to a top candidate, m_t is the mass of the top quark, $M_{\text{all except } b}$ is the invariant mass of all objects assigned to a top candidate except for the b -tagged jet, and m_W is the mass of the W boson.

This function is constructed under the assumption that objects, coming from the decay of the same top quark, are closer to each other in ΔR than the objects coming from the decays of different top quarks. As illustrated in Figure 6.3, this assumption holds true in most cases. The

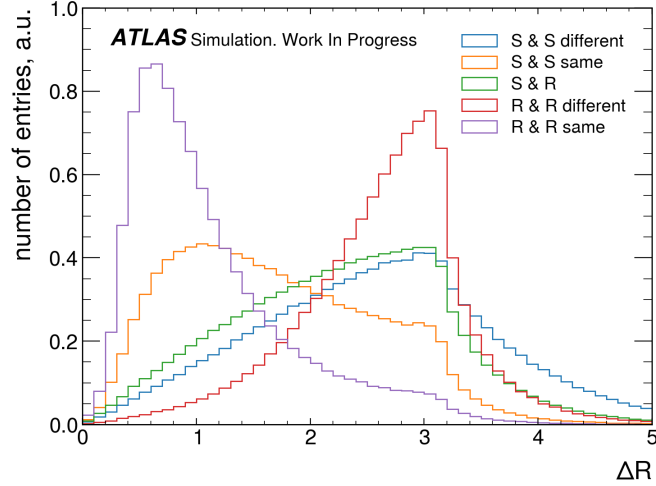


Figure 6.3: ΔR between objects coming from the same and different top quark decays. In the legend, the spectator top quarks are denoted with "S" and resonant top quarks – with "R". The histograms with "different" in the label include ΔR between the objects, coming from the decays of different top quarks, while the histograms with "same" in the label include ΔR between the objects, coming from the decay of the same top quark.

difference is more pronounced for the objects, coming from the resonant top quarks, however it can also be clearly seen for the spectator top quark decay products. Additionally, the invariant mass of all objects assigned to one top candidate should be close to the mass of the top quark, and the invariant mass of all objects coming from the decay of the W boson (all objects assigned to a top candidate except for the b -quark) should be close to the mass of the W boson. Multiplication by 10^{-2} is done in order to make all terms in the loss function of the same order of magnitude, so that they all contribute equally. In particular, for the wrongly formed top candidates the first term in the loss function would be of the same order of magnitude as the other two, resulting in equally-sized penalty for large ΔR and the large discrepancy in invariant masses.

6.6.2 Neutrino momentum reconstruction

In this study, no distinction is made between neutrino and antineutrino, and they both are referred to as a *neutrino*. The algorithm, used for reconstructing the neutrino momenta, is based on solving the kinematic equations for the decays of the b quark and the W boson, combined with constraints from the missing transverse momentum [170]. The algorithm was taken directly from the paper with some additions to ensure its robustness and to obtain the reconstructed neutrino momenta in as many events as possible. To explain where these additions come from it is necessary to outline the reconstruction steps.

This algorithm relies heavily on geometrical shapes, such as ellipsoids and ellipses, and it operates in several coordinate systems, which share the origin point. In each coordinate system, the momenta of the objects are represented by a radius-vector. So, *momentum lies on a curve* means that the end of the radius-vector lies on the curve, and in other words the components of the momentum satisfy the equation of the curve.

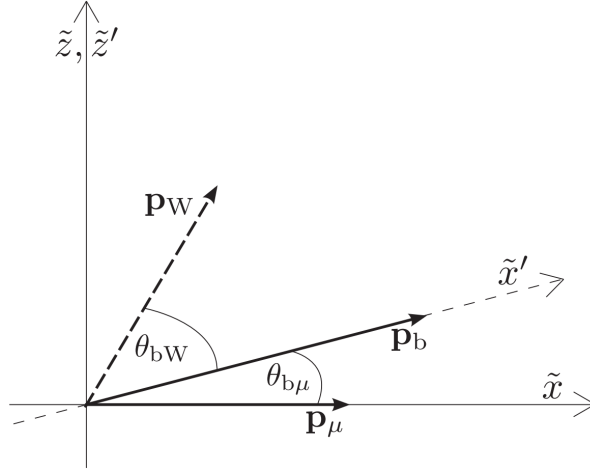


Figure 6.4: Coordinate systems used for neutrino momentum reconstruction [170]. Here, without loss of generality, a lepton is considered to be a muon. The momenta of the lepton, b -quark and the W boson are shown, and the angles between them are defined. Coordinate systems $\tilde{F}'(\tilde{x}', \tilde{y}', \tilde{z}')$ and $\tilde{F}(\tilde{x}, \tilde{y}, \tilde{z})$ share the z -axis with the laboratory coordinate system.

The general idea

The algorithm for neutrino momenta reconstruction receives as input four four-vectors: two corresponding to the four-momenta of leptons, and the other two to the four-momenta of the b -quarks (or b -jets), as well as the two components of the MET. First, each pair of a lepton and a b -quark is considered separately from the other pair, and the kinematic equations for the decays of the top quark and the W boson are solved together. The equation for energy and momentum conservation in the decay of a top quark to a W boson and a b -quark reads

$$m_t^2 = E_t^2 - \mathbf{p}_t^2 = (E_b + E_W)^2 - (\mathbf{p}_b + \mathbf{p}_W)^2 = m_b^2 + m_W^2 + 2E_b E_W - 2p_b p_W \cos \theta_{bW}, \quad (6.2)$$

where E and m are energy and mass of a particle, \mathbf{p} is the vector and p is the absolute value of the momentum, and θ_{bW} is the angle between the momenta of the b -quark and the W boson. Defining \tilde{x}'_0 as

$$\tilde{x}'_0 \equiv -\frac{1}{2E_b}(m_t^2 - m_W^2 - m_b^2), \quad (6.3)$$

it follows that the momentum of the W boson $\mathbf{p}_W = (\tilde{x}', \tilde{y}', \tilde{z}')$ in the coordinate system $\tilde{F}'(\tilde{x}', \tilde{y}', \tilde{z}')$, where the \tilde{x}' axis direction coincides with the direction of the momentum of the b -quark, as shown in Figure 6.4, is constrained to the surface

$$\left(\frac{\tilde{x}'}{\gamma_b}\right)^2 + \tilde{y}'^2 + \tilde{z}'^2 + 2\beta_b \tilde{x}'_0 \tilde{x}' + (m_W^2 - \tilde{x}'_0^2) = 0, \quad (6.4)$$

where $\beta_b = p_b/E_b$ is the relativistic speed of the b -quark, and $\gamma_b = (1 - \beta_b^2)^{-0.5}$ is its Lorentz factor. The equation defines an ellipsoid of revolution around the \tilde{x}' axis.

Similarly, for the decay of the W boson to a lepton and a neutrino, the equation constraining the momentum of the neutrino can be obtained from Equation 6.4 by substituting the top quark with the W boson, W boson with the neutrino, and the b -quark with the lepton:

$$\left(\frac{\tilde{x}}{\gamma_{\text{lepton}}}\right)^2 + \tilde{y}^2 + \tilde{z}^2 + 2\beta_{\text{lepton}} \tilde{x}_0 \tilde{x} + (m_\nu^2 - \tilde{x}_0^2) = 0, \quad (6.5)$$

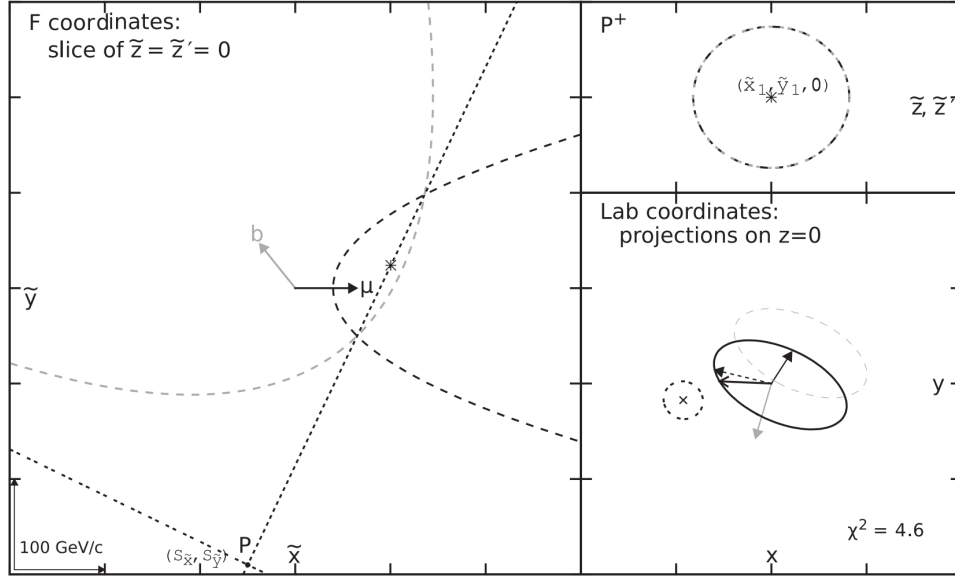


Figure 6.5: An example of reconstructing the restrictions on the momentum of the W boson. Momenta of the b -quark and the lepton are shown in the left panel with arrows, the dashed lines show projections of ellipsoids constraining the momentum of the W boson onto the transverse plane. The dotted line P shows the projection of the surface containing the intersection of the two ellipsoids. On the right, the upper panel shows the intersection of the ellipsoids in one of the planes of P , and the lower panel shows the momenta of the lepton (black), b -quark (gray) and neutrino (dashed), as well as the projection of the ellipse from the upper panel on the transverse plane (light gray dashes). The ellipse constraining the possible neutrino solutions, obtained from the one constraining the momentum of the W boson, is shown as a solid black line, and the \times and the dotted line represent the MET and its uncertainty [170].

where

$$\tilde{x}_0 \equiv -\frac{1}{2E_{\text{lepton}}}(m_W^2 - m_{\text{lepton}}^2 - m_\nu^2), \quad (6.6)$$

$\beta_{\text{lepton}} = p_{\text{lepton}}/E_{\text{lepton}}$ is the relativistic speed of the lepton, and $\gamma_{\text{lepton}} = (1 - \beta_{\text{lepton}}^2)^{-0.5}$ is its Lorentz factor. The components of the neutrino momentum are given in the coordinate system, where the \tilde{x} axis is directed along the lepton momentum, and the equation defines an ellipsoid of revolution around this axis. In order to derive the constraints for the momentum of the W boson from the constraints on the momentum of the neutrino, one can use the relation between the three momenta

$$\mathbf{p}_\nu = \mathbf{p}_W - \mathbf{p}_{\text{lepton}}. \quad (6.7)$$

Figure 6.5 shows projections of both ellipsoids restricting the momentum of the W boson onto the plane $\tilde{z} = 0$.

Given that the restrictions applied by the decay kinematics are compatible with each other and with the parameters of the objects, the kinematically possible momenta of the W boson are constrained by the intersection of the two ellipsoids, an ellipse. It follows from Equation 6.7 that the conditions for the momentum of the W boson can be interpreted unambiguously as conditions for the momentum of the neutrino and therefore that momentum is constrained to an ellipse as well. The same procedure can be done for the second lepton and b -quark pair,

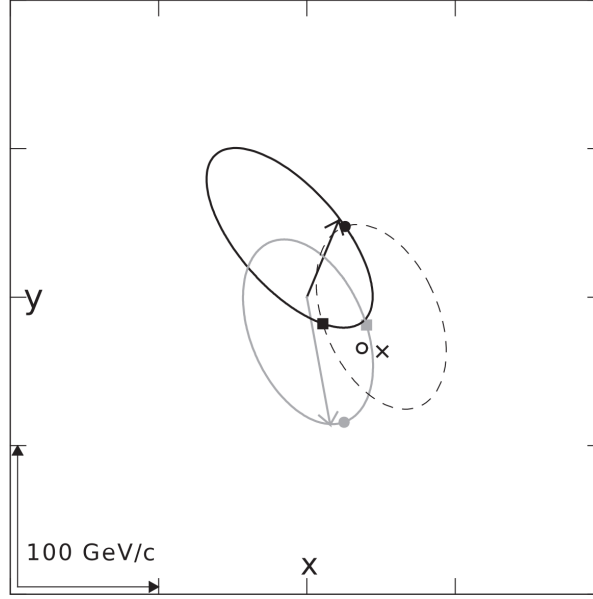


Figure 6.6: An example of ellipses used to constrain neutrino transverse momenta. The black arrow shows the momentum of the first neutrino, the gray arrow shows the momentum of the second neutrino. The black and gray ellipses depict the constraints on the transverse momenta of the two neutrinos, and the dashed ellipse depicts the constraints on the momentum of the first neutrino obtained from the constraints on the momentum of the second one. \times shows the reconstructed MET, and the \circ shows the sum of the neutrino transverse momenta. The ellipse construction is done under assumption that they are equal. In this example, the ellipses have two intersection points, and therefore there are two possible solutions. [170]

thus creating a similar ellipse for the second neutrino. Here, specifics of transitions between the coordinate systems are omitted, as the shapes do not change with these transitions. After this, the ellipses can be projected onto the transverse plane, where the neutrino momenta are further constrained by the missing transverse energy: the sum of the two neutrino transverse momenta must be equal to the MET. The transverse momentum of one of the neutrinos can be expressed in terms of the MET and the transverse momentum of the other neutrino:

$$\begin{pmatrix} p_x^{(\nu_2)} \\ p_y^{(\nu_2)} \end{pmatrix} = \begin{pmatrix} E_{T,x}^{\text{miss}} - p_x^{(\nu_1)} \\ E_{T,y}^{\text{miss}} - p_y^{(\nu_1)} \end{pmatrix}. \quad (6.8)$$

Thus, two ellipses constrain the transverse momentum of the first neutrino. The first ellipse is obtained using the decay equations of the first pair of top quark and W boson, and the second ellipse is obtained for the second pair, where the transverse momentum for the second neutrino is substituted using Equation 6.8. These ellipses are shown in Figure 6.6.

As the transverse momentum of the neutrino must satisfy both conditions, it should lie on both constructed ellipses simultaneously, and therefore the points of the ellipse intersection define the possible solutions for the neutrino transverse momentum. The three-dimensional momentum of the neutrino is obtained from the chosen transverse momentum by finding the corresponding points on the three-dimensional ellipse using its projection onto the transverse plane. Since the transverse momentum of the second neutrino is unambiguously determined by that of the first one, and there can be 0, 2 or 4 points of intersection between two ellipses, this results in 0, 2,

or 4 possible solutions for the neutrino transverse momenta. The algorithm does not provide a way to choose between multiple solutions, as no additional constraints or information are available to determine the most accurate one. For this analysis, the previously introduced in 6.1 loss function was used to determine the best solution. In this application there are only two top candidates, entering the calculation of the function, the ones with the two reconstructed neutrinos.

Modifications to the algorithm

In addition to the four vectors of the objects and the missing transverse momentum value, the algorithm also uses the masses of the top quark and the W boson. Possible solutions for neutrino momenta exist only when the kinematic equations are compatible with each other, in other words, when intersecting ellipses can be constructed. Even in the case where truth particles from the MC generation are used and the missing transverse momentum is calculated using the true momenta of the neutrinos, the ellipses, created by the algorithm, do not always intersect. This is explained by the fact that both top quark and W boson have decay widths, and therefore the invariant mass of the decay products varies, and different masses of the top quark and the W boson should be used in the kinematic equations. In the case, when the invariant masses constructed from the truth decay products of the top quarks and the W bosons are used in the reconstruction, the solution is found every time. This highlights the sensitivity of the reconstruction to precise mass values and proves that the imprecise masses of the top quark and the W boson are the primary cause of failure of the neutrino reconstruction when using truth information.

When the algorithm is applied to the real experimental data, reconstructing the precise masses of the top quark and W boson becomes impossible, and in addition to this, measurement and reconstruction affect the four-momenta of the particles and jets, which can also lead to incompatibility of the kinematic restrictions.

As suggested by the developers of the algorithm, in the case when the ellipses exist, but do not intersect, the points of closest approach are used to find an estimate of the solution. In our implementation, the middle of the line, connecting the points of the closest approach, is taken as a solution in this case. This also ensures permutation invariance of the solution since the middle of the line does not depend on the ordering of the ellipses. Figure 6.7 shows an example of such reconstruction. The blue ellipse restricts the momentum of the first neutrino using the decay kinematics of the first top quark and W boson, and the red ellipse restricts that momentum based on the decay kinematics of the second top quark and W boson, as well as on the missing transverse momentum.

There are cases, in which one of the ellipses does not exist. This occurs when the kinematic conditions from the decays of the W boson and the top quark are incompatible with each other. This incompatibility results in a necessity to extract a square root of a negative value. In this case, in order to extract some solution for the neutrino momentum, this negative value is substituted with 0, which effectively shrinks the ellipse to a single point. The precise calculations do not play a significant role, and the important aspect is that the parameter depends on the kinematic properties and masses of the particles. One interpretation of this approach is that the masses of the top quark and the W boson are changed as minimally as possible in order to make the kinematic equations compatible with each other. This is a simplification, as the change only occurs in the calculation of this one parameter and does not affect the other derivations, but this interpretation allows to understand the process better. The proper parameter change is not performed as it would require significant computational power to determine the suitable masses. After this is done and the nonexistent ellipse is substituted with a point, the middle of the line,

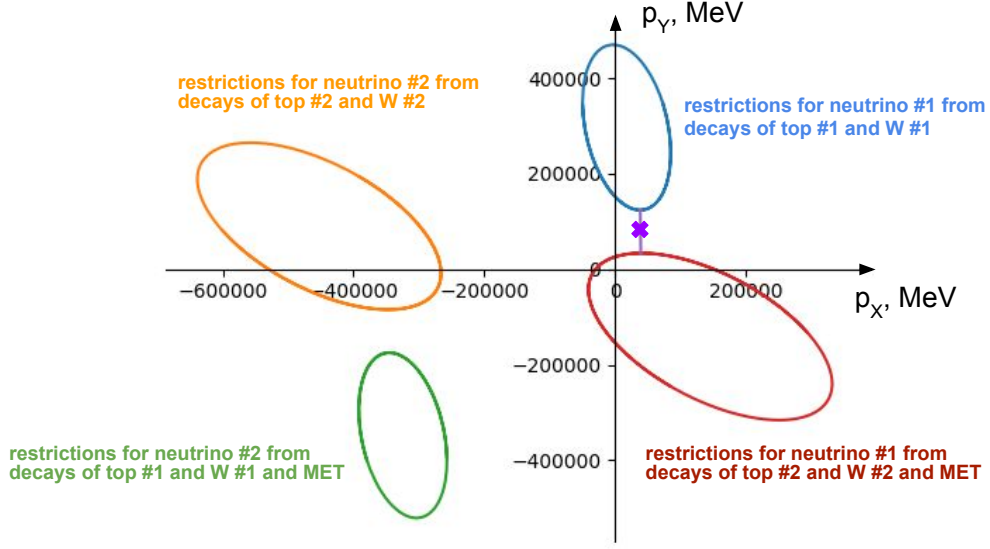


Figure 6.7: An example of ellipses restricting the transverse momenta of the two neutrinos in the transverse plane. The blue ellipse restricts the transverse momentum of the first neutrino and obtained from decay kinematics of the first top quark and W boson, the orange ellipse restricts the transverse momentum of the second neutrino using the decay kinematics of the second top quark and W boson, and the red and green ellipses are obtained from the blue and the orange ones by expressing the transverse momenta of the neutrino using the MET and the transverse momentum of the other neutrino. The purple line connects the points of closest approach on the ellipses restricting the transverse momentum of the first neutrino, and the purple cross shows the middle point that is taken as an estimation of the transverse momentum of the first neutrino.

connecting this point to the closest point on the existing ellipse, is used to find the solution for the neutrino with an existing ellipse. The transverse momentum of the other neutrino can be found by subtracting the transverse momentum of the first neutrino from the MET. However, as the kinematic equations for the second neutrino are incompatible with each other, no restrictions on the longitudinal momentum component can be applied. That component is then arbitrarily assigned the same value as the longitudinal component of the first neutrino momentum.

This solution cannot be extended to the cases, where both ellipses do not exist, and in such cases no neutrino momenta are reconstructed.

The second modification to the code, published in the paper, was necessary because the algorithm sometimes shows unstable behavior in the cases with non-intersecting ellipses. Not only is a non-existing intersection found sometimes, but the result is also not permutation invariant (it depends on the order of the four-momenta passed as the input to the algorithm), which creates instabilities in the obtained results. To avoid this problem, a check of whether an intersection exists is performed before the search for intersection points. This addition resulted in permutation invariance of the algorithm for every case, significantly improving the robustness of neutrino momentum solutions.

6.6.3 Studies with various degrees of truth information

The effect of different steps of resonance reconstruction algorithm on the resolution is investigated by varying the degree of truth information provided to it. There are two major potential sources of error: forming the top candidates and reconstructing the neutrino momenta. To study the impact of the first source, three different ways of grouping the objects were studied, including:

- Leptonic and hadronic top candidates are formed using truth information,
- Hadronic top candidates are formed using truth information, but leptonic top candidates are formed using the loss function from Equation 6.1,
- Leptonic and hadronic top candidates are formed using the loss function from Equation 6.1.

In the final states with more than two leptons present the neutrino reconstruction algorithm cannot by design provide an accurate result, as it assumes that all the MET is coming from only two neutrinos. Therefore, for this study only the events with exactly two leptons with same sign of electric charge were selected to isolate the effects caused by the reconstruction itself. For each of the group formation methods described above, three ways of obtaining the neutrino momenta were investigated:

- Using truth neutrino momenta,
- Reconstructing neutrino momenta and choosing the result closest in $\Delta R = \sqrt{\Delta\eta^2 + \Delta\phi^2}$ to the truth neutrino momenta,
- Reconstructing neutrino momenta and choosing the result using the loss function from Equation 6.1.

Considering all these possibilities, there are nine different ways to reconstruct the final state by using varying amounts of truth information, with case 1 being the one using only truth information and case 9 using no truth information. The cases are numbered sequentially, with higher case numbers indicating less reliance on truth information. Additionally, one more case (case 0) was considered where all top candidates are formed using truth information, truth neutrino momenta are used, but instead of defining the top candidates coming from the resonance

Table 6.4: The studied cases with varying degrees of truth information used for resonance reconstruction.

| | Top candidates | | Neutrino momenta | | Resonant top quark selection |
|---|----------------|---------------|------------------|---------------|---------------------------------|
| | hadronic | leptonic | values | selection | |
| 0 | truth | truth | truth | truth | truth |
| 1 | truth | truth | truth | truth | highest- p_T |
| 2 | truth | truth | reconstructed | truth | highest- p_T |
| 3 | truth | truth | reconstructed | loss function | highest- p_T |
| 4 | truth | loss function | truth | truth | highest- p_T |
| 5 | truth | loss function | reconstructed | truth | highest- p_T |
| 6 | truth | loss function | reconstructed | loss function | highest- p_T |
| 7 | loss function | loss function | truth | truth | highest- p_T |
| 8 | loss function | loss function | reconstructed | truth | highest- p_T |
| 9 | loss function | loss function | reconstructed | loss function | highest- p_T |

using p_T , truth information is used. The summary of all the studied variants is presented in Table 6.4.

Three different sets of objects were used for reconstruction:

- **‘Truth particle’** – all objects are truth particles (stable particles defined by the MC generator), the MET is obtained from the sum of neutrino four-momenta.
- **‘Truth jet’** – leptons and neutrinos are truth particles, the other objects are *truth jets* (jets reconstructed using the anti- k_T reconstruction algorithm using truth particles as input for reconstruction), the MET is obtained from the sum of neutrino four momenta.
- **‘Jet’** – leptons and neutrinos are truth particles, the jets are reconstructed from the detector response, the detector-measured MET is used.

The aim of this study is determining which part of the reconstruction process affects the resolution the most. Figure 6.8 shows the reconstructed mass for different reconstruction strategies for the sample of H/A events with the resonance mass of 1 TeV and $\tan\beta = 1$ with only s-channel four top quark production. Figure 6.8 (a) showcases the effect of neutrino momenta reconstruction, Figure 6.8 (b) showcases the effect of top candidate formation, and Figure 6.8 (c) showcases the effect of using different sets of objects for reconstruction. On the plots in this section only the events, in which it was possible to reconstruct the resonance mass, are shown. In the cases, when the neutrino momentum reconstruction fails, the event is not included in the histograms.

Clearly the resolution degrades as less truth information is used. However, it is not possible to single out one source. It is also visible that moving from truth parton level to detector level negatively affects the obtained resolution. The peak near the mass of the top quark for case 0, where only truth information is used are caused by the presence of *merged jets*. *Merged jets* are jets, which are constructed using products of more than one top quark decay. Such jets are matched to more than one top on truth level, but during reconstruction they are assigned to only one of the four groups of objects, which causes other groups to have too few objects and therefore to have a smaller contribution to the reconstructed resonant particle’s mass. This problem disappears as soon as the resonant top quarks are chosen using transverse momenta and not truth information. It is clear that using truth jets and jets increases the width of the distribution, however the peak at the true signal mass of 1000 GeV is still clearly visible.

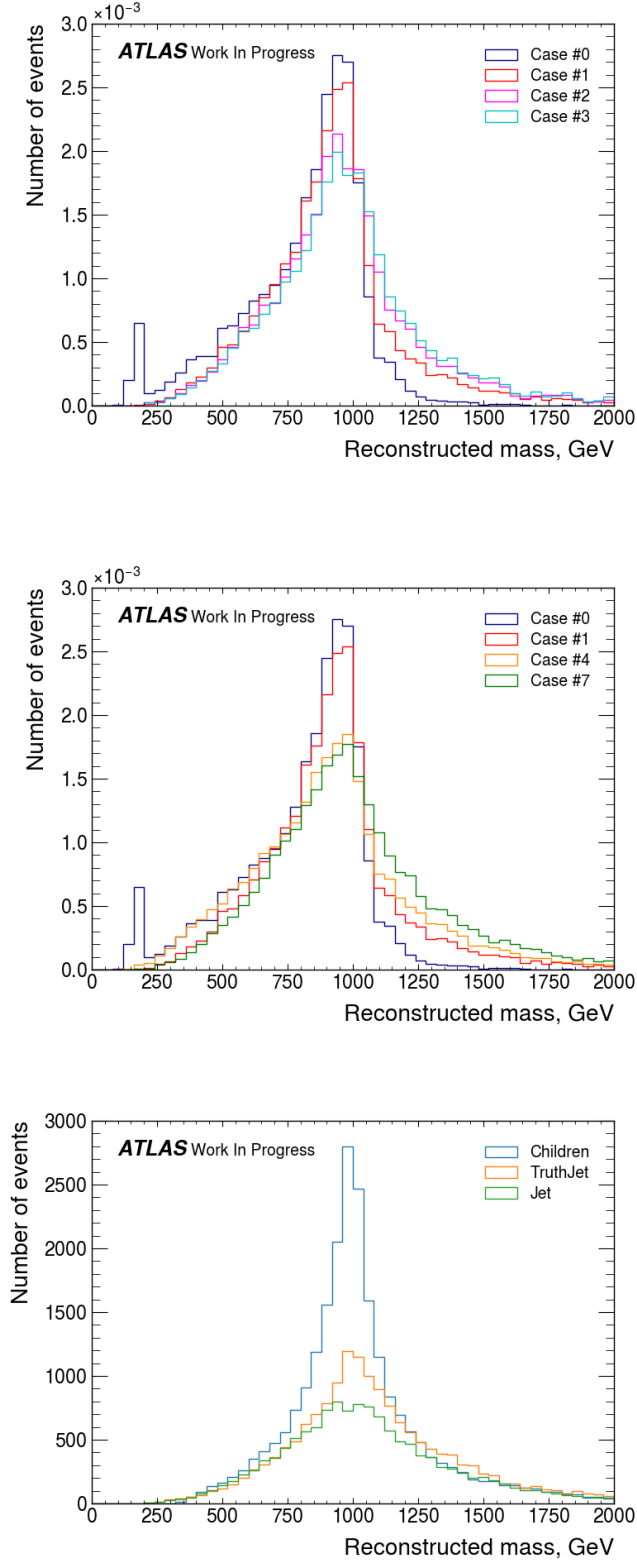


Figure 6.8: The reconstructed resonance mass for the signal with a mass of 1 TeV. Plot (a) shows the effects of the neutrino reconstruction method, plot (b) shows the effects of the formation of the top candidates and plot (c) shows the effects of the choice of objects using for the reconstruction.

(a) Reconstructed mass using different neutrino momenta. The ‘Jet’ set of objects is used for the reconstruction. All top candidates are formed according to truth information. Truth neutrino momenta are used in cases 0 and 1, reconstructed neutrino momenta selected to closely match the truth neutrino momenta are used in case 2, and reconstructed neutrino momenta selected using the loss function are used in case 3. The selection of the resonant top quarks is done using truth information for case 0 and using the p_T requirements for the other cases.

(b) Reconstructed mass using different strategies of forming the top candidates. The ‘Jet’ set of objects is used for the reconstruction. Truth neutrino momenta are used in all cases. Truth information is used for top candidate formation in cases 0 and 1. In case 4, the leptonic top candidates are formed using the loss function, but hadronic top candidates are formed using truth information. In case 7, all top candidates are formed using the loss function. The selection of the resonant top candidates is done using truth information for case 0 and using the p_T requirements for the other cases.

(c) Reconstructed mass for the three sets of objects for the mass reconstruction strategy 9: neutrino momenta are reconstructed, all top candidates are formed using the loss function, and the resonant top candidates are selected using the p_T requirements.

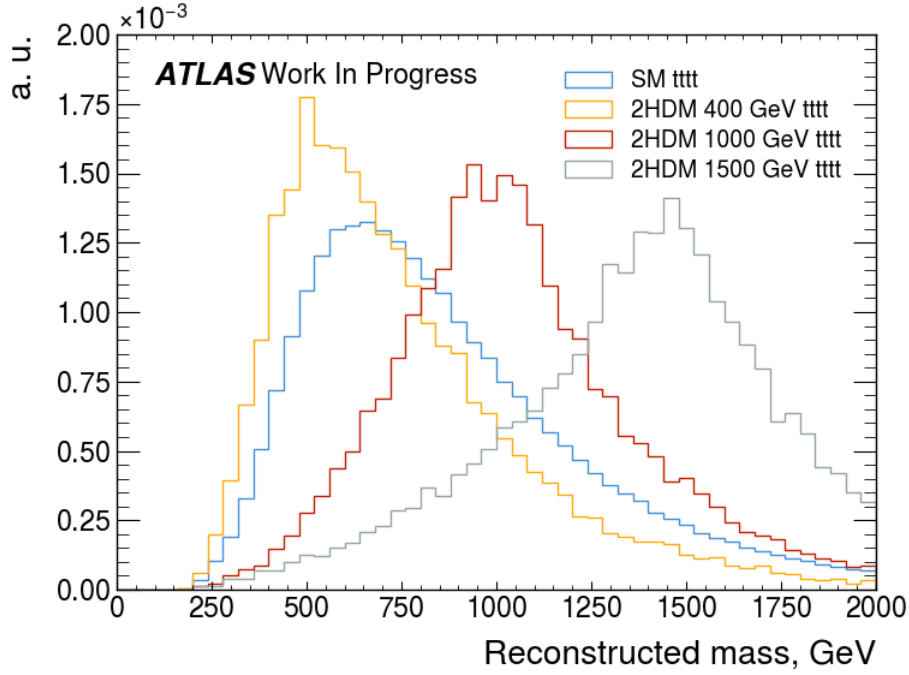


Figure 6.9: Reconstructed resonance masses for four samples, Standard Model and 400 GeV, 1 TeV and 1.5 TeV 2HDM signals, for case with no truth information used and using reconstructed jets. The histograms are normalized to the same area.

Apart from the sample with mass of the H/A particles of 1 TeV, samples with this mass being 400 GeV and 1.5 TeV were processed, as well as a sample containing Standard Model four top quark production, which does not have any resonance. In Figure 6.9 the case with no truth information used is presented. For this plot, the ‘Jet’ set of objects was used for all samples. The higher mass signals have clear peaks, which can be distinguished from the Standard Model background, while the 400 GeV signal is harder to distinguish. The peak in the distribution for the Standard Model events is present due to threshold events of the event and object selection and is not caused by resonant production of the four-top-quark final state.

For all histograms their full widths at half maximum (FWHM) were taken as an estimate for the resonance mass resolution. In Figure 6.10, the dependence of the FWHM on the case number is presented. The mass reconstruction was performed for the four generated samples, mentioned before, using the ‘Jet’ set of objects. The value of FWHM shows the approximate resolution that the algorithm can provide, and the lines show the change of that resolution depending on the amount of truth information used for the reconstruction. It is clear that the FWHM increases gradually and there is no single step, responsible for a big loss of resolution.

This study was performed with events that have exactly two leptons on the truth level, however no such selection can be applied to the experimental data. In particular, presence of leptonically-decaying tau leptons cannot be identified. In these events, as well as in the events with three or more leptons, more than two neutrinos contribute to the MET, which degrades the resolution of the mass reconstruction algorithm. Figure 6.11 shows the distributions of the reconstructed mass for the 2HDM H/A sample with resonance mass of 1 TeV and $\tan\beta = 1$ for the ‘Jet’ set of objects and reconstruction strategy 9 with no truth information used. The mass was reconstructed for three sets of events: one with exactly two leptons (electrons or muons) on truth level and no tau leptons, another with exactly two leptons on truth level and no conditions

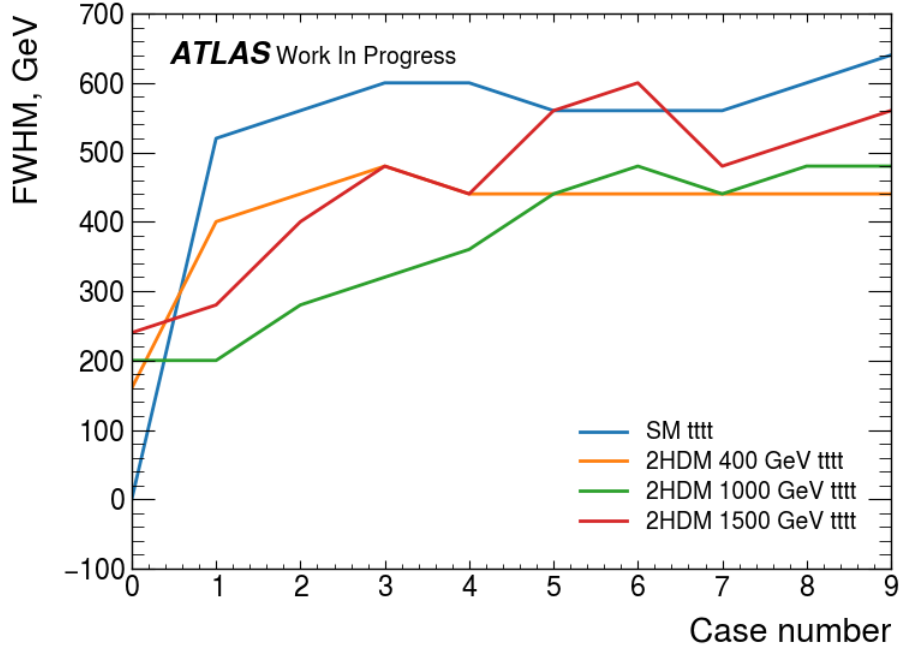


Figure 6.10: Dependence of the reconstructed resonance mass resolution on the case number for the four samples. Reconstructed jets are used for the mass reconstruction.

on the presence of tau leptons, and one set of events with at least two leptons at truth level and no conditions on the presence of tau leptons. Clearly the resolution degrades as the event selection conditions loosen, however loosening the selection increases the statistics of available data.

6.7 Background estimation

Several processes can mimic the target signal final state, and depending on whether real same-sign-multi-lepton final state is produced, in which case the background is irreducible, or whether the final state is only reconstructed as such, in which case the background contribution can be reduced. The main background contributions in the signal region come from SM $t\bar{t}t\bar{t}$ and $t\bar{t}V$ processes. Due to known mismodeling of the $t\bar{t}W$ process, a data-driven method is used to estimate this background, while estimation of the SM $t\bar{t}t\bar{t}$, $t\bar{t}H$ and $t\bar{t}Z$ background contributions are based on the simulation prediction. Such estimation of the $t\bar{t}W$ background was introduced in the Run 2 SM $t\bar{t}t\bar{t}$ analysis [31], where the number of events is parameterized based on the number of jets, and the method provides a better description of the showering and allows to avoid introducing significant systematic uncertainties due to mismodeling. Smaller contributions originate from events with non-prompt (not coming from the primary interaction vertex) or fake leptons, this background is estimated using the simulated prediction with normalization constrained using a template fit in dedicated control regions. Additionally, events with misidentified sign of the lepton electric charge contribute to background in the signal region. Their contribution for Run 2 can be estimated using the ECIDS tool mentioned earlier, and currently strategies for Run 3 and potential improvements that can be obtained for Run 2 are under investigation.

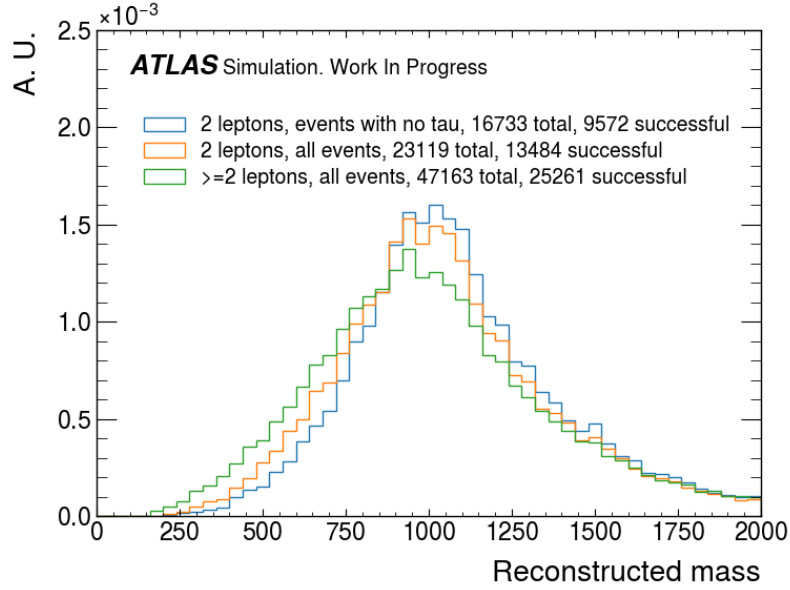


Figure 6.11: Reconstructed mass for the 2HDM H/A sample with resonance mass of 1 TeV and $\tan \beta = 1$. The distributions are shown for events with exactly two leptons (electrons or muons) and no tau leptons on truth level, for events with exactly two leptons and no requirements on tau lepton absence, and for events with at least two leptons on truth level and no other event selection criteria applied. The reconstruction of the mass is performed without using any truth information. All histograms are normalized to the same area, the legend contains information about the total number of events that pass the applied selection and about the number of events with successfully reconstructed resonance mass.

6.8 Systematic uncertainties

6.8.1 Experimental uncertainties

Experimental uncertainties are detector-related and reflect the uncertainties of measuring data.

- **Luminosity.** The uncertainty on the integrated luminosity of Run 2 is 0.83%, and the uncertainty on the integrated luminosity for the data-taking period of 2022–2023 of Run 3 is 2%.
- **Pileup.** The distribution of pileup in the simulated samples is reweighted to match the one observed in data. An uncertainty is applied to that reweighting.
- **Leptons.** Lepton systematic uncertainties arise from several factors, including trigger efficiency, lepton reconstruction, identification and isolation, and the scale and resolution of lepton energy and momentum scale. In total, 8 nuisance parameters are considered for electrons and 13 for muons.
- **Jets.** Uncertainties on jets originate from the calibration of the jet energy scale (JES) and resolution (JER), as well as scale factors applied to correct the differences between the data and the simulated samples. The JES uncertainty is implemented as a set of 32 nuisance parameters, the JER uncertainty is implemented as a set of 28 nuisance parameters, and the jet vertex tagging uncertainty is represented by one nuisance parameter obtained by varying the scale factor used to correct the jet vertex tagging efficiency within the measured uncertainty. The uncertainties on jet flavor tagging arise from the scale factors applied to simulated samples to correct the flavor tagging efficiencies to those seen in data. In total, 6 nuisance parameters are considered for this uncertainty.
- **Missing transverse momentum.** These uncertainties originate from a possible miscalibration of the soft-track component of the missing transverse momentum, and are modeled as three nuisance parameters.

6.8.2 Theory uncertainties

For signal ($t\bar{t}Z'$ and $t\bar{t}H/A$) and dominant irreducible background (SM $t\bar{t}t\bar{t}$, SM $t\bar{t}t$, $t\bar{t}W$, $t\bar{t}Z$, SM $t\bar{t}H$) samples, a so-called 7-point variation method is applied in order to estimate the uncertainty originating from missing higher-order corrections in the generated samples. This method involves generating samples with seven different pairs of renormalization and factorization scale values and taking the envelope of the variation of the samples.

For the $t\bar{t}H/A$ and $t\bar{t}Z'$ samples, the uncertainty on the choice of PDF is estimated as a flat uncertainty of 1%.

For the SM $t\bar{t}t\bar{t}$ sample, a flat uncertainty of 1% on the choice of the PDF is applied, alternative samples are used to estimate the uncertainties originating from the choice of the generator and the showering and hadronization algorithm, and an uncertainty of 20% is applied for the cross-section [171].

For the SM $t\bar{t}t$ sample, the uncertainty on the choice of the PDF is estimated using an envelope of differences between the nominal and alternative PDF choices, a 30% uncertainty on the cross-section is applied [171]. Additionally, a 50% uncertainty on cross-section for events with at least four truth b -jets is applied in order to compensate for lack of theoretical predictions of the production of additional b -jets for this process. The uncertainty originating from the choice between the four- and five-flavor schemes is estimated using alternative generated samples.

For the $t\bar{t}W$ sample, the uncertainty on the choice of generator is estimated using an alternative sample, a 50% uncertainty on cross-section is applied for events with at least one b -jet that is not coming from a top quark decay, and an additional 50% cross-section uncertainty is applied for events with two or more b -jets that do not originate from the decay of a top quark.

For the $t\bar{t}Z$ sample, a 1% uncertainty on the PDF is applied, the generator choice uncertainty is estimated using an alternative sample, a 12% uncertainty on the cross-section is applied [172], and the events with additional b -jets are treated the same way as for $t\bar{t}W$ sample.

For the SM $t\bar{t}H$ sample a flat uncertainty of 1% is applied to account for PDF uncertainties, alternative samples are used to estimate the uncertainties related to choice of the generator and the parton and hadronization algorithm, a 10% uncertainty on the cross-section prediction is applied [172], and the event with additional b -jets are treated the same way as for the $t\bar{t}W$ sample.

For the tZ and tWH samples, an uncertainty of 30% is applied on the cross-section [173, 174].

For the VV sample, an uncertainty of 20%/50%/60% is applied for events with $\leq 3/4/\geq 5$ jets [175], and for events with at least one truth b -jet not from a top-quark decay an additional uncertainty of 50% is applied.

For the $t\bar{t}VV$, $VVVV$, and VH samples a conservative uncertainty of 50% is applied on the cross-section, and the events with additional b -jets are treated the same way as for the VV samples.

The uncertainty on electron charge misidentification is estimated separately in the conversion and the $t\bar{t}W$ control regions and treated as correlated across all regions.

The normalizations of the backgrounds coming from material and virtual photon conversion, as well as from heavy flavor decays, are free parameters in the fit, and uncertainties arise from the shape of the distributions. The uncertainty is obtained by comparing the data with simulation for every background process.

A normalization uncertainty of 100% is assigned for processes involving leptons that originate from light-meson decays or jets that are wrongly identified as leptons [176], and an uncertainty of 30% is assigned for other background, while the uncertainties on the shapes for these processes are negligibly small.

6.9 Analysis region definition

The phase space of the analysis is divided into signal, control and validation regions, each group of regions serving a particular purpose. The signal regions are designed to minimize background contribution, the control regions provide constraints on the background normalization and uncertainties in the profile likelihood fit, and the validation regions are used to check the validity of the modeling and background estimation.

6.9.1 Signal regions

Events in the signal regions have to contain at least 6 jets, and a requirement of $H_T > 500$ GeV is placed on the scalar sum of the transverse momenta of leptons and jets in the event. Using the number of leptons and the number of b -jets in an event, division of varying granularity can be achieved. *Baseline SR* is the loosest signal region, including events with any number of leptons and at least 2 b -jets. *SR $4b$* is the region that also includes events with any number of leptons, however at least 4 b -jets are required. This tighter selection ensures that the region is

more enriched in signal events than the baseline SR, however due to the more strict selection the region has much fewer events.

Other regions can be defined, with the name $SR\ XbYl$ meaning that the events from the baseline SR with X b -jets and Y leptons are selected.

6.9.2 Control regions

Four control regions are designed to constrain the $t\bar{t}W$ background. All events must have at least four jets. Requirements on H_T and the number of jets are made to ensure orthogonality to the signal region. The regions are defined as follows:

- **CR $t\bar{t}W^+$ +jets**: a positive sum of lepton electric charges, at least two b -tagged jets, at least one muon. Additional requirements: $|\eta(e)| < 1.5$; when $N_b = 2$: $H_T < 500$ GeV or $N_j < 6$; when $N_b \geq 3$: $H_T < 500$ GeV. Events with exactly two leptons, one of which is a muon, are selected for this region. As the leptons have the same sign of electric charge, they cannot both originate from the decays of the $t\bar{t}$ pair, and therefore one of them must originate from the decay of the W boson, which is why the charge of the W boson is estimated to be the same as the electric charges of the two leptons.
- **CR $t\bar{t}W^-$ +jets**: a negative sum of lepton electric charges, at least two b -tagged jets, at least one muon. Additional requirements: $|\eta(e)| < 1.5$; when $N_b = 2$: $H_T < 500$ GeV or $N_j < 6$; when $N_b \geq 3$: $H_T < 500$ GeV. The charge of the W boson is estimated in the same way as described for the previous control region.
- **CR 1b(+)**: a positive sum of lepton electric charges, exactly one b -tagged jet. Additional requirements: $H_T > 500$ GeV, the two leading leptons do not originate from photon conversion. Events with two or three leptons are selected for this region.
- **CR 1b(-)**: a negative sum of lepton electric charges, exactly one b -tagged jet. Additional requirements: $H_T > 500$ GeV, the two leading leptons do not originate from photon conversion. Events with two or three leptons are selected for this region.

The first two control regions are used to constrain the flavor composition of the $t\bar{t}W$ background, and the last two regions are used to determine the jet multiplicity spectrum. For all of these regions, the jet multiplicity value is the one that enters the fit.

For constraining the background coming from events with fake or non-prompt leptons, three control regions are designed. Each focuses on one of the sources of such leptons: virtual photon (γ^*), photon conversion in the detector material, and decays of heavy flavor quarks. The regions are defined as follows:

- **CR Low m_{γ^*}** includes events with a virtual photon leading to a creation of an electron-positron pair, of which only one lepton is reconstructed. These events are required to have two leptons, among which at least one is an electron, between 4 and 6 jets, at least one b -jet, and two same-sign leptons, at least one of which is an electron. The invariant mass of the system formed by the electron and the closest track at the conversion vertex should be below 0.1 GeV, at least one of the leptons must be a virtual photon conversion candidate, and no leptons should be material conversion candidates.
- **CR Mat. Conv.** includes events with single reconstructed non-prompt electron originating from photon conversion in the detector material. These events are required to have two leptons, among which at least one is an electron, between 4 and 6 jets, at least one b -jet, and two same-sign leptons, at least one of which is an electron. The invariant mass of the system formed by the electron and the closest track at the conversion vertex should be below 0.1 GeV, and at least one of the leptons must be a conversion candidate.

- **CR HF $e\mu$** region includes events with a single reconstructed non-prompt electron or muon from heavy flavor decay. The events should contain at least one jet, exactly one b -jet, and exactly three leptons. Two leading leptons should not be material conversion candidates. Additional requirements: $100 < H_T < 275$ GeV; $E_T^{\text{miss}} > 35$ GeV for events with two electrons, and $100 < H_T < 300$ GeV; $E_T^{\text{miss}} > 50$ GeV for events with two muons.

For the first two regions the value that is fitted is the event yield, while for the last two it is the transverse momentum of the third-leading lepton.

6.9.3 Validation regions

Validation regions are defined to verify the normalization and modeling of the $t\bar{t}Z$ and $t\bar{t}W$ backgrounds as follows:

- **VR $t\bar{t}Z$** includes events with three leptons, at least 4 jets, at least two b -jets, with the invariant mass of the opposite-sign-same-flavor leptons system around the mass of the Z boson ($m_{\text{OSSF}} \in [81, 101]$ GeV), and $|\eta(e)| < 1.5$.
- **VR $t\bar{t}W$ +jets-like** includes events with exactly two leptons, one of which is a muon, at least four jets, at least two b -jets. Additional requirements: when $N_b = 2$, $H_T < 500$ GeV or $N_j < 6$; when $N_b \geq 3$, $H_T < 500$ GeV.
- **VR 1b-like** includes events with at least four jets, exactly one b -jet, two or three leptons, with none of the leading two leptons originating from photon conversion, and $H_T > 500$ GeV.
- **VR SR-like** includes events with at least six jets, at least two b -jets, and $H_T > 500$ GeV.
- **VR 4j1b** and **VR 4j2b** include events with at least four jets and at least one (or two) b -jets.

6.10 Statistical analysis

The statistical analysis is based on the same principles as described in Chapter 5. Model-dependent interpretation is performed using a profile likelihood fit in the analysis regions, and a model-independent result can be obtained using the BUMPHUNTER tool for the reconstructed resonance mass distribution. The exact configuration of the fit and the exact way in which BUMPHUNTER will be applied are not yet finalized, and this section presents studies showing the results that can be obtained using the reconstructed resonance mass. The studies were performed for two signal samples: one modeled using the generic top-philic Z' model with the mass of the Z' boson of 1 TeV, the coupling strength $c_t = 3.0$ and the chirality parameter $\theta = \pi/4$, and for another sample modeled using the 2HDM including only the scalar boson H with the mass of 1 TeV and $\tan\beta = 1$ with the assumption that the alignment limit holds true. The samples available at the time of writing this thesis were used, and they include s-channel four-top-quark production, as well as production of three-top-quark final states for the Z' model. The 2HDM samples include only s- and t-channel four-top-quark production. For the studies of the model-dependent result, a statistics-only fit to Asimov data was performed. All studies were done using only generated samples without data-driven background estimation.

6.10.1 Model-dependent result

The statistical analysis for a model-dependent interpretation is based on a binned profile likelihood fit, and the definitions of the likelihood function and of the test statistic are the same

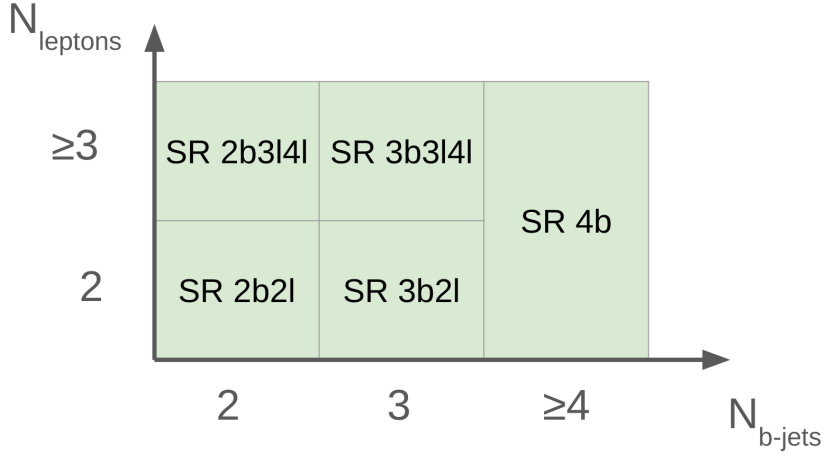


Figure 6.12: The division of the baseline signal region to obtain the signal regions used in the fit.

as previously defined in Chapter 5. Several analysis regions are used in the fit, and different variables are fitted in all of them.

It was determined during the previous $t\bar{t}H/A$ search that the H_T , which is the scalar sum of the transverse momenta of all objects in an event, is the kinematic variable with the highest separation power among the variables used in the analysis, and therefore in this section a fit using the reconstructed resonance mass is compared to the one obtained using the H_T variable.

The analysis regions that are used in the fit were introduced in section 6.9. Five signal regions in total enter the fit, they are all obtained from the baseline SR by splitting it depending on the number of b -jets and leptons in the event. A schematic depiction of these regions is shown in Figure 6.12.

Two fit configurations are evaluated, called *HT fit* and *mass fit*. The variables entering the fit in each region are summarized in Table 6.6. Statistics-only fits for the hypothesis of signal presence to background-only Asimov pseudo-data were performed at this stage in order to compare the two approaches and no data-driven background estimation was done. The Asimov pseudo-data sets are constructed by creating histograms with the bin content exactly the same as the number of expected background events, which leads to non-integer numbers of “data” events.

The comparison of expected limits that the two fit configurations can provide for a set of signal samples is presented in Table 6.7, and sample pre-fit distributions from the SR 4b are shown in Figure 6.13.

Figure 6.14 shows sample pre-fit background distributions in the control regions. More background categories are present on these plots than on the plots in Figure 6.13 to show the differences in event composition in the control regions.

The mass fit configuration performance is comparable to the performance of the HT fit, which shows that the reconstructed mass has a good discriminating power. Multivariate classifiers will be used in the analysis in order to achieve good signal and background separation, and the reconstructed mass could be added as one of the input variables in these classifiers.

6.10.2 Model-independent result

The most significant benefit that resonance reconstruction can provide is the possibility to obtain a model-independent result. The BUMPHUNTER tool, introduced previously in Chapter 5, can be

Table 6.6: Two studied fit configurations.

| Region | Fitted distribution | |
|------------------------|-------------------------------|--------------------|
| | HT fit | Mass fit |
| CR Mat. Conv. | Event yield | |
| CR Low m_{γ^*} | Event yield | |
| CR HF $e\mu$ | p_T of third-leading lepton | |
| CR $t\bar{t}W^+$ +jets | Jet multiplicity | |
| CR $t\bar{t}W^-$ +jets | Jet multiplicity | |
| CR $1b(+)$ | Jet multiplicity | |
| CR $1b(-)$ | Jet multiplicity | |
| SR 2b2l | H_T | reconstructed mass |
| SR 2b3l4l | | |
| SR 3b2l | | |
| SR 3b3l4l | | |
| SR 4b | | |

Table 6.7: Expected limits for the two signal models obtained with a statistics-only Asimov fit.

| Fit configuration Signal model | HT fit | Mass fit |
|--|------------------------|------------------------|
| 2HDM H $m_H = 1$ TeV alignment limit $\tan \beta = 1$ | $4.5^{+2.0}_{-1.4}$ fb | $4.9^{+2.2}_{-1.5}$ fb |
| Z' $m_{Z'} = 1$ TeV $c_t = 3.0$ $\theta = \pi/4$ | $6.8^{+3.0}_{-2.0}$ fb | $7.1^{+3.1}_{-2.1}$ fb |

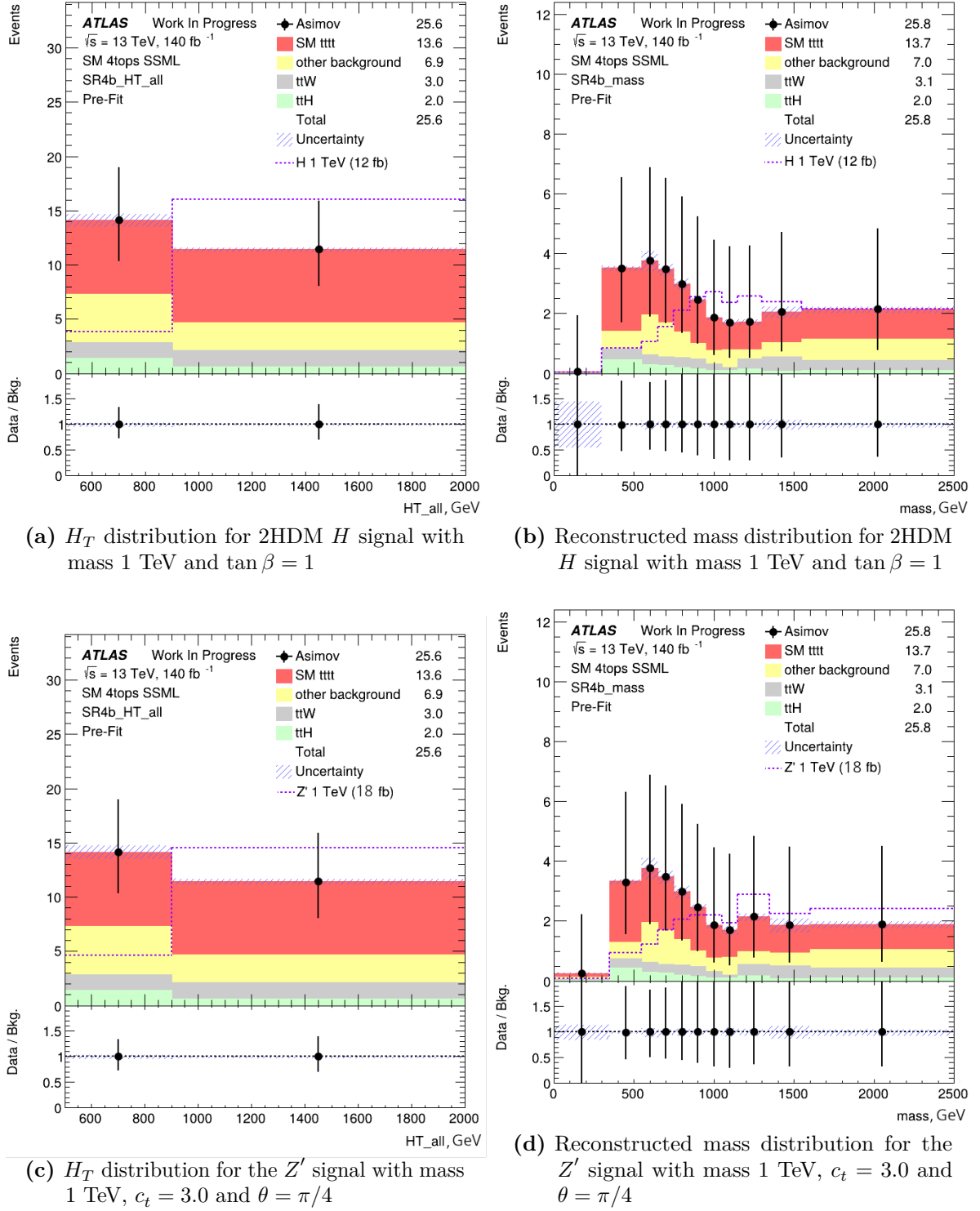


Figure 6.13: Pre-fit distributions for the Asimov fit of H_T and reconstructed mass in the SR 4b region for the two studied signal models. The distributions for the signals are shown with the dashed line and are scaled by an arbitrary value for better visibility.

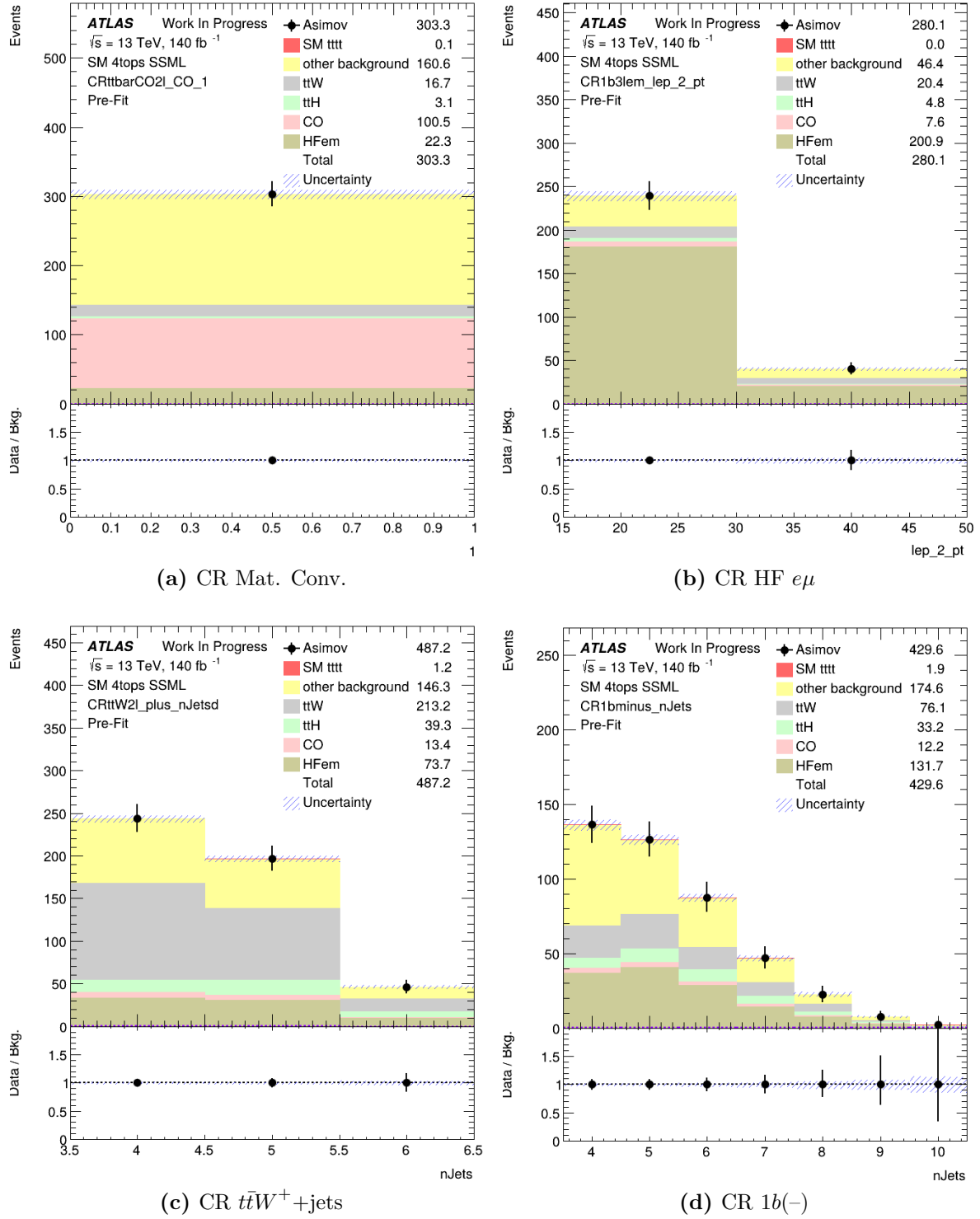


Figure 6.14: Pre-fit distributions of the fitted variables for background events in several control regions of the fit. The distributions are the same for both fit configurations and for both studied signal variants.

Table 6.8: Cross sections of reliably detectable signals of both types in both signal regions for the bump scans performed using the reconstructed mass and the H_T distributions.

| Signal model \ Distribution | Reconstructed mass | | H_T | |
|--|--------------------|-------|-------------|-------|
| | Baseline SR | SR 4b | Baseline SR | SR 4b |
| 2HDM H $m_H = 1$ TeV alignment limit $\tan \beta = 1$ | 20 fb | 12 fb | 19 fb | 13 fb |
| Z' $m_{Z'} = 1$ TeV $c_t = 3.0$ $\theta = \pi/4$ | 29 fb | 20 fb | 26 fb | 20 fb |

used to search for deviations between the data and the background distribution. This study was performed using the `pyBumpHunter` library [177]. This section summarizes the studies performed using the simulated events and aimed at determining if it would be possible to detect a signal if it is present in the experimental data. Two signal regions are investigated: the baseline SR and the SR 4b. The looser selection of the baseline SR ensures sufficient number of events, and therefore a lower statistical uncertainty than in the SR 4b. On the other hand, the stricter event selection of the SR 4b makes it more signal-enriched, and therefore the signal peak will be more prominent over the background distribution. As previously, the 2HDM H signal with a mass of 1 TeV and $\tan \beta = 1$ and the vector Z' signal with a mass of 1 TeV, $c_t = 3.0$ and $\theta = \pi/4$ are selected for the study. Figure 6.15 shows an example of search for deviations, or *bump scan*, for both signal models in both studied regions, and the tool successfully identifies the bump location at around 1 TeV. The *data* distributions were obtained by adding a signal histogram with an arbitrarily chosen cross section of 12 fb on top of the background distribution, which was obtained purely from the simulated samples without the data-driven background estimation.

During a *signal injection test* signals with varying cross sections are injected into the background distribution, and a bump scan is performed for every injected signal. For every bump scan, the significance of the result is calculated, and if that significance is larger than 3σ , the signal is considered to be *reliably detectable*. Table 6.8 presents the cross sections of the reliably detectable signals for both studied models and both considered signal regions.

A comparison between the reconstructed mass and H_T was conducted for this interpretation as well for the signal models considered by this search. However, the H_T variable is not Lorentz-invariant, and therefore it cannot provide a model-independent result. It is used in this study as the kinematic variable with the highest discriminating power for the studied models in order to compare the results that it provides with those obtained using the reconstructed mass. The reconstructed mass is Lorentz-invariant and therefore is suitable for providing a truly model-independent interpretation of the result. Figure 6.16 shows the H_T and reconstructed mass distribution for the two signal models in the SR 4b region, for the SM three- and four-top-quark events, and for the other background types.

Signal injection test is performed for H_T as well, and the cross sections of reliably detectable signals are presented in Table 6.8. For the two studied models H_T shows a similar performance to the reconstructed mass. It can also be observed that despite the large statistical uncertainty

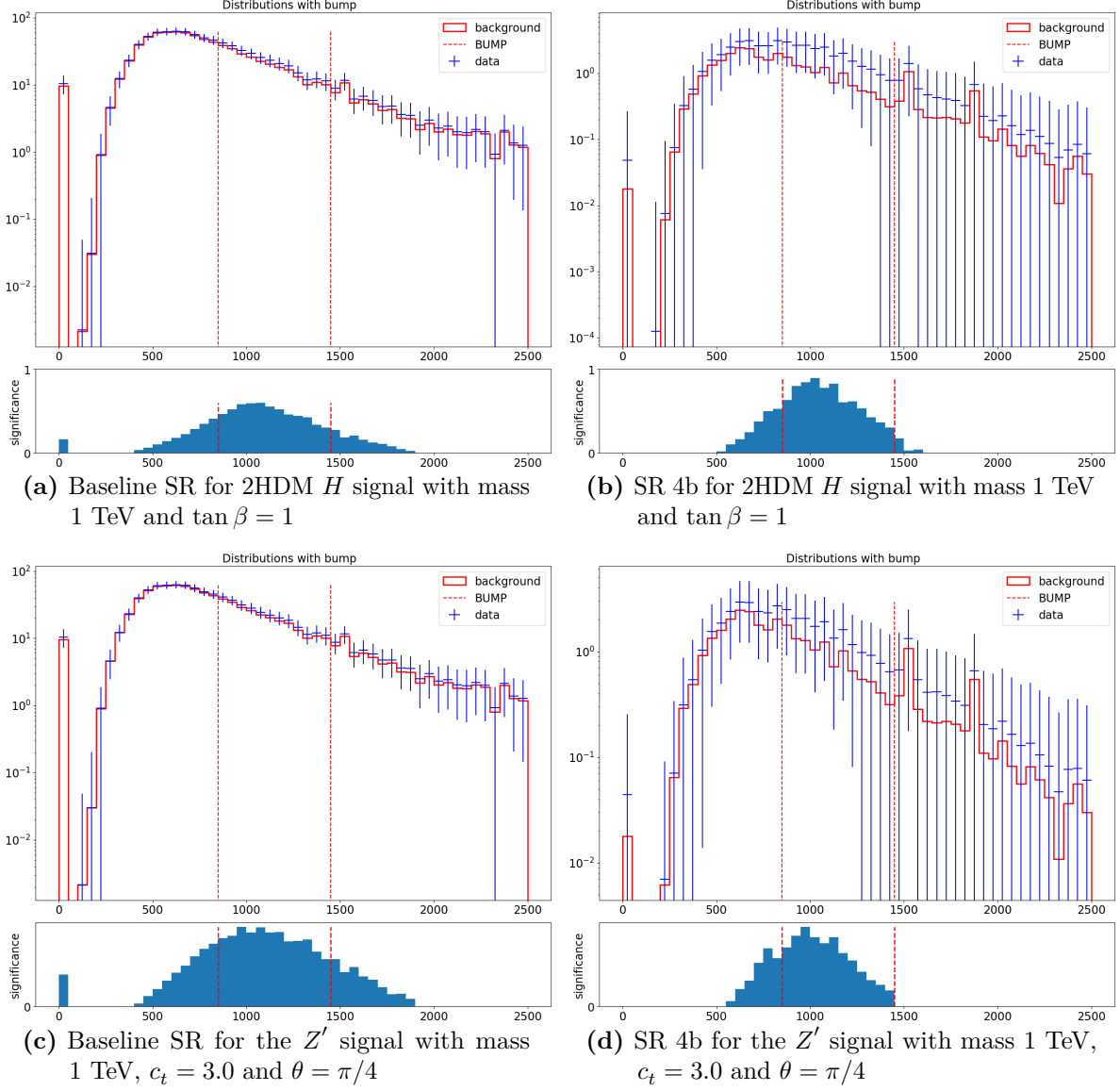


Figure 6.15: Bump scans for the two signal models with an arbitrary production cross section of 12 fb in the baseline SR and the SR 4b. The vertical lines show the window with the most significant deviation between the “data” and the background distributions. The plots are made using simulated events, and the “data” histograms are obtained by adding signal contributions to the simulated background events.

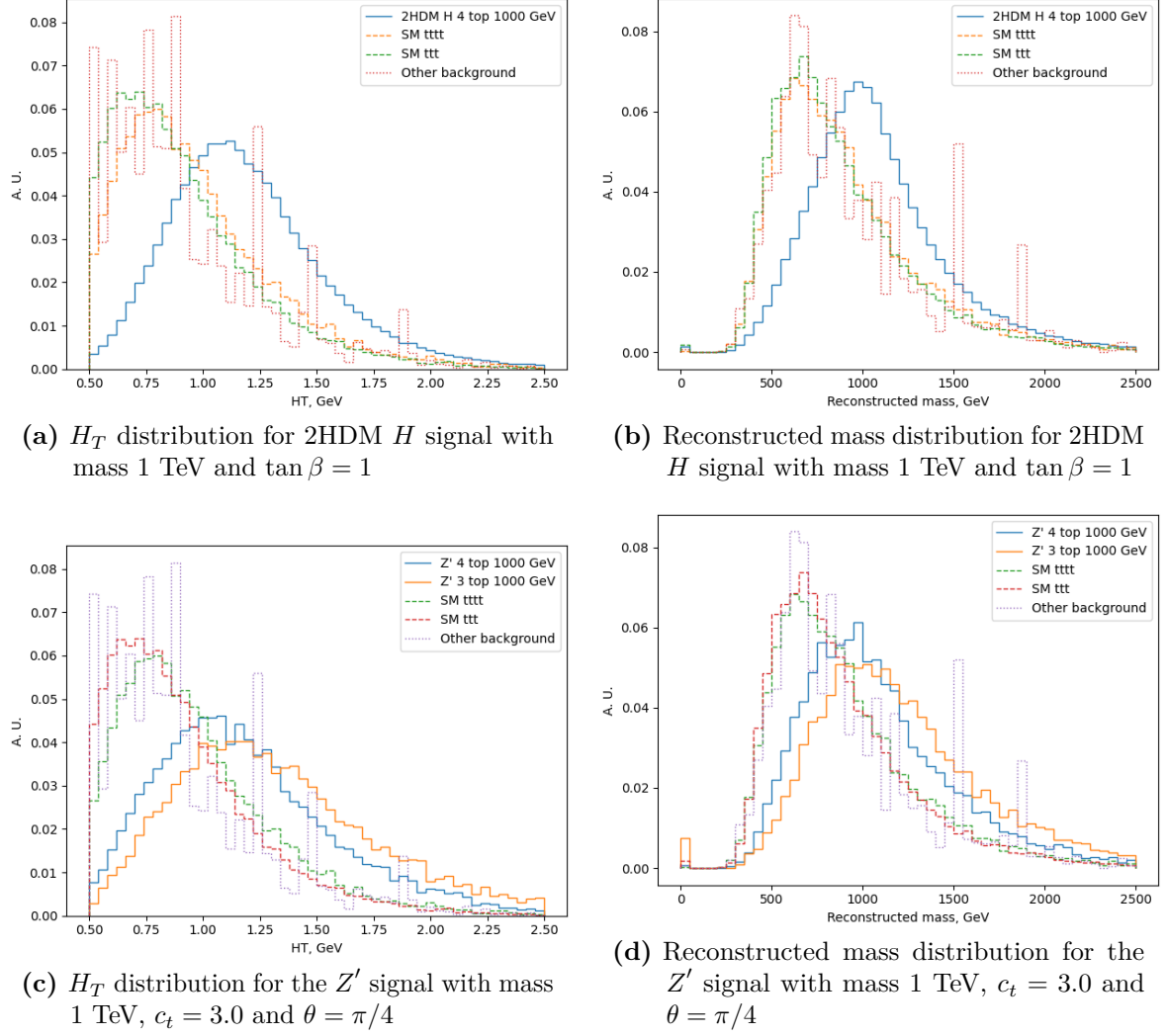


Figure 6.16: Distribution of the H_T variable and of the reconstructed mass in the SR 4b region for the two studied signals.

in the SR 4b region, signals with smaller cross sections can be reliably detected in this region than in the baseline SR.

Conclusions

Searches for new physics are an important part of modern particle physics, with experimental setups designed explicitly for such studies or optimized for both precision measurements of SM parameters and identification of physics BSM. The dataset collected by the ATLAS detector during the LHC Run 2 provides unprecedented opportunities to explore rare processes, such as the production of multi-top-quark final states, recently observed by both ATLAS and CMS. The excess in the number of observed events compared to the SM prediction hints at possible BSM contribution to this production, which are predicted by several BSM theories. Two searches for new physics in the multi-top-quark final state are presented in this thesis.

The first search targets heavy resonances with masses between 1 and 3 TeV using single-lepton final states in the ATLAS Run 2 dataset. The single-lepton signature allows effective use of single-lepton triggers while enabling direct reconstruction of the resonance through two reclustered jets, formed from its decay products. The invariant mass of these jets serves as the primary discriminating variable, providing both model-independent results, obtained by searching for localized excesses, and model-dependent results, obtained by performing a profile likelihood fit for a simplified top-philic vector resonance model. This search employs a data-driven background estimation, with the shape of the background distribution sampled from the data in a dedicated source region of the phase-space and its normalization determined in the signal-enriched signal regions using the simulated events. The model-independent result is obtained by searching for localized excesses in the reconstructed resonance mass distribution in the signal-enriched regions. The analysis observed no significant deviations from SM predictions, and exclusion limits, ranging from 20.6 fb to 118.6 fb, were set for various model parameters.

The second search focuses on SSML final states and benefits from better modeling techniques and better flavor-tagging algorithms. The development of this analysis is in progress and its setup is not yet finalized. This ongoing analysis employs data-driven background estimation and introduces an algorithm for reconstructing the resonance mass, overcoming the challenge of handling several neutrinos produced in the event, making this reconstruction more difficult, compared to the one in the previous search. The reconstructed mass demonstrates strong discriminating power between signal and background, comparable to the best kinematic variable H_T . Additionally, the reconstructed mass enables model-independent searches for localized excesses, extending the approach used in the single-lepton analysis. Furthermore, addition of the reconstructed mass as an input variable to the multivariate classifiers that will be used for

separation of signal and background in the future has a potential to improve the separation power of the classifier.

The larger statistics of the ongoing LHC Run 3 will benefit searches in the rare multi-top-quark final states. In addition, the improved Monte Carlo modeling of the background processes and the more advanced b -tagging algorithms further improve the sensitivity of the search. Modern machine learning classifiers will be used in the analysis to provide a model-dependent result, and the reconstructed resonance mass can be used to provide a model-independent result for the first time in final states with multiple leptons.

Future LHC runs, with their higher luminosity, necessitate significant upgrades to the ATLAS detector, particularly the complete replacement of the tracking system with the Inner Tracker (ITk). The ITk construction is a complicated process requiring collaborative effort from multiple institutes, including DESY, where modules for the ITk strip tracker are assembled and quality control is performed. This thesis describes the full module assembly process and all module quality control steps, including one of the most critical and demanding steps, the module thermal cycling. The thermal cycling is a stress-test, performed for every assembled module using dedicated setups. Careful tuning of parameters is required to ensure that the procedure is performed according to specifications. The DESY-specific PLC-controlled setup was successfully integrated into the common software framework designed for the thermal cycling, and DESY successfully qualified for module production with this setup. As the ITk project is entering the module production phase, it becomes crucial to monitor the process and identify deviations and irregularities in the procedures to ensure good quality of the assembled modules. For this purpose, a tool was created, interfacing with the ATLAS ITk production database, where all data about the performed tests is stored. This software compares the results of the IV curves measured at different module production steps and allows to monitor the quality of the production process.

Currently, the ITk project is entering the production phase. In the coming years the assembly of the ITk will conclude and the fully-instrumented detector will replace the Inner Detector to enable data-taking during the next LHC phase.

With ongoing advancements in analysis techniques, object reconstruction, and detector performance, coupled with the increased collision rates of future LHC runs, the potential for breakthroughs in BSM physics continues to grow. The work presented in this thesis contributes to these efforts, paving the way for further progress in the search for new physics.

Appendix

A Variables for communication with the PLC

Table A.1 lists the variables that are used for writing data into the PLC, and Table A.2 lists the variables that are used for reading data from the PLC.

Table A.1: Input variables of the PLC

| Variable name | Type | Units | Variable purpose |
|---------------------------------|------|-----------------------------|---|
| General thermal cycling control | | | |
| ModuleTestStop | Bool | – | Signaling to the PLC that the module test is finished and that the thermal cycling can be continued. |
| emergency_warmup | Bool | – | Signaling to the PLC that the thermal cycling needs to be interrupted and the box has to be warmed up to room temperature. |
| ncycle | Int | – | Setting the total number of thermal cycles (default 10). |
| mode | Int | – | Setting the operating mode of the cold-box: 0 – 'idle' for switching everything off, 1 – 'cycling' for automatic thermal cycling, 2 – 'manual' for manual testing with a possibility to switch the individual parts on and off manually. |
| Chuck.set_state_X | Bool | – | Turning the Peltier elements for chuck X on/off. |
| temperature.low | Int | $0.1 \times ^\circ\text{C}$ | Setting the lowest temperature of the cycles (default -35°C). |
| temperature.high | Int | $0.1 \times ^\circ\text{C}$ | Setting the highest temperature of the cycles (default $+20^\circ\text{C}$). |

Table A.1: Input variables of the PLC (Continued)

| Variable name | Type | Units | Variable purpose |
|---------------------------------------|-------|---------------------------------|--|
| Communication with the chiller | | | |
| chiller.pump | Int | % | Communicating the flow of the liquid in the chiller to the PLC. |
| chiller.temperature_external | Int | $0.1 \times ^\circ\text{C}$ | Communicating the temperature of the chiller coolant inside of the box to the PLC. |
| chiller.temperature_internal | Int | $0.1 \times ^\circ\text{C}$ | Communicating the temperature of the chiller coolant inside of the chiller to the PLC. |
| Module power and bias voltage control | | | |
| HV.set_state_X | Bool | – | Turning the output of the high voltage power supply for chuck X on/off. |
| HV.set_voltage_X | Float | V | Setting the bias voltage for the module on chuck X. |
| HV.compliance_current_X | Float | μA | Setting the current compliance limit for the module on chuck X. |
| HV.ramprate | Float | $0.1 \frac{\text{V}}{\text{s}}$ | Setting the ramp rate for the high voltage power supplies. |
| LV.set_state | Bool | – | Turn the output of the low voltage power supplies for all chucks on/off. |

Table A.2: Output variables of the PLC

| Variable name | Type | Units | Variable purpose |
|---------------------------------|------|-------|--|
| General thermal cycling control | | | |
| ModuleTestReady | Bool | – | Indicating if the module testing step of the thermal cycling is reached and the module test can be performed. |
| lid.state | Bool | – | Indicating if the coldbox is open. |
| bypass.state | Bool | – | Indicating if the bypass is on. |
| PLC.error_code | Int | – | Indicating if any safety feature integrated in the PLC was triggered: 0 – everything is ok, 1 – humidity is too high, 2 – temperature is too high, 3 – communication with the chiller is lost, 4 – error when setting the currents of the Peltier elements, 5 – error in communication with the power supply for the Peltier elements, 6 – error in the PLC, 7 – emergency warmup is triggered externally. |

Table A.2: Output variables of the PLC (Continued)

| Variable name | Type | Units | Variable purpose |
|---------------------------------------|-------|-----------------------------|---|
| Environment monitoring | | | |
| thermometer.CBX | Int | $0.1 \times ^\circ\text{C}$ | Reporting the temperature of the further from the module side of the Peltier elements in chuck X. |
| thermometer.CX | Int | $0.1 \times ^\circ\text{C}$ | Reporting the temperature of the closer to the module side of the Peltier elements in chuck X. |
| thermometer.AIR1 | Int | $0.1 \times ^\circ\text{C}$ | Reporting the temperature of the outgoing dry air from chucks 1 and 2. |
| thermometer.AIR2 | Int | $0.1 \times ^\circ\text{C}$ | Reporting the temperature of the outgoing dry air from chucks 3 and 4. |
| gas_flow | Int | $0.01 \times \text{l/min}$ | Reporting the flow of dry air to the modules. |
| RH.Y | Float | % | Reporting the relative humidity measured by sensor Y. |
| DP.1 | Float | $0.1 \times ^\circ\text{C}$ | Reporting the dew point value for the outgoing dry air from chucks 1 and 2. |
| DP.2 | Float | $0.1 \times ^\circ\text{C}$ | Reporting the dew point value for the outgoing dry air from chucks 3 and 4. |
| Peltier element monitoring | | | |
| peltier.current_X | Int | $0.01 \times \text{A}$ | Reporting the current supplied to the Peltier elements in chuck X. |
| peltier.voltage_X | Int | $0.01 \times \text{V}$ | Reporting the voltage supplied to the Peltier elements in chuck X. |
| peltier.state | Int | – | Indicating the state the Peltier elements are in: 0 – off, 1 – warmup, 2 – cooldown. |
| Communication with the chiller | | | |
| chiller.state | Bool | – | Turning the chiller on/off. |
| chiller.set_temperature | Int | $0.1 \times ^\circ\text{C}$ | Setting the target temperature for the chiller. |
| chiller.set_pump | Int | $0.1 \times ^\circ\text{C}$ | Setting the coolant flow in the chiller. |
| Module power and bias voltage control | | | |
| HV.on_X | Bool | – | Indicating if the high voltage output for the module on chuck X is enabled. |
| HV.voltage_reached_X | Bool | – | Indicating if the high voltage power supply for the module on chuck X has finished to ramp the voltage. |
| HV.hit_compliance_X | Bool | – | Indicating if the compliance current limit for the module on chuck X was reached. |
| HV.voltage_X | Float | V | Reporting the bias voltage applied to the module on chuck X. |
| HV.current_X | Float | μA | Reporting the high voltage power supply current value for the module on chuck X. |
| LV.state | Bool | – | Indicating if the low voltage power supplies for powering the modules are on. |

Table A.2: Output variables of the PLC (Continued)

| Variable name | Type | Units | Variable purpose |
|---------------|-------|-------|---|
| LV.current_X | Float | A | Reporting the low voltage power supply current value for the module on chuck X. |

List of Figures

| | | |
|-----|--|----|
| 1.1 | Schematic view of the Standard Model particles [19]. | 7 |
| 1.2 | Sample diagrams for production of the Z' particle, showcasing different possible production modes. (a) s-channel production via strong interaction, (b) production along with a top quark and another quark via electroweak interaction, (c) production along with a top quark and a W boson via mixed strong and electroweak interactions [33]. | 14 |
| 1.3 | A Feynman diagram showing the t-channel production of the Z' particle. | 14 |
| 1.4 | Feynman diagram showing the production of a scalar or pseudoscalar Higgs boson along with a pair of two top quarks, with the subsequent decay of the Higgs boson into a pair of top quarks. | 17 |
| 1.5 | Sample Feynman diagrams of four top quark production at leading order in the SM [38]. | 19 |
| 2.1 | Structure of the CERN accelerator complex [46]. | 22 |
| 2.2 | Schematic view of the ATLAS detector [48]. | 23 |
| 2.3 | Schematic view of the ATLAS Inner Detector [47, 50]. | 24 |
| 2.4 | Schematic view of ATLAS calorimeters [47]. | 25 |
| 2.5 | Schematic view of the ATLAS Muon System [47]. | 26 |
| 2.6 | Schematic view of the ATLAS forward detectors. IP – particle interaction point in the middle of ATLAS detector [47]. | 27 |
| 3.1 | Visualization of a quadrant of the ITk [59]. Only the sensitive units of each system are shown without support structures and cabling. The pixel subsystem is shown in green, and the strip subsystem is shown in blue. The beam collision point is marked with $\eta = 0.0$, $z = 0$ mm lines. | 30 |
| 3.2 | Cross-sectional view of a quadrant of the ITk. The horizontal axis is directed along the beam with the interaction point being at $z = 0$, the vertical axis shows the radial distance from the interaction point. The pixel layers are shown in red and the strip layers are shown in blue [60]. | 30 |
| 3.3 | Material distribution within the ITk volume in units of radiation length for various ITk components [60]. | 31 |
| 3.4 | Picture of an assembled stave [63]. A module is shown by the white rectangle, and the yellow rectangle surrounds the electronics used for reading out the data from the whole stave. | 32 |

| | | |
|------|---|----|
| 3.5 | Picture of an assembled petal with module type labels [62]. | 32 |
| 3.6 | Schematic view of ITk strip module parts (left) [58], and a photo of an ITk strip endcap R4 module assembled at DESY. The module is placed on a test frame, used for testing it electrically. | 33 |
| 3.7 | Tooling for assembling R2 modules. | 34 |
| 3.8 | Left: the process of attaching an HV-tab. Right: the attached tab on the back plane of an R2 sensor. The sensor is placed on a sensor jig with the back side facing up. | 34 |
| 3.9 | The glue dispensing robot (left) and a close-up view showing the position of a syringe filled with glue (right). | 35 |
| 3.10 | Front-end wire bonds, that connect the front-end chips to the sensor strips, placed in four rows [63]. | 36 |
| 3.11 | Examples of nominal and failing IV curves. | 37 |
| 3.12 | Setup for measuring IV curves for bare sensors. | 38 |
| 3.13 | Setup for single module testing: a light-tight box with an electrically insulated jig for module placement. Dry air is supplied to the setup, humidity and temperature inside of the box are measured by environment sensors. | 39 |
| 3.14 | Example of two IV curves and the different current scaling approaches | 42 |
| 3.15 | Distribution of coefficients for scaling from the reported test temperature to +20°C and coefficients obtained with minimization. | 43 |
| 3.16 | Dependence of the ratio of non-flagged procedures on the allowed current difference for the (a) – HV-tab attachment, (b) – shipping, (c) – storage. Orange, green, red and purple lines show the fractions of passed comparisons if only one of the criteria is used. Blue line shows the fraction if all criteria are used together. | 44 |
| 3.17 | Dependence of the ratio of non-flagged procedures on the allowed breakdown voltage difference for the (a) – HV-tab attachment, (b) – shipping, (c) – storage. Orange, green, red and purple lines show the fractions of passed comparisons if only one of the criteria is used. Blue line shows the fraction if all criteria are used together. | 45 |
| 3.18 | Numbers of flagged procedures for various institutions doing the test before HV-tab attachment (a), after shipping (b) and after long storage (c). | 47 |
| 3.19 | Numbers of flagged shipments for issues which occurred during shipping for comparison of IV curves before and after shipping between ATLAS sites. "All ok" means that no issues were observed for the shipping. | 48 |
| 3.20 | Numbers of flagged shipments for relative humidity level during shipping for comparison of IV curves before and after shipping between ATLAS sites. | 48 |
| 3.21 | Dependence of the percentage of flagged sensors in a shipment on the total number of sensors in the shipment. Each point corresponds to one shipment, with its x coordinate reflecting the number of sensors in the shipment and the y component reflecting the fraction of the sensors that are flagged. | 49 |
| 3.22 | Results of the comparison of the IV curves of the last test before HV-tab attachment and the first test after HV-tab attachment at the top, and the last test after the HV-tab attachment at the bottom, for different institutions. | 51 |
| 3.23 | Results of the comparison of the IV curves of the last test before HV-tab attachment and the first test after HV-tab attachment on the left, and the last test after HV-tab attachment on the right, for different sensor types. | 52 |
| 3.24 | Results of the comparison of the IV curves of the last test before distribution and the first test after it at the top, and the last test after the distribution at the bottom, for different institutions. | 52 |

| | | |
|------|---|----|
| 3.25 | Results of the comparison of the IV curves of the last test before distribution and the first test after it on the left, and the last test after distribution on the right, for different sensor types. | 53 |
| 3.26 | Results of the sensor recovery monitoring for various recovery techniques (left) and sensor types (right). | 54 |
| 3.27 | Sensor recovery information for sensor testing institutions. | 54 |
| 3.28 | Schematic cross section of a fully depleted silicon strip sensor. A depleted active zone without free charge carriers is maintained by applying bias voltage, and the charges created by a passing charged particle drift to the electrodes in the electric field. Image adapted from [69]. | 55 |
| 3.29 | The principle of binary readout. (a): current pulses of different amplitudes without noise. (b): dependence of hit fraction on the threshold charge for the case without noise. (c): current pulses of different amplitudes in the non-ideal case, the noise for the middle pulse is represented by the gray-shaded area. (d): dependence of hit fraction on the threshold charge for the case with noise. [64] | 56 |
| 3.30 | Example plots of a three-point gain measurement. Image adapted from [63]. | 58 |
| 3.31 | Left: 3D model of an endcap coldbox. Right: Cross section of a chuck. | 59 |
| 3.32 | The main components of the thermal cycling setup. | 60 |
| 3.33 | Module placement inside of the coldbox and the flow of dry air. | 61 |
| 3.34 | The electronics of the thermal cycling setup, including the PLC, the power supplies for the modules and the Peltier elements, the interlock control module and the relays for switching the state of the Peltier elements and the polarity of their voltage. | 62 |
| 3.35 | Left: coldbox safety interlock. Right: chiller flow bypass. | 62 |
| 3.36 | Top: schematic timeline of the thermal cycling procedure. Bottom: overview of the performed tests and the states of the module's components [77]. | 63 |
| 3.37 | Temperature change steps. Only the beginning and the end of the thermal cycling procedure is shown. The yellow line shows the temperature of the module and the green line shows the temperature that the chiller is set to. | 64 |
| 3.38 | Components required for the thermal cycling, including software and hardware parts (image made by Lukas Bayer). | 68 |
| 3.39 | Grafana display with plots from successful thermal cycling of two modules on chucks 3 and 4. The plots of the temperature of the Peltier elements, of the gradient of the modules' temperature, and of the temperature of the coolant are shown. The temperature gradient of $2.5^{\circ}\text{C}/\text{min}$ corresponds to $0.042^{\circ}\text{C}/\text{s}$ | 71 |
| 3.40 | Grafana display with plots from successful thermal cycling of two modules on chucks 3 and 4. The plots of the temperature of dry air at the output from the modules, the flow of dry air, relative humidity, and the dew point are shown. | 72 |
| 3.41 | Grafana display with plots from successful thermal cycling of two modules on chucks 3 and 4. The plots of the module bias voltage, the current powering the modules, and the current in the Peltier elements are shown. | 73 |
| 3.42 | Noise measurements for one of the hybrids of a preproduction R4 module. Each point corresponds to one channel. The left plot shows the channels corresponding to strips not covered by the hybrid, and the right plot shows the channels corresponding to the strips that the hybrid is glued on top of. The noise is given in units of equivalent noise charge (ENC). | 74 |
| 4.1 | Schematic passage of an electron through the ATLAS detector. The solid red line shows the trajectory of the electron, and the dashed line shows the trajectory of a photon produced by the interaction of the electron with detector material [92]. | 76 |

| | | |
|------|---|-----|
| 4.2 | Schematic diagram of the supercluster reconstruction procedure. The seed clusters are shown in red, and the satellite clusters in blue [93]. | 77 |
| 4.3 | Jet energy calibration steps [99]. | 84 |
| 5.1 | Sample Feynman diagrams of the tree-level s-channel production of Z' with association with (a) $t\bar{t}$, (b) tj , where j denotes any light quark, (c) tW . [109] . . | 90 |
| 5.2 | Feynman diagram of tree-level t-channel Z' production in association with $t\bar{t}$. . . | 90 |
| 5.3 | Examples of ditop mass distributions made using reweighted samples and the samples generated with the required parameters. The left plot shows reweighting applied for varying the chirality angle for the tWZ' events with the mass of the Z' boson of 1 TeV, and the right plot shows the reweighting applied in order to vary the coupling strength for the tjZ' events with the mass of the Z' boson of 1 TeV. For each plot, the nominal sample (solid blue line) was reweighted to different c_t or θ hypotheses (solid lines of other colors). The distributions for the generated signals are shown as dots. | 92 |
| 5.4 | The Feynman diagram of the single lepton final state with highlighted b - and additional jets. | 96 |
| 5.5 | Distributions of the number of additional jets on the left and the number of b -jets on the right for signal samples with different masses of the Z' particle and for the most significant background samples [109]. | 97 |
| 5.6 | Analysis regions defined using the number of additional jets (“a”) and the number of b -jets (“b”) in an event. Blue – source region, green – validation regions, red – signal regions [109]. | 97 |
| 5.7 | Visualization of one of the real data events in the ($\geq 4a, \geq 4b$) region. Red line is the muon track, b -tagged jets are shown in blue, RC jets in green and small-radius non- b -tagged jets in yellow [109]. | 98 |
| 5.8 | Background composition in the analysis regions. | 99 |
| 5.9 | Comparison of the shapes of the ditop mass (m_{JJ}) distribution for the simulated background events in the analysis region with the shape of that distribution in the (2a, 2b) source region. For each region, the distribution from the source region is scaled to match the integral of the background distribution in that region. The lower panel shows the ratio with the orange area showing the Poisson uncertainty of the denominator (2a, 2b) scaled. | 100 |
| 5.10 | The distribution of the ditop mass (m_{JJ}) for the data in the source region and the fitted to it dijet function. The bands show the uncertainties of the fit due to variations of the three parameters of the function. [109] | 100 |
| 5.11 | $t\bar{t}$ +jets background composition. | 102 |
| 5.12 | The distribution of the fitted signal strengths for the 500 pseudo-data sets sampled from the background distribution. All signal masses between 1 and 3 teV are presented, the signal model parameters are $c_t = 1$, $\theta = 0$ | 105 |
| 5.13 | Left: the mean signal bias values and the constructed polynomial envelope. Right: the mean of the Gaussian fit to the signal bias distribution divided by the standard deviation of that fit. All values are for the signals in the whole mass range, $c_t = 1$ and $\theta = 0$ | 106 |
| 5.14 | Comparison of the ditop mass (m_{JJ}) distribution obtained from data and the background prediction in the validation regions. The plot on the left corresponds to the (2a, 3b) region, and the plot on the right corresponds to the ($\geq 4a$, 2b) region. The data distribution agrees with the background prediction, and signal contamination for a Z' signal with mass 1.5 TeV $c_t = 1$ and $\theta = \pi/2$ is negligible in both validation regions [109]. | 109 |

| | | |
|------|--|-----|
| 5.15 | Results of the model-independent search in the signal regions with the windows with the most significant deviation highlighted by the two vertical lines. For reference, the expected distribution given a presence of a signal with mass 1.5 TeV $c_t = 1$ and $\theta = \pi/2$ and with an arbitrarily large cross section is shown on each plot [109]. | 111 |
| 5.16 | The ditop mass distributions in the signal regions before the profile likelihood fit. The colored red histogram shows the signal stacked on top of the background, and the dotted line shows the signal distribution normalized to the total number of background events overlaid with the background histogram. | 112 |
| 5.17 | The ditop mass distributions in the signal regions after the profile likelihood fit. The colored red histogram shows the signal stacked on top of the background, and the dotted line shows the signal distribution normalized to the total number of background events overlaid with the background histogram. | 113 |
| 5.18 | The expected signal strength limits for all considered parameters of the signal. The top table shows the limits for $\theta = 0$, while the bottom table shows the limits for $\theta = \pi/2$. All considered masses and coupling strengths are presented in each table [109]. | 114 |
| 5.19 | The observed signal strength limits for all considered parameters of the signal. The top table shows the limits for $\theta = 0$, while the bottom table shows the limits for $\theta = \pi/2$. All considered masses and coupling strengths are presented in each table [109]. | 115 |
| 5.20 | The expected and observed cross section limits as function of the signal mass for chirality angle $\theta = 0$ on the left and $\theta = \pi/2$ on the right. Both plots show the limits for $c_t = 1$ and $c_t = 4$, as well as the theoretical predictions for these parameters of the signal model [109]. | 116 |
| 5.21 | $t\bar{t}Z'$ (vector) and $t\bar{t}H/A$ (scalar) signal invariant mass distribution comparison in the $(\geq 4a, \geq 4b)$ region. The histograms are normalized to the same area. | 118 |
| 6.1 | A Feynman diagram of the SSML four top final state with exactly two leptons with the same sign electric charge [164]. | 120 |
| 6.2 | Comparison of transverse momenta of resonant and spectator top quarks. Left: the absolute values of the transverse momenta. Right: the difference between the momenta of the resonant and spectator top quarks in every event. For entries to the right of the red line the transverse momenta of the resonant top quarks are bigger than the transverse momenta of the spectator top quarks. | 126 |
| 6.3 | ΔR between objects coming from the same and different top quark decays. In the legend, the spectator top quarks are denoted with "S" and resonant top quarks – with "R". The histograms with "different" in the label include ΔR between the objects, coming from the decays of different top quarks, while the histograms with "same" in the label include ΔR between the objects, coming from the decay of the same top quark. | 128 |
| 6.4 | Coordinate systems used for neutrino momentum reconstruction [170]. Here, without loss of generality, a lepton is considered to be a muon. The momenta of the lepton, b -quark and the W boson are shown, and the angles between them are defined. Coordinate systems $\tilde{F}'(\tilde{x}', \tilde{y}', \tilde{z}')$ and $\tilde{F}(\tilde{x}, \tilde{y}, \tilde{z})$ share the z -axis with the laboratory coordinate system. | 129 |

- 6.5 An example of reconstructing the restrictions on the momentum of the W boson. Momenta of the b -quark and the lepton are shown in the left panel with arrows, the dashed lines show projections of ellipsoids constraining the momentum of the W boson onto the transverse plane. The dotted line P shows the projection of the surface containing the intersection of the two ellipsoids. On the right, the upper panel shows the intersection of the ellipsoids in one of the planes of P , and the lower panel shows the momenta of the lepton (black), b -quark (gray) and neutrino (dashed), as well as the projection of the ellipse from the upper panel on the transverse plane (light gray dashes). The ellipse constraining the possible neutrino solutions, obtained from the one constraining the momentum of the W boson, is shown as a solid black line, and the \times and the dotted line represent the MET and its uncertainty [170]. 130
- 6.6 An example of ellipses used to constrain neutrino transverse momenta. The black arrow shows the momentum of the first neutrino, the gray arrow shows the momentum of the second neutrino. The black and gray ellipses depict the constraints on the transverse momenta of the two neutrinos, and the dashed ellipse depicts the constraints on the momentum of the first neutrino obtained from the constraints on the momentum of the second one. \times shows the reconstructed MET, and the \circ shows the sum of the neutrino transverse momenta. The ellipse construction is done under assumption that they are equal. In this example, the ellipses have two intersection points, and therefore there are two possible solutions. [170] 131
- 6.7 An example of ellipses restricting the transverse momenta of the two neutrinos in the transverse plane. The blue ellipse restricts the transverse momentum of the first neutrino and obtained from decay kinematics of the first top quark and W boson, the orange ellipse restricts the transverse momentum of the second neutrino using the decay kinematics of the second top quark and W boson, and the red and green ellipses are obtained from the blue and the orange ones by expressing the transverse momenta of the neutrino using the MET and the transverse momentum of the other neutrino. The purple line connects the points of closest approach on the ellipses restricting the transverse momentum of the first neutrino, and the purple cross shows the middle point that is taken as an estimation of the transverse momentum of the first neutrino. 133
- 6.8 The reconstructed resonance mass for the signal with a mass of 1 TeV. Plot (a) shows the effects of the neutrino reconstruction method, plot (b) shows the effects of the formation of the top candidates and plot (c) shows the effects of the choice of objects using for the reconstruction. 136
- 6.9 Reconstructed resonance masses for four samples, Standard Model and 400 GeV, 1 TeV and 1.5 TeV 2HDM signals, for case with no truth information used and using reconstructed jets. The histograms are normalized to the same area. . . . 137
- 6.10 Dependence of the reconstructed resonance mass resolution on the case number for the four samples. Reconstructed jets are used for the mass reconstruction. . . 138

| | | |
|------|--|-----|
| 6.11 | Reconstructed mass for the 2HDM H/A sample with resonance mass of 1 TeV and $\tan\beta = 1$. The distributions are shown for events with exactly two leptons (electrons or muons) and no tau leptons on truth level, for events with exactly two leptons and no requirements on tau lepton absence, and for events with at least two leptons on truth level and no other event selection criteria applied. The reconstruction of the mass is performed without using any truth information. All histograms are normalized to the same area, the legend contains information about the total number of events that pass the applied selection and about the number of events with successfully reconstructed resonance mass. | 139 |
| 6.12 | The division of the baseline signal region to obtain the signal regions used in the fit. | 144 |
| 6.13 | Pre-fit distributions for the Asimov fit of H_T and reconstructed mass in the SR 4b region for the two studied signal models. The distributions for the signals are shown with the dashed line and are scaled by an arbitrary value for better visibility. | 146 |
| 6.14 | Pre-fit distributions of the fitted variables for background events in several control regions of the fit. The distributions are the same for both fit configurations and for both studied signal variants. | 147 |
| 6.15 | Bump scans for the two signal models with an arbitrary production cross section of 12 fb in the baseline SR and the SR 4b. The vertical lines show the window with the most significant deviation between the “data” and the background distributions. The plots are made using simulated events, and the “data” histograms are obtained by adding signal contributions to the simulated background events. | 149 |
| 6.16 | Distribution of the H_T variable and of the reconstructed mass in the SR 4b region for the two studied signals. | 150 |

List of Tables

| | | |
|-----|---|-----|
| 1.1 | The 2HDM model types which lead to natural flavor conservation. The three right columns depict the Higgs doublet, to which the corresponding particles couple. | 17 |
| 1.2 | Distribution of final state composition by lepton count. | 18 |
| 3.1 | Results of IV comparison for all three studied categories, broken down by individual comparison criteria. | 46 |
| 5.1 | The generators and the parameters used to model the signal and background processes. | 94 |
| 5.2 | Cross section uncertainties for background processes. | 103 |
| 5.3 | The contribution from different systematic uncertainties relative to the total uncertainty for two signal scenarios. | 117 |
| 5.4 | Obtained limits for $t\bar{t}Z'$ and $t\bar{t}H/A$ signals with mass of 1 TeV. | 117 |
| 6.1 | Summary of the simulated background samples used in the analysis. | 123 |
| 6.3 | Overlap removal criteria | 124 |
| 6.4 | The studied cases with varying degrees of truth information used for resonance reconstruction. | 135 |
| 6.6 | Two studied fit configurations. | 145 |
| 6.7 | Expected limits for the two signal models obtained with a statistics-only Asimov fit. | 145 |
| 6.8 | Cross sections of reliably detectable signals of both types in both signal regions for the bump scans performed using the reconstructed mass and the H_T distributions. | 148 |
| A.1 | Input variables of the PLC | 155 |
| A.1 | Input variables of the PLC (Continued) | 156 |
| A.2 | Output variables of the PLC | 156 |
| A.2 | Output variables of the PLC (Continued) | 157 |
| A.2 | Output variables of the PLC (Continued) | 158 |

Bibliography

- [1] G. Arnison et al., “Experimental observation of lepton pairs of invariant mass around 95 GeV/c² at the CERN SPS collider”, *Physics Letters B* **126** (1983) pp. 398–410, doi: 10.1016/0370-2693(83)90188-0.
- [2] G. Arnison et al., “Experimental observation of isolated large transverse energy electrons with associated missing energy at $\sqrt{s}=540$ GeV”, *Physics Letters B* **122** (1983) pp. 103–116, doi: 10.1016/0370-2693(83)91177-2.
- [3] PLUTO Collaboration, “Jet Analysis of the Υ (9.46) Decay Into Charged Hadrons”, *Phys. Lett. B* **82** (1979) pp. 449–455, doi: 10.1016/0370-2693(79)90265-X.
- [4] D0 Collaboration, “Observation of the Top Quark”, *Physical Review Letters* **74** (1995) pp. 2632–2637, doi: 10.1103/physrevlett.74.2632.
- [5] CDF Collaboration, “Observation of Top Quark Production in $\bar{p}p$ Collisions with the Collider Detector at Fermilab”, *Physical Review Letters* **74** (1995) pp. 2626–2631, doi: 10.1103/physrevlett.74.2626.
- [6] J. J. Aubert et al., “Experimental Observation of a Heavy Particle J ”, *Phys. Rev. Lett.* **33** (1974) pp. 1404–1406, doi: 10.1103/PhysRevLett.33.1404.
- [7] J. E. Augustin et al., “Discovery of a Narrow Resonance in e^+e^- Annihilation”, *Phys. Rev. Lett.* **33** (1974) pp. 1406–1408, doi: 10.1103/PhysRevLett.33.1406.
- [8] ATLAS Collaboration, “Observation of a new particle in the search for the Standard Model Higgs boson with the ATLAS detector at the LHC”, *Phys. Lett. B* **716** (2012) p. 1, doi: 10.1016/j.physletb.2012.08.020, [arXiv:1207.7214](#).
- [9] CMS Collaboration, “Observation of a new boson at a mass of 125 GeV with the CMS experiment at the LHC”, *Phys. Lett. B* **716** (2012) p. 30, doi: 10.1016/j.physletb.2012.08.021, [arXiv:1207.7235](#).
- [10] M. E. Peskin and D. V. Schroeder, “An Introduction to quantum field theory”. Addison-Wesley (1995).
- [11] M. D. Schwartz, “Quantum Field Theory and the Standard Model”. Cambridge University Press (2014).

- [12] G. Altarelli, “The Standard Model of Particle Physics”, (2005).
- [13] Bose, “Plancks Gesetz und Lichtquantenhypothese”, *Zeitschrift fuer Physik* **26** (1924) p. 178–181, doi: 10.1007/bf01327326.
- [14] *Proceedings of the Royal Society of London. Series A, Containing Papers of a Mathematical and Physical Character* **112** (1926) p. 661–677, doi: 10.1098/rspa.1926.0133.
- [15] A. Zannoni, “On the Quantization of the Monoatomic Ideal Gas”, (1999).
- [16] S. L. Glashow, “Partial-symmetries of weak interactions”, *Nuclear Physics* **22** (1961) pp. 579–588, doi: 10.1016/0029-5582(61)90469-2.
- [17] A. Salam, “Weak and electromagnetic interactions”, in *Selected Papers of Abdus Salam*, pp. 244–254. WORLD SCIENTIFIC, (1994).
- [18] S. Weinberg, “A Model of Leptons”, *Physical Review Letters* **19** (1967) pp. 1264–1266, doi: 10.1103/physrevlett.19.1264.
- [19] C. Burgard, “Example: Standard model of physics”.
<https://texample.net/tikz/examples/model-physics/>.
- [20] P. W. Anderson, “Plasmons, Gauge Invariance, and Mass”, *Phys. Rev.* **130** (1963) pp. 439–442, doi: 10.1103/PhysRev.130.439.
- [21] F. Englert and R. Brout, “Broken Symmetry and the Mass of Gauge Vector Mesons”, *Physical Review Letters* **13** (1964) p. 321–323, doi: 10.1103/physrevlett.13.321.
- [22] P. W. Higgs, “Broken Symmetries and the Masses of Gauge Bosons”, *Physical Review Letters* **13** (1964) p. 508–509, doi: 10.1103/physrevlett.13.508.
- [23] G. S. Guralnik, C. R. Hagen, and T. W. B. Kibble, “Global Conservation Laws and Massless Particles”, *Physical Review Letters* **13** (1964) p. 585–587, doi: 10.1103/physrevlett.13.585.
- [24] K. von Meyenn, “Über das Relativitätsprinzip und die aus demselben gezogenen Folgerungen”, p. 160–214. Vieweg+Teubner Verlag, (1990). doi: 10.1007/978-3-322-83770-7_6.
- [25] V. C. Rubin and J. Ford, W. Kent, “Rotation of the Andromeda Nebula from a Spectroscopic Survey of Emission Regions”, *The Astrophysical Journal* **159** (1970) p. 379, doi: 10.1086/150317.
- [26] H. W. Babcock, “The rotation of the Andromeda Nebula”, *Lick Observatory Bulletin* **498** (1939) pp. 41–51, doi: 10.5479/ADS/bib/1939LicOB.19.41B.
- [27] Super-Kamiokande Collaboration, “Evidence for Oscillation of Atmospheric Neutrinos”, *Phys. Rev. Lett.* **81** (1998) pp. 1562–1567, doi: 10.1103/PhysRevLett.81.1562.
- [28] SNO Collaboration, “Measurement of the Rate of $\nu_e + d \rightarrow p + p + e^-$ Interactions Produced by ^8B Solar Neutrinos at the Sudbury Neutrino Observatory”, *Phys. Rev. Lett.* **87** (2001) p. 071301, doi: 10.1103/PhysRevLett.87.071301.
- [29] Z. Maki, M. Nakagawa, and S. Sakata, “Remarks on the Unified Model of Elementary Particles”, *Progress of Theoretical Physics* **28** (1962) p. 870–880, doi: 10.1143/ptp.28.870.

-
- [30] B. Pontecorvo, “Inverse beta processes and nonconservation of lepton charge”, *Zh. Eksp. Teor. Fiz.* **34** (1957) p. 247.
 - [31] ATLAS Collaboration, “Observation of four-top-quark production in the multilepton final state with the ATLAS detector”, *The European Physical Journal C* **83** (2023) p. 496, doi: 10.1140/epjc/s10052-023-11573-0.
 - [32] CMS Collaboration, “Observation of four top quark production in proton-proton collisions at $\sqrt{s}=13\text{TeV}$ ”, *Physics Letters B* **847** (2023) p. 138290, doi: <https://doi.org/10.1016/j.physletb.2023.138290>.
 - [33] N. Greiner et al., “Model-independent production of a top-philic resonance at the LHC”, *Journal of High Energy Physics* **2015** (2015) p. 29, doi: 10.1007/JHEP04(2015)029.
 - [34] G. Branco et al., “Theory and phenomenology of two-Higgs-doublet models”, *Physics Reports* **516** (2012), no. 1, pp. 1–102, doi: <https://doi.org/10.1016/j.physrep.2012.02.002>. Theory and phenomenology of two-Higgs-doublet models.
 - [35] J. Bernon et al., “Scrutinizing the alignment limit in two-Higgs-doublet models: $m_h = 125 \text{ GeV}$ ”, *Phys. Rev. D* **92** (2015) p. 075004, doi: 10.1103/PhysRevD.92.075004.
 - [36] Kukla, Romain, “Probing composite models at the LHC with exotic quarks production”, *EPJ Web Conf.* **138** (2017) p. 01009, doi: 10.1051/epjconf/201713801009.
 - [37] P. A. Zyla et al., “Review of Particle Physics”, *Progress of Theoretical and Experimental Physics* **2020** (2020) doi: 10.1093/ptep/ptaa104.
 - [38] CMS Collaboration, “Evidence for four-top quark production in proton-proton collisions at $\sqrt{s} = 13 \text{ TeV}$ ”, *Physics Letters B* **844** (2023) p. 138076, doi: 10.1016/j.physletb.2023.138076.
 - [39] M. van Beekveld, A. Kulesza, and L. Moreno Valero, “Threshold Resummation for the Production of Four Top Quarks at the LHC”, *Phys. Rev. Lett.* **131** (2023) p. 211901, doi: 10.1103/PhysRevLett.131.211901.
 - [40] L. Evans and P. Bryant, “LHC Machine”, *Journal of Instrumentation* **3** (2008) p. S08001, doi: 10.1088/1748-0221/3/08/S08001.
 - [41] “LEP design report”. Report. CERN, Geneva (1984). Copies shelved as reports in LEP, PS and SPS libraries.
 - [42] ATLAS Collaboration, “ATLAS: technical proposal for a general-purpose pp experiment at the Large Hadron Collider at CERN”. LHC technical proposal. CERN, Geneva (1994).
 - [43] CMS Collaboration, “Technical proposal”. LHC technical proposal. CERN, Geneva (1994). Cover title : CMS, the Compact Muon Solenoid : technical proposal.
 - [44] ALICE Collaboration, “ALICE: Technical proposal for a Large Ion collider Experiment at the CERN LHC”. LHC technical proposal. CERN, Geneva (1995).
 - [45] LHCb Collaboration, “LHCb : Technical Proposal”. CERN, Geneva (1998).
 - [46] E. Lopienska, “The CERN accelerator complex, layout in 2022. Complexe des accélérateurs du CERN en janvier 2022” (2022). General Photo.

- [47] ATLAS Collaboration, “The ATLAS Experiment at the CERN Large Hadron Collider”, *Journal of Instrumentation* **3** (2008) p. S08003–S08003, doi: 10.1088/1748-0221/3/08/s08003.
- [48] R. M. Bianchi and A. Collaboration, “ATLAS experiment schematic or layout illustration”, (2022). General Photo.
- [49] A. La Rosa, “The ATLAS Insertable B-Layer: from construction to operation” (2016), doi: 10.48550/ARXIV.1610.01994.
- [50] ATLAS Collaboration, “Alignment of the ATLAS Inner Detector in Run 2”, *The European Physical Journal C* **80** (2020) doi: 10.1140/epjc/s10052-020-08700-6.
- [51] B. Stelzer, “The New Small Wheel Upgrade Project of the ATLAS Experiment”, *Nuclear and Particle Physics Proceedings* **273–275** (2016) p. 1160–1165, doi: 10.1016/j.nuclphysbps.2015.09.182.
- [52] ATLAS Collaboration, “The ATLAS experiment at the CERN Large Hadron Collider: a description of the detector configuration for Run 3”, *Journal of Instrumentation* **19** (2024) p. P05063, doi: 10.1088/1748-0221/19/05/P05063.
- [53] ATLAS Collaboration, “Operation of the ATLAS trigger system in Run 2”, *Journal of Instrumentation* **15** (2020) p. P10004–P10004, doi: 10.1088/1748-0221/15/10/p10004.
- [54] ATLAS Collaboration, “Triggering in ATLAS in Run 2 and Run 3”, *PoS EPS-HEP2021* (2022) p. 788, doi: 10.22323/1.398.0788.
- [55] ATLAS Collaboration, “ATLAS inner detector: Technical Design Report, 1”. Technical design report. ATLAS. CERN, Geneva (1997).
- [56] O. Aberle, et. al., “High-Luminosity Large Hadron Collider (HL-LHC): Technical Design Report”, *CERN Yellow Reports: Monographs* (2020).
- [57] ATLAS Collaboration, “Technical Design Report for the ATLAS Inner Tracker Pixel Detector”, technical report, Geneva (2017). <https://cds.cern.ch/record/2285585>, doi: 10.17181/CERN.FOZZ.ZP3Q.
- [58] ATLAS Collaboration, “Technical Design Report for the ATLAS Inner Tracker Strip Detector”, technical report, Geneva (2017). <https://cds.cern.ch/record/2257755>.
- [59] ATLAS Collaboration, “ATLAS Schematics”. <https://atlas.cern/Resources/Schematics>.
- [60] ATLAS Collaboration, “Expected tracking and related performance with the updated ATLAS Inner Tracker layout at the High-Luminosity LHC”, technical report, Geneva (2021). <https://cds.cern.ch/record/2776651>.
- [61] A.L. Heggelund on behalf of the ATLAS collaboration, “Overview of the ATLAS ITk pixel detector”, *Journal of Instrumentation* **18** (2023) p. C02014, doi: 10.1088/1748-0221/18/02/C02014.
- [62] S. Diez, “The ATLAS ITk strip local support structures”, *Nuclear Instruments and Methods in Physics Research Section A: Accelerators, Spectrometers, Detectors and Associated Equipment* **1066** (2024) p. 169552, doi: <https://doi.org/10.1016/j.nima.2024.169552>.

-
- [63] L. Poley et al., “The ABC130 barrel module prototyping programme for the ATLAS strip tracker”, *Journal of Instrumentation* **15** (2020) p. P09004, doi: 10.1088/1748-0221/15/09/P09004.
- [64] H. Kolanoski and N. Wermes, “Particle Detectors: Fundamentals and Applications”. Oxford University Press (2020).
- [65] Loctite, “LOCTITE ECCOBOND F 112”. https://www.henkel-adhesives.com/de/de/produkt/electrically-non-conductive-adhesives/loctite_eccobondf1120.html.
- [66] OGP, “Smartscope Flash CNC 300”. <https://www.ogpnet.com/products/metrology-systems/multisensor-metrology-systems/smartscope-video-multisensor-systems/smartscope-flash/smartscope-flash-302/>.
- [67] Elizaveta Sitnikova, “IV_comparison”. https://gitlab.cern.ch/esitniko/iv_comparison.
- [68] ATLAS Collaboration, “ATLAS ITk Production Database use and tools” (2024).
- [69] C. Klein et al., “Initial tests of large format sensors for the ATLAS ITk strip tracker”, *Nuclear Instruments and Methods in Physics Research Section A: Accelerators, Spectrometers, Detectors and Associated Equipment* **986** (2021) p. 164677, doi: <https://doi.org/10.1016/j.nima.2020.164677>.
- [70] ATLAS ITk Collaboration, “Module electrical testing”. <https://edms.cern.ch/document/2228451/3.7>.
- [71] ATLAS ITk Collaboration, “Endcap module coldbox”. <https://edms.cern.ch/document/2415369/3>.
- [72] Siemens, “SIMATIC S7-1200”. <https://www.siemens.com/de/de/produkte/automatisierung/systeme/industrie/sps/s7-1200.html>.
- [73] Julabo DYNEO DD-1000F Refrigerated / heating circulator. <https://www.julabo.com/en/products/refrigerated-circulators/refrigerated-heating-circulators/dyneo-dd-1000f>.
- [74] Diligent Nexys Video board. <https://diligent.com/reference/programmable-logic/nexys-video/start>.
- [75] ATLAS ITk Collaboration, “FMC-0514-DP”. <https://edms.cern.ch/document/2227474/1>.
- [76] Julabo, “Thermal H5”. <https://www.julabo.com/de/produkte/zubehoer/temperierfluessigkeiten-wasserbad-schutzmittel/thermal-h5-8940107>.
- [77] ATLAS Collaboration, “Thermal Cycling Sequence”. <https://gitlab.cern.ch/groups/ColdJigDCS/-/wikis/Thermal%20Cycling%20Sequence>.
- [78] K. Ang, G. Chong, and Y. Li, “PID Control System Analysis, Design, and Technology”, *Control Systems Technology, IEEE Transactions on* **13** (2005) pp. 559 – 576, doi: 10.1109/TCST.2005.847331.
- [79] Siemens, “Siemens TIA Portal”. <https://www.siemens.com/global/en/products/automation/industry-software/automation-software/tia-portal.html>.

- [80] “pySerial”. <https://pyserial.readthedocs.io/en/latest/index.html>.
- [81] ATLAS Collaboration, “ColdJigLib2”.
<https://gitlab.cern.ch/ColdJigDCS/coldjiglib2>.
- [82] Influx database. <https://www.influxdata.com/index/>.
- [83] ATLAS Collaboration, “ITSDAQ”.
<https://gitlab.cern.ch/atlas-itk-strips-daq/itsdaq-sw>.
- [84] Grafana. <https://grafana.com/>.
- [85] ATLAS Collaboration, “coldbox_controller_WebGUI”.
https://gitlab.cern.ch/ColdJigDCS/coldbox_controller_webgui.
- [86] The Modbus Organization, “MODBUS APPLICATION PROTOCOL SPECIFICATION”.
https://www.modbus.org/docs/Modbus_Application_Protocol_V1_1b3.pdf.
- [87] R. Frühwirth, “Application of Kalman filtering to track and vertex fitting”, *Nuclear Instruments and Methods in Physics Research Section A: Accelerators, Spectrometers, Detectors and Associated Equipment* **262** (1987) p. 444–450, doi: 10.1016/0168-9002(87)90887-4.
- [88] ATLAS Collaboration, “Performance of the ATLAS track reconstruction algorithms in dense environments in LHC Run 2”, *The European Physical Journal C* **77** (2017) p. 673, doi: 10.1140/epjc/s10052-017-5225-7.
- [89] T. Cornelissen et al., “The new ATLAS track reconstruction (NEWT)”, *Journal of Physics: Conference Series* **119** (2008) p. 032014, doi: 10.1088/1742-6596/119/3/032014.
- [90] ATLAS Collaboration, “Software Performance of the ATLAS Track Reconstruction for LHC Run 3”, *Computing and Software for Big Science* **8** (2024) doi: 10.1007/s41781-023-00111-y.
- [91] ATLAS Collaboration, “Performance of the ATLAS Inner Detector Track and Vertex Reconstruction in the High Pile-Up LHC Environment”, technical report, Geneva (2012).
<https://cds.cern.ch/record/1435196>.
- [92] ATLAS Collaboration, “Electron reconstruction and identification in the ATLAS experiment using the 2015 and 2016 LHC proton–proton collision data at $\sqrt{s} = 13$ TeV”, *The European Physical Journal C* **79** (2019) doi: 10.1140/epjc/s10052-019-7140-6.
- [93] ATLAS Collaboration, “Electron and photon performance measurements with the ATLAS detector using the 2015–2017 LHC proton-proton collision data”, *Journal of Instrumentation* **14** (2019) p. P12006–P12006, doi: 10.1088/1748-0221/14/12/p12006.
- [94] ATLAS Collaboration, “Improved electron reconstruction in ATLAS using the Gaussian Sum Filter-based model for bremsstrahlung”, technical report, Geneva (2012).
<https://cds.cern.ch/record/1449796>.
- [95] ATLAS Collaboration, “Muon reconstruction and identification efficiency in ATLAS using the full Run 2 pp collision data set at $\sqrt{s}=13$ TeV”, *The European Physical Journal C* **81** (2021) doi: 10.1140/epjc/s10052-021-09233-2.

-
- [96] J. Illingworth and J. Kittler, “A survey of the hough transform”, *Computer Vision, Graphics, and Image Processing* **44** (1988) p. 87–116, doi: 10.1016/s0734-189x(88)80033-1.
 - [97] ATLAS Collaboration, “Jet reconstruction and performance using particle flow with the ATLAS Detector”, *The European Physical Journal C* **77** (2017) doi: 10.1140/epjc/s10052-017-5031-2.
 - [98] M. Cacciari, G. P. Salam, and G. Soyez, “The anti-ktjet clustering algorithm”, *Journal of High Energy Physics* **2008** (2008) p. 063–063, doi: 10.1088/1126-6708/2008/04/063.
 - [99] ATLAS Collaboration, “Jet energy scale and resolution measured in proton–proton collisions at $\sqrt{s}=13$ TeV with the ATLAS detector”, *The European Physical Journal C* **81** (2021) doi: 10.1140/epjc/s10052-021-09402-3.
 - [100] S. D. Ellis and D. E. Soper, “Successive combination jet algorithm for hadron collisions”, *Physical Review D* **48** (1993) p. 3160–3166, doi: 10.1103/physrevd.48.3160.
 - [101] ATLAS Collaboration, “ATLAS flavour-tagging algorithms for the LHC Run 2 pp collision dataset”, *The European Physical Journal C* **83** (2023) doi: 10.1140/epjc/s10052-023-11699-1.
 - [102] ATLAS Collaboration, “Flavour tagging with graph neural networks with the ATLAS detector”, technical report, Geneva (2023). <https://cds.cern.ch/record/2860610>, arXiv:2306.04415.
 - [103] ATLAS Collaboration, “Neural Network Jet Flavour Tagging with the Upgraded ATLAS Inner Tracker Detector at the High-Luminosity LHC”, technical report, Geneva (2022). <https://cds.cern.ch/record/2839913>.
 - [104] ATLAS Collaboration, “Topological b -hadron decay reconstruction and identification of b -jets with the JetFitter package in the ATLAS experiment at the LHC”, technical report, Geneva (2018). <https://cds.cern.ch/record/2645405>.
 - [105] ATLAS Collaboration, “Tau Lepton Reconstruction in ATLAS”, *Nuclear and Particle Physics Proceedings* **287–288** (2017) p. 111–114, doi: 10.1016/j.nuclphysbps.2017.03.056.
 - [106] ATLAS Collaboration, “Reconstruction, Identification, and Calibration of hadronically decaying tau leptons with the ATLAS detector for the LHC Run 3 and reprocessed Run 2 data”, technical report, Geneva (2022). <https://cds.cern.ch/record/2827111>.
 - [107] ATLAS Collaboration, “Performance of missing transverse momentum reconstruction with the ATLAS detector using proton–proton collisions at $\sqrt{s}=13$ TeV”, *The European Physical Journal C* **78** (2018) doi: 10.1140/epjc/s10052-018-6288-9.
 - [108] ATLAS Collaboration, “ E_T^{miss} performance in the ATLAS detector using 2015-2016 LHC p-p collisions”, technical report, Geneva (2018). <https://cds.cern.ch/record/2625233>.
 - [109] ATLAS Collaboration, “Search for top-philic heavy resonances in pp collisions at $\sqrt{s} = 13$ TeV with the ATLAS detector”, *The European Physical Journal C* **84** (2024) p. 157, doi: 10.1140/epjc/s10052-023-12318-9.
 - [110] G. Choudalakis, “On hypothesis testing, trials factor, hypertests and the BumpHunter”, in *PHYSTAT 2011* (2011). arXiv:1101.0390.

- [111] ATLAS Collaboration, “Luminosity determination in pp collisions at $\sqrt{s} = 13$ TeV using the ATLAS detector at the LHC”, technical report, Geneva (2019).
<https://cds.cern.ch/record/2677054>.
- [112] J. Alwall et al., “The automated computation of tree-level and next-to-leading order differential cross sections, and their matching to parton shower simulations”, *Journal of High Energy Physics* **2014** (2014) doi: 10.1007/jhep07(2014)079.
- [113] R. D. Ball et al., “Parton distributions for the LHC run II”, *Journal of High Energy Physics* **2015** (2015) doi: 10.1007/jhep04(2015)040.
- [114] T. Sjöstrand et al., “An introduction to PYTHIA 8.2”, *Computer Physics Communications* **191** (2015) p. 159–177, doi: 10.1016/j.cpc.2015.01.024.
- [115] “ATLAS Pythia 8 tunes to 7 TeV data”, technical report, Geneva (2014).
<https://cds.cern.ch/record/1966419>.
- [116] O. Mattelaer, “On the maximal use of Monte Carlo samples: re-weighting events at NLO accuracy”, *The European Physical Journal C* **76** (2016) doi: 10.1140/epjc/s10052-016-4533-7.
- [117] ATLAS Collaboration, “The ATLAS Simulation Infrastructure”, *The European Physical Journal C* **70** (2010) pp. 823–874, doi: 10.1140/epjc/s10052-010-1429-9.
- [118] S. Agostinelli et al., “Geant4—a simulation toolkit”, *Nuclear Instruments and Methods in Physics Research Section A: Accelerators, Spectrometers, Detectors and Associated Equipment* **506** (2003), no. 3, pp. 250–303, doi: [https://doi.org/10.1016/S0168-9002\(03\)01368-8](https://doi.org/10.1016/S0168-9002(03)01368-8).
- [119] ATLAS Collaboration, “The simulation principle and performance of the ATLAS fast calorimeter simulation FastCaloSim”, technical report, Geneva (2010).
<https://cds.cern.ch/record/1300517>.
- [120] ATLAS Collaboration, “Summary of ATLAS Pythia 8 tunes”, technical report, Geneva (2012). <https://cds.cern.ch/record/1474107>.
- [121] A. D. Martin, W. J. Stirling, R. S. Thorne, and G. Watt, “Parton distributions for the LHC”, *The European Physical Journal C* **63** (2009) p. 189–285, doi: 10.1140/epjc/s10052-009-1072-5.
- [122] T. Gleisberg et al., “Event generation with SHERPA 1.1”, *Journal of High Energy Physics* **2009** (2009) p. 007–007, doi: 10.1088/1126-6708/2009/02/007.
- [123] D. J. Lange, “The EvtGen particle decay simulation package”, *Nuclear Instruments and Methods in Physics Research Section A: Accelerators, Spectrometers, Detectors and Associated Equipment* **462** (2001) p. 152–155, doi: 10.1016/s0168-9002(01)00089-4.
- [124] S. Frixione, G. Ridolfi, and P. Nason, “A positive-weight next-to-leading-order Monte Carlo for heavy flavour hadroproduction”, *Journal of High Energy Physics* **2007** (2007) p. 126–126, doi: 10.1088/1126-6708/2007/09/126.
- [125] P. Nason, “A New Method for Combining NLO QCD with Shower Monte Carlo Algorithms”, *Journal of High Energy Physics* **2004** (2004) p. 040–040, doi: 10.1088/1126-6708/2004/11/040.

-
- [126] S. Frixione, P. Nason, and C. Oleari, “Matching NLO QCD computations with parton shower simulations: the POWHEG method”, *Journal of High Energy Physics* **2007** (2007) p. 070–070, doi: 10.1088/1126-6708/2007/11/070.
- [127] S. Alioli, P. Nason, C. Oleari, and E. Re, “A general framework for implementing NLO calculations in shower Monte Carlo programs: the POWHEG BOX”, *Journal of High Energy Physics* **2010** (2010) doi: 10.1007/jhep06(2010)043.
- [128] ATLAS Collaboration, “Studies on top-quark Monte Carlo modelling for Top2016”, technical report, Geneva (2016). <https://cds.cern.ch/record/2216168>.
- [129] S. Frixione et al., “Single-top hadroproduction in association with a W boson”, *Journal of High Energy Physics* **2008** (2008) p. 029–029, doi: 10.1088/1126-6708/2008/07/029.
- [130] M. Bähr et al., “Herwig++ physics and manual”, *The European Physical Journal C* **58** (2008) p. 639–707, doi: 10.1140/epjc/s10052-008-0798-9.
- [131] J. Bellm et al., “Herwig 7.0/Herwig++ 3.0 release note”, *The European Physical Journal C* **76** (2016) doi: 10.1140/epjc/s10052-016-4018-8.
- [132] L. A. Harland-Lang, A. D. Martin, P. Motylinski, and R. S. Thorne, “Parton distributions in the LHC era: MMHT 2014 PDFs”, *The European Physical Journal C* **75** (2015) doi: 10.1140/epjc/s10052-015-3397-6.
- [133] B. Nachman et al., “Jets from jets: re-clustering as a tool for large radius jet reconstruction and grooming at the LHC”, *Journal of High Energy Physics* **2015** (2015) doi: 10.1007/jhep02(2015)075.
- [134] D. Krohn, J. Thaler, and L.-T. Wang, “Jet trimming”, *Journal of High Energy Physics* **2010** (2010) doi: 10.1007/jhep02(2010)084.
- [135] ATLAS Collaboration, “Performance of the ATLAS muon triggers in Run 2”, *Journal of Instrumentation* **15** (2020) p. P09015–P09015, doi: 10.1088/1748-0221/15/09/p09015.
- [136] ATLAS Collaboration, “Performance of electron and photon triggers in ATLAS during LHC Run 2”, *The European Physical Journal C* **80** (2020) doi: 10.1140/epjc/s10052-019-7500-2.
- [137] T. H. Kittelmann, V. Tsulaia, J. Boudreau, and E. Moyse, “The virtual point 1 event display for the ATLAS experiment”, *J. Phys. Conf. Ser.* **219** (2010) p. 032012, doi: 10.1088/1742-6596/219/3/032012.
- [138] ATLAS Collaboration, “Search for pair production of up-type vector-like quarks and for four-top-quark events in final states with multiple b-jets with the ATLAS detector”, *Journal of High Energy Physics* **2018** (2018) doi: 10.1007/jhep07(2018)089.
- [139] ATLAS Collaboration, “Measurements of top-quark pair differential cross-sections in the lepton+jets channel in pp collisions at $\sqrt{s} = 13$ TeV using the ATLAS detector”, *Journal of High Energy Physics* **2017** (2017) doi: 10.1007/jhep11(2017)191.
- [140] ATLAS Collaboration, “Search for the standard model Higgs boson produced in association with top quarks and decaying into a $b\bar{b}$ pair in pp collisions at $\sqrt{s} = 13$ TeV with the ATLAS detector”, *Physical Review D* **97** (2018) doi: 10.1103/physrevd.97.072016.

- [141] ATLAS Collaboration, “Search for new resonances in mass distributions of jet pairs using 139 fb1 of pp collisions at $\sqrt{s} = 13$ TeV with the ATLAS detector”, *Journal of High Energy Physics* **2020** (2020) doi: 10.1007/jhep03(2020)145.
- [142] ATLAS Collaboration, “Search for new massive particles decaying into a top-anti-top quark pair using top-tagged jets with 2015-2018 data at $\sqrt{s} = 13$ TeV”, technical report, Geneva (2018). <https://cds.cern.ch/record/2646839>.
- [143] ATLAS Collaboration, “Performance of pile-up mitigation techniques for jets in pp collisions at $\sqrt{s} = 8$ TeV using the ATLAS detector”, *The European Physical Journal C* **76** (2016) doi: 10.1140/epjc/s10052-016-4395-z.
- [144] ATLAS Collaboration, “Jet Calibration and Systematic Uncertainties for Jets Reconstructed in the ATLAS Detector at $\sqrt{s} = 13$ TeV”, technical report, Geneva (2015). <https://cds.cern.ch/record/2037613>.
- [145] ATLAS Collaboration, “Jet energy measurement with the ATLAS detector in proton-proton collisions at $\sqrt{s} = 7$ TeV”, *The European Physical Journal C* **73** (2013) doi: 10.1140/epjc/s10052-013-2304-2.
- [146] ATLAS Collaboration, “ATLAS b-jet identification performance and efficiency measurement with $t\bar{t}$ events in pp collisions at $\sqrt{s} = 13$ TeV”, *The European Physical Journal C* **79** (2019) doi: 10.1140/epjc/s10052-019-7450-8.
- [147] ATLAS Collaboration, “Calibration of the light-flavour jet mistagging efficiency of the b-tagging algorithms with Z+jets events using 139 fb⁻¹ of ATLAS proton–proton collision data at $\sqrt{s} = 13$ TeV”, *The European Physical Journal C* **83** (2023) doi: 10.1140/epjc/s10052-023-11736-z.
- [148] ATLAS Collaboration, “Measurement of the c-jet mistagging efficiency in $t\bar{t}$ events using pp collision data at $\sqrt{s} = 13$ TeV collected with the ATLAS detector”, *The European Physical Journal C* **82** (2022) doi: 10.1140/epjc/s10052-021-09843-w.
- [149] ATLAS Collaboration, “Muon reconstruction performance of the ATLAS detector in proton–proton collision data at $\sqrt{s} = 13$ TeV”, *The European Physical Journal C* **76** (2016) doi: 10.1140/epjc/s10052-016-4120-y.
- [150] ATLAS Collaboration, “Measurements of inclusive and differential fiducial cross-sections of $t\bar{t}$ production with additional heavy-flavour jets in proton-proton collisions at $\sqrt{s} = 13$ TeV with the ATLAS detector”, *Journal of High Energy Physics* **2019** (2019) doi: 10.1007/jhep04(2019)046.
- [151] CMS Collaboration, “Measurement of the $t\bar{t}b\bar{b}$ production cross section in the all-jet final state in pp collisions at $\sqrt{s} = 13$ TeV”, *Physics Letters B* **803** (2020) p. 135285, doi: 10.1016/j.physletb.2020.135285.
- [152] CERN, “CERN Yellow Reports: Monographs, Vol 2 (2017): Handbook of LHC Higgs cross sections: 4. Deciphering the nature of the Higgs sector”, (2017). doi: 10.23731/CYRM-2017-002.
- [153] ATLAS Collaboration, “Combined measurements of Higgs boson production and decay using up to 80 fb⁻¹ of proton-proton collision data at $\sqrt{s} = 13$ TeV collected with the ATLAS experiment”, *Physical Review D* **101** (2020) doi: 10.1103/physrevd.101.012002.

-
- [154] ATLAS Collaboration, “Evidence for $t\bar{t}\bar{t}\bar{t}$ production in the multilepton final state in proton–proton collisions at $\sqrt{s} = 13$ TeV with the ATLAS detector”, *The European Physical Journal C* **80** (2020) doi: 10.1140/epjc/s10052-020-08509-3.
 - [155] J. Alwall et al., “Comparative study of various algorithms for the merging of parton showers and matrix elements in hadronic collisions”, *The European Physical Journal C* **53** (2007) p. 473–500, doi: 10.1140/epjc/s10052-007-0490-5.
 - [156] ATLAS Collaboration, “Measurement of the $t\bar{t}t\bar{t}$ production cross section in pp collisions at $\sqrt{s} = 13$ TeV with the ATLAS detector”, *Journal of High Energy Physics* **2021** (2021) doi: 10.1007/jhep11(2021)118.
 - [157] J. Butterworth et al., “PDF4LHC recommendations for LHC Run II”, *Journal of Physics G: Nuclear and Particle Physics* **43** (2016) p. 023001, doi: 10.1088/0954-3899/43/2/023001.
 - [158] ATLAS Collaboration, “Recommendations for the Modeling of Smooth Backgrounds”, technical report, Geneva (2020). <https://cds.cern.ch/record/2743717>.
 - [159] G. Cowan, K. Cranmer, E. Gross, and O. Vitells, “Asymptotic formulae for likelihood-based tests of new physics”, *The European Physical Journal C* **71** (2011) doi: 10.1140/epjc/s10052-011-1554-0.
 - [160] A. L. Read, “Presentation of search results: theCLstechnique”, *Journal of Physics G: Nuclear and Particle Physics* **28** (2002) p. 2693–2704, doi: 10.1088/0954-3899/28/10/313.
 - [161] “RECAST for ATLAS”. <https://recast.docs.cern.ch/>.
 - [162] “Docker”. <https://docs.docker.com/build-cloud/>.
 - [163] ATLAS Collaboration, “Search for $t\bar{t}H/A$ to $t\bar{t}t\bar{t}$ production in the multilepton final state in proton–proton collisions at $\sqrt{s} = 13$ TeV with the ATLAS detector”, *Journal of High Energy Physics* **2023** (2023) p. 203, doi: 10.1007/JHEP07(2023)203.
 - [164] J. H. Kim, K. Kong, S. J. Lee, and G. Mohlabeng, “Probing TeV scale top-philic resonances with boosted top-tagging at the high luminosity LHC”, *Phys. Rev. D* **94** (2016) p. 035023, doi: 10.1103/PhysRevD.94.035023.
 - [165] ATLAS Collaboration, “Preliminary analysis of the luminosity calibration for the ATLAS 13.6 TeV data recorded in 2023”, technical report, Geneva (2024). <https://cds.cern.ch/record/2900949>.
 - [166] P. Artoisenet, R. Frederix, O. Mattelaer, and R. Rietkerk, “Automatic spin-entangled decays of heavy resonances in Monte Carlo simulations”, *Journal of High Energy Physics* **2013** (2013) doi: 10.1007/jhep03(2013)015.
 - [167] C. Bierlich et al., “A comprehensive guide to the physics and usage of PYTHIA 8.3”, *SciPost Physics Codebases* (2022) doi: 10.21468/scipostphyscodeb.8.
 - [168] E. Bothmann et al., “Event generation with Sherpa 2.2”, *SciPost Physics* **7** (2019) doi: 10.21468/scipostphys.7.3.034.
 - [169] ATLAS Collaboration, “Electron Charge ID Selector Tool”. <https://twiki.cern.ch/twiki/bin/viewauth/AtlasProtected/ElectronChargeFlipTaggerTool>.

- [170] B. A. Betchart, R. Demina, and A. Harel, “Analytic solutions for neutrino momenta in decay of top quarks”, *Nuclear Instruments and Methods in Physics Research Section A: Accelerators, Spectrometers, Detectors and Associated Equipment* **736** (2014) p. 169–178, doi: 10.1016/j.nima.2013.10.039.
- [171] R. Frederix, D. Pagani, and M. Zaro, “Large NLO corrections in $t\bar{t}W^\pm$ and $t\bar{t}t\bar{t}$ hadroproduction from supposedly subleading EW contributions”, *Journal of High Energy Physics* **2018** (2018) p. 31, doi: 10.1007/JHEP02(2018)031.
- [172] ATLAS Collaboration, “Measurement of $W^\pm Z$ production cross sections and gauge boson polarisation in pp collisions at $\sqrt{s} = 13$ TeV with the ATLAS detector”, *Eur. Phys. J. C* **79** (2019) p. 535, doi: 10.1140/epjc/s10052-019-7027-6, arXiv:1902.05759.
- [173] ATLAS Collaboration, “Measurement of the production cross-section of a single top quark in association with a Z boson in proton–proton collisions at 13 TeV with the ATLAS detector”, technical report, Geneva (2017). <https://cds.cern.ch/record/2273868>.
- [174] F. Demartin et al., “ $t\bar{t}WH$ associated production at the LHC”, *The European Physical Journal C* **77** (2017) p. 34, doi: 10.1140/epjc/s10052-017-4601-7.
- [175] ATLAS Collaboration, “Measurement of $W^\pm Z$ production cross sections and gauge boson polarisation in pp collisions at $\sqrt{s} = 13$ TeV with the ATLAS detector”, *The European Physical Journal C* **79** (2019) p. 535, doi: 10.1140/epjc/s10052-019-7027-6.
- [176] ATLAS Collaboration, “Analysis of $t\bar{t}H$ and $t\bar{t}W$ production in multilepton final states with the ATLAS detector”, technical report, Geneva (2019). <https://cds.cern.ch/record/2693930>.
- [177] L. Vaslin, “pyBumpHunter”. doi: 10.5281/zenodo.7684558.

Acknowledgements

I would like to express my deepest gratitude to my PhD supervisors, Krisztian Peters and Sergio Díez Cornell, for their exceptional guidance throughout my doctoral journey. Their insight, encouragement, and support were invaluable, and this work would not have been possible without them. I am also sincerely thankful to Kerstin Tackmann, my supervisor from the University of Hamburg, for her advice and guidance during my PhD.

I am thankful to the DESY ATLAS group for such a warm and supportive working environment. This positive atmosphere greatly contributed to my productivity and growth.

I am especially grateful to the postdoctoral researchers who supported me during the early stages of my PhD. Petar Bokan and Philipp Gadow helped me navigate the complexities of the ATLAS experiment, teaching me about various aspects of the projects and offering invaluable guidance in adapting to the dynamics of such a large and diverse collaboration.

I would also like to thank the DESY ATLAS ITk module building team, particularly Sarah Heim and Christian Sander, for their exceptional organization and leadership, which allowed me to contribute meaningfully to multiple aspects of the ITk project. Additionally, I extend my sincere thanks to Lukas Bayer, Ben Brüers, Sören Ahrens, and Torsten Külper for their indispensable help in finalizing the thermal cycling setup. I am also grateful to Luise Poley, Vitaliy Fadeyev, and Xavi Fernandez-Tejero for sharing their expertise and providing valuable insights during the creation of the module production monitoring tool.

For the first search for new physics in multi-top-quark final states, I am deeply appreciative of Alicia Wongel and Elise Le Boulicaut Ennis, the two main analyzers in this project, for helping me to contribute to the final results of the analysis.

Regarding the second search for BSM physics in multi-top-quark final states, I am particularly thankful to Tom Nommensen for his valuable insights and discussions on various aspects of the reconstruction algorithms, as well as to Neelam Kumari for her patience and the many fruitful discussions that aided me in finalizing the mass reconstruction algorithm.

It was a great pleasure to be part of these two analysis teams and I am grateful to the team members for all the discussions that we had during the analysis meetings.

Lastly, I would like to thank my family – my parents, my brother, and my partner – for their unwavering support and encouragement, and for their ability to help me navigate stress and offer a fresh perspective during challenging times. Without their moral support, I could not have succeeded in my PhD work.